

UC Berkeley

UC Berkeley Electronic Theses and Dissertations

Title

Gas Diffusion in Metals: Fundamental Study of Helium-Point Defect Interactions in Iron and Kinetics of Hydrogen Desorption from Zirconium Hydride

Permalink

<https://escholarship.org/uc/item/3j97w6bw>

Author

Hu, Xunxiang

Publication Date

2013

Peer reviewed|Thesis/dissertation

Gas Diffusion in Metals: Fundamental Study of Helium-Point Defect Interactions in Iron
and Kinetics of Hydrogen Desorption from Zirconium Hydride

By

Xunxiang Hu

A dissertation submitted in partial satisfaction of the

requirements for the degree of

Doctor of Philosophy

in

Engineering – Nuclear Engineering

in the

Graduate Division

of the

University of California, Berkeley

Committee in charge:

Professor Brian D. Wirth, Chair

Professor Jasmina Vujic

Professor Mark Asta

Spring 2013

Abstract

Gas Diffusion in Metals: Fundamental Study of Helium-Point Defect Interactions in Iron and Kinetics of Hydrogen Desorption from Zirconium Hydride

by

Xunxiang Hu

Doctor of Philosophy in Engineering – Nuclear Engineering

University of California, Berkeley

Professor Brian D. Wirth, Chair

The behavior of gaseous foreign species (e.g., helium and hydrogen), which are either generated, adsorbed or implanted within the structural materials (e.g., iron and zirconium) exposed to irradiation environments, is an important and largely unsolved topic, as they intensively interact with the irradiation-induced defects, or bond with the lattice atoms to form new compounds, and impose significant effects on their microstructural and mechanical properties in fission and fusion reactors. This research investigates two cases of gas diffusion in metals (i.e., the helium-point defect interactions in iron and kinetics of hydrogen desorption from zirconium hydride) through extensive experimental and modeling studies, with the objective of improving the understanding of helium effects on the microstructures of iron under irradiation and demonstrating the kinetics of hydrogen diffusion and precipitation behavior in zirconium that are crucial to predict cladding failures and hydride fuel performance.

The study of helium effects in structural materials aims to develop a self-consistent, experimentally validated model of helium – point defect, defect cluster and intrinsic defects through detailed inter-comparisons between experimental measurements on helium ion implanted iron single crystals and computational models. The combination of thermal helium desorption spectrometry (THDS) experiment with the cluster dynamic model helps to reveal the influence of impurities on the energetics and kinetics of the He-defect interactions and to realize the identification of possible mechanisms governing helium desorption peaks. Positron annihilation spectroscopy is employed to acquire additional information on He-vacancy cluster evolution, which provides an opportunity to validate the model qualitatively. The inclusion of He – self-interstitial clusters extends the cluster dynamic model while MD simulations explore the effects of dislocation loops on helium clustering. In addition, the influence of pre-existing defects on helium behavior in iron is studied by applying a hybrid model, which includes the defect evolution during neutron irradiation and the subsequent He ion implantation and THDS. These modeling predictions will be assessed in future experiments.

The hydrogen desorption process from zirconium hydride and zirconium in vacuum is also studied by coordinated experimental and modeling methods. The production and verification of the desired δ -zirconium hydride is discussed while thermal desorption spectroscopy (TDS) is employed to obtain the hydrogen desorption spectra directly. In addition, a one-dimensional two-phase moving boundary model coupled with a kinetic description of hydrogen desorption from a two-phase region of δ -ZrH_{1.6±n} and α -Zr is developed to compare with the TDS experimental results.

To my family

Table of Contents

LIST OF FIGURES	V
LIST OF TABLES	X
ACKNOWLEDGEMENTS	XI
CHAPTER 1 INTRODUCTION	1
1.1 FUNDAMENTAL STUDY OF HELIUM-POINT DEFECT INTERACTIONS IN IRON	1
1.1.1 Background	1
1.1.2 Materials challenges of fission and fusion	2
1.1.3 Helium effects on properties of materials	5
1.1.4 Previous work on understanding the mechanisms of helium effects	8
1.1.5 Research objectives and approach	10
1.2 KINETICS OF HYDROGEN DESORPTION FROM ZIRCONIUM HYDRIDE	12
1.2.1 Zirconium hydride produced in structural components	12
1.2.1.1 Background	12
1.2.1.2 Generation of zirconium hydride	13
1.2.2 Zirconium hydride used in hydride fuel	13
CHAPTER 2 EXPERIMENTAL STUDIES OF HELIUM-POINT DEFECT INTERACTION ..	15
2.1 THERMAL HELIUM DESORPTION SPECTROMETRY (THDS)	15
2.1.1 Introduction	15
2.1.2 Thermal helium desorption spectrum of He-implanted poly- and single-crystalline (PC and SC) iron following linear temperature ramping profile ..	21
2.1.3 Helium desorption spectra of new samples with stated purity of 99.98% ..	23
2.2 POSITRON ANNIHILATION SPECTROSCOPY (PAS)	27
2.2.1 Introduction	27
2.2.2 Data analysis	30
2.2.3 Positron lifetime measurements of helium implanted single-crystal irons ..	32
2.3 CONCLUSION	35
CHAPTER 3 SPATIALLY DEPENDENT CLUSTER DYNAMICS MODEL BASED ON RATE THEORY	37
3.1 PHYSICAL PROCESS	37
3.2 MODEL CONSTRUCTION	38
3.3 PARAMETERIZATION	44
3.4 NUMERICAL SOLUTION	49
3.5 MODELING RESULTS	50
3.5.1 Simulation of THDS using a linear temperature profile	50
3.5.2 Simulation of THDS using a step-like temperature profile	53
3.5.3 Binding energies for small He_xV_y clusters	54
3.5.4 Cluster evolution	55
3.6 PHASE-CUT METHOD TO IMPROVE THE COMPUTING EFFICIENCY	56
3.7 CONCLUSION	59
CHAPTER 4 QUANTITATIVE AND QUALITATIVE ANALYSIS OF HE-POINT DEFECT INTERACTIONS	60
4.1 INFLUENCE OF CARBON ON ENERGETICS AND KINETICS OF HE – POINT DEFECT INTERACTION	60
4.1.1 THDS results of He implanted single crystal irons with different purities ..	60

4.1.2 Modeling the He desorption from the new, 99.98% pure single crystal iron samples following a linear temperature profile	62
4.2 MECHANISTIC INTERPRETATION OF HELIUM DESORPTION PEAKS AND HELIUM-VACANCY CLUSTER EVOLUTION	65
4.3 PREDICTION OF LONG LIFETIME IN PAL	68
4.4 COMPARISON OF THE CLUSTER EVOLUTIONS PREDICTED BY THE MODEL USING TWO DIFFERENT BATCHES OF ENERGETIC PARAMETERS	72
4.5 CONCLUSION	77
CHAPTER 5 INFLUENCE OF THE INTERACTIONS OF HELIUM AND SELF-INTERSTITIALS ON HELIUM BEHAVIOR IN IRON	78
5.1 INFLUENCE OF HE-SIA INTERACTIONS ON THDS SIMULATION	78
5.1.1 Inclusion of He-SIA interactions in the model	78
5.1.2 Energetics of He-SIA clusters	80
5.1.3 Modeling results	83
5.2 MD SIMULATIONS OF THE INFLUENCE OF SELF-INTERSTITIAL LOOP ON HE CLUSTERING IN BCC IRON	87
5.3 COMPARISON OF MD SIMULATION AND CLUSTER DYNAMIC MODELING ON THE HELIUM IMPLANTATION IN BCC IRON	91
5.4 CONCLUSION	95
CHAPTER 6 INFLUENCE OF PRE-EXISTING POINT DEFECTS AND DEFECT CLUSTERS ON HELIUM BEHAVIOR IN IRON	97
6.1 PLANS OF THE EXPERIMENTAL STUDY	97
6.2 NEUTRON IRRADIATION	98
6.2.1 Model construction	98
6.2.2 Parameterization	100
6.2.3 Results	106
6.3 THERMAL HELIUM DESORPTION	111
6.3.1 THDS of He implanted samples at lower fluence ($1 \times 10^{18} / m^2$)	112
6.3.2 THDS of He implanted samples at higher fluence ($1 \times 10^{19} / m^2$)	115
6.4 CONCLUSION	117
CHAPTER 7 KINETICS OF HYDROGEN DESORPTION FROM ZIRCONIUM HYDRIDE AND ZR METAL IN VACUUM	118
7.1 SYNTHESIS OF ZIRCONIUM HYDRIDE	118
7.1.1 Hydriding system	118
7.1.2 Experimental procedure	119
7.1.3 Characterization of the produced zirconium hydride	124
7.2 THERMAL DESORPTION SPECTROMETRY (TDS)	127
7.3 A CONTINUOUS HYDROGEN DESORPTION MODEL FROM ZIRCONIUM HYDRIDE AND SUBSEQUENT METAL IN VACUUM	128
7.3.1 Problem description	129
7.3.2 Determination of initial and boundary conditions by applying the kinetics of hydrogen desorption from δ -ZrH _{1.6±n} and α -Zr	131
7.3.3 Numerical analysis	133
7.3.4 Results and discussions	134
7.4 CONCLUSION	137
CHAPTER 8 CONCLUSION AND FUTURE WORK	138
8.1 CONCLUSION	138
8.1.1 Fundamental study of helium-point defect interactions in iron	138

8.1.2 Kinetics of hydrogen desorption from zirconium hydride	139
8.2 FUTURE WORK	139
8.2.1 Future work for the helium-point defect interactions in iron	139
8.2.2 Future work for the kinetics of hydrogen desorption from zirconium hydride and Zr.....	140
REFERENCES.....	141

List of Figures

Figure 1-1. Influence of the helium concentration (pre-implanted at 1023 K) on the creep properties of AISI 316 SS: (a) creep rupture time; (b) creep rupture elongation, as reproduced from Ref. [39].	7
Figure 1-2. Illustration of an integrated experimental and computational approach to the multiscale investigation of materials behavior in the fusion environment. The central part of the figure describes a hierarchical approach based on passing information or parameters, and connecting key mechanisms (denoted by arrows), starting from the electronic/atomic up to structural length and time scales. A number of microstructural characterization techniques important for validating model predictions are represented on the lower right side, including the techniques of positron annihilation spectroscopy (PAS), small angle neutron scattering (SANS) and TEM. The upper left side of the diagram represents experimental techniques to measure mechanical properties, as reproduced from Ref. [46].	11
Figure 2-1. The principle of a THDS procedure when probing He-point defect interaction.	16
Figure 2-2. (a). Schematic illustration of THDS system in UC Berkeley; (b). Picture of partial system of THDS.	17
Figure 2-3. Background and total pressure of the system for the non-implanted iron sample in the annealing process, as reproduced from [183].	18
Figure 2-4. Illustration of the system dynamic process.	19
Figure 2-5. Schematic illustration of the calibration system.	20
Figure 2-6. Thermal helium desorption spectra of the samples: high purity single- and poly-crystalline irons, low purity poly-crystal iron, as reproduced from Ref. [54].	22
Figure 2-7. Desorption spectra of high purity single-crystal irons implanted with ^4He at: (a) 10 keV, $1 \times 10^{15} \text{ He/cm}^2$; (b) 20 keV, $1 \times 10^{15} \text{ He/cm}^2$; (c) 40 keV, $1 \times 10^{15} \text{ He/cm}^2$.	25
Figure 2-8. Helium and vacancy distribution for (a) 20 keV and (b) 40 keV helium implantation in iron calculated by SRIM 2008.	26
Figure 2-9. (a) Decay scheme of ^{22}Na , as reproduced from Ref. [107]; (b) Positron evolution in material.	28
Figure 2-10. Schematic diagram of the positron lifetime spectrometer.	29
Figure 2-11. Positron lifetime spectrum for single-crystal iron with a purity of 99.98%.	30
Figure 2-12. Helium desorption spectrum of high purity (99.98%) single crystal iron following implantation of 40 keV, $1 \times 10^{15} / \text{cm}^2$. Three temperature points of	

interest (i.e., I as irradiated; II 300 °C; III 750 °C) are marked to do the positron lifetime analysis.	32
Figure 2-13. Positron lifetime measurement and analysis for three different conditions: (a) as irradiated; (b) annealing at 300 °C; (c) annealing at 750 °C.	33
Figure 2-14. Two components analysis of the positron annihilation lifetime spectrum after each step of the annealing for the high purity single-crystal irons implanted by He-4 of 40 keV, 1×10^{15} He/cm ²	35
Figure 3-1. Schematic illustration of defect configurations and jumps processes related to He diffusion under irradiation. (1) migration of interstitial He; (2) migration of vacancy; (3) transformation of a substitutional to an interstitial He atom by thermally activated dissociation; (4) jump of a He atom from one to another vacancy as a basic step in the vacancy mechanism; (5) transformation of a substitutional to an interstitial He atom due to its replacement by a self-interstitial.	37
Figure 3-2. Helium concentration and damage distribution as a function of depth for (a) 5 keV and (b) 10 keV He-ion implantation in irons calculated by TRIM/SRIM 2008.	45
Figure 3-3. 3-D view of the binding energies of (a) helium, (b) vacancy, and (c) interstitial to the He-vacancy clusters.	48
Figure 3-4. Binding energies of He, vacancy, interstitial to He-vacancy clusters as a function of He/V ratio.	49
Figure 3-5. Comparison of experimentally measured thermal helium desorption from high purity (99.94%) single crystal iron implanted with 10 keV He to a fluence of 10^{14} He/cm ² , with the modeling results, as reproduced from Ref. [71].	51
Figure 3-6. Experimental (gray dots) and predicted (solid lines) He desorption spectra from single crystal iron with a purity of 99.94% implanted with ⁴ He ions, for different implantation energy (5 keV and 10 keV) and fluence (10^{18} He/m ² and 10^{19} He/m ²), as reproduced from Ref. [72].	52
Figure 3-7. Experimental (green circle) and modeling (red solid line) prediction of the helium desorption spectra in single crystal iron with a purity of 99.94% implanted with ⁴ He ions, following step-like temperature profiles denoted by purple (set temperatures) and blue lines (measured temperatures), for the specimen with the implantation condition of 5 keV, 10^{19} He/m ²	53
Figure 3-8. Cluster evolution in He-V phase space at five representative depth positions in alpha iron following He ion implantation at 810 °C, obtained with a small phase space size, as reproduced from Ref. [128].	57
Figure 3-9. Cluster evolution in He-V phase space at five representative depth positions in alpha iron following He ion implantation at 900 °C, obtained with a large phase space size and the phase-cut method, as reproduced from Ref. [128].	58

Figure 4-1. He desorption spectrum of the single crystal irons with the purities of 99.94% (green line) and 99.98% (blue line) implanted with He ion at 10 keV, 1×10^{15} He/cm ² .	61
Figure 4-2. Experimental (open symbols) and predicted (red solid lines and black dash lines) He desorption spectra in single crystal iron of high purity following implantation of (a) 10 keV, 1×10^{15} He/cm ² ; (b) 20 keV, 1×10^{15} He/cm ² ; (c) 40 keV, 1×10^{15} He/cm ² . Black dash lines are the modeling predictions using the previously defined set of kinetic parameters, as described in Chapter 3.	64
Figure 4-3. Experimental (open symbols) and predicted (solid lines) He desorption spectra in single crystalline iron of high purity (99.98%) following implantation of 40keV, 1×10^{15} He/cm ² ; Major shrinkage of small clusters are labeled nearby the corresponding He desorption peaks; Three points of interest are marked for the cluster evolution analysis.	66
Figure 4-4. Computed cluster distribution for the three selected points: (a) after irradiation, (b) at 573 K, (c) at 1023 K.	67
Figure 4-5. (a) Correlation between positron lifetime and the number of vacancies in a void in BCC iron; (b) Correlation between positron lifetime and the number of He atoms in the He-vacancy clusters, as reproduced from Ref. [111].	69
Figure 4-6. Measured and calculated positron long lifetimes for the three selected points.	72
Figure 4-7. He-vacancy cluster phase space snapshots showing the cluster distribution evolution during the thermal annealing (at 1 °C/s heating rate) at a depth of 37 nm for the specimen implanted with 10 keV He to a fluence of 10^{18} He/m ² for two different cases: (a) using the energetic parameters for the modeling of the old samples; (b) using the energetic parameters for the modeling of the new samples.	74
Figure 4-8. He-vacancy cluster phase space snapshots showing the cluster distribution evolution during the thermal annealing (at 1 °C/s heating rate) at a depth of 37 nm for the specimen implanted with 10 keV He to a fluence of 10^{19} He/m ² for two different cases: (a) using the energetic parameters for the modeling of the old samples; (b) using the energetic parameters for the modeling of the new samples.	76
Figure 5-1. Schematic illustration of the cluster transitions in a 2-D phase space.	79
Figure 5-2. The He-binding energies of complexes containing 1, 2, and 4 interstitial heliums with 1, 2, 6, 11, and 20 SIA clusters obtained from conjugate gradient molecular statics calculations, as reproduced from Ref.[62]. The data of the complex containing 3 interstitial helium is obtained by interpolation of the existing data.	80
Figure 5-3. Binding energies of (a, b) He and (c, d) self-interstitial to He-SIA clusters.	82
Figure 5-4. Comparison of the simulations that include and exclude He-SIA interactions for the THDS measurement of the single crystal iron implanted by 10 keV He ion to a fluence of 10^{14} He /cm ² .	83

Figure 5-5. The fraction of retained He in different complexes during the annealing process.	85
Figure 5-6. He-vacancy/SIA cluster phase space snapshots showing the cluster distribution evolution during the thermal annealing (at 1 °C/s heating rate) at a depth of 37 nm for the specimen implanted with 10 keV He to a fluence of 10^{14} He/cm ²	86
Figure 5-7. Snapshots of the different stages for the helium implantation in BCC iron: (a) without dislocation loop; (b) with dislocation loop. SIA atoms are denoted by grey color; He atoms are denoted by blue color.	88
Figure 5-8. Number of interstitial helium not in clusters during the implantation process for the two simulation conditions that included a dislocation loop versus being performed in an otherwise perfect crystal.....	89
Figure 5-9. Cluster distribution analysis in the He implantation process for two simulation conditions: (a) without dislocation; (b) with dislocation.	90
Figure 5-10. He-V cluster distribution at the end of the He implantation process: (a) simulation with one mobile He cluster; (b) simulation with six mobile He clusters; (c) simulation with six mobile He clusters and modified D_0	93
Figure 5-11. Comparison of the results from MD and three different clusters dynamic simulations.	94
Figure 6-1. PKA spectrum in neutron irradiated iron in HFIR.....	102
Figure 6-2. Visible interstitial clusters (with diameters greater than 1.3 nm) concentrations during the neutron irradiation process.....	107
Figure 6-3. Model predictions of the evolution of interstitial cluster size distribution in iron exposed to neutron irradiation in HFIR at (a) 300 °C and (b) 500 °C.	109
Figure 6-4. The average size of the visible interstitial clusters as a function of irradiation damage. The experimental data are from Ref. [152].	110
Figure 6-5. Modeling predictions comparing the influence of pre-existing defect microstructures induced by neutron irradiation at 300 °C and 1.2 dpa on the THDS for the samples implanted with 10 keV He to a fluence of 10^{18} He/m ²	112
Figure 6-6. He-vacancy cluster phase space snapshots showing the cluster distribution evolution during the thermal annealing (at 1 °C/s heating rate) at a depth of 37 nm for the specimen implanted with 10 keV He to a fluence of 10^{18} He/m ² for two different cases: (a) previous results without neutron irradiation; (b) new modeling including neutron irradiation.....	113
Figure 6-7. Modeling predictions including and excluding neutron irradiation of the THDS for the samples implanted with 10 keV He to a fluence of 10^{19} He/m ²	115
Figure 6-8. He-vacancy cluster phase space snapshots showing the cluster distribution evolution during the thermal annealing (at 1 °C/s heating rate) at a depth of	

37 nm for the specimen implanted with 10 keV He to a fluence of 10^{19} He/m ² for two different cases: (a) previous results without neutron irradiation; (b) new modeling including neutron irradiation.....	116
Figure 7-1. (a) Picture of the hydriding system; (b) Schematic illustration of the hydriding system.	119
Figure 7-2. Phase diagram for Zr-H system [161] with equilibrium H ₂ isobars labeled as	121
Figure 7-3. Characteristic diffusion times as a function of temperature for a specimen with a thickness of 1 mm.	121
Figure 7-4. Hydrogen permeation rate as a function of system pressure under different temperature conditions.....	122
Figure 7-5. Temperature profile and hydrogen pressure during a typical hydriding process.	123
Figure 7-6. Surface view of ZrHTGA-2 (a) before and (b) after hydriding.	124
Figure 7-7. Powder X-ray diffraction patterns for (a) ZrHTGA-4, (b) ZrHTGA-6, and ZrHTGA-10.	125
Figure 7-8. Hydrogen desorption spectrum and temperature profiles in TDS experiment of ZrHTGA-10.....	128
Figure 7-9. (a) Schematic illustration of the concentration profile at time t in the vicinity of the two-phase interface in planar geometry; (b) Numerical method employed to analyze movement of the interface.	130
Figure 7-10. Evolution of H/Zr ratio distribution throughout the δ -ZrH _{1.6±n} disc.	134

List of Tables

Table 1-1. Austenitic stainless steels: spallation, fusion and Generation IV fission applications, as reproduced from Ref. [29].	4
Table 1-2. Ferritic/martensitic steels: fusion, and Generation IV fission applications as reproduced from Ref. [29].	4
Table 1-3. Irradiation conditions and measured swelling for Type 316 Stainless Steel irradiated in HFIR, as reproduced from Ref. [38].	5
Table 3-1. Binding Energies of small interstitial and vacancy clusters in iron according to Ref. [126].	46
Table 3-2. Comparison of the binding energies for small He_xV_y ($x, y = 1-5$) clusters predicted by ab initio (indicated by 'A'), MD (indicated by 'M'), and thermodynamic (indicated by 'T') calculations. The asterisks label optimized values used in the modeling, as reproduced from Ref. [72].	55
Table 4-1. Chemical analysis of the two batches of single-crystal irons (in a unit of weight percentage, %).	62
Table 4-2. Comparison of the binding energies (eV) of helium for small He-V clusters calculated by different methods and used in different batches of samples.	65
Table 4-3. Positron lifetimes and concentrations of the major clusters at point I.	70
Table 4-4. Positron lifetimes and concentrations of the major clusters at point II.	71
Table 4-5. Positron lifetimes and concentrations of the major clusters at point III.	71
Table 5-1. Migration energies and diffusivity coefficients of the mobile He clusters.	95
Table 6-1. Irradiation conditions for single crystal irons placed in HFIR.	97
Table 6-2. Mobility set for interstitial clusters/loops and single vacancy.	101
Table 6-3. Fractions of surviving point defects contained in small clusters and survival efficiency of point defects, for four different cascade energy intervals.	103
Table 6-4. Intra-cascade cluster production probabilities in 1/PKA.	104
Table 6-5. Intra-cascade cluster production rates in $1/(\text{cm}^3 \text{ s})$	106
Table 6-6. Groups of the visible interstitial clusters.	110
Table 7-1. Lattice parameters of phases present in the samples determined through Rietveld refinement.	126
Table 7-2. H/Zr ratio calculated by different methods for the three samples.	126

Acknowledgements

I would like to express my deepest gratitude to all who contribute and support my doctoral dissertation and graduate student life at University of California, Berkeley.

First, it has been my great privilege and great pleasure to work under the supervision of my advisor, Professor Brian D. Wirth. I could not have completed my research work without his insightful advice, persistent encouragement, and constant support. Working with Brian is the most brilliant decision that I have ever made since I came to USA. I also want to express my sincere respect to his academic enthusiasm and professional dedication.

Special thanks are given to Dr. Donghua Xu for leading me to the current research field and guiding me to do THDS and PAS experiments and cluster dynamics modeling. I would like to express my sincere appreciation to him and show my earnest respect to his academic passion and talents.

I also want to pay my sincere respect to Professors at UC Berkeley, Mark Asta, Joonhong Ahn, and Jasmina Vujic, who have not only given precious lectures to me but also offered great advice during my qualifying exam.

I also specially give my appreciation to Dr. Kurt A. Terrani who has hosted and supported me to work at Oak Ridge National Laboratory (ORNL) for the project of hydrogen desorption from zirconium hydride.

In addition, I would like to thank my current and past colleagues in the great Wirth Research Group.

I would like to express my deep gratitude to my parents, parents-in-law, and brother for all of their support, endless love, and encouragement.

Finally, I take this opportunity to express my deepest love and overwhelming thank to my wife, Jiao, for her sacrifice and love.

Chapter 1

Introduction

1.1 Fundamental study of helium-point defect interactions in iron

1.1.1 Background

With the United Nations predicting world population growth from 6.6 billion in 2007 to 8.2 billion by 2030 [1], demand for energy must increase substantially over that period [2]. Various energy analysis [3] have concluded that the world will need greatly increased energy supply in the next 20 years, especially cleanly-generated electricity. The World Energy Outlook 2012 and Electricity Information 2012 from the OECD's International Energy Agency (IEA) states that electricity demand is increasing twice as fast as overall energy use and is likely to rise 67% from 2010 to 2035. Currently, fossil fuels (i.e. coal 40.4%, natural gas 22.2%) still dominates the world's electricity mix. However, as observed by Holdren [4] early in the 1990s, the era of cheap energy, but energy that has a significant detrimental effect on our environment, is coming to an end. Environmental concerns associated with fossil fuels are creating increased interest in alternative non-fossil energy sources. The renewable energy sources for electricity constitute a diverse group, from wind, solar, tidal and wave energy to hydro, geothermal and biomass-based power generation. Apart from hydropower in the few places where it is very plentiful, none of these is suitable, intrinsically or economically, for large-scale power generation where continuous, reliable supply is needed. In contrast, fission and fusion energy are two potential environmentally sustainable large-scale energy options [5-10].

Nuclear (fission) power generation is an established part of the world's electricity mix providing in 2011 some 12.3% of world electricity [11]. It is especially suitable for large-scale, continuous electricity demand, which requires reliability, and hence ideally matched to increasing energy demand worldwide. The renewed interest in fission is more focused on advanced fission energy, reflected in the U.S. Department of Energy Global Nuclear Energy Partnership and Generation IV advanced reactor programs [7], with reactors designed for better economics and safety. Today's drivers for the use of nuclear power have evolved:

(1) Increasing energy demand

Global population growth in combination with industrial development will lead to a doubling of electricity consumption by 2030.

(2) Climate change

Increased awareness of the dangers and effects of global warming and climate change has led decision makers, media and the public to realize that the use of fossil fuel must be reduced and replaced by low-emission sources of energy, such as nuclear power, the only readily available large-scale alternative to fossil fuels for production of continuous, reliable supply of electricity.

(3) Security of supply

A major topic on many political agendas is security of supply, as countries realize how vulnerable they are to interrupted deliveries of oil and gas. The abundance of naturally occurring uranium makes nuclear power attractive from an energy security standpoint.

(4) Economics

Several studies [12-16] show that nuclear energy is the most cost-effective of the available base-load technologies. In addition, as carbon emission reductions are encouraged through various forms of government incentives and trading schemes, the economic benefits of nuclear power will increase further.

(5) Insurance against future price exposure

A longer-term advantage of uranium over fossil fuels is the low impact that increased fuel prices will have on the final electricity production costs, since a large proportion of those costs are in the capital cost of the plant. This insensitivity to fuel price fluctuations offers a way to stabilize power prices in deregulated markets.

In contrast to fission, fusion is one of the most attractive long term energy options, having the potential to fill anticipated worldwide energy needs in the second half of this century. There is an essentially unlimited fuel supply, deuterium from the ocean and tritium from transmutation of lithium using neutrons produced in the D-T fusion reaction. Fusion will not produce CO₂ or SO₂ and thus will not contribute to global warming or acid rain. For fusion to find its way into the energy market place, it must compete economically with other energy options, and it must be developed as a safe and environmentally acceptable energy source, particularly from the viewpoint of radioactivity.

The economics, safety, reliability, and efficiency of both advanced fission and future fusion energy systems will ultimately depend on developing new high-performance structural materials that can provide extended service under extremely hostile conditions [17-25].

1.1.2 Materials challenges of fission and fusion

Fission and fusion reactor service conditions are characterized by combinations of high temperature, large time-varying stresses, chemically reactive environments, and intense neutron radiation fields [21, 25]. The structural materials in the first commercial fission reactors were exposed to maximum neutron doses of ~ 1 dpa (displacement per atom, which is used to normalize radiation damage across different reactor types; for one dpa,

on average each atom has been knocked out of its lattice site once) and maximum temperatures of ~ 300 °C. Existing (2nd generation) fission power light water reactors have core internal structure confronted with maximum doses of 30 dpa and temperatures of < 350 °C, and fast breeder reactor internal structures have displacement damage levels up to ~ 100 dpa with maximum temperatures of ~ 600 °C. Today, uprating and life extension of commercial light water reactors (LWRs) and demands by advanced fission reactor systems in the Generation IV initiative have pushed the environments of fission systems to be harsher, i.e. higher temperatures, higher pressure, higher neutron fluxes and greater fluences [7].

Compared to fission systems, the performance demands on the structural materials of future fusion power are harsher and beyond the capability of current materials, which is one of the reasons that the United States National Academy of Engineering has recently ranked the quest for fusion as one of the top grand challenges for engineering in the 21st century [26]. The first demonstration fusion reactor is expected to have a maximum structural dose of ~ 50 to 150 dpa at maximum temperature of 550 to 1000 °C, depending on the design [21].

In fission and fusion systems, exposure to high-energy radiation severely damages the microstructure of materials by violently displacing atoms from their lattice sites many times and creating damaging concentrations of helium and hydrogen. The resulting microstructural and damage evolution cause profound macroscopic property changes that degrade the performance and lifetime limits of the materials. Under irradiation, there are several major degradation phenomena that can impact structure materials performance [21]. Low temperature radiation hardening and embrittlement is of primary concern for doses above 0.1 dpa and temperature up to $\sim 0.35 T_M$, where T_M is the melting temperature in Kelvin. In intermediate temperature regimes from 0.3 to 0.6 T_M , and under a radiation damage level of ~ 10 dpa, phase instabilities driven by radiation-induced segregation and radiation-enhanced diffusion and precipitation along with dimensional instabilities driven by volumetric swelling are the key concerns. At higher temperature and dose, defined as greater than $\sim 0.4 T_M$ and ~ 10 dpa, respectively, thermal and irradiation creep, which involves the permanent plastic deformation of the materials at applied stress levels below the yield stress, can cause significant strains in the material ultimately leading to rupture. Finally, high temperature He embrittlement of grain boundaries can cause intergranular fracture at low stresses, particularly for doses > 10 dpa (He concentrations > 100 appm) and temperatures above 0.5 T_M .

Helium is of particular interest in materials research for several different nuclear systems [5, 6, 25, 27, 28, 29]. The generation of helium leads to the question of where the helium comes from. Radiation damage is continuously initiated with the formation of energetic primary knock-on atoms through collisions between high-energy neutrons (especially in fusion environment) and lattice atoms. Meanwhile, high quantities of insoluble helium and hydrogen gas are generated in (n, α) and (n, p) transmutation reactions, which have threshold energies above several MeV, hence are not normally produced in high concentration in fission neutron irradiations but occur more frequently in fast neutron irradiation. Moreover, the D-T reaction can also produce He nuclei with energies up to

3.5 MeV in the fusion reactors, which can enter the materials through direct implantation [28]. Besides fission and fusion, the production of a large amount of helium accompanied with the generation of irradiation damages also occurs in spallation neutron sources. To illustrate the material challenges, the operating requirements for two of the principal structural materials used in component design for different nuclear systems, austenitic stainless steels and ferritic/martensitic stainless steels, are summarized in Tables 1-1 and 1-2.

Table 1-1. Austenitic stainless steels: spallation, fusion and Generation IV fission applications, as reproduced from Ref. [29].

System (working fluid)	Component	Temperature, °C	Maximum dose, dpa	Maximum He, appm	Candidate alloys
SNS (mercury)	Spallation target module	80 ~ 150	5	200	316LN
ITER (water)	First wall/blanket	100 ~ 300	3	75	316LN
SCWR (SC water)	Fuel assembly	280 ~ 620	15	200	Advanced low swelling steels
	Core support/internals	280 ~ 500	0.1 ~ 20	250	

Note: SNS (Spallation Neutron Source), SCWR (Super-Critical Water-cooled Reactor)

Table 1-2. Ferritic/martensitic steels: fusion, and Generation IV fission applications as reproduced from Ref. [29].

System (working fluid)	Component	Temperature, °C	Maximum dose, dpa	Maximum He, appm	Candidate alloys
SSTR (WATER)	First wall/blanket	300 ~ 550	100	> 1000	Low activation 8~9% Cr ferritic- martensitic steels
HCLL (He)		270 ~ 550	100	> 1000	
HCPB (He)		300 ~ 550	100	> 1000	
SCWR (SC water)	Fuel assembly	280 ~ 620	15	20	Advanced 8~12% ferritic- martensitic steels
	Core support/internals	280 ~ 500	0.1 ~ 20	20	
LFR (Pb-Bi, Pb)	Fuel assembly	300 ~ 550	150	15	

Note: SSTR (Steady State Tokamak Reactor), HCLL (Helium-Cooled Lithium-Lead blanket concept), HCPB (advanced Helium Cooled Pebble Bed blanket concept), LFR (Lead-cooled Fast Reactor), appm (atomic parts per million).

1.1.3 Helium effects on properties of materials

As discussed in Section 1.1.2, a large amount of helium will be generated in different nuclear systems and the effect of helium on the properties of structural materials is one of the major degradation phenomena under irradiation [30], leading us to probe the mechanisms and the consequences.

Helium has extremely low solubility in most metals, and resides in the materials primarily in the state of being trapped by atomic defects such as vacancies, interstitials and their clusters, as well as extended defects such as dislocations, grain boundaries, and cavities or precipitate interfaces [31]. Under certain circumstances, the small He-containing complexes can reach a critical state and trigger the nucleation and growth of large He bubbles, and at larger sizes the He bubbles can convert to unstably growing voids [32, 33]. The formation of He bubbles in the grains or along the grain boundaries leads to swelling, significant radiation hardening or degradation in creep rupture behavior, and can further result in premature failure of the materials under relatively low stress [34]. The relatively high He production rates for fusion reactors promote low temperature embrittlement (via additional matrix hardening), void swelling, and high temperature He embrittlement. The higher He generation rates can also alter radiation-induced precipitation processes over a wide temperature range [35] and may cause a reduction in the fast fracture resistance of metals at temperature well below $0.5 T_M$ due to enhanced grain boundary decohesion effects [36].

A large number of experimental studies [37] exist related to helium effects in metals, particularly for austenitic steels due to their propensity to swelling and the versatile use as reactor materials. To illustrate the swelling effects induced by the existence of helium, partial experimental results from Wiffen and Bloom [38] are listed in Table 1-3.

Table 1-3. Irradiation conditions and measured swelling for Type 316 Stainless Steel irradiated in HFIR, as reproduced from Ref. [38].

Specimen Position	Irradiation Temperature (°C)	Displacement damage (dpa)	Helium Content (appm)	Measured Swelling, %	
				Solution Treated	20% Cold worked
4	379	97	4020	6.7	1.6
5	456	107	4820	8.7	0.80
6	528	114	5450	8.3	2.6
1	535	52	1930	3.5	0.52
8	574	58	1791	3.3	N/A
7	602	119	5940	8.0	3.3
8	679	121	6090	14.1	16.8

The presence of helium inside the materials can also alter the creep properties, which has been shown by many researchers. For example, the dependence of creep rupture properties on implanted helium concentration up to high concentrations (1000 appm He) has been investigated for AISI 316 SS [39]. The rupture properties, time to rupture and

rupture strain, are plotted versus pre-implanted helium concentration in Fig. 1-1(a) and 1-1(b), respectively.

While austenitic steels exhibit quite pronounced swelling and degradation of creep rupture properties, reduced activation ferritic/martensitic (F/M) steels are good candidate structural materials for future fusion reactors and spallation targets [40]. Compared to austenitic steels, they have excellent thermomechanical properties (high strength, low thermal expansion, high thermal conductivity) and lower damage accumulation and moderate swelling under irradiation [37]. However, irradiation can still change the mechanical properties of F/M steels, by inducing hardening, loss of ductility, shift in the ductile to brittle transition temperature and reduction of fracture toughness and creep resistance starting at low doses. Helium, produced by transmutation during irradiation, also impacts the performance of the F/M steels. These effects have been investigated in numerous experimental studies [41-43].

The above examples demonstrate the importance of helium effects on the properties of materials, which lead us to confront a very important problem. This problem is to understand how helium affects the mechanical properties of irradiated materials, which is particularly crucial for the development of radiation resistant materials for future fusion reactors [32, 33, 34, 44].

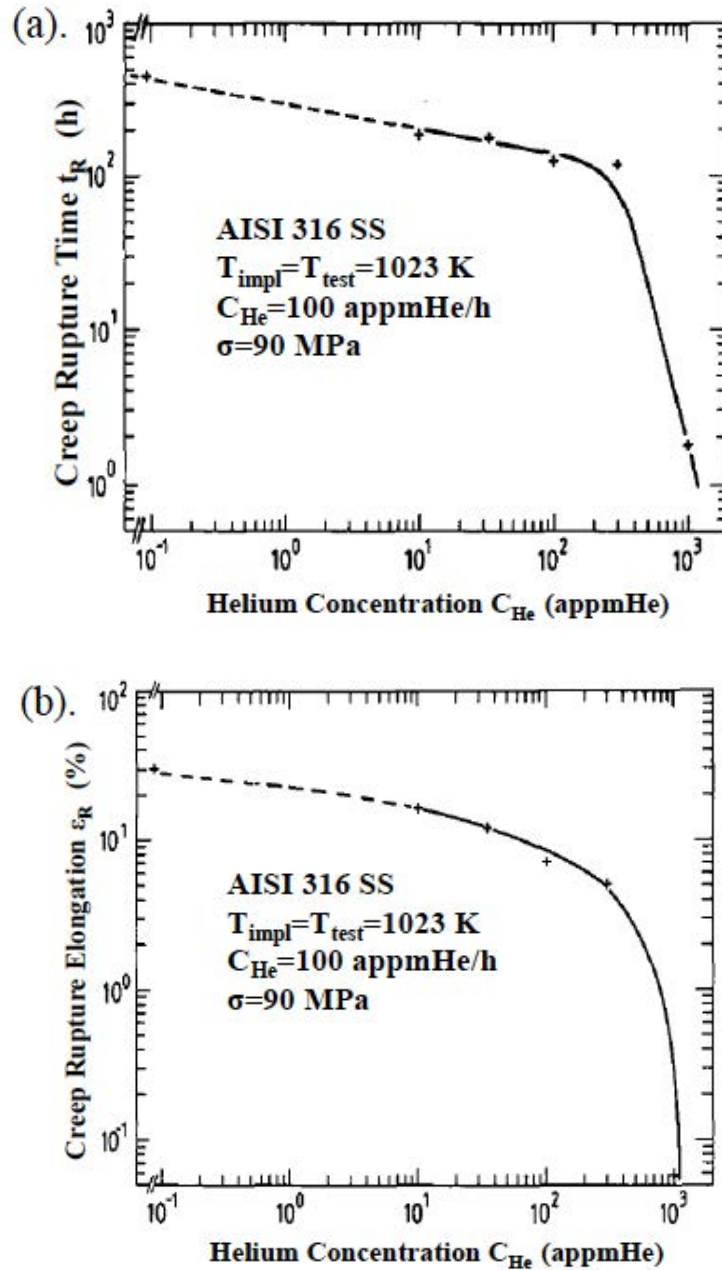


Figure 1-1. Influence of the helium concentration (pre-implanted at 1023 K) on the creep properties of AISI 316 SS: (a) creep rupture time; (b) creep rupture elongation, as reproduced from Ref. [39].

1.1.4 Previous work on understanding the mechanisms of helium effects

The key to understanding helium effects is to determine the mechanisms by which helium atoms migrate and interact with various microstructural features in irradiated materials. This is an inherently multiscale problem spanning from atomistic to macroscopic dimensions in both time and space [45, 46] and requires the use of both experiments and modeling.

As discussed in Section 1.1.3, a large number of experimental studies exist, focusing on He effects on the properties of the studied materials. However, the number of experiments devoted to obtaining basic, fundamental parameters of He diffusion and He-point defects interaction and providing data for validating the developed models is rather limited due to the difficulty of the problem. On the nano-, micro- or macro-scopic level, a variety of experimental techniques, such as optical or electron microscopy [e.g., 47, 48], nuclear reaction depth profiling [49], positron annihilation spectroscopy (lifetime and coincidence Doppler broadening) [50], thermal desorption [51-54], can be conducted to analyze He behavior and the coupled He and defect evolution in body-centered-cubic (BCC) iron and ferritic alloys. Rothaut, Schroeder and Ullmaier [55] examined the influence of annealing time, applied tensile stress, temperature and helium content on the size distribution and density of helium bubbles within the grains of AISI Type 316 SS by TEM. Arakawa, Imamura, etc. [47] studied the formation process of point defect clusters in high-purity (99.999%) iron under the irradiation with low energy (5keV) Helium ions by in situ TEM. Lewis and Farrell [49] utilized the techniques of ion implantation and nuclear reaction depth profiling to measure helium migration during irradiation at elevated temperatures in iron. Ishizaki, Xu, et al. [50] conducted a series of isochronal annealing experiments for iron irradiated with He to study the interactions between gas atoms and vacancy clusters by using positron annihilation lifetime (PAL) and coincidence Doppler broadening (CDB) measurements. Xu, Cao, et al. [51] carried out the PAL and CDB measurements to analyze the formation and stability of He bubbles in iron irradiated with He ions. Vassen, Trinkaus and Jung [52] investigated thermal helium desorption from homogeneously implanted iron foils during linear heating and isothermal annealing and concluded that the substitutional helium atoms migrate by a dissociative mechanism. Sugano, Morishita, et al. [51] performed thermal desorption spectrometry (TDS) analysis and TEM observation to investigate microstructural evolution in iron and Fe-Cr alloys during thermal annealing after irradiation with He ions. Xu and Wirth [54] performed TDS measurements for single-crystalline iron samples implanted with He ions in a linear annealing process to avoid the effects of grain boundaries, providing a platform to do a comparison with the models.

As discussed in the previous sections, helium effects on structural materials are particularly significant and challenging in fusion environment because of the large 14 MeV peaked neutron spectrum, which will produce a large quantity of helium. The threshold (several MeV) transmutation reactions do not occur at sufficient rates in fission reactors, making the experimental study of helium point defect interactions and helium bubble nucleation very challenging [28]. The deficiency in experimental studies demands the development of accurate, predictive models that can be applied to different conditions.

As in most material science problems, there is not a single model capable of covering the broad range of time and length scales required to understand damage production and accumulation. Multiscale modeling nowadays is recognized as a major tool in the investigation of radiation damage effects [45, 46], as it allows one to establish solid foundations to the understanding of the relationship between irradiation and the induced mechanical response of the target materials, starting at the atomic scale.

The theoretical foundation for analyzing He-point defect interactions was laid in the 1970s and 80s. Russell [57] developed a general theory of void nucleation in irradiated metals, which included spontaneous void nucleation driven by inert gas. Trinkaus [33] reviewed the theoretical work on the energetics and formation kinetics of helium bubbles in metals, providing a thermodynamic method to calculate the formation energies of helium bubbles and analyzing the bubbles formation kinetics. Ghoniem, Sharafat, et al. [58] used a theoretical model to describe helium transport and clustering during irradiation, including diffusional reactions of helium with vacancies and vacancy clusters, with extended sinks for helium absorption, and direct reactions with displacement producing particles. Stoller and Odette [59] applied a hard sphere equation of state to computing the critical bubble radius and critical helium number for bubble-to-void conversion in austenitic steels. Mansur, Lee, et al. [30] summarized the key theoretical relationship describing helium effects on swelling and helium diffusion. Vassen, Trinkaus and Jung [52] combined TDS and models to study the helium diffusion mechanisms and provided the helium dissociation energies. However, these researches are mostly focusing on fission-related conditions, or austenitic steels that are no longer under consideration for fusion.

Due to the growing interest in fusion energy, a resurgence of research activities on helium has occurred. Thanks to the recent availability of computing power, the kinetics and energetics of helium interactions with various defects in BCC iron have been studied computationally by applying *ab initio* and molecular statics (MS)/dynamics (MD) approaches. Morishita, Sugano and Wirth [60] evaluated the energies of He-vacancy cluster formation in BCC iron using a MD simulation technique. By using the calculated energies, the longer timescale behavior of He-vacancy clusters was investigated by kinetic Monte Carlo. Fu and Willaime [61] performed density functional theory calculations to study the dissociation and migration of helium in BCC iron, and the stability of small helium-vacancy clusters, providing the helium migration energies and binding energies of helium and vacancy to He-vacancy clusters. Ventelon, Wirth and Domain [62] simulated the effects of He on the behavior of self-interstitial atom (SIA) clusters in BCC iron by atomistic MD and MS simulation techniques using semi-empirical interatomic potentials, revealing that strong binding energies exist between He and SIA clusters. Seletskaya, Osetsky, et al. [63] addressed the study of relaxation, formation and binding energies of small helium clusters in iron by using electronic structure calculations. Heinisch, Gao, et al. [64] determined the formation energies, binding energies and migration energies of helium in and near the core of edge dislocations in BCC iron by atomistic simulations. Kurtz and Heinisch [65] explored the effects of grain boundary structure and properties on the binding of He to boundaries in iron. Stewart, Osetskiy and Stoller [66] performed atomistic studies of formation and

diffusion of helium clusters and bubbles in BCC iron, where migration energies and diffusivity coefficients of helium clusters are given.

These calculations provide more accurate values for He migration and small He-vacancy complex stabilities, and helped in the development of long-term evolution models such as rate theory (RT) or kinetic Monte Carlo (kMC). Ortiz, Caturla, et al. [67] used a rate theory model to address the evolution of interstitial helium, He-vacancy complexes, vacancy clusters and SIA clusters, providing a detailed description of the diffusion mechanisms of He. They also studied the evolution of damage defects using both kinetic Monte Carlo and rate theory approaches [68]. Golubov, Stoller, et al. [69, 70] developed a new method of solving the two-dimensional master equation describing He-vacancy cluster evolution to study the kinetics of coarsening of helium bubbles during implantation and post-implantation annealing. Xu and Wirth [71, 72] proposed a spatially dependent rate theory model to investigate the helium-point defect interactions, the predicted results of which showed good agreement with the thermal helium desorption experiment, one among the few experiments from which information on He behavior in iron can be obtained albeit indirectly. These models, coupled to the experiments designed for their validation, are starting to provide a more clear understanding of the basic phenomena of the helium-point defect interactions in irradiated materials.

Despite all of these experimental and modeling efforts, the overall picture of He in BCC iron or ferritic alloys remains disconnected, incomplete and not self-consistent. Furthermore, the lack of available materials irradiation testing environments that can provide both representative displacement damage rates and representative rates of producing transmutation elements similar to fusion environment emphasizes the necessity for a coordinated scientific effort combining experiment, modeling and theory to develop a fundamental understanding of helium effects in the irradiated materials.

1.1.5 Research objectives and approach

This research aims to investigate the helium-point defect interactions and their long-term evolution in BCC iron and provide a general understanding of the basic mechanisms inducing the helium effects on the mechanical properties of materials, by integrating experimental and modeling research approaches.

It has been commonly recognized that the complexity of modern engineering materials and multiple degradation processes occurring in the severe irradiation environment requires multiscale modeling and experimental approaches [46]. Fig. 1-2 provides a schematic view of an integrated experimental and computational approach to the multiscale investigation of materials behavior.

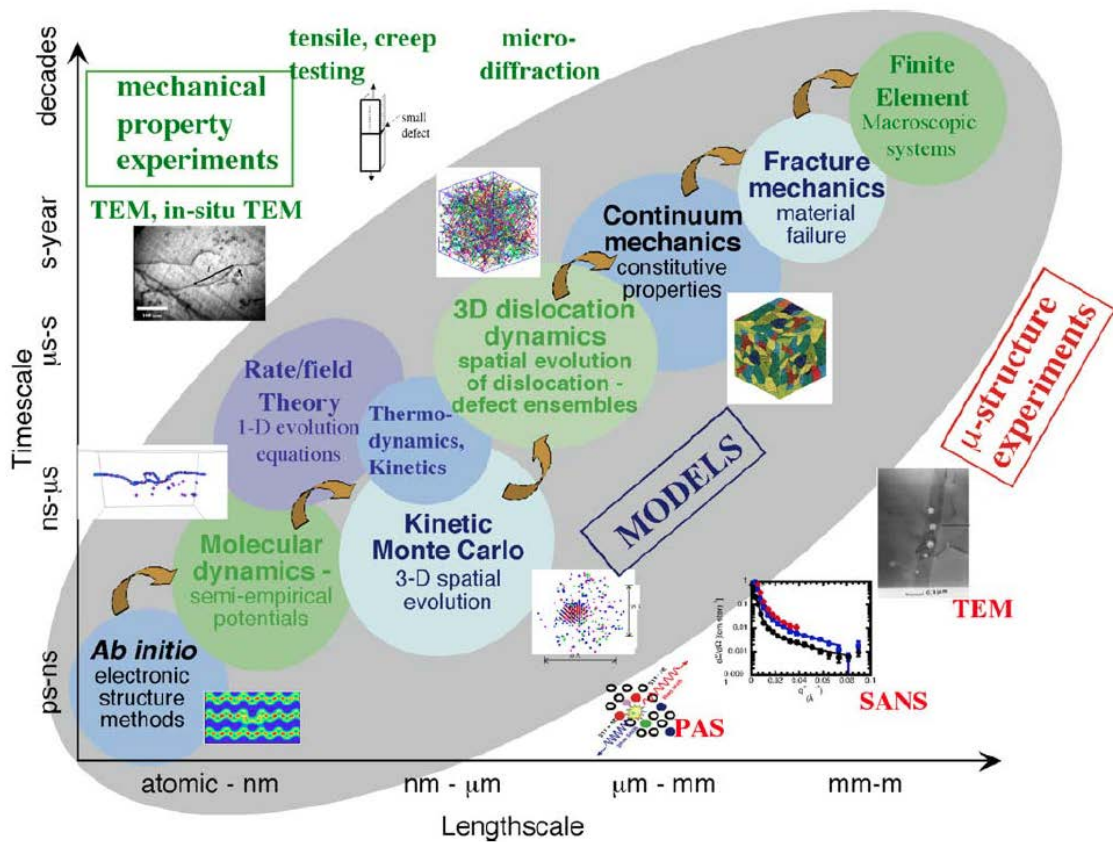


Figure 1-2. Illustration of an integrated experimental and computational approach to the multiscale investigation of materials behavior in the fusion environment. The central part of the figure describes a hierarchical approach based on passing information or parameters, and connecting key mechanisms (denoted by arrows), starting from the electronic/atomic up to structural length and time scales. A number of microstructural characterization techniques important for validating model predictions are represented on the lower right side, including the techniques of positron annihilation spectroscopy (PAS), small angle neutron scattering (SANS) and TEM. The upper left side of the diagram represents experimental techniques to measure mechanical properties, as reproduced from Ref. [46].

Nevertheless, this research will not cover all of the aspects illustrated in Fig. 1-2. The focus is on the helium-point defect interactions spanning from the atomistic scale to nano-scale in size, and from picoseconds to years in time. The experimental studies consist of thermal helium desorption spectrometry (THDS) and positron annihilation spectroscopy (PAS). THDS is employed to obtain the helium desorption spectra of single-crystalline iron samples implanted by different ion irradiation conditions during annealing processes. The spectra can be analyzed to indicate the evolution of He-point defects complexes coordinated with the cluster dynamic model. It can also provide the reference for the validation of the developed models by comparing the modeling predicted helium flux at the sample surface with the THDS results. PAS is a powerful technique in examining the defect cluster distribution and evolution in the region where TEM cannot distinguish with the current resolution. This technique is more

straightforward, from which the information of the defects, i.e. size and concentration, at different annealing stages can be obtained. The information can also be compared with the modeling results directly. As to the computational study, a spatially dependent cluster dynamics model will be used to couple with the experimental results to unveil the basis of the helium-point defects interaction by applying the pre-existing energetics and kinetics parameters. Furthermore, the impurities effects on these parameters will also be discussed. The purpose is to provide a self-consistent model experiencing the verification of experiments. The combination of experiments and modeling will exhibit a general picture of the underlying microscopic mechanisms of the helium-point defects interactions.

1.2 Kinetics of hydrogen desorption from zirconium hydride

1.2.1 Zirconium hydride produced in structural components

1.2.1.1 Background

Zirconium and its alloys are widely used in nuclear and chemical industries because of their low neutron absorption [73] and their excellent mechanical and corrosion properties [74]. In today's nuclear reactors, optimized zircaloy and zirconium–niobium alloys are used for structural components like fuel cladding, control rod guide tubes, and grid spacers [75]. In the nuclear reactor environment, both the fuel and the fuel cladding evolve under the influence of various driving forces such as temperature, radiation damage, fission product creation, stress, corrosive environment, etc. [74]. During in-reactor operation the zirconium cladding is subject to environmental degradation. The cladding tube is under stress from the pressure of the fission gases emitted by the uranium pellet and can develop chemical bonding with the pellet itself. The typical temperature of the inner cladding wall is about 400 °C. The outer wall of the cladding is in contact with the cooling water and its temperature is approximately 350 °C. At this boundary waterside corrosion can occur, leading to hydrogen pickup by the cladding. Radiation damage also affects the properties of the cladding. Typically during the 3 years operating lifetime of the fuel rod each atom in the zirconium cladding is displaced 20 times (20 dpa).

In light water reactors, there is considerable experience on the behavior of zirconium alloy cladding up to burnup levels of 30-35 GWd/ton and corresponding exposures [76]. However, driven by the need to minimizing waste volume, increase capacity factors, and reduce fuel costs, the industry has increased the average discharge fuel burnup with a consequent increase in exposure time [77]. Such increases take the fuel into an operation regime in which fuel degradation mechanisms are less well understood. In addition to the increase in radiation damage, increased corrosion of the fuel cladding can occur, with a concomitant increase in hydrogen ingress. This increased corrosion is caused not only by increased exposure but also by the fact that the primary water chemistry is more aggressive, due to the additions necessary to operate at higher burnup. All of these factors

combine to impose heavy duty on the fuel cladding [78]. Some of the principal mechanisms of cladding failure are related to hydrogen ingress, especially because of the formation of brittle hydride with consequent degradation of mechanical properties [79].

1.2.1.2 Generation of zirconium hydride

In the reactor environment, zirconium cladding reacts with the cooling water to form a layer of zirconia (ZrO_2) on the cladding surface. The reaction (1-1) liberates hydrogen that can be absorbed by the cladding:



Hydrogen is also generated by radiolysis [80] according to the following reaction:



Some of the radiolysis produced hydrogen ions or neutral atoms are transported to the surface of the cladding and can be absorbed. This is called hydrogen pick-up. The absorbed hydrogen migrates through the materials in response to thermodynamic driving forces, such as concentration and thermal gradients, which can cause local concentration in the form of blisters or rims. The hydrogen entering the cladding remains in solid solution until the solubility limit is reached. The terminal solid solubility of hydrogen in zircaloy ($C_{\alpha-Zr}^H$) has previously been measured and is given by

$$C_{\alpha-Zr}^H = A \exp(-E_H / T) , \quad (1-3)$$

where A is a constant, 1.2×10^5 wt. ppm, and E_H is the difference in partial molar heat of solution of hydrogen in solid solution and partial molar heat of solution of hydrogen in hydrides, which is 4300 K [81-83]. The stable hydride phase at low temperature is the delta hydride phase, which is in fact the phase normally observed experimentally [84, 85], although the gamma phase can be observed at high hydrogen contents [86]. Hydrogen normally precipitates as platelets whose normals are perpendicular to the direction of applied tensile stress [76].

1.2.2 Zirconium hydride used in hydride fuel

Hydrogen-based nuclear fuels have been utilized in numerous occasions, particularly in the Systems Nuclear Auxiliary Power Program (SNAP) [87] and as fuel for Training, Research, Isotopes, General Atomic (TRIGA) research reactors [88]. Additionally, hydride fuel is a potential alternative to uranium oxide fuel for light water reactors. One common type of hydride fuel consists of metallic uranium dispersed in a zirconium hydride matrix with a nominal composition of $U_{0.31}ZrH_{1.6}$. Fuel mixtures with plutonium or thorium are also possible. Although hydride fuels have not been used in large high

power reactors yet, the performance of the test reactors has led to interest in using hydride fuel in large reactors to generate electricity [87, 89]. As to the advantages of hydride fuels, hydrogen bound in the fuel acts as a neutron moderator augmenting the coolant for this purpose, permitting more compact core designs with higher power density. It also has a prompt negative fuel-temperature reactivity feedback, enhancing the safety of the reactor. From a materials perspective, hydride fuel has a much higher thermal conductivity than oxide fuel, resulting in operating temperatures low enough (< 650 °C) even at high linear heat rates (40 kW/m) to avoid fission-gas release and to reduce stored energy. However, the rate of solid fission-product swelling is three times larger than that of oxide fuel [90].

Hydride fuel is produced by contacting U-Zr alloys (~ 45 wt.%U) with hydrogen gas at high temperature, while controlling the hydrogen pressure during fabrication establishes the H/Zr ratio (typical 1.6). The Zr-H phase diagram is well established [91], as is the equilibrium hydrogen pressure as a function of temperature and H/Zr ratio, shown in Eq. (1-4) [92]. In Eq. (1-4), C is the hydrogen to zirconium ratio.

$$P_{H_2-eq}[MPa] = \left(\frac{C}{2-C} \right)^2 \exp \left(5.72 + 5.21C - \frac{172 [kJ\ mol^{-1}]}{RT [K]} \right) \quad (1-4)$$

Hydride fuel is not as well characterized as oxide fuel and has one major feature that is potentially troubling when used in power reactors. Namely, hydrogen can be released from the fuel at elevated temperatures. Under operating conditions, hydrogen in the fuel will reach an equilibrium pressure in the confined space of the fuel pin. Although the thermodynamic driving force for hydrogen loss from the zirconium hydride matrix in the fuel at high temperature exists, and the desorption and adsorption of hydrogen from zirconium hydride have been well studied, there are still uncertainties about the kinetics of this process [93-96]. In our study, the hydrogen desorption process from zirconium hydride and zirconium metal in vacuum is studied by coordinated experimental and modeling methods. The production and verification of the desired δ -zirconium hydride is discussed while Thermal Desorption Spectroscopy (TDS) is employed to obtain the hydrogen desorption spectra directly. In addition, a one-dimensional two-phase moving boundary model coupled with a kinetic description of hydrogen desorption from a two-phase region of δ -ZrH_{1.6±n} and α -Zr is developed to reproduce the TDS experimental results.

Chapter 2

Experimental Studies of Helium-Point Defect Interaction

2.1 Thermal helium desorption spectrometry (THDS)

2.1.1 Introduction

Probing defects in a metal by helium was an idea emerging from desorption experiments by Carter [97], Redhead [98], and Kornelsen [31] in 1960s and 70s. The procedure of a THDS experiment is described in Fig. 2-1. The basic ideas are quite straightforward, namely, implant the samples with helium ion, heat the sample and measure the released helium.

Helium is used as a probe because of its unique properties. Due to its high heat of solution, helium is practically insoluble in perfect metals lattice, but it is strongly trapped by vacancies. The measured spectra can be analyzed by means of first-order kinetics for determining the activation energy and the rate constant of the process.

While the principles are straightforward, however, the technical requirement for the system is strict. For the samples, it is necessary to work with clean and well-defined surfaces, under which the recoil implantation of surface impurities is avoided, and the penetration of helium is not hindered by surface adsorbates. Therefore the technique requires ultra high vacuum conditions. Special attention should be paid to the helium background of the vacuum chamber, and an acceptable partial pressure of helium is of the order of 10^{-10} Pa. A typical dose of implanted helium is $10^{12} \sim 10^{14}$ ions per square centimeter. The helium release rate to be measured is usually very weak, which means that a mass spectrometer with high sensitivity is necessary. The sample is usually heated with a constant heating rate, thus a computer controlled heating system is needed.

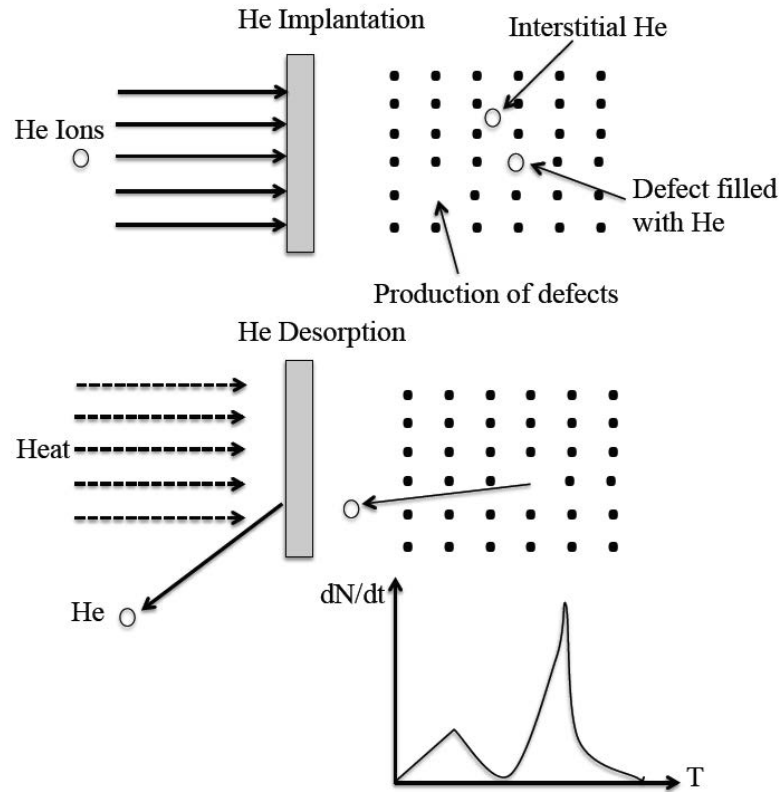
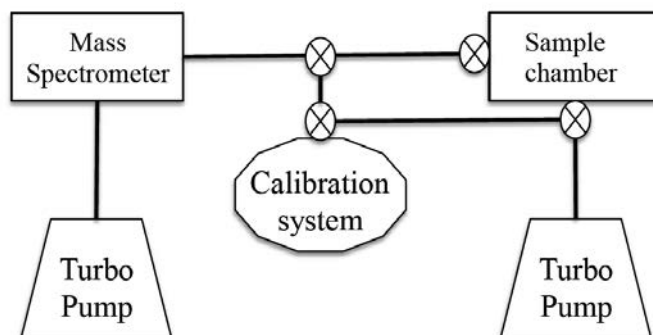


Figure 2-1. The principle of a THDS procedure when probing He-point defect interaction.

In a THDS measurement, the vacuum level should be of the order of 10^{-8} Pa with a negligible helium background [99]. These facts have to be taken account when designing the vacuum system and choosing the pump configuration. A schematic illustration of UC Berkeley ultra high vacuum TDS system is shown in Fig. 2-2(a).

(a).



(b).

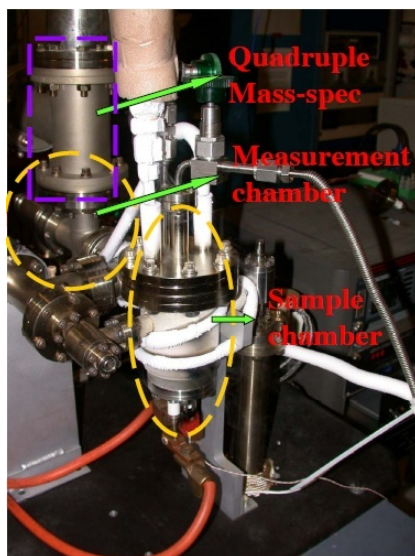


Figure 2-2. (a). Schematic illustration of THDS system in UC Berkeley; (b). Picture of partial system of THDS.

Fig. 2-2(b) shows a photograph of the Berkeley THDS system. The system is constructed with electro polished commercial stainless steel vacuum components and all-metal valves. The total chamber volume is approximately 2.5 L, pumped with two Pfeiffer turbo pumps supplemented by roughing pumps. The two-turbo pump setup allows the mass spectrometer to always remain under vacuum, with only the sample chamber brought to atmospheric pressure for sample changes. After baking 24 hours at 150°C, a pressure level of 10^{-8} Pa (7.5×10^{-11} torr) can be obtained. Bayard-Albert type hot cathode ionization gauges are used for pressure measurement. A cooling system using liquid nitrogen prevents the overheat of the sample chamber.

The samples are placed in a tungsten crucible that is heated by a (150 A, 20 V) tungsten filament. A type C thermocouple is used for temperature measurement. Proportional integral derivative (PID) temperature control is implemented with LabVIEW™. Different heating schedules can be programmed with the system, using either linear or linear-step heating processes. LabVIEW™ is also used for recording all system data

during a desorption experiment (temperature, pressure, helium desorption spectrum and time).

Fig. 2-3 indicates that the background currents of different species from a non-implanted control specimen remains at a relatively low level, especially for the species of interest, helium, with a nearly constant value at a low level ($\sim 10^{-13}$ A) from room temperature up to 1300 °C. In addition, the total pressure of our system is very low ($\sim 10^{-9}$ Torr) and stable over the entire temperature range.

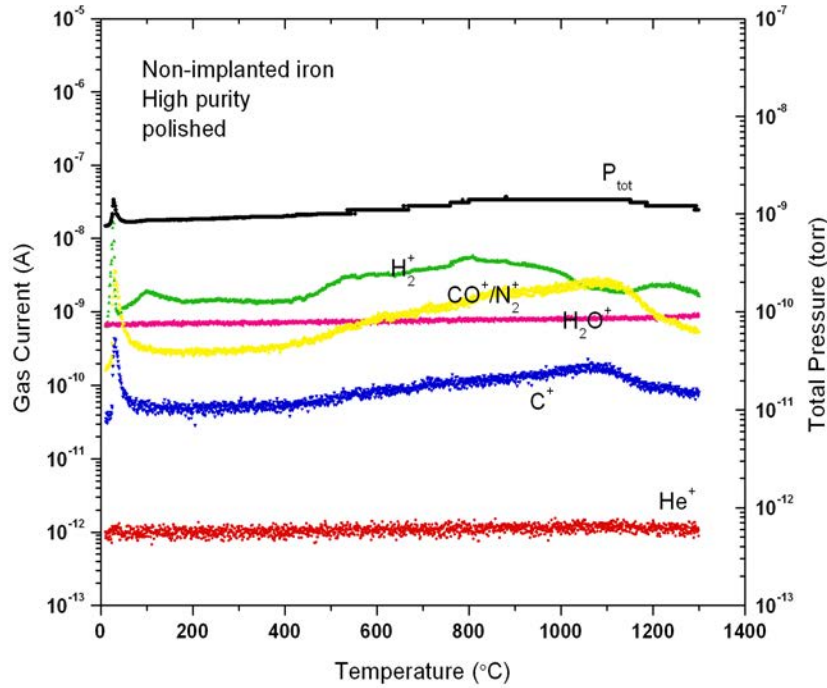


Figure 2-3. Background and total pressure of the system for the non-implanted iron sample in the annealing process, as reproduced from [183].

Helium detection in the THDS is preformed with a Pfeiffer quadrupole mass spectrometer equipped with a Channeltron type electron multiplier. A linear relationship exists between ion current in the mass spectrometer and helium partial pressure:

$$I(A) \propto P_{He} \text{ (torr)} . \quad (2-1)$$

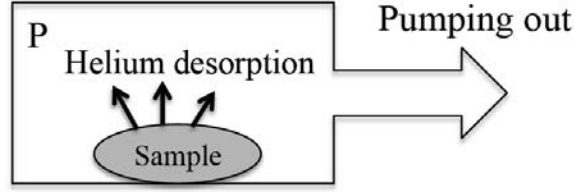


Figure 2-4. Illustration of the system dynamic process.

As shown in Fig.2-4, the change of the helium amount in the controlled volume can be expressed as

$$R_{change} = R_{desorption} - R_{pumping} . \quad (2-2)$$

The change rate of the total quantity of helium in the system can be written as

$$R_{change} = \frac{V}{k_B T} \frac{dP}{dt} ; \quad (2-3)$$

while the rate of helium removal from the system is

$$R_{pumping} = \frac{V}{k_B T} \frac{P}{\tau} , \quad (2-4)$$

where V is the volume of the system; P is the pressure; k_B is the Boltzmann constant; T is the temperature, assuming the major part of the system is at that temperature; t is the time; $\tau = V / S$ is the pumping time constant with S being the pumping speed of the system.

Thus the desired helium desorption rate from the sample will be given by

$$R_{desorption} = \frac{dN}{dt} = \frac{V}{k_B T} \left(\frac{dP}{dt} + \frac{P}{\tau} \right) , \quad (2-5)$$

where N is the desorbed helium atom number from the sample.

The THDS system can operate in two modes, either static or dynamic. If the pumping speed is negligible, the system operates in the static mode, and if the pumping speed is relatively high, it is called the dynamic mode of operation, in which the Berkeley THDS system is normally operated. The $dP(t)/dt$ term in Eq. (2-5) is minimized in this dynamic mode, thus the helium desorption rate is approximately proportional to the detected helium number in the system by the mass spectrometer.

The detected helium information is obtained in the form of an electrical current (I) with a unit of ampere (A) by the mass spectrometer. A calibration process is required to convert

the current to the helium atom number, especially because the sensitivity of the multiplier may be altered as a function of time. The calibration system consists of a known-volume reservoir (0.5L), the MKS Baratron type pressure manometers and the He input subsystem. Fig. 2-5 shows the basic structure of the calibration system.

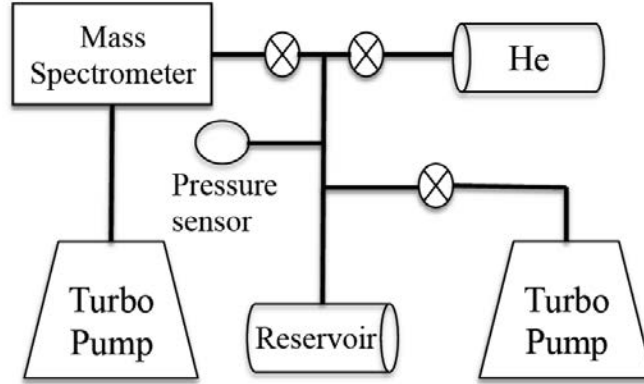


Figure 2-5. Schematic illustration of the calibration system.

The procedure to execute calibration of the system is the following: (i) obtain a ultra high vacuum on the order of 10^{-7} torr for the reservoir; (ii) introduce a small amount of helium to the reservoir; (iii) pump partial helium out of the reservoir by the turbo pump connected with the mass spectrometer; (iv) record the pressure change and the measured helium desorption spectrum; (v) repeat step (iv) for several times to reduce the errors. Some simple calculations can then be performed, including computing the number (N) of the released helium based on the reservoir pressure change by the equation of state and integrating the measured helium spectrum to obtain the total integrated electric current ($Q_{\text{electricity}} = I \times t$). Finally, we can acquire the calibration coefficient as a unit of He number per Coulomb,

$$C_{\text{calibration}} = \frac{N}{Q_{\text{electricity}}} . \quad (2-6)$$

As to the data analysis, it is noted that the first-order chemical reaction model is usually applied to analyzing the given helium desorption spectrum [100]. The first-order rate of He desorption from a sample is given by:

$$\frac{dN}{dt} = -Nv \exp\left(\frac{-Q}{kT}\right), \quad (2-7)$$

where N is the number of remaining helium atoms in the sample, Q is the activation energy, v is the attempt frequency, T is temperature, and k is Boltzmann's constant. With

a linear heating rate and by solving the equation d^2N/dt^2 , the temperature at which the desorption rate is maximum is:

$$-\frac{Q}{kT_{\max}^2} = \frac{\nu}{\beta} \exp\left(-\frac{Q}{kT_{\max}}\right), \quad (2-8)$$

where T_{\max} is the temperature at which the desorption rate is a maximum and β is the heating rate. Eq. (2-8) is used to calculate the activation energy, Q . The attempt frequency, ν , is usually taken as the Debye frequency, $1 \times 10^{13} \text{ s}^{-1}$, which is on the order of the atomic vibration frequency in solids. It can also be calculated by two sets of experimental data at different heating rate to produce T_{\max} vs. β . Then a back-calculation of the desorption rate using these computed parameters will compare with the experimentally-obtained helium desorption spectrum, however they do not necessarily provide good agreement [53]. In addition to the first-order kinetic model, some other kinetic models, i.e. Johnson-Mehl-Avrami (JMA) model [101, 102], the combination of JMA and first-order model [53], have also been used to analyze the given desorption spectra. Nevertheless, these types of analyses do not provide a clear description of the helium interactions inside the sample.

Since multiple He interactions are anticipated to govern the He desorption, the data analysis is more complicated than the simple kinetic models. THDS experiments should be closely coupled with the multiscale simulations. In this chapter, only the THDS experimental results will be shown without detailed interpretation of these data.

2.1.2 Thermal helium desorption spectrum of He-implanted poly- and single-crystalline (PC and SC) iron following linear temperature ramping profile

All of the previous thermal desorption experiments on iron appear to have only used poly-crystalline specimens. It is thus not clear what kind of role the grain boundary has played in the resulting desorption signals. Xu and Wirth [54] analyzed the helium desorption spectra of the He-implanted poly- and single-crystalline iron samples.

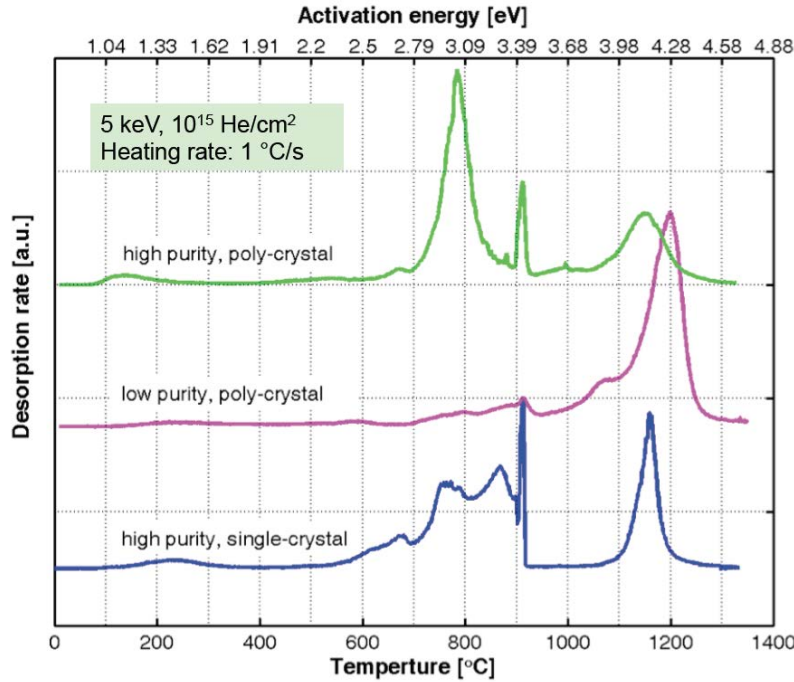


Figure 2-6. Thermal helium desorption spectra of the samples: high purity single- and poly-crystalline irons, low purity poly-crystal iron, as reproduced from Ref. [54].

In this study, small specimens ($\sim 0.5\text{-}1 \times 2.5 \times 3.5$ mm) were cut from the plates or disks, mechanically polished to $1\text{ }\mu\text{m}$ grade smoothness, and then commercially implanted at room temperature with ^4He ions at 5 or 10 keV to fluences of 10^{14} or 10^{15} He/cm^2 . The helium implantation flux was $\sim 7\text{-}10 \times 10^{10}$ $\text{He}/(\text{cm}^2\text{s})$. Partial He current was measured in our ultrahigh THDS as a function of temperature during constant rate ($1\text{ }^\circ\text{C}/\text{s}$) ramping on each of these He-implanted specimens from room temperature up to $1300\text{ }^\circ\text{C}$. The details can be found in [54], and here only the major features will be shown by comparing the helium desorption spectra from the single-crystal and poly-crystal irons with different impurities, which were implanted with 5keV He ions to a fluence of 10^{15} He/cm^2 , during thermal annealing with a constant heating rate of $1\text{ }^\circ\text{C}/\text{s}$, as shown in Fig. 2-6.

For the high purity single-crystal iron specimens, the curve clearly shows two well-separated major desorption groups within the BCC temperature range (up to $912\text{ }^\circ\text{C}$, where the appearance of the sharp peak marks the alpha-gamma phase transformation of iron): Group I below $\sim 300\text{ }^\circ\text{C}$ and Group II from $\sim 550\text{ }^\circ\text{C}$ to $912\text{ }^\circ\text{C}$. The temperature range in which significant helium release occurs is above $600\text{ }^\circ\text{C}$. It should be noticed that the ‘high purity’ nomenclature used here is only corresponding to the low purity poly-crystal irons. Similar to the single-crystal iron, the poly-crystal sample’s spectrum also exhibits a sharp alpha-gamma phase transformation peak. The second similarity involves the multiple He release groups in well-separated temperature ranges, although there are differences in the details of each grouping. For the low purity polycrystalline iron sample, it indicates that a large helium releasing peak appears around $1200\text{ }^\circ\text{C}$.

Comparing the spectra of low purity and high purity poly-crystal irons, the helium desorption peaks shift from high temperature (1200 °C) to low temperature region (800 °C) with increasing alloy purity. Also for the high purity poly-crystal iron specimen, a sharp helium releasing peak is observed, indicating the alpha-gamma phase transformation is much more significant than that of low purity poly-crystal iron. This results from that the presence of impurities that changed the energetics and kinetics of He-V clusters. The presence of impurities enhances the stability of He-V clusters [133] so helium will not be released until the temperature is high enough to provide sufficient driving force to the helium release process.

The discrepancy between the helium desorption spectra of poly- and single-crystal irons suggests that it is not appropriate to validate the modeling results using the experimental data from poly-crystal iron samples which include grain boundaries unless the impurities and extended defects are explicitly included in the model. The desorption data from single-crystal iron are expected to provide a more reasonable reference for future modeling. Furthermore, the difference between different samples also leads us to consider the impurity effects on the helium desorption spectrum and the inherent helium-point defect interactions.

2.1.3 Helium desorption spectra of new samples with stated purity of 99.98%

In order to increase the amount of experimental data from single-crystalline iron, the helium desorption spectra obtained from the new single crystal iron specimens purchased from Goodfellow, with a stated purity of 99.98% are shown in Fig. 2-7, as a function of the energy of the implanted helium ions and an implantation fluence of 10^{15} He/cm². The samples are prepared in the same way as in the previous work before being placed in the THDS measurement system.

There also exists a sharp peak for each of the spectra, which is also observed for other experimental conditions. In Ref. [53], it shows the strong evidence leading to the conclusion that this peak is primarily due to the alpha-gamma (BCC-FCC) phase transformation. Therefore, in this work, as what we did before, this peak is used to calibrate the temperature reading by setting this peak position to 912°C (the well known value of BCC-FCC phase transformation in pure iron) and utilizing a linear-correction to the other temperature values. The helium release spectra also exhibit two main helium release groups, Group I below ~300°C and Group II from ~450°C to 912°C. The group I release characteristics are similar to previous measurements, although Fig. 2-7(b) for 20 keV He does not show the obvious release peak around 200 °C. In the group II, a significantly large peak is observed around 600 °C, which is a substantially lower temperature than observed previously. Comparing Figs. 2-7(a) to (c), it is shown that the main release peak shifts to higher temperature with increasing He ion implantation energy, consistent with past measurements. However, another difference with previous measurements is associated with a number of small fluctuations in helium desorption that are observed after the concentrated helium release in the main release peak that continue up to the phase transformation point. In Fig. 2-7(c), there is an obvious peak in the plateau just before the BCC-FCC transformation. The other similar feature is that helium

retained into the FCC phase does not desorb until $\sim 1200^{\circ}\text{C}$. As mentioned, the group II helium desorption region is shifted to lower temperature, beginning at around 450°C , as compared to the previous measurements on single crystal iron with a slightly lower stated purity of 99.94%.

The shift of the desorption peaks for different implantation energies in this batch of samples as well as in the previous studies can be understood by conducting SRIM calculations. Probabilistic depth distribution of generated Frenkel pairs (represented by vacancy) and stopped helium ions during helium implantation in iron were evaluated using SRIM 2008 [103], and the results are shown in Fig. 2-8.

For 20 and 40 keV implantation energies, the maximum production of Frenkel pairs occurs at ~ 75 and 125 nm beneath the implanted surface, while the maximum points for the helium distribution occur at ~ 95 and 170 nm, respectively. Furthermore, on the average, 95 and 129 Frenkel pairs are generated per helium ion for the two energies, respectively. From a straightforward view, the deeper distribution of the helium and defects for the higher implantation energy makes the helium desorption more difficult. Helium thus needs more time to move to the surface of the samples which induces the shift of the major peaks of the helium desorption spectra.

The helium desorption spectra shown in Section 2.1.2 and 2.1.3 will provide a platform to verify the overall accuracy of the developed model. Additionally, the difference between the desorption spectra of different samples also allow us to investigate the influence of impurities on the kinetics and energetics of the helium-point defects interactions.

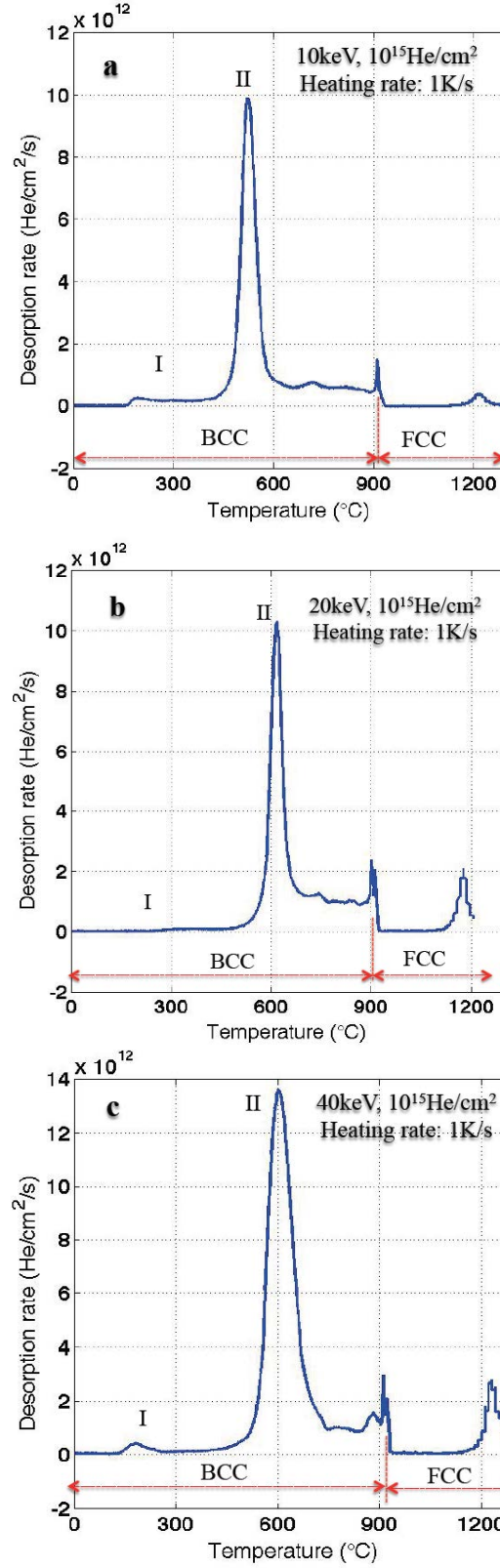


Figure 2-7. Desorption spectra of high purity single-crystal irons implanted with ⁴He at: (a) 10 keV, 1x10¹⁵ He/cm²; (b) 20 keV, 1x10¹⁵ He/cm²; (c) 40 keV, 1x10¹⁵ He/cm².

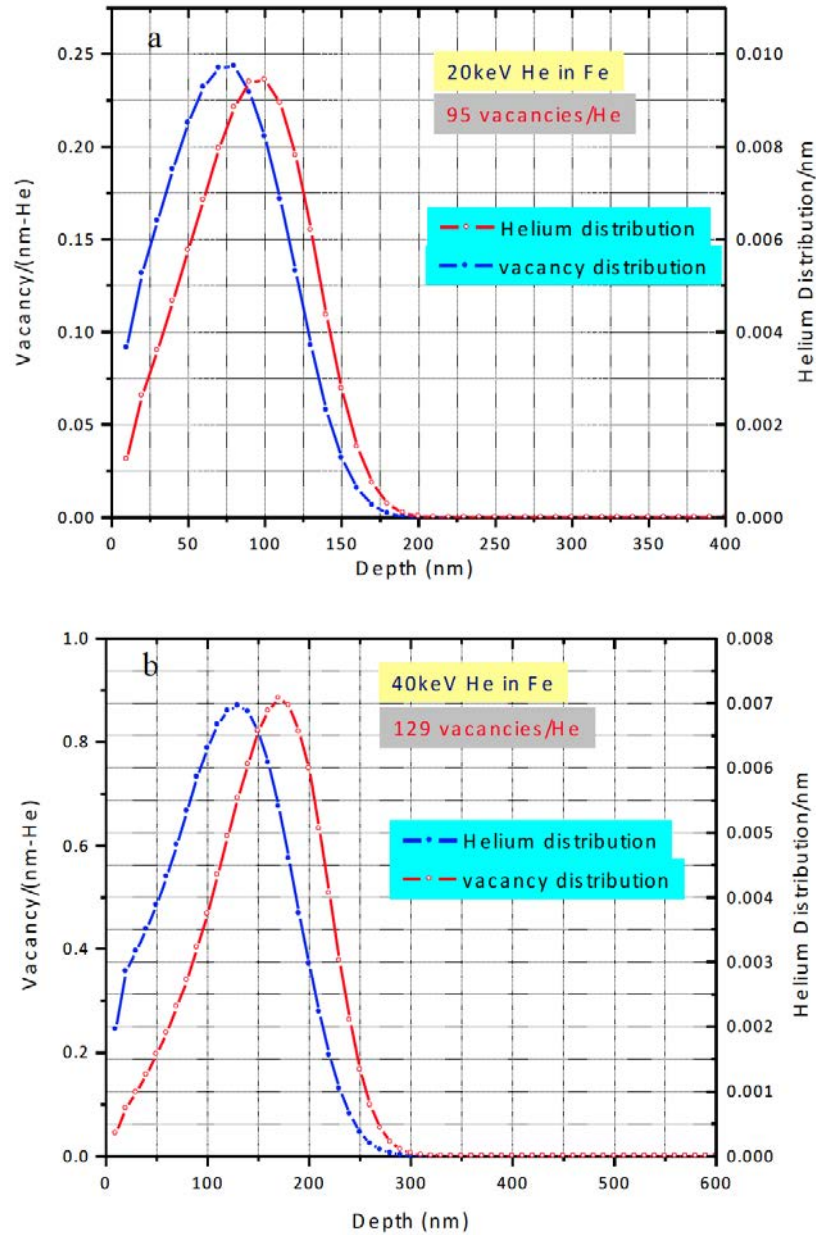


Figure 2-8. Helium and vacancy distribution for (a) 20 keV and (b) 40 keV helium implantation in iron calculated by SRIM 2008.

2.2 Positron annihilation spectroscopy (PAS)

2.2.1 Introduction

Positron annihilation spectroscopy (PAS) is well established as a powerful tool for detecting defects on an atomic scale in metals and semiconductors [104-108]. Owing to the ability of the positron to annihilate from a variety of specific states in solids, ranging from an extended state in a defect-free lattice to highly localized states in lattice defects, PAS can yield unique information regarding various properties of materials [106]. The unique aspects of PAS arise from the fact that the positron-electron pair annihilation process, which proceeds by the emission of γ rays, can yield detailed information regarding both the electron density and the electron momenta in the region from which the positron annihilates. The specific technique used in our study is the positron annihilation lifetime (PAL) measurement.

Conventional sources of positrons for PAS are artificial radioisotopes (e.g. ^{22}Na , ^{64}Cu , ^{58}Co) emitting β^+ , of which the most frequently used is ^{22}Na with a half-life $T_{1/2}=2.602$ y. Its decay scheme is shown in Fig. 2-9(a) [107]. End-point energy of ^{22}Na is at 545 keV. An important feature of the ^{22}Na decay is simultaneous emission (within a few picoseconds) of β^+ - and γ -radiation ($E_\gamma=1274$ keV). When a positron is injected into a solid, it becomes thermalized within a few picoseconds by a succession of ionizing collisions, electron-hole excitation, and phonon interactions. After reaching thermal equilibrium with the host, the positron evolves in a diffusion process, during which the positron interacts with its surroundings and eventually annihilates with an electron, shown in Fig. 2-9(b). The electromagnetic interaction between electrons and positrons makes possible annihilation of e^+e^- pairs in which the total energy of the annihilation pair may be transferred to the generated photons γ (with energies of ~ 511 keV).

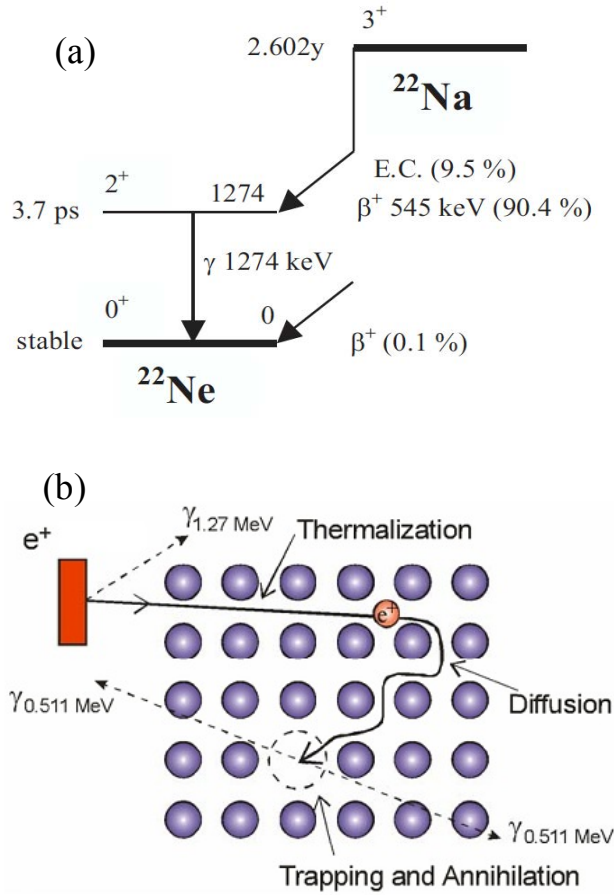


Figure 2-9. (a) Decay scheme of ^{22}Na , as reproduced from Ref. [107]; (b) Positron evolution in material.

Positron lifetime is usually obtained from the time interval between the 1274 keV γ -ray accompanying the β^+ decay of the ^{22}Na and the positron annihilation γ -rays of 511 keV, which is the basic principle for the construction of positron lifetime spectrometer. Fig. 2-10 shows a schematic diagram of our PAL spectrometer. BaF_2 scintillators are coupled to photomultiplier tubes (PMT) and the applied voltage on PMTs is 2900 V, which is considerably lower than the maximum rating value (3500 V). The operating mode is double-stop setup, in which three PMTs are used. The 1274 keV γ -ray is detected by PMT1, while a pair of 511 keV γ -rays is detected by PMT2 and PMT3, which are placed face to face on the opposite sides of the source-sample assembly.

In our PAS setup, a digital oscilloscope (LeCroy Wavepro 7300A), which has 4 channel inputs, a sampling rate of 10 GS/s and an analog bandwidth of 3 GHz, is employed to convert the waveforms of the scintillation detectors into digitized data. The anode outputs of the PMTs are connected directly to CH1, CH2, and CH3 of the digital oscilloscope. The waveforms of the output pulses are digitized and stored when the oscilloscope is triggered by a coincidence signal.

The measurements are conducted at room temperature, using conventional sample-source-sample sandwich geometry. The positron source was made from a $^{22}\text{NaCl}$ solution evaporated onto the surface of the samples. The system timing resolution is ~ 170 ps.

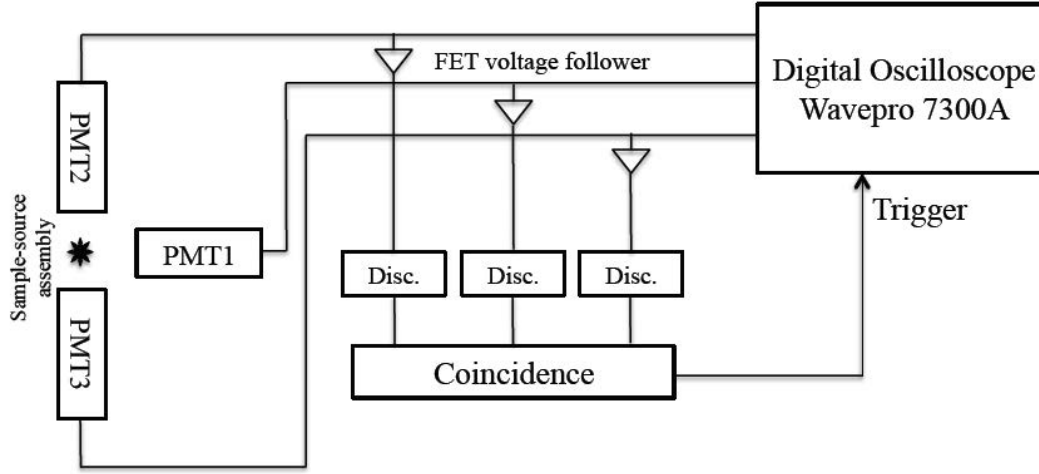


Figure 2-10. Schematic diagram of the positron lifetime spectrometer.

In the double-stop operating mode, the time interval Δt between the 1274 keV γ -ray and the 511 keV positron annihilation γ -ray is calculated as

$$\Delta t = T_{stop} - T_{start} \quad (2-9)$$

where

$$T_{stop} = [T_{CF}(PMT2, 511\text{keV}) + T_{CF}(PMT3, 511\text{keV})] / 2 \quad (2-10)$$

and

$$T_{start} = T_{CF}(PMT1, 1.274\text{keV}). \quad (2-11)$$

It is noted that T_{CF} is the time at which the pulse crosses the constant fraction of 25% of the amplitude.

A typical positron lifetime spectrum for single-crystal iron with a purity of 99.98% obtained from this facility is shown in Fig. 2-11.

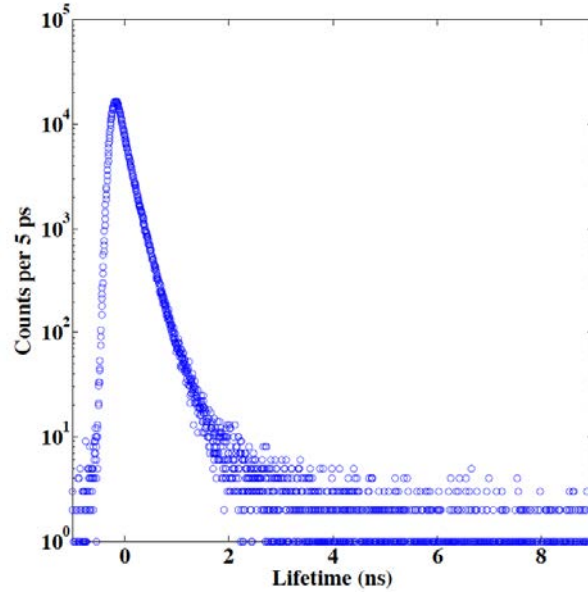


Figure 2-11. Positron lifetime spectrum for single-crystal iron with a purity of 99.98%.

2.2.2 Data analysis

The classical trapping model analysis of positron annihilation behavior [104] indicates that the spectrum of positron lifetime is a sum of exponential components

$$N(t) = \sum_{i=1}^n f_i \lambda_i \exp(-\lambda_i t), \quad (2-12)$$

where λ_i is the positron annihilation rate and expressed as $\lambda_i = \tau_i^{-1}$ (τ_i is the positron lifetime in type i defect); f_i is the fraction of the positron annihilating in the type i defect.

The number of components n is equal to the number of different states which positrons can annihilate from, e.g., in the case of k types of defects $n=k+1$. Generally n should be regarded as an unknown parameter. In practice only up to three components can typically be resolved in spectra without involving any constraints on parameters.

The experimentally obtained spectra differ from the analytical description Eq. (2-12) by convolution with time resolution function R (i.e., a pure Gaussian, $R=G(\text{FWHM}, t)$), which is the response of the spectrometer to prompt coincidences. The R function resembles Gaussian like shape and is characterized by the full width at half maximum (FWHM). The exponential component, convoluted with the R function, is expressed by [109, 110]:

$$F(f, \tau, t_k) = \frac{f}{2} [Y(\tau, t_k) - Y(\tau, t_{k+1}) - \phi(t_{k+1}/s) + \phi(t_k/s)], \quad (2-13)$$

where t_k is the mean time related to the k th channel and

$$s = \frac{FWHM}{2\sqrt{\ln 2}}, \quad (2-14)$$

$$Y(\tau, t) = \exp\left(\frac{s^2}{4\tau^2}\right) \phi\left(\frac{s}{2\tau} - \frac{t}{s}\right) \exp\left(-\frac{t}{\tau}\right), \quad (2-15)$$

$$\phi(x) = 1 - \text{erf}(x). \quad (2-16)$$

For $t \gg s$ (practically for $t > 2FWHM$), $\phi(t)$ is a hardly changeable function of t , so the difference of the ϕ in Eq. (2-13) can be estimated to be zero.

Combining Eqs. (2-13) ~ (2-16), the expression of $F(f, \tau, t_k)$ is

$$\begin{aligned} F(f, \tau, t_k) &\equiv \frac{f}{2} [Y(\tau, t_k) - Y(\tau, t_{k+1})] \\ &= \frac{1}{2} f \exp\left(\frac{s^2}{4\tau^2}\right) \left[\exp\left(-\frac{t_k}{\tau}\right) - \exp\left(-\frac{t_{k+1}}{\tau}\right) \right] \phi\left(\frac{s}{2\tau} - \frac{t_k}{s}\right) \\ &= \frac{1}{2} \left[1 - \text{erf}\left(\frac{s}{2\tau} - \frac{t_k}{s}\right) \right] \frac{f}{\tau} \exp\left(\frac{s^2}{4\tau^2}\right) \exp\left(-\frac{t_k}{\tau}\right) \Delta t \\ &= \frac{1}{2} \left[1 - \text{erf}\left(\frac{s}{2\tau} - \frac{t_k}{s}\right) \right] \frac{f}{\tau} \exp\left(\frac{s^2}{4\tau^2} - \frac{t_k}{\tau}\right) \Delta t \\ &= \frac{1}{2} \Delta t \left\{ 1 - \text{erf}\left[\frac{2\sqrt{\ln 2}}{FWHM} \left(\frac{FWHM^2}{8(\ln 2)\tau} - t_k \right) \right] \right\} \frac{f}{\tau} \exp\left(\frac{FWHM^2}{16(\ln 2)\tau^2} - \frac{t_k}{\tau}\right) \end{aligned} \quad (2-17)$$

where Δt is the width of a channel.

Therefore, the measured spectrum can be fit by the following expression:

$$N(t) = \sum_{i=1}^n F(f_i, \tau_i, t) \quad (2-18)$$

In our study, 2 or 3 components are usually applied. The fit function of 'cftool' in MATLAB is employed here to extract the interesting parameters.

2.2.3 Positron lifetime measurements of helium implanted single-crystal irons

The positron lifetime measurements were conducted for the single-crystal iron samples implanted by 40 keV helium ions to a fluence of $1 \times 10^{15} / \text{cm}^2$. All of the samples have experienced the same treatments as those used in THDS experiments. In order to obtain the evolution information of the He-V clusters at different annealing stages, three interesting temperature points have been chosen, as shown in Fig. 2-12. The first point of interest is the initial condition of the samples after helium implantation at room temperature. Points II (300 °C) and III (750 °C) are picked up after the two major helium desorption peaks.

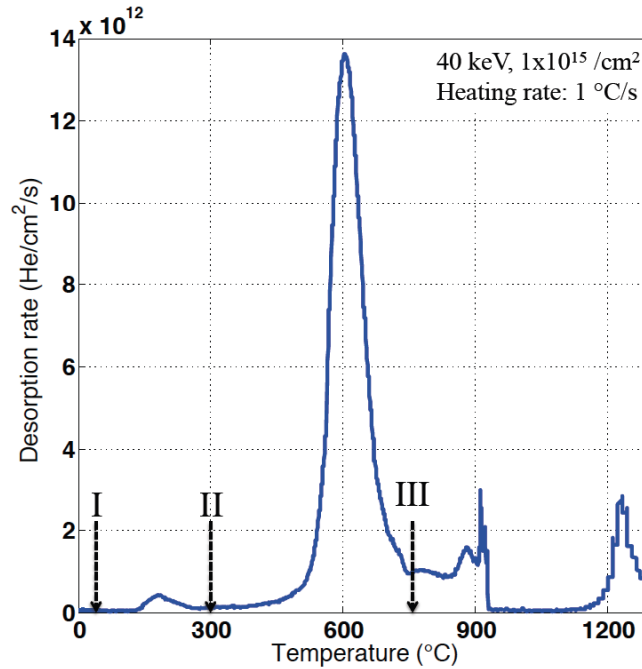
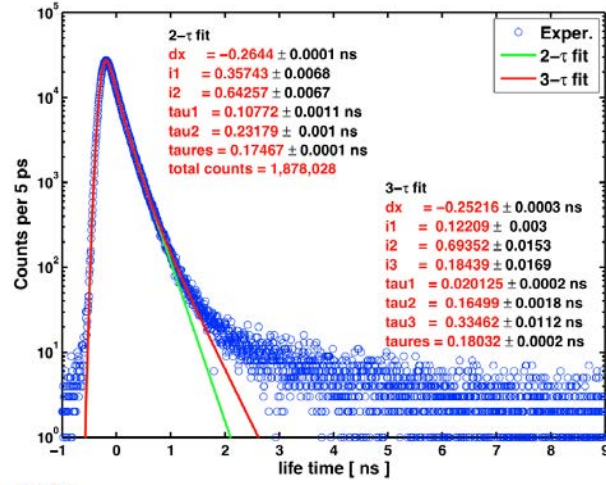


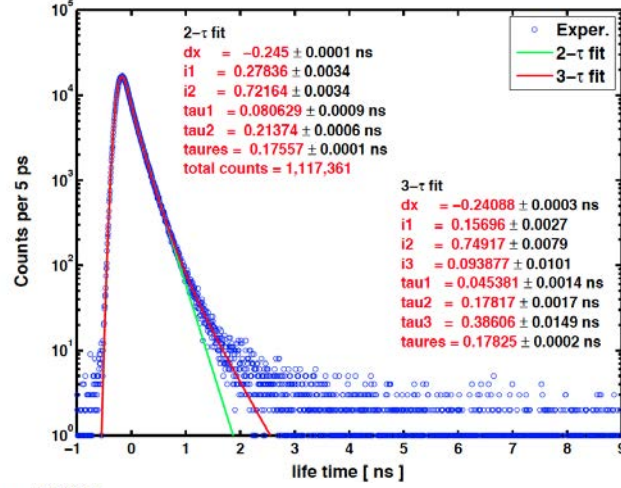
Figure 2-12. Helium desorption spectrum of high purity (99.98%) single crystal iron following implantation of 40 keV, $1 \times 10^{15} / \text{cm}^2$. Three temperature points of interest (i.e., I as irradiated; II 300 °C; III 750 °C) are marked to do the positron lifetime analysis.

Since the PAL measurement makes use of the conventional sample-source-sample sandwich geometry, two samples are necessary for each measurement. For the points of II and III, two identical samples are placed in the THDS system and heated to the same temperature together, respectively. Then the two samples are removed and transferred to the PAL sample preparation region. The ‘sandwich’ sample assembly is made by depositing $^{22}\text{NaCl}$ solution onto the surface of one sample, covering the sample surface with the other one after the hot surface is dried, and packing the samples using aluminum foil. Finally, the sample assembly is placed in the system to process the data collection.

a. As irradiated



b. 300°C



c. 750°C

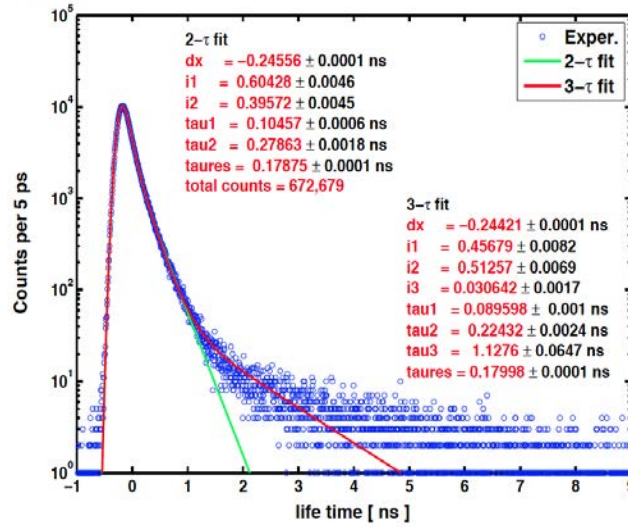


Figure 2-13. Positron lifetime measurement and analysis for three different conditions: (a) as irradiated; (b) annealing at 300 °C; (c) annealing at 750 °C.

Fig. 2-13 demonstrates the PAL measurements and analysis for the three points of interest. Both two and three components analysis are employed for each measurement. The lifetime, analyzed by resolving two and three main lifetime components as decaying exponentials, gave a satisfactory fit to the overall data.

We focus on the two components analysis to indicate the comparison of the three different conditions. Fig. 2-14 shows the lifetime and intensity change as a function of the annealing temperature. Fig. 2-14(a) shows the resulting two lifetime parameters at the three conditions in blue and green symbols for the short (τ_1) and long (τ_2) lifetime component, respectively, and the mean lifetime in red. The mean lifetime of positron can

be obtained by a simple linear calculation, $\bar{\tau} = \sum_{i=1}^n \tau_i f_i$. The long lifetime is interesting because this parameter is corresponding to the collective lifetime of the positrons in the defects, from which the defect information can be derived. Fig. 2-14(b) shows the intensity of the long lifetime component, representing the defect concentration.

The long lifetime decreases from 231 to 214 ps from the as-implanted condition to the annealing temperature of 300 °C, then increases to 278 ps following annealing to 750 °C. These lifetime values can be translated to specific cluster sizes based on theoretical calculations from Troev et al. [111], which calculated that a lifetime of 231 ps is consistent with either a 4-V cluster or a 6V-1He cluster, 213 ps is corresponding to a 2-V or a 5V-He cluster, and 278 ps is related to the existence of 10-V cluster or He₂V_m (m>10). The fact that the measured positron lifetime is a collective result needs to be emphasized. Moreover, the existence of helium enhances the complication of assessing and interpreting the positron lifetime. However, the deduction provides a straightforward view of the size of the defects inside the material at different annealing steps.

The decrease in long lifetime value with increasing intensity after annealing to 300 °C is consistent with more small He-V clusters produced by interstitial helium dissolving into the vacancy clusters after the first small helium releasing peak. The total concentration of the defects is increasing. Likewise, the increase in long lifetime value and decrease in intensity after annealing to 750 °C (relative to 300 °C) indicates a decrease in overall He-vacancy cluster density and increase in size after the major helium desorption peak.

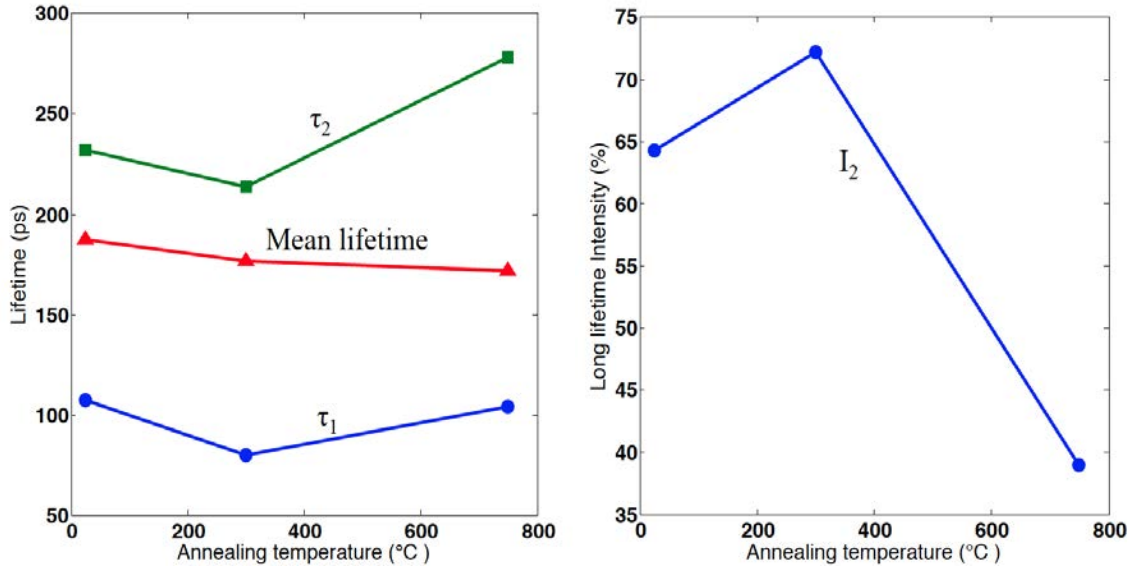


Figure 2-14. Two components analysis of the positron annihilation lifetime spectrum after each step of the annealing for the high purity single-crystal irons implanted by He-4 of 40 keV, 1×10^{15} He/cm².

Based on the above analysis, combined with the THDS result, an overall road map of the He-V clusters can be achieved. At the very beginning, only small He-vacancy/vacancy clusters are formed after He implantation. With increasing temperature, some fraction of helium will diffuse to the surface of the sample and desorb. The initially formed vacancy clusters will dissolve to smaller clusters or single vacancies, which is driven thermodynamically. Meanwhile, more and more interstitial helium will react with the vacancy clusters to generate He-V clusters. When the temperature is high enough, the He-V clusters will be unstable, and the dissociation of helium becomes significant enough to be observed as a major helium desorption in THDS result. After this release, the total concentration of He-V clusters will decrease while the stable and larger He-V cluster at high temperatures will survive.

The PAL analysis can only provide a qualitative idea about the helium-vacancy cluster evolution. Some important information, e.g., detailed distribution of the clusters, the dominant clusters contributing to the helium desorption, etc., cannot be derived from the current measurement. However, the combination of experiment and modeling provides a way to solve this problem.

2.3 Conclusion

Two experimental techniques, i.e., THDS and PAL, are introduced in this chapter along with representative results from He implanted iron specimens. THDS measures the helium desorption rate out from sample surface, which reflects the invisible helium-point defects interactions beneath the surface indirectly. PAL measurements at different

annealing stages show the basic idea of the cluster evolution. However, very limited information can be extracted from these two experimental methods. In order to obtain the insights of the helium-point defects interactions, the combination of experiments and modeling is necessary. For THDS, this combination helps to understand the physical mechanisms of the interactions that control the desorption flux. Correspondingly, the THDS results can provide a platform to verify the overall accuracy of the developed model. For PAL, the coordinated model analysis can indicate the detailed distribution of helium defects clusters, which can be compared with the PAL measurements directly.

In the following chapter, a cluster dynamic model based on classical rate theory will be introduced.

Chapter 3

Spatially Dependent Cluster Dynamics Model Based on Rate Theory

Complete interpretation of the experimental data introduced in Chapter 2 requires detailed modeling which takes into account the migration, trapping and de-trapping kinetics of helium with defects and/or defect clusters, as well as self-clustering. The duration of the mentioned experiments spans from hundred of seconds to several years, and the behavior of fusion reactor materials must be predicted for decades in service. Hence, the long-term evolution of defects and defect clusters needs to be considered. This involves inherently a multiscale phenomenon, as emphasized in Chapter 1. In this chapter, a kinetic model following the evolution of defects produced by He implantation in BCC iron is introduced.

3.1 Physical process

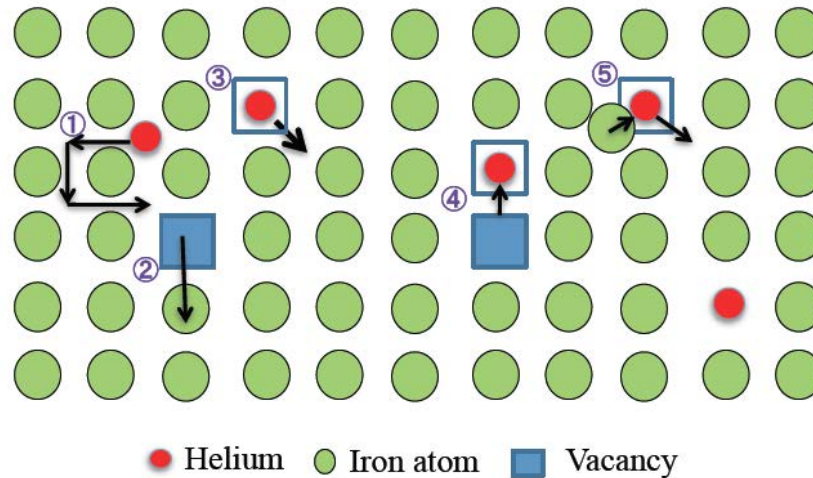


Figure 3-1. Schematic illustration of defect configurations and jumps processes related to He diffusion under irradiation. (1) migration of interstitial He; (2) migration of vacancy; (3) transformation of a substitutional to an interstitial He atom by thermally activated dissociation; (4) jump of a He atom from one to another vacancy as a basic step in the vacancy mechanism; (5) transformation of a substitutional to an interstitial He atom due to its replacement by a self-interstitial.

Due to its extremely low solubility in metals, helium occurs in metals only when it is forced there, for instance by He-implantation or by (n, α) reactions of neutrons with matrix nuclei during high energy neutron irradiation. On the other hand, the collisions between energetic particles and lattice atoms generate primary recoiling atoms (PRAs) with energies up to several hundred keV. The PRAs, in turn, generate a branching cascade of recoiling atoms that are displaced from lattice sites. Eventually, vacancies, self-interstitials and their clusters are formed and retained. Hence, the accumulation of helium in metals is nearly always accompanied by displacement damage.

He diffusion is a basic requirement for bubble nucleation and growth. It is the result of random jumps of He atoms from one to another lattice site. As shown in Fig. 3-1, the most important types of lattice sites and migration modes of He atoms in metals (e.g., iron) under irradiation are illustrated.

The most important positions for He atoms in a lattice are interstitial and substitutional (He atom in a vacancy) sites [112]. The preferential positions and the dominant migration mode depend on the temperature as well as on the presence of other intrinsic or irradiation induced defects that can act as traps for He atoms, particularly in the presence of vacancies and He-vacancy clusters. Because of the strong binding of He atoms to vacancies (with energies of a few eV), the substitutional site is the preferential one if the vacancy concentration is significant. In He diffusion, He interstitial migration, vacancy migration, the removal of a He atom from a vacancy or a He-vacancy cluster by thermal activation and the recombination of vacancy/vacancy clusters with self-interstitial are the most important basic processes.

As to the mentioned experimental conditions, He implantation into single crystal iron, there are three basic types of point defects, i.e., vacancy (V), self-interstitial (SIA), interstitial helium. The migration of each species leads to reactions which generate different clusters, such as vacancy or SIA clusters, resulting from the agglomeration of vacancies or SIAs, and He-V or He-SIA clusters produced through the capture of He atoms by vacancy/vacancy clusters/He-V clusters, SIA/SIA clusters/He-SIA clusters. The stabilities of these clusters vary for different temperatures, indicating that the clusters will experience growth/dissociation by absorbing/emitting defects driven by thermal activation. These physical processes constitute the base for the model construction.

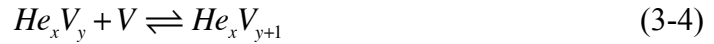
3.2 Model construction

In the classical rate theory [113-115], a defect/cluster is defined by its character, atomic configuration (i.e., planar loop, sphere, stacking fault tetrahedron, loop Burgers vector, etc.), and size (i.e., number of point defects contained). All of the clusters considered in the present calculations can be formulized as $He_x V_y$ with $0 \leq x \leq nh$ and $-ni \leq y \leq nv$, where nh , ni , nv are the maximum numbers of He, SIA and vacancy in a cluster which define the boundaries of the selected He-V phase space, and where a negative y value refers to a $He_x I_{|y|}$ cluster. Since the probability that interstitials and vacancies co-exist in a single cluster is very low due to their strong tendency for recombination, no mixed I-V

clusters are considered. In this chapter, the interactions between He and SIA are not considered because they are generally believed to be weaker than the He-V interactions, thus in the formula y can be negative only when $x=0$. Since the clusters can grow to larger ones, the originally defined phase space size changes, and the initial n_h , n_i , n_v values may become insufficient and need to be modified whenever a threshold value of the concentration of the largest cluster is reached along the three boundaries.

The dynamic evolution of the defined clusters results from the interactions between the clusters and the mobile species. The transition of any cluster can be realized through annihilation (being transformed to another) or generation (being transformed from another). Capture and dissociation of the mobile species from the corresponding clusters are the two possible ways for each transition mechanism.

In general, a typical He_xV_y cluster can be generated by the capturing of a mobile species He_mV_n by another mobile or immobile cluster $He_{x-m}V_{y-n}$, or by the dissociation of He_mV_n from the mobile or immobile $He_{x+m}V_{y+n}$. Meanwhile, a He_xV_y cluster can be transformed (annihilated) to other sizes by capturing a mobile species He_mV_n (forming $He_{x+m}V_{y+n}$), or by dissociating a mobile species He_mV_n (forming $He_{x-m}V_{y-n}$). Some examples of the binary reactions in the model are provided below:



Note that for the dissociation processes, we only consider the release of a single point defect (i.e., V, I, He) at a time and neglect the possibility of the emission of a di-SIA by

any cluster. As shown in Eq. (3-9) and (3-10), the release of single vacancy from SIA clusters and the release of single SIA from vacancy clusters are forbidden because of their strong binding energies.

As mentioned at the beginning of this chapter, the classical rate theory defines a defect/cluster by its character, atomic configuration and size, but not by its spatial position since the theory assumes that the concentration of each cluster is homogeneous on a mean field basis [115]. While this homogeneous, or no-spatial-dependence, assumption is suitable for neutron irradiation of bulk material, in many other situations such as shallow ion implantations, very thin specimens or bulk specimens with heterogeneous microstructure, the accurate treatment of spatially varying damage production or special effects such as surface sinks and dislocation interaction does necessitate the inclusion of a spatial dependence into rate theory based models [115]. The current version of our model [71, 72] developed by Xu incorporates one spatial dimension intended to account for situations where key physical variables depend on position in one primary spatial direction.

In the present study of He-ion implantation in single crystal iron samples, the primary direction is the sample depth direction along which the defect evolution is expected to vary significantly due to the effect of the surface as a strong sink for defects. Due to the low energy of He-ion (tens of keV), the damage production and the retained He also strongly vary along the depth direction within the range of He implantation. Hence, one more dimension is added, which is spatial grids, nx . The four parameters, nh, ni, nv, nx , are now defining the phase space in the model. The inclusion of the spatial grids also allows the diffusion of mobile species along the depth (He-ion implantation) direction and makes the model more complicated.

With the knowledge discussed above, we are able to build up the basic scheme of the partial differential equation (PDE) describing the evolution of the clusters. Note that each defect/cluster at each spatial grid requires one PDE. The structure of the PDE varies according to the type of the defect/cluster. In this model, only single vacancy, self-interstitial, di-interstitials (I_2), interstitial helium are considered as mobile. All of the other clusters are immobile.

If the defect cluster is immobile, the equation is constructed as,

$$\frac{\partial C_{immobile}}{\partial t} = G_T + G_E - A_T - A_E, \quad (3-11)$$

where G refers to summed generation (formation) rates, A indicates the summed annihilation (consumption) rates, T means generation or annihilation by trapping events, E refers to generation or annihilation by emission events.

Different from Eq. (3-11), the equation for I_2 , which is mobile, is structured as

$$\frac{\partial C_{I_2}}{\partial t} = D_{I_2} \frac{\partial^2 C_{I_2}}{\partial x^2} + G_T + G_E - A_T - A_E - 1.15 \times \rho_{dislocation} \times D_{I_2} \times C_{I_2}, \quad (3-12)$$

where the first term on the right hand side is added to describe the diffusion of I_2 across neighboring spatial positions (x), and the last term is for the loss of I_2 to dislocation sinks with a bias factor of 1.15. A typical magnitude of the dislocation density, $10^{14}/m^2$, has been adopted in all of the calculations while other values, namely, $10^{13}/m^2$ and $10^{14}/m^2$, have also been investigated in Ref. [72] which revealed no significant difference.

The equation for interstitial He is expressed as

$$\frac{\partial C_{He}}{\partial t} = \phi \times P_{He}(x) + D_{He} \frac{\partial^2 C_{He}}{\partial x^2} + G_T + G_E - A_T - A_E, \quad (3-13)$$

where the first term on the right hand side is inserted to account for the generation of He by implantation, with ϕ being the implantation flux and $P_{He}(x)$ being spatially dependent He-stopping probability function predicted by SRIM/TRIM [103]. Note that although interstitial He is a point defect, it can still be generated by trapping reactions (e.g., Eq. (3-2)), and can also lose its identity by emitting a SIA, i.e., $He \rightarrow HeV + I$. At present, we do not consider He loss to sinks, since it cannot lose its identity, nor do we consider its binding with, dissociation from or diffusion along, dislocation lines in the present model due to the uncertainty in the dislocation structures/types which would affect how strongly the dislocations interact with He according to some atomic calculations [116].

The equations for single SIA and V are structured as, respectively,

$$\frac{\partial C_I}{\partial t} = \phi \times P_{FP}(x) + D_I \frac{\partial^2 C_I}{\partial x^2} + G_T + G_E - A_T - 1.15 \times \rho_{dislocation} \times D_I \times C_I, \quad (3-14)$$

and

$$\frac{\partial C_V}{\partial t} = \phi \times P_{FP}(x) + D_V \frac{\partial^2 C_V}{\partial x^2} + G_T + G_E - A_T - 1.0 \times \rho_{dislocation} \times D_V \times (C_V - C_V^{eq.}), \quad (3-15)$$

where $P_{FP}(x)$ is the SRIM/TRIM predicted generation probability function for Frenkel pairs, and $C_V^{eq.}$ is the thermal equilibrium concentration of single vacancy. Note that single SIA and V cannot undergo any type of emission and thus the A_E term disappears in Eqs. (3-14) and (3-15).

The defect kinetics of the entire system is thus described by a system of coupled PDEs, with one PDE for each composition in the two-dimensional phase space formed by a He-number axis and a V-number.

For all the mobile species (Eqs. (3-12)-(3-15)), the second derivative of concentration over x is numerically evaluated by the common finite difference formalism, i.e.,

$$\left. \frac{\partial^2 C}{\partial x^2} \right|_{x_i} = \frac{\frac{C_{x_{i+1}} - C_{x_i}}{x_{i+1} - x_i} - \frac{C_{x_i} - C_{x_{i-1}}}{x_i - x_{i-1}}}{\frac{x_{i+1} - x_{i-1}}{2}}, \quad (3-16)$$

at all interior spatial grid x_2 through x_{nx-1} where nx is the total number of spatial grids. Meanwhile, a Dirichlet boundary condition is used, which sets all defect concentrations equal to zero at x_1 and x_{nx} , i.e., both surface are treated as perfect sinks for all the defects.

Next, we need to define the cluster transition by mathematic expressions. In the classical rate theory, the cluster transitions are assumed to follow the kinetic law of mass action derived by Bronsted [117]. As shown in Eqs. (3-1)-(3-10), reactions between point defects and clusters are supposed to occur via binary reactions of the type



The symbols k_{A+B}^+ and k_C^- refer to the trapping (capture) and dissociation rate constants for the reaction, respectively. Assuming that the reaction rates follow the kinetic law of mass action, the generation-recombination (GR) rate corresponding to reaction (3-17), i.e., the net difference between the generation and the loss rate, can be written as

$$GR_{A+B} = k_{A+B}^+ C_A C_B - k_C^- C_C. \quad (3-18)$$

A convenient way to obtain the rate constant in the forward direction is the theory of diffusion-limited reactions. First presented by von Smoluchowski [118] in 1917 for the coagulation in colloidal solutions and derived later by Waite [113] on a statistical basis, the forward rate constant of diffusion limited reaction $A + B \rightarrow C$ is determined mainly by the diffusion of the reactants toward each other and is written as follows

$$k_{A+B}^+ = 4\pi(r_A + r_B)(D_A + D_B), \quad (3-19)$$

where D_A and D_B are the diffusion coefficients of the reacting species A and B, respectively; r_A and r_B are the capture radii of species A and B. The diffusion coefficient can be written as

$$D = D_0 \exp\left(-\frac{E_m}{kT}\right), \quad (3-20)$$

where D_0 is the pre-factor (2×10^{-4} cm²/s is used initially for all mobile species); E_m is the migration energy of the mobile species; k is Boltzmann's constant, and T is the

absolute temperature. From ab initio calculations [119], 0.42, 0.34, and 0.06 eV are used as the migration energies for I₂, I, and He in BCC iron, respectively, and we have treated the vacancy migration energy (0.67±x eV) as an optimization parameter.

It is assumed that a reaction between two defects takes place spontaneously if the defects are located within a critical distance which is the sum of their capture radii. This parameter thus defines the distance at which defects interact with each other. In this work, the interaction volume of a defect is approximated by a sphere of radius r . Since the interstitial-type defects develop a larger strain field than vacancy-type defects, a bias factor is introduced to the expression of the capture radii of interstitial clusters. For different types of defects, the radii of the defect clusters are given by

$$r_{V_n} = \left(\frac{3n\Omega}{4\pi} \right)^{1/3}, \quad (3-21)$$

$$r_{I_n} = 1.15 \times \left(\frac{3n\Omega}{4\pi} \right)^{1/3}, \quad (3-22)$$

where r_{V_n} is the capture radius of a vacancy cluster containing n vacancies and r_{I_n} is the capture radius of an interstitial cluster comprising n interstitials. Ω is the atomic volume.

Having quantified the formation rate constant of reaction (3-17), we also need to derive the corresponding backward rate constant, i.e., the frequency at which the inverse reaction $C \rightarrow A + B$ occurs. To do so, we consider the fact that in steady state, formation and dissociation rates must be equal, i.e., $GR_{A+B} = 0$. This leads to the well-known law of mass action:

$$\frac{k_C^-}{k_{A+B}^+} = \frac{C_A C_B}{C_C} \Big|_{eq}. \quad (3-23)$$

Alternatively, this expression can be written in terms of the energetics of defects, which enables us to express the dissociation rate k_C^- as follows,

$$k_C^- = k_{A+B}^+ N_s \exp \left(- \frac{G_A^f + G_B^f - G_C^f}{kT} \right), \quad (3-24)$$

where G_A^f , G_B^f , and G_C^f are the Gibbs free formation energies of species, A, B, and C, respectively. These energies are related to the binding energies E_b^i by $E_b^i = G_A^f + G_B^f - G_C^f$. N_s is the number of available sites, which is assumed to be the same for all defects considered here.

It should be pointed out that the formulation of reaction kinetics and reaction constants for the classical rate theory are most suitable for reactions induced by three dimensional migration of defect clusters. Several MD simulations [120-124] suggest that the interstitial clusters induced by irradiation in metals in the form of dislocation loops can rotate and change direction while migrating one dimensionally along the Burger vector and thus displayed mixed 1D and 3D diffusion. Heinisch et al. [125] show that the KMC calculation of the frequency of rotation suggests that a wide range of rotation falls closer to the 3D reaction kinetics. Therefore, the 3D kinetics is used throughout this study [71, 72, 115].

3.3 Parameterization

As shown in Eqs. (3-13)-(3-15), He implantation is one of the sources for the generation of the point defects, i.e., SIA, V, and He. TRIM/SRIM calculations on the 5 and 10 keV He-ion implantation in iron, shown in Fig. 3-2, are taken as an example to indicate the spatially dependent He-stopping probability function and Frenkel pair generation function. Note that only Frenkel pair production is assumed by each He implantation event in this study, although the He implantation at higher incident ion energies can induce the cascade and cause the generation of small defect clusters in iron [115]. Additionally, the damage and He production plots are fit by a Gaussian function and Fourier function, respectively, in order to simplify the calculation. Considering that the spatial range of the stopped He ions and the created point defects is well within 100 nm beneath the iron surface, a maximum depth of 500 nm is used in the modeling.

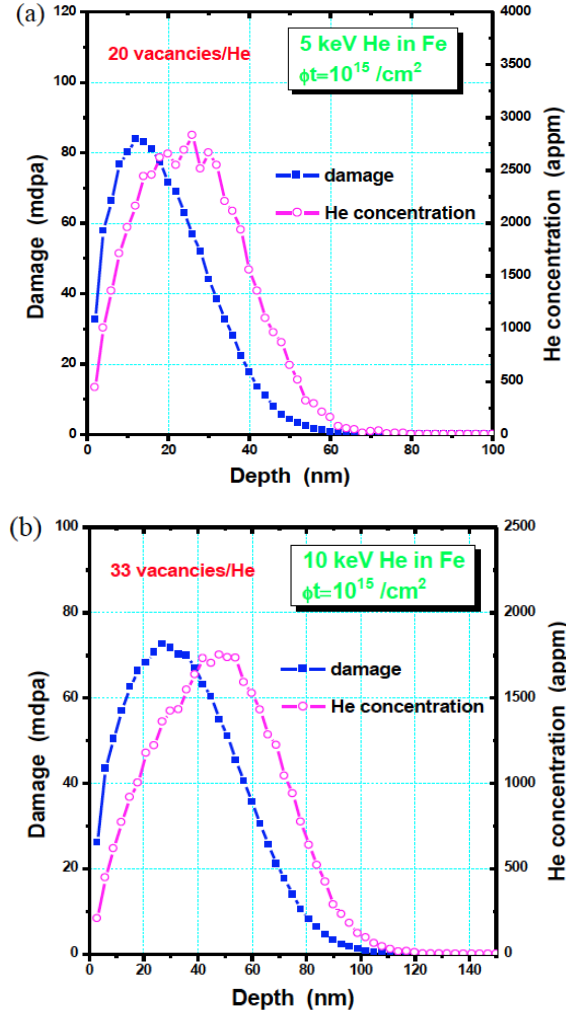


Figure 3-2. Helium concentration and damage distribution as a function of depth for (a) 5 keV and (b) 10 keV He-ion implantation in iron calculated by TRIM/SRIM 2008.

To express the dissociation processes of the clusters, the binding energies of He, SIA, V to the clusters must be known. Thanks to the extensive studies on the energetics and kinetics of V clusters, SIA clusters and He-vacancy clusters for iron in the past 30 years, we are able to complete the parameterization of the equations described in Section 3.2.

In this work, we used the binding energies of vacancy and interstitial clusters calculated by Fu et al. [61] using density functional theory (DFT). For the formation energies of the single SIA and single vacancy, 3.77 and 2.07 eV are used, respectively. Table 3-1 summarizes the binding energies obtained from Ref.[126] for small interstitial and vacancy clusters.

Table 3-1. Binding Energies of small interstitial and vacancy clusters in iron according to Ref. [126].

	I_n (eV)	V_n (eV)
n=2	0.80	0.30
n=3	0.92	0.37
n=4	1.64	0.62

For large clusters, an extrapolation was used to calculate their binding energies. MD simulation done by Soneda et al. [122] indicates that the formation energies of interstitial and vacancy clusters follow the 2/3 law, namely,

$$E_{I_n, V_n}^f(n) = A \times n^{2/3}, \quad (3-25)$$

where A is a constant which can be obtained by the known formation energies; n is the number of I or V included in the clusters.

The binding energy of the point defect (e.g., I, V) with clusters (e.g., I_n , V_n) can be written as

$$E_{I_n, V_n}^b = E_{I, V}^f + E_{I_{n-1}, V_{n-1}}^f - E_{I_n, V_n}^f. \quad (3-26)$$

Combining the Eqs. (3-25) and (3-26), the binding energies for larger clusters ($n > 4$) based on ab initio calculation can be obtained, namely,

$$E_{I_n}^b = 3.77 + (E_{I_2}^b - 3.77) [n^{2/3} - (n-1)^{2/3}] / (2^{2/3} - 1) [eV], \quad (3-27)$$

$$E_{V_n}^b = 2.07 + (E_{V_2}^b - 2.07) [n^{2/3} - (n-1)^{2/3}] / (2^{2/3} - 1) [eV], \quad (3-28)$$

For the $He_x V_y$, only the binding energies for some small clusters ($x < 5$, $y < 5$) are studied by MD or ab initio [119]. Since the calculation will evolve in the He-V clusters including hundreds of defects or even larger, the binding energies for those big clusters are necessary. Fortunately, the formation energies of $He_x V_y$ ($x > 0, y \geq 0$) can be calculated using thermodynamics and based on the formalism proposed by Trinkaus [33], including the He equation of state. The formation process of He-vacancy clusters is anticipated to occur by three steps: formation of a cavity consisting of y vacancies, introduction of helium into the rigid cavity, and relaxation of the resulting cluster.

Yet in this work, we adopt two different treatments. We use the Gibbs free energy instead of the Helmholtz free energy for bulk He. And, instead of using the first order approximation based on the starting un-relaxed state for the change of the rigid terms during relaxation as included in Eq. (17a) of Trinkaus, we treat the elastic relaxation in a more thorough way by numerically solving for the zero point of the real derivative of the total energy, and then use the so-found relaxed radius to back calculate the total energy which involves integrals for the He-related terms. It should be mentioned that the choice

of the reference radius for the integrals affects only the exact formation energies of those clusters with at least one helium, but does not affect the resulting binding energies of He or V to the clusters due to its cancellation as follows [71]:

$$E_b^{He,V} = G_{f,1}^{He,V} - \mu^{He,V in bubble} = G_{f,1}^{He,V} - \frac{\partial G^{bubble}}{\partial n_{He,V}} \approx G_{f,1}^{He,V} + G_{f,n-1}^{bubble} - G_{f,n}^{bubble}. \quad (3-29)$$

For the He-vacancy clusters, the emission of SIA is also allowed in this work. Likewise, the binding energies of SIA to the clusters are acquired by

$$E_b^{SIA} = G_{f,1}^{SIA} + G_{f,n+1}^{bubble} - G_{f,n}^{bubble}. \quad (3-30)$$

Fig. 3-3 shows the binding energies of He, vacancy, and SIA to the He-vacancy clusters in a 3-D view. Fig. 3-3(a) indicates negative He binding energies occur at large He/V ratio, greater than 2.0, which means that it is very easy for He to be dissociated from the clusters when He atoms dominate the cluster or it is less likely to form the clusters of which the He atoms are much more than vacancy. Fig. 3-3(b) shows that the vacancy binding energies are pretty low when the He/V ratio is low, indicating it is easy for vacancy to be desorbed from the clusters with a low He/V ratio. The most stable clusters have He/V ratio around 1 since the binding energies are big, which is consistent with previous MD studies [60]. Fig. 3-3(c) demonstrates that the interstitial binding energies have a similar trend with helium binding energies, which is more obvious when plotted as shown in Fig. 3-4. Likewise, negative values occur when the He/V ratio is greater than 2.0. Moreover, the binding energies all roughly scale with He/V ratio, as shown in Fig. 3-4.

The binding energies listed here constitute the database for description of the cluster transitions and also provide the initial values for the parameter optimization in the modeling.

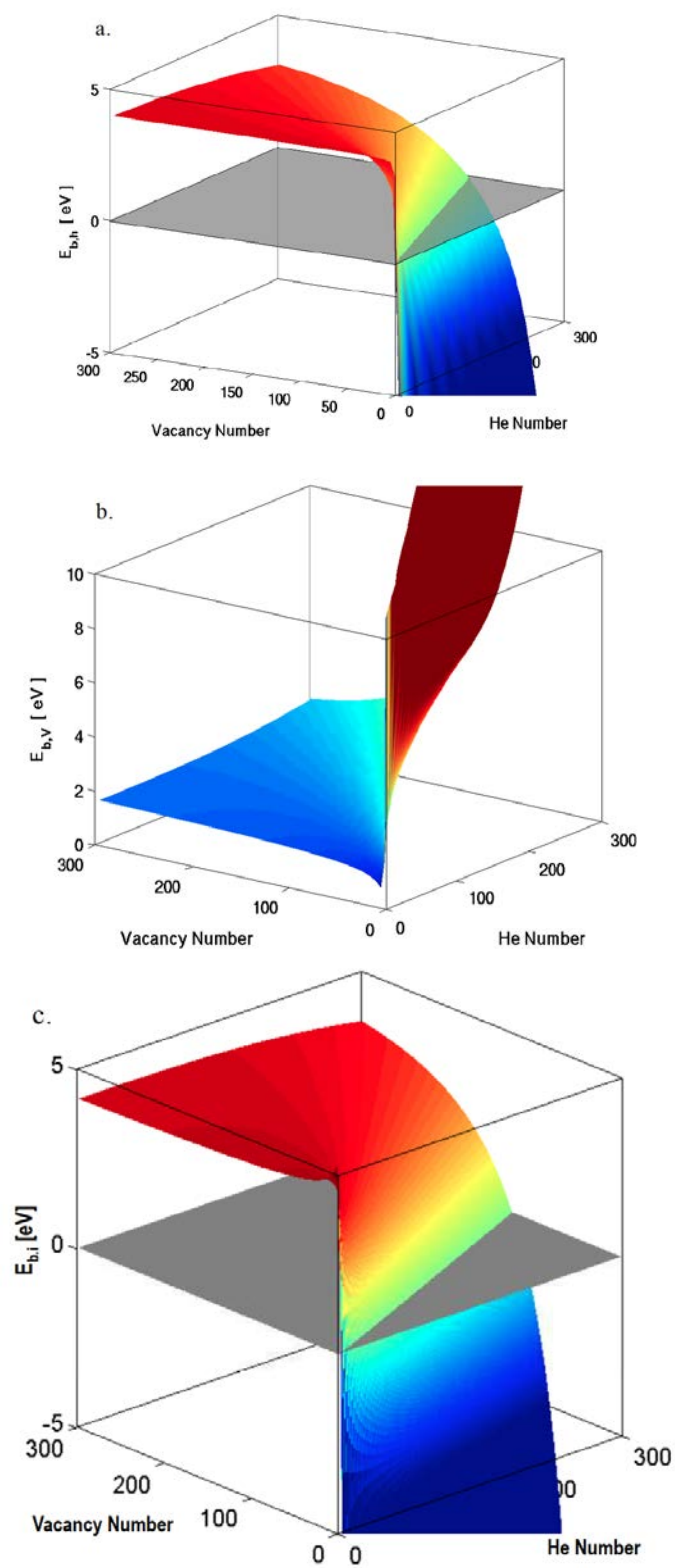


Figure 3-3. 3-D view of the binding energies of (a) helium, (b) vacancy, and (c) interstitial to the He-vacancy clusters.

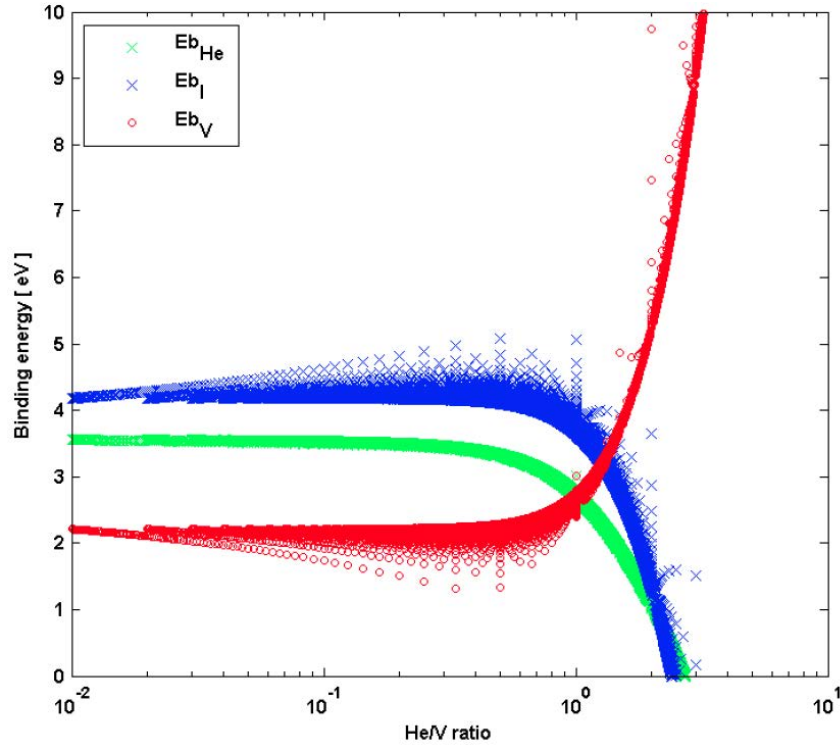


Figure 3-4. Binding energies of He, vacancy, interstitial to He-vacancy clusters as a function of He/V ratio.

3.4 Numerical solution

The PDEs represented by Eqs. (3-11)-(3-15) are converted to ordinary differential equations (ODEs) by applying the discretization form of the second derivative of concentration over x , Eq. (3-16). Thus, each defined cluster requires one ODE to describe its behavior. Hence, the total number of ODEs is equal to the total number of clusters $(n_i + (n_v + 1) \times (n_h + 1) - 1)$ multiplied by the total number of depth grids (x). The problem is simplified to solve the initial value ODE, namely,

$$C' = f(t, C), \quad C(t_0) = C_0. \quad (3-31)$$

Xu [71, 72, 115, 127, 128] developed a parallel cluster dynamics code named as PARASPACE, an abbreviation of PARAllel SPAtially-dependent Cluster Evolution, which takes use of the fully implicit backward-differentiation-formula (BDF) approach with adaptive order (up to 5th) and adaptive time step. The general formula for a BDF can be written as

$$\sum_{k=0}^s a_k C_{n+k} = h\beta f(t_{n+s}, C_{n+s}), \quad (3-32)$$

where h denotes the step size and $t_n = t_0 + nh$. The coefficients a_k and β are chosen so that the method achieves order s , which is the maximum possible.

In the computing process, to advance the integration to a new time step, all the concentrations at the new time step are vectorized and assembled into non-linear algebraic equations, which are then solved through Newton iterations. The implementation of Newton iterations requires repeated rate (time derivatives of all concentrations) evaluations and Jacobian matrix evaluations. Each step in a Newton iteration requires solving a linear algebraic equation system of generic type $AX = B$ (A is a matrix, X and B are both vectors) which is conducted by using external linear solvers such as PARDISO [129, 130] and ILUPACK [131] that have been developed on the basis of LU-factorization. The code is able to handle annealing problems that involve varied temperatures by recalculating all parameters, which are functions of temperature, at every time step.

Moreover, PARASPACE implements OpenMP parallelism, which allows for flexible combination of parallel and sequential code segments. The iterations throughout the code are parallelized wherever possible. It is also important to note that sparse matrix notation is employed which allows for the handling of huge matrices of dimensions $> 10^7$ by 10^7 with more than 10^9 non-zero elements.

3.5 Modeling results

3.5.1 Simulation of THDS using a linear temperature profile

In order to verify the developed model, the experiments described in Chapter 2 are used to show the self-consistence of the model. For the THDS experiments, the helium implantation and the annealing processes are simulated, and the He desorption flux is computed using Fick's First Law [132] after obtaining the cluster distribution at each time point.

Xu et.al [71, 72] have attempted to simulate the helium desorption spectra from single crystal iron with a purity of 99.94% implanted by ^4He ion with implantation energies of 5 or 10 keV to a fluence of 10^{18} or 10^{19} He/m². Fig. 3-5 presents the modeled desorption signal for the 10 keV and 10^{18} He/m² implantation condition, using the binding energies for He_xV_y obtained directly from the thermodynamic calculations. Considering the effect of the impurities (e.g., carbon) [133], the vacancy migration energy is set to 0.9 eV [71] instead of the ab initio value of 0.67 eV.

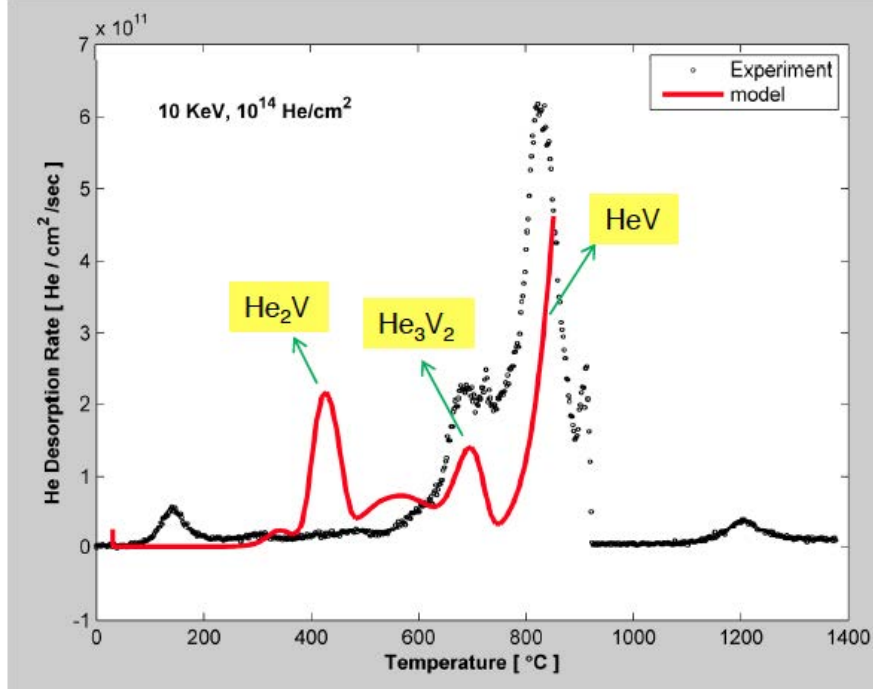


Figure 3-5. Comparison of experimentally measured thermal helium desorption from high purity (99.94%) single crystal iron implanted with 10 keV He to a fluence of 10^{14} He/cm², with the modeling results, as reproduced from Ref. [71].

Notably, Fig.3-5 indicates that the initial parameterization produces some similarity between the model and the experiment. The model prediction includes several obvious He releasing peaks. The first predicted releasing peak takes place around 410 °C. The predicted peak at 700 °C almost has the same position with the experimental signal. Similarly, a dominant releasing peak occurs for both experiment and model at high temperature region (i.e., greater than 800 °C). An analysis of the detailed cluster evolution, i.e., the variation with time in the concentrations of all clusters, results in the identification of the most important dissociation processes (i.e., He₂V, He₃V₂, and HeV as denoted in Fig. 3-5) contributing to the formation of the three major peaks. Therefore, we attempt to perform a parameter optimization, which aimed at improving the agreement between the model and the experiments, and focus on tuning the binding energies of these critical clusters in addition to the vacancy migration energy ($E_{m,v}$).

The solid lines in Fig. 3-6 [72] represent the predicted spectra in the BCC region with the best overall agreement with the experiments obtained so far with the model using a single set of optimized parameters: $E_{m,v} = 0.8 \text{ eV}$, $E_{bHe,HeV} = 3.2 \text{ eV} (= E_{bV,HeV})$, $E_{bHe,He2V} = 1.12 \text{ eV}$, $E_{bHe,He3V2} = 2.45 \text{ eV}$, $E_{bHe,He4V2} = 1.18 \text{ eV}$, $E_{bHe,He5V3} = 2.17 \text{ eV}$, where $E_{bHe,HemVn}$ is the binding energy of He with the He_mV_n cluster, discussed in Section 3.3. As can be seen in Fig. 3-6, quite similar to the experimental observations, the model predicts two well separated major desorption groups within BCC temperature range, one below

300 °C, and the other above 550 °C. Moreover, the main peak positions are also reproduced fairly well by the model. On the other hand, the model requires further improvement or optimization to better reproduce the intensities of the desorption peaks as well as the splitting of the strongest peak around 800 °C within BCC region for the two higher fluence (10^{19} He/m²) specimens.

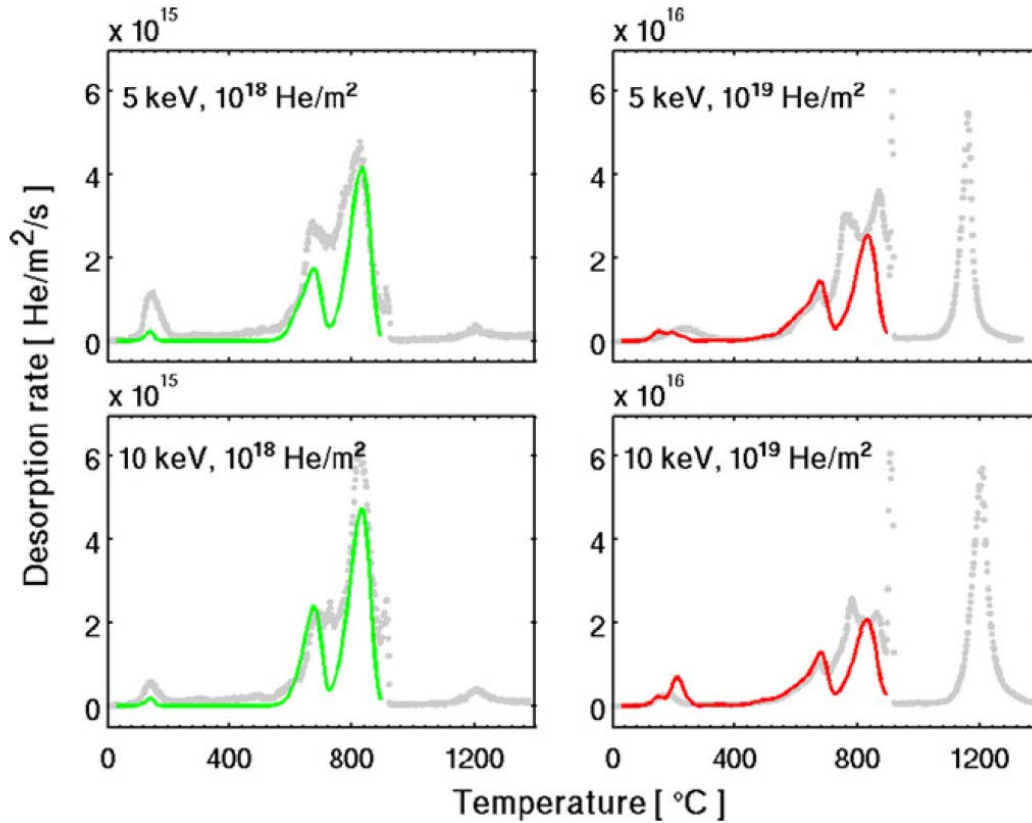


Figure 3-6. Experimental (gray dots) and predicted (solid lines) He desorption spectra from single crystal iron with a purity of 99.94% implanted with ⁴He ions, for different implantation energy (5 keV and 10 keV) and fluence (10^{18} He/m² and 10^{19} He/m²), as reproduced from Ref. [72].

Larger values of the vacancy migration energy than the value of 0.67 eV predicted by ab initio have also been reported in other computational studies [119]. A typical explanation for this discrepancy is the inhibition of vacancy mobility by impurities, particularly carbon in iron. The carbon effect on the energetics and kinetics of the He-point defects interaction will be further discussed in next chapter.

3.5.2 Simulation of THDS using a step-like temperature profile

In order to show the self-consistence of the developed model, a different annealing process (shown in Fig. 3-7) of the He implanted single crystal iron is simulated by the model using the same set of the parameters as described in Section 3.5.1.

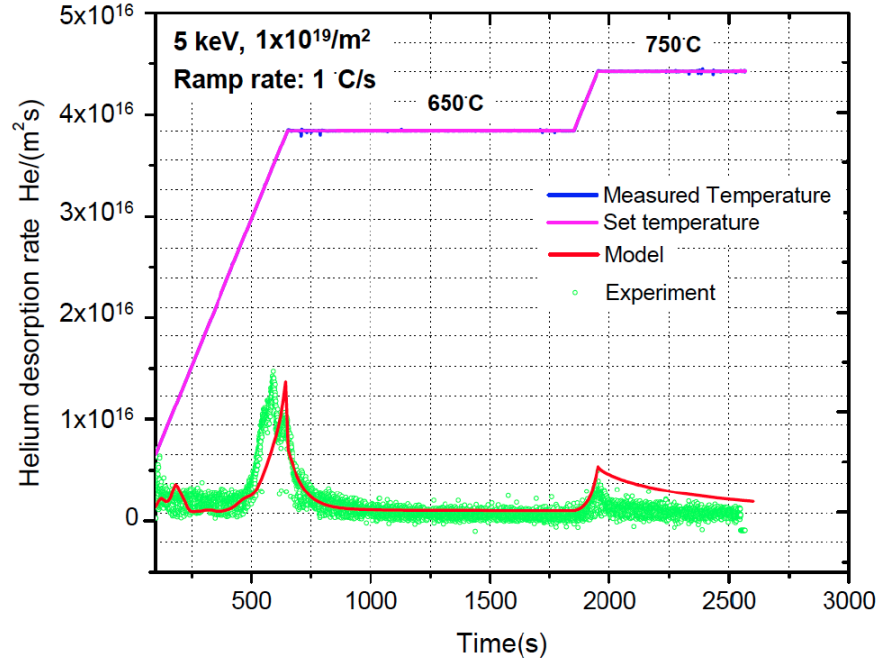


Figure 3-7. Experimental (green circle) and modeling (red solid line) prediction of the helium desorption spectra in single crystal iron with a purity of 99.94% implanted with ^4He ions, following step-like temperature profiles denoted by purple (set temperatures) and blue lines (measured temperatures), for the specimen with the implantation condition of 5 keV, 10^{19} He/m 2 .

Overall, the experiment and the modeling results show a very good agreement with each other. In Fig. 3-7, the temperature increases to 650 °C with a ramp rate of 1 °C/s, then holds at 650 °C for 20 minute, then increases to 750 °C with a ramp rate of 1 °C/s, and remains for 10 minutes. The experimentally obtained spectrum indicates that the major helium releasing peak starts from 500 °C and drops when the temperature arrives the plateau of 650 °C. The helium release rate remains at a low value when the temperature remains constant. As the temperature starts to increase from 650 °C to 750 °C, a small helium desorption peak is evident. Similar to the 650 °C plateau, the release rate becomes flat again in the plateau of 750 °C. The experimental observation shows that helium desorption is driven thermodynamically. When the temperature reaches 650 °C, the temperature is high enough to induce the dissociation of the He-vacancy clusters which are unstable at this temperature, resulting in a significant helium release. However, if the temperature is kept constant at 650 °C, the desorption rate decreases since the unstable clusters are consumed and the stable ones still do not thermally release He at this

temperature. The increase of temperature in the next stage provides some dissociation of the clusters with greater binding energies and produces another helium desorption peak. Then the constant temperature region experiences the same situation as the plateau of 650 °C. The model prediction reproduces the three helium desorption peaks at different stages, and the changes of helium desorption rate during the transition regions. Additionally, the positions of the peaks from experiment and simulation match well with each other.

3.5.3 Binding energies for small He_xV_y clusters

Table 3-2 compares the He, vacancy, SIA binding energies for small He_xV_y ($x, y = 1-5$) clusters predicted by ab initio [119], molecular dynamics [134], and thermodynamic calculations [71], including the values (labeled by asterisk) optimized for the simulations discussed in Section 3.5.1 and 3.5.2. It can be seen from Table 3-2 that the optimized values are closer to thermodynamic predictions than to ab initio or MD calculations. The fact that thermodynamic predictions do need to be modified for the small clusters is not surprising since thermodynamics is not expected to be applicable to very small clusters. On the other hand, the clear disagreement among ab initio, MD, and the thermodynamic calculations on the energetic of small clusters highlights the importance of finding the correct way to extrapolate the ab initio or MD data to larger He_xV_y clusters. Here we emphasize that in order to reliably validate the energetics of He_xV_y clusters it is important to examine a wide temperature regime as well as varying experimental conditions.

Table 3-2. Comparison of the binding energies for small He_xV_y ($x, y = 1-5$) clusters predicted by ab initio (indicated by ‘A’), MD (indicated by ‘M’), and thermodynamic (indicated by ‘T’) calculations. The asterisks label optimized values used in the modeling, as reproduced from Ref. [72].

		He_1			He_2			He_3			He_4			He_5		
		A	M	T	A	M	T	A	M	T	A	M	T	A	M	T
E_{bHe}	V_1	2.3	3.7	3.29	1.84	2.19	1.72	1.83	2.09	0.16	1.91	2.19	-1.16	n/a	1.99	-2.31
				3.2*			1.12*									
	V_2	2.85	3.71	3.75	2.75	3.8	3.17	2.07	2.81	2.29	2.36	2.48	1.43	n/a	2.52	0.65
										2.45*			1.18*			
	V_3	3.3	4.34	3.82	2.96	4.01	3.56	2.91	4.09	3.09	2.57	3.1	2.51	n/a	3.11	1.92
																2.1*
E_{bV}	V_4	3.84	4.72	3.85	3.12	4.23	3.71	3.16	4.2	3.44	3.05	4.23	3.06	n/a	3.13	2.62
	V_5	n/a	4.92	3.87	n/a	4.43	3.77	n/a	4.3	3.6	n/a	4.3	3.35	n/a	4.32	3.04
	V_1	2.3	3.7	3.39	3.71	5.13	10.1	4.59	5.82	18.94	5.52	6.55	29.54	n/a	5.8	41.71
				3.2*												
	V_2	0.78	0.19	0.57	1.61	1.8	2.01	1.85	2.52	4.14	2.3	2.81	6.73	n/a	3.33	9.69
	V_3	0.83	0.97	0.5	1.04	1.18	0.9	1.8	2.47	1.7	2.03	3.09	2.77	n/a	3.68	4.05
E_{bI}	V_4	1.16	1.01	0.59	1.32	1.23	0.74	1.57	1.33	1.09	1.97	2.46	1.64	n/a	2.48	2.34
	V_5	n/a	0.82	0.68	n/a	1.02	0.74	n/a	1.13	0.91	n/a	1.2	1.21	n/a	2.38	1.63
	V_1	n/a	6.39	5.26	n/a	4.78	3.81	n/a	4.07	1.68	n/a	3.78	-0.91	n/a	3.25	-3.87
	V_2	n/a	5.61	5.32	n/a	5.4	4.92	n/a	4.12	4.13	n/a	3.5	3.05	n/a	2.9	1.77
	V_3	n/a	5.57	5.23	n/a	5.35	5.09	n/a	5.25	4.74	n/a	4.12	4.19	n/a	4.1	3.48
	V_4	n/a	5.76	5.15	n/a	5.56	5.08	n/a	5.45	4.91	n/a	5.38	4.61	n/a	4.2	4.2
	V_5	n/a	5.49	5.08	n/a	5.36	5.04	n/a	5.24	4.95	n/a	5.14	4.78	n/a	5.11	4.52

3.5.4 Cluster evolution

While the small clusters listed above with optimized energies are important species to accurately model the desorption spectra, they are not the sole players. In fact, helium release is intimately coupled to the overall cluster evolution dynamics and each desorption group involves a collective action of a distribution of cluster sizes. In Ref. [71] and [72], Xu and Wirth investigated the cluster evolution at a selected depth (37 nm) during the annealing process of the lower (10^{18} He/m²) and the higher (10^{19} He/m²) fluence single crystal iron (99.94%) specimens implanted with 10 keV He ions, respectively.

For the lower fluence implantation, the He-vacancy clusters are rather small, with most clusters containing less than 10 He and less than 10 V, and the composition distribution is rather diffuse in both He and V directions. However, along the He direction it is confined by a boundary corresponding to a He/V ratio a bit larger than 2.5. The clusters with He/V ratio larger than this boundary value are essentially not formed because the binding energies with He or SIA are either very small positive or even negative within our thermodynamic model, as discussed in Section 3.3. With increasing temperature, the small clusters (e.g., He_2V) with high concentrations start to dissolve, while other clusters also experience significant evolution. Clusters with high He/V ratios become unstable

and emit vacancies while those with low He/V ratios emit He. The de-trapped He partly diffuses to the surface to desorb, and partly re-traps with other clusters, which induces the formation of the relatively large clusters with up to 30 vacancies. Meanwhile the maximum helium number is still less than 10 due to the fact that vacancy binding energy for a fixed He number first decreases and then increases as the vacancy number increases. When temperature is high enough (i.e., greater than 550 °C) to provide the driving force for the dissociation of large clusters, the clusters start to dissolve, resulting in significant helium desorption. The remaining He exists in the form of a HeV cluster in BCC temperature region. When temperature is even higher, namely, 1200 °C, they will dissociate to induce the formation of the He desorption peak as shown in Fig. 3-6.

The higher fluence specimens follow quite a different evolution path. Initially, the cluster distribution, although similarly diffuse as in the low fluence specimens, is preferentially elongated along the He direction. Then the diffuse cluster distribution rapidly evolves into a line in the phase space with a He/V ratio of ~ 1.6 by 350 °C. Next, as the temperature rises, the line shrinks due to the emission of He and V, leading to the formation of larger He-V clusters with He/V ratio of ~ 1 . According to the thermodynamic binding energy model, both the He and vacancy binding energies increase as the cluster size increases at a fixed He/V ratio of ~ 1 . This quickly results in a fast growth of the larger clusters while the small clusters continue to dissolve. The very small clusters such as He₃V₂ and HeV as well as larger clusters (e.g., He₄₀₀V₄₀₀) throughout the whole process contribute to the He desorption flux to the free surface. The ripened clusters which do not have enough time or thermal energy to be fully dissociated in BCC temperature regime will be carried over to higher temperatures in the FCC regime. More details can be found in Refs. [71] and [72].

3.6 Phase-cut method to improve the computing efficiency

As mentioned in Section 3.4, to model the evolution of He-V clusters by solving the rate equations, a phase space size needs to be prescribed first by setting a maximum He number nh , a maximum vacancy number nv , and a maximum SIA number ni , which defines the two-dimensional phase space with a total number of $ni+(nh+1)\times(nv+1)-1$ (note the '-1' is to exclude the He₀V₀). Since the prescribed phase space should fully cover the largest cluster actually formed in experiments, the number of PDEs and the corresponding number of ODEs after spatial discretization can become overwhelmingly large when significant cluster growth occurs through nucleation or Ostwald ripening. For instance, to model the formation of a maximum bubble size of He₅₀₀V₅₀₀ (diameter ~ 2 nm in alpha iron) experimentally observed would require solving more than 250000 PDEs, equivalent to 1×10^7 ODEs if there are 40 spatial meshes, which is a challenging computational task. In this code, a 'phase-cut' method that can significantly reduce the computing load is proposed.

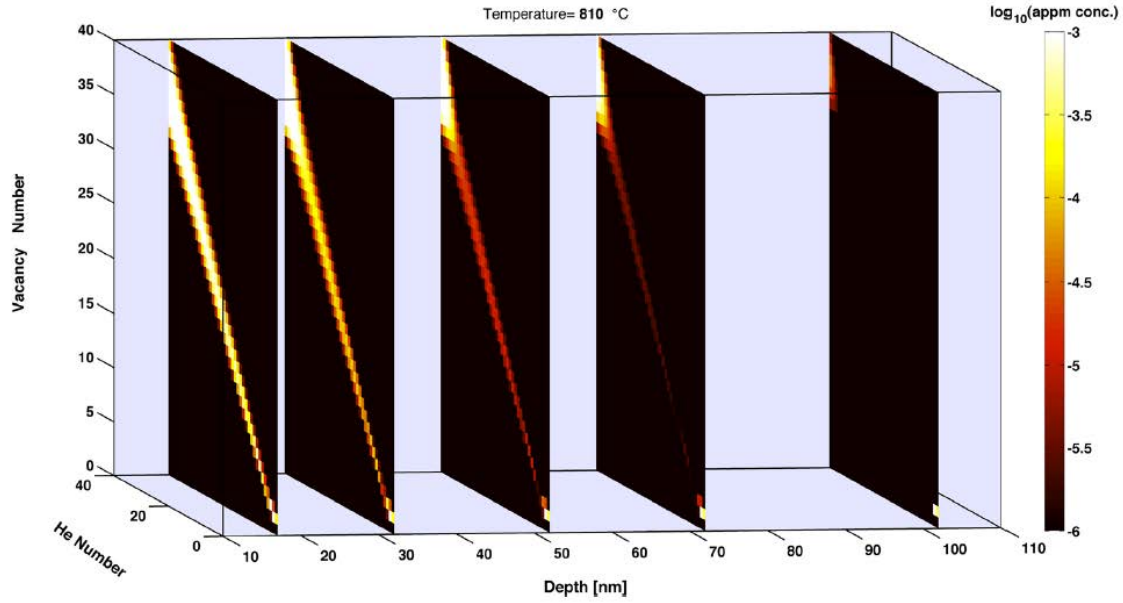


Figure 3-8. Cluster evolution in He-V phase space at five representative depth positions in alpha iron following He ion implantation at 810 °C, obtained with a small phase space size, as reproduced from Ref. [128].

Here, the He desorption experiment described in Section 3.5 for the single crystal iron specimens implanted with 10 keV He ion to a fluence of 10^{19} He/m² is taken as an example. Without knowing a priori the largest cluster sizes to be incurred in the modeled physical process, an arbitrary small system size with $n_h=40$, $n_v=40$, $n_i=800$ was initially used, where the n_i number was chosen to be relatively greater since the total number of equations only slightly depends on n_i and that SIA are more mobile than vacancies and hence may form larger clusters. Fig. 3-8 shows the evolution of cluster concentrations in the two-dimensional phase space at five representative depth positions at 810 °C during the annealing process. The evolution process is discussed in Section 3.5.4. With the temperature increasing, significant coarsening takes place and much larger clusters are rapidly formed at the expense of smaller clusters. The front of the growing composition line rapidly reaches the prescribed phase boundary, as shown in Fig. 3-8. The concentration pileup and then reflection at the phase boundary is evidently a computational artifact resulting from the insufficient phase space size prescribed.

Evidently, a larger system size, with greater n_h and n_v values, must be used to avoid the computational artifacts. One can simply redo the calculation by starting with greater n_h and n_v without any other change. By setting $n_h=500$, $n_v=500$, the cluster evolution was fully contained by the prescribed phase space, as shown in Ref. [128]. However, solving the ~ 10 million coupled stiff ODEs demanded 11 gigabyte (GB) memory and 31 hours using the PARASPACE with four Intel cores (Xeon X5660). In contrast, implementing the phase-cut method, as detailed below, lowered the computational cost to only 3.2 GB memory and 7.25 hours on the same machine.

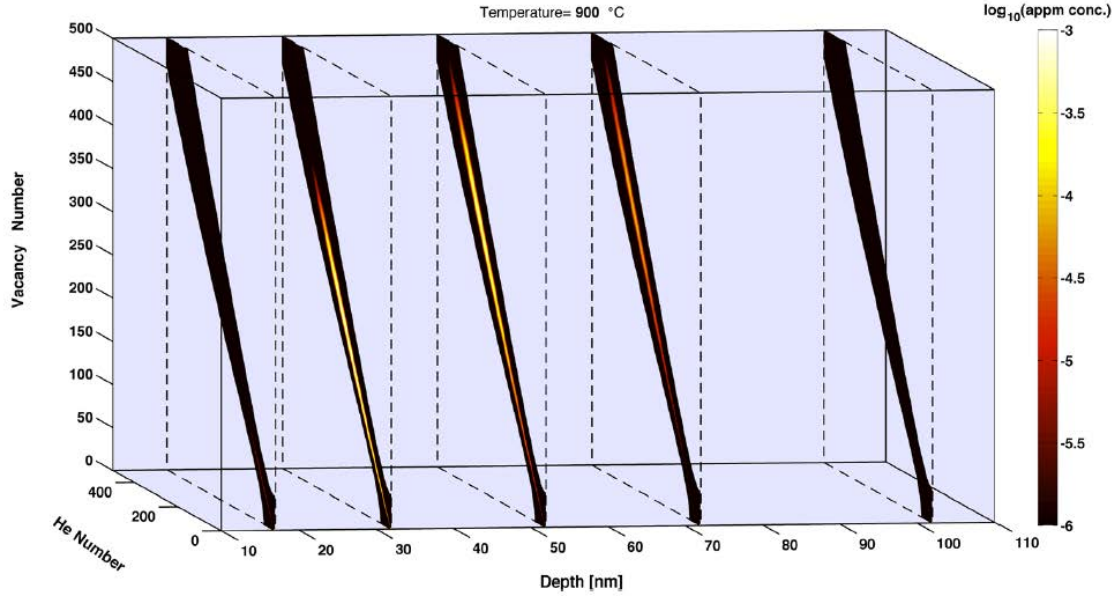


Figure 3-9. Cluster evolution in He-V phase space at five representative depth positions in alpha iron following He ion implantation at 900 °C, obtained with a large phase space size and the phase-cut method, as reproduced from Ref. [128].

The previous analysis shows that the cluster evolution is confined to a rather narrow path in the phase space and hence tracking the concentrations of those clusters outside the growth path is no longer necessary. It would be helpful if the growth path could be analytically determined. Conservatively, the code is using a small scale calculation to probe the trend of growth for the current problem. Here, Fig. 3-8 and the discussion in Section 3.5.4 indicates a growth path approximately along a line corresponding to a He/V ratio of ~ 1.1 , with small amount of expansion in line width and slight rotation (due to He desorption and vacancy production) as the growth front travels towards larger cluster sizes. Based on this, we define somewhat arbitrarily the lower and the upper borders (the black region shown in Fig. 3-9) of the growth path as:

$$\min\left(\sqrt{\max\left(x^2\left[0.82 + 0.02(x/150)^{1.5}\right]^2 - 40^2, 0\right)}, 500\right), \quad (3-33)$$

and

$$\min\left(\sqrt{x^2\left[1.2 + 0.01(x/150)^{1.5}\right]^2 + 40^2}, 500\right), \quad (3-34)$$

respectively, where x is the He number. Note that the 1.5^{th} power terms in these two expressions were used to create slight rotation on the basis of the two asymptotic lines of $0.82x$ and $1.2x$ at large x values, corresponding to He/V ratios of 1.2 and 0.83, respectively. Obviously, other functional forms could be used as well. We then ‘cut’ the

phase space by selecting out the compositions within the zone enclosed by the two borders and only allowing interactions for which both ‘reactants’ and ‘products’ are among the allowed compositions. In Ref. [128], it also indicates the same precision between the cut-phase method and the full-phase-space calculation.

3.7 Conclusion

A spatially dependent cluster dynamic model based on the classical rate theory is introduced in this chapter. The model successfully reproduces the helium desorption spectra in the BCC temperature region for the single crystal iron specimens following helium implantation. Additionally, the model predicts the depth dependence of the clusters as a function of time and temperature during the desorption measurement. This provides an opportunity for additional microstructural characterization methods to ensure the self-consistency of the modeling predictions with the experimental results and validation of the identification of He-point defect interactions. Moreover, a phase cut method is discussed briefly here to improve the computing efficiency, which may be applicable to other multi-species kinetic phenomena driven by irradiation and/or thermal annealing.

Chapter 4

Quantitative and Qualitative Analysis of He-Point Defect Interactions

In order to provide the insight into the physical mechanisms of He – point defect interactions that dominates the micro- and macro-structural changes of materials exposed to extreme irradiation environments, it is necessary to combine experiments (e.g., thermal helium desorption measurements, positron lifetime measurements) with computational modeling (e.g., reproducing the desorption spectra, predicting the cluster distribution). On the one hand, the experimental data provides a platform to validate the model by applying the model to simulating the same experimental process; on the other one, the modeling helps to understand the mechanisms of the observations in the experiments.

In this chapter, the model introduced in Chapter 3 is applied to qualifying the energetics and kinetics of He – point defect interactions in high purity (99.98%) single crystal iron following He ion implantations. The predicted cluster distributions at three annealing temperature points are analyzed to reproduce the positron lifetime measurements described in Chapter 2 qualitatively. The temperature-dependent cluster evolution is discussed for two different modeling conditions.

4.1 Influence of carbon on energetics and kinetics of He – point defect interaction

4.1.1 THDS results of He implanted single crystal irons with different purities

As described in Chapter 2, the helium desorption measurements are performed in two batches of single crystal irons with different purities (i.e., 99.94% and 99.98%) following various He implantation.

By comparing the desorption spectra, the two batches of samples share some common features. For example, a sharp peak appears around 900 °C denoting the BCC-FCC transformation. Two major helium release groups are observed for both batches of samples in BCC temperature region. Helium release peaks shift to higher temperatures as He implantation energies increase. Retained He is released in FCC temperature region at same temperature positions. Meanwhile, there are also some obvious different observations. The spectra for the high purity samples are generally less diffuse than the old samples with a stated purity of 99.94%. Some small fluctuations exist after the major He release in the BCC region. The most significant difference is that the major He desorption group shifts to a relatively lower temperature region (around 500 °C) for the

new samples with higher purities. This shift of release peaks to lower temperature is more prominently demonstrated by the direct comparison in Fig. 4-1 of the He desorption from the previous specimens with stated purity of 99.94% in the same conditions of 10 keV He implantation. The retained helium desorbed in FCC temperature region for high purity samples is much less than that for low purity samples. Due to the significant He desorption in BCC region of the high purity samples, the sharp peak demonstrating the phase transformation is smaller compared to that of the spectrum of low purity samples.

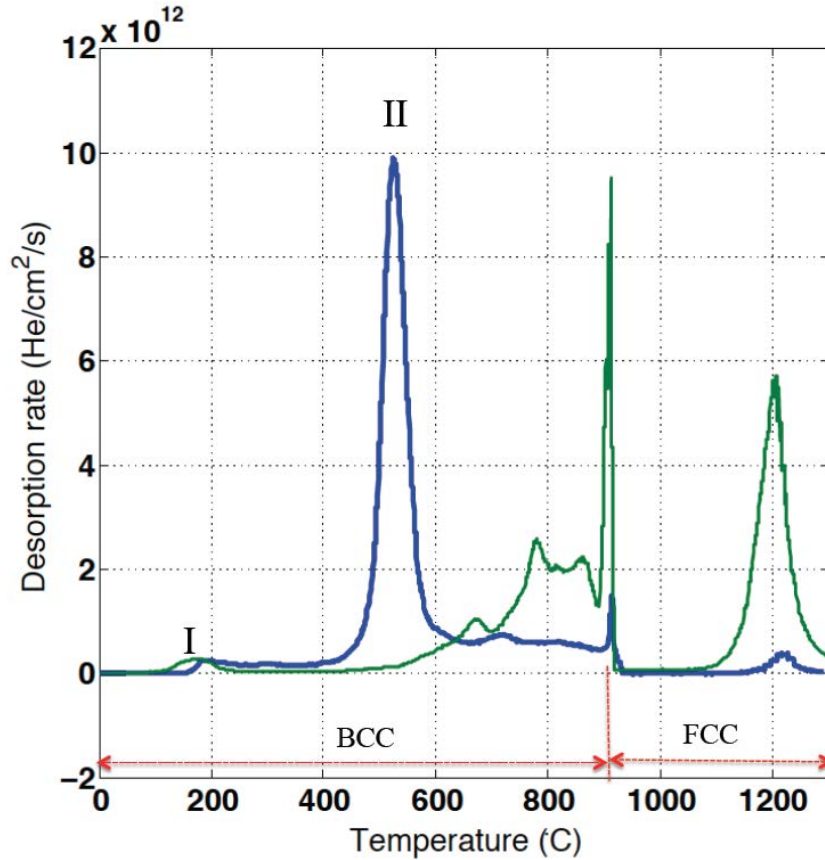


Figure 4-1. He desorption spectrum of the single crystal irons with the purities of 99.94% (green line) and 99.98% (blue line) implanted with He ion at 10 keV, 1×10^{15} He/cm².

The observed difference of the He desorption spectra for these two batches of single crystal iron specimens can be rationalized by considering the presence of impurities in the experimental samples. Table 4-1 shows the results of chemical analysis on the two sets of single crystal iron samples. The analysis is conducted by Luvak Inc., where carbon is determined by the combustion infrared detection method and all other elements are measured by direct current plasma emission spectroscopy. The analysis indicates that the new samples with a stated purity of 99.98% have significantly decreased carbon content, but increased levels of nitrogen and oxygen.

Table 4-1. Chemical analysis of the two batches of single-crystal irons (in a unit of weight percentage, %).

	C	N	O	Cu	Mg	Ni	Fe
Old sample	0.023	0.002	0.0045	<0.01	0.01	<0.01	Balance
New sample	0.007	0.0095	0.132	0.0385	0.049	0.0135	Balance

Because carbon is a common impurity in iron and is known to strongly interact with vacancies [135, 136], it is reasonable to ascribe the less diffuse feature of the high purity single crystal iron spectra to the lower content of carbon. As shown in Table 4-1, the most crucial distinctions are the carbon content in the samples while the other impurities' effect can be neglected due to their substitutional positions. Carbon is known to affect the migration of intrinsic defects in alpha iron, particularly vacancy. Some researchers [137, 138] have pointed out that the effective migration energy of vacancy in BCC iron measured experimentally varies between 0.6 to 1.5 eV with higher values for specimens with higher carbon content. As well, experiments provide evidence of various carbon-defect complexes, in particular carbon-vacancy clusters [139]. To some extent, these are consistent with our observations and suggest a straightforward explanation of our experimental results. However, it is important to note that the difference in carbon content may not completely explain the differences between the two sets of results, and future research will seek to better define the role of the various interstitial impurities.

Moreover, how the energetics of helium and helium-vacancy clusters change cannot be seen clearly only by the experiment. In the following section, we try to use our spatially dependent cluster dynamics code to model the new helium spectra and compare the energies applied here to the previous simulations. This will provide us an overview of the energetic changes in details.

4.1.2 Modeling the He desorption from the new, 99.98% pure single crystal iron samples following a linear temperature profile

A good overall agreement was obtained between the model and the thermal desorption experiments for the single crystal iron specimens with a purity of 99.94%, as a result of optimizing the migration and binding energies describing the vacancy and small helium-vacancy clusters shown in Chapter 3. The new helium desorption spectra provides another opportunity to evaluate the self-consistency of the model and energetic parameters. However, as shown in Fig. 4-2, the model predictions using these previous parameters (black dash line) are not at all consistent with the new experimental results (blue symbols). Clearly, the previous set of energetic parameters describing the vacancy migration and the binding of He and vacancies to small He-vacancy clusters is not able to predict this new set of experimental data for specimens of slightly higher purity. Consequently, an additional optimization of vacancy migration and small He-vacancy cluster binding energies has been performed, which leads to an improved, but not perfect, agreement between the model and the experiments. The new model predictions are

shown as solid red lines in Fig. 4-2. The resulting energetic parameters are provided in Table 4-2. Although the current parameterization of the model does a reasonable job of predicting the two well-separated desorption groups, the position of the main release peak for an implantation energy of 10 keV is not in good agreement with the experimental results (as shown in Fig. 4-2(a)). The other unfavorable aspect is that the plateau in the experimental spectra was not predicted by the model, which predicts a secondary peak following the main peak.

The parameterization in this simulation requires modifications of the vacancy migration energy to 0.73 eV, which is smaller than the value used previously, and the binding energies of small He-V clusters as listed in Table 4-2. It is clear that the binding energies necessary to improve the agreement between the modeling predictions and the experimental results are smaller than those previously used, with the exception of the helium binding energy to the He₂V cluster. This result is in general agreement with the interpretation of an impurity effect on the migration and binding energetics of the vacancy and small He-V clusters, and the measurement of reduced carbon levels in the 99.98% versus 99.94% single crystal iron specimens. Note that the currently used values are much closer to the ab initio values, which are considered to be relatively more accurate compared to other simulation methods.

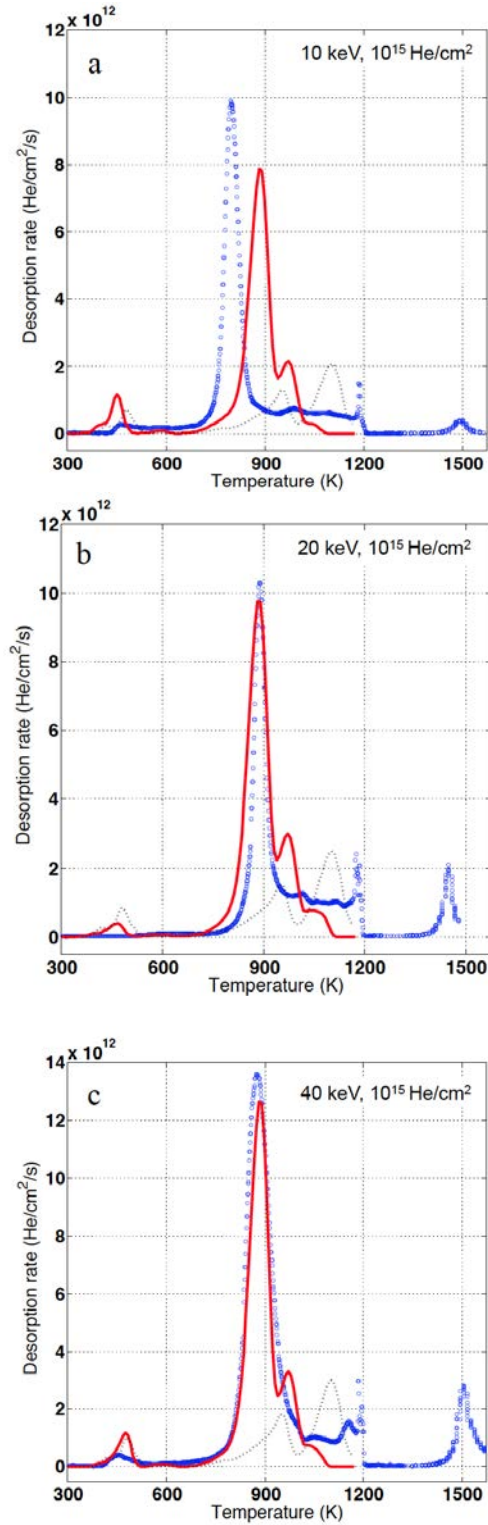


Figure 4-2. Experimental (open symbols) and predicted (red solid lines and black dash lines) He desorption spectra in single crystal iron of high purity following implantation of (a) 10 keV, $1 \times 10^{15} \text{ He}/\text{cm}^2$; (b) 20 keV, $1 \times 10^{15} \text{ He}/\text{cm}^2$; (c) 40 keV, $1 \times 10^{15} \text{ He}/\text{cm}^2$. Black dash lines are the modeling predictions using the previously defined set of kinetic parameters, as described in Chapter 3.

As discussed above, carbon is known to significantly reduce the mobility of single vacancies and small vacancy clusters. Thus, the reduction of the vacancy migration energy required to model the data derived from these single crystal iron specimens is consistent with the measurement of lower carbon levels shown in Table 4-1. As well, Ortiz et al. [133] recently developed a rate theory model that explicitly includes a few small carbon-containing clusters $\text{He}_n\text{V}_m\text{C}_p$ ($n,m,p=0,1,2$), based on ab initio calculated values of the vacancy migration energy, and shown that a similar prediction can be obtained by either explicitly including these carbon-defect complexes or more simply by considering an effective vacancy migration energy that is increased with carbon content. Ortiz's model is also consistent with our current results, although as already mentioned, additional research will be required to fully determine the effect of carbon versus oxygen or nitrogen impurity levels.

Table 4-2. Comparison of the binding energies (eV) of helium for small He-V clusters calculated by different methods and used in different batches of samples.

Clusters	New Samples – stated purity = 99.98%	Old Samples – stated purity = 99.94%	Ab initio (from Ref. 119)	MD (from Ref. 134)	Thermodynamic (from Ref. 71)
HeV	2.56	3.20	2.3	3.7	3.39
He ₂ V ₂	2.98	3.17	2.75	3.8	3.17
He ₂ V	1.13	1.12	1.84	2.19	1.72
He ₃ V ₂	2.25	2.45	2.07	2.81	2.29
He ₄ V ₂	1.10	1.18	2.36	2.48	1.43
He ₅ V ₃	1.70	2.17	n/a	3.11	1.92

4.2 Mechanistic interpretation of helium desorption peaks and helium-vacancy cluster evolution

The combination of the modeling and the thermal desorption measurements allows identification of possible mechanisms governing helium desorption peaks. Since plenty of information can be extracted from the model, it is possible to obtain the distributions of the clusters at any time point. For each desorption peak, the He-vacancy cluster distributions at each depth grid are obtained at the starting and end temperature points (defining the temperature region of the interesting He release peak), respectively. Then the integration of the cluster concentrations versus sample depths gives the total concentration in the bulk sample for each cluster. Eventually, comparing the concentrations at these two different temperature points for each cluster leads to the identification of the specific clusters, which contribute mostly to the He desorption peak at the defined temperature region.

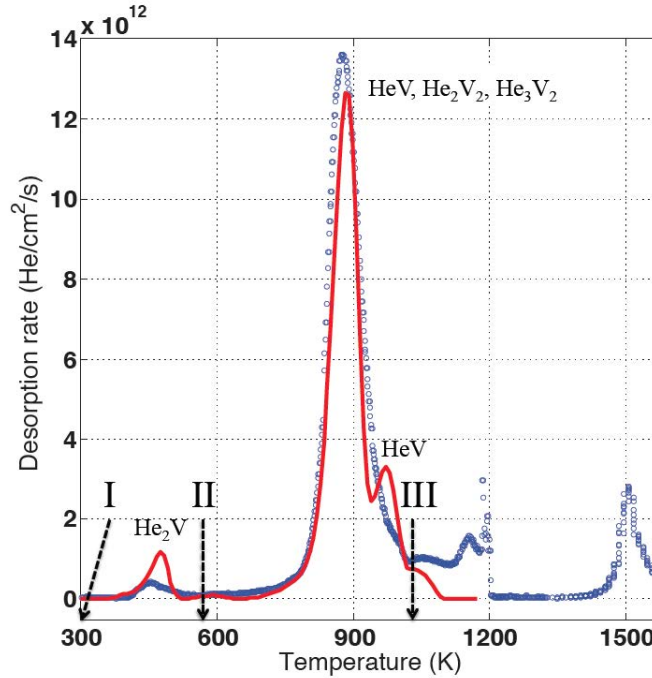


Figure 4-3. Experimental (open symbols) and predicted (solid lines) He desorption spectra in single crystalline iron of high purity (99.98%) following implantation of 40keV, 1×10^{15} He/cm²; Major shrinkage of small clusters are labeled nearby the corresponding He desorption peaks; Three points of interest are marked for the cluster evolution analysis.

The main release mechanisms predicted in the measurements with 40 keV He to a fluence of 1×10^{15} He/cm² are listed on the desorption spectra shown in Fig. 4-3. Evaluations of the change in the He-vacancy cluster populations in the model indicate that the shrinkage of He₂V is responsible for the helium desorption peak in Group I. The dissociation reactions responsible for the main helium release peak derive from the large decrease of three small clusters, HeV, He₂V₂, and He₃V₂, which release a large amount of interstitial helium into the matrix. This helium then rapidly diffuses to the surface and is released or encounters another cluster causing growth. The predicted peak around 973 K, which is not clearly observed in the experiment, is due to dissociation of HeV. While it is important to note that the helium desorption peaks actually result from the collective evolution of many different He-V clusters, we have identified the most significant cluster evolutions that dominate the helium release process.

In addition, the model can predict the depth dependence of the helium cluster populations as a function of time and temperature during desorption measurement. This provides an opportunity for additional microstructural characterization methods to ensure self-consistency and to validate the helium - point defect interaction mechanisms. Fig. 4-3 shows three interesting temperature points that bracket the two major helium desorption groups within the BCC region; (I) room temperature immediately following the completion of the He ion implantation, (II) at 573 K after the first He desorption peak, and (III) at 1023 K after the main He release peak. Fig. 4-4 shows the depth-integrated He-vacancy cluster size distributions at these three temperatures.

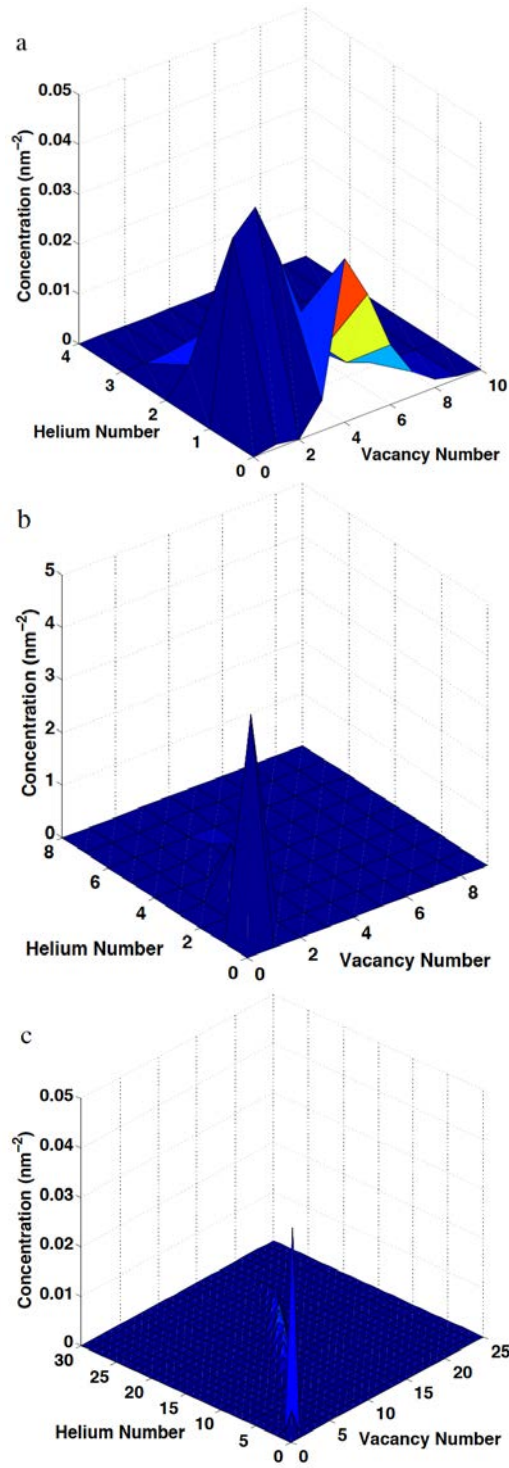


Figure 4-4. Computed cluster distribution for the three selected points: (a) after irradiation, (b) at 573 K, (c) at 1023 K.

Fig. 4-4(a) shows the cluster distribution at point I, following the completion of the He ion implantation, for which the model predicts a cluster distribution that includes vacancy clusters with size from 1 to 7, and containing between 1 to 4 He atoms. Notably, there is a peak in the vacancy size distribution (i.e., around 5 vacancies) that does not contain any He, although the HeV and He₂V clusters have the largest density. Fig. 4-4(b) shows the cluster distribution at 573 K, following a temperature ramp of 1 K/s. At this temperature, the bare vacancy clusters (without He) have dissolved, and the size distribution has narrowed and somewhat expanded in size up to 9 vacancies and 7 He atoms. Meanwhile, the depth-integrated cluster density has actually increased with the HeV clusters, making up about 75% of the total cluster population. Fig. 4-4(c) shows the cluster distribution at 1023 K, which indicates a substantial decrease in the overall cluster concentration, and a sizeable population of He-V clusters having a He:V ratio about 1.3 is observed, with the largest cluster containing 24 He and 18 V. These modeling results indicate fairly significant changes to the He-V cluster populations that have been evident through measurements of the positron annihilation lifetime, as shown in Chapter 2.

4.3 Prediction of long lifetime in PAL

From the model calculations, we can obtain the detailed cluster distribution at any time, which can be compared to the information obtained with long positron lifetime. The cluster distribution analysis in Section 4.2 shows the consistence with the experimental observations. In this section, a more straightforward way is proposed to predict the positron long lifetime based on the modeling results, which helps to execute a direct comparison with the experimental measurement.

The positron lifetime reflects the overall defect information inside the sample. In this specific case, it is the collective consequence of the positron annihilation lifetimes in all the He-vacancy clusters. Here, an initial method is used to combine the modeled helium-vacancy cluster distribution and the theoretical positron lifetime at the three selected points. The contributions of different clusters are expressed by their density fractions of the total cluster concentration. In this simple model, a linear correlation between the cluster concentration and the contribution of the corresponding cluster to the total positron long lifetime is assumed. So the contribution of each cluster multiplied by the related lifetime gives the ‘sub-lifetime’. The sum of all of the thus computed values is considered as the collective positron long lifetime in the defect region.

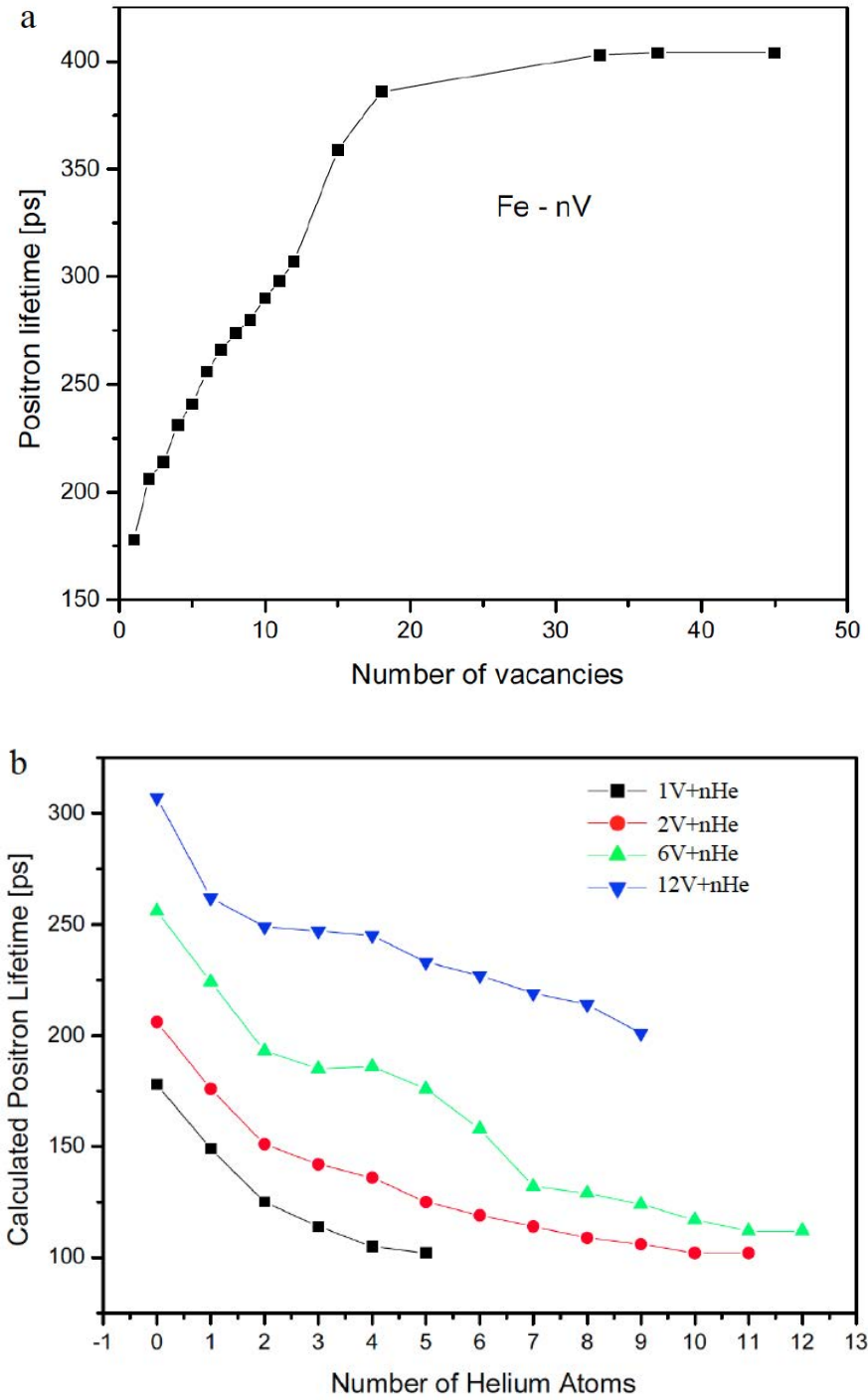


Figure 4-5. (a) Correlation between positron lifetime and the number of vacancies in a void in BCC iron; (b) Correlation between positron lifetime and the number of He atoms in the He-vacancy clusters, as reproduced from Ref. [111].

While the cluster distribution across the depth direction at any time can be obtained from the modeling, the theoretical positron lifetime for various sizes of clusters are extracted from Troev et al.[111] directly or by interpolation, as shown in Fig.4-5. When the He-V cluster is big enough (e.g. He_mV_n , $m>24$, $n>15$), we assume that the positron lifetime is saturated, at a value of 308 ps. Table 4-3, 4-4, 4-5 indicate the analysis processes of the three selected points. Note that the concentration of each cluster is the integrated value with respect to depth.

Table 4-3. Positron lifetimes and concentrations of the major clusters at point I.

Clusters	Theoretical positron lifetime (ps)	Concentration (#/nm ²)	Percentage (%)	Lifetime contribution	Clusters	Theoretical positron lifetime (ps)	Concentration (#/nm ²)	Percentage (%)	Lifetime contribution
V	180	0.0009	0.36	0.64	HeV ₆	225	0.0029	1.15	2.60
V ₂	208	0.0002	0.08	0.17	HeV ₇	231	0.001	0.40	0.92
V ₃	214	0.0062	2.47	5.28	HeV ₈	237	0.0003	0.12	0.28
V ₄	233	0.033	13.13	30.58	HeV ₉	243	0.0001	0.04	0.10
V ₅	240	0.0241	9.59	23.01	He ₂ V	125	0.0053	2.11	2.64
V ₆	260	0.0121	4.81	12.51	He ₂ V ₂	154	0.0109	4.34	6.68
V ₇	270	0.005	1.99	5.37	He ₂ V ₃	163	0.008	3.18	5.19
V ₈	275	0.0017	0.68	1.86	He ₂ V ₄	172	0.0042	1.67	2.87
V ₉	285	0.0005	0.20	0.57	He ₂ V ₅	181	0.0018	0.72	1.30
V ₁₀	292	0.0002	0.08	0.23	He ₂ V ₆	190	0.0007	0.28	0.53
HeV	150	0.0366	14.56	21.84	He ₂ V ₇	199.5	0.0002	0.08	0.16
HeV ₂	179	0.0411	16.35	29.26	He ₂ V ₈	208	0.0001	0.04	0.08
HeV ₃	190.5	0.0297	11.81	22.51	He ₃ V ₂	140	0.0002	0.08	0.11
HeV ₄	202	0.0166	6.60	13.34	He ₃ V ₃	151.5	0.0002	0.08	0.12
HeV ₅	213	0.0075	2.98	6.35	He ₃ V ₄	163	0.0001	0.04	0.06

Table 4-4. Positron lifetimes and concentrations of the major clusters at point II.

Clusters	Theoretical positron lifetime (ps)	Concentration (#/nm ²)	Percentage (%)	Lifetime contribution	Clusters	Theoretical positron lifetime (ps)	Concentration (#/nm ²)	Percentage (%)	Lifetime contribution
V ₅	240	0.0071	0.13	0.31	He ₂ V ₇	199.5	0.006	0.11	0.22
V ₆	260	0.0121	0.22	0.57	He ₂ V ₈	209	0.0039	0.07	0.15
V ₇	270	0.0121	0.22	0.59	He ₂ V ₉	218.5	0.0022	0.04	0.09
V ₈	275	0.0093	0.17	0.46	He ₃ V ₂	140	0.9031	16.41	22.97
V ₉	280	0.006	0.11	0.31	He ₃ V ₃	151.5	0.0227	0.41	0.62
HeV	150	4.1574	75.54	113.30	He ₃ V ₄	163	0.0129	0.23	0.38
HeV ₂	179	0.0034	0.06	0.11	He ₃ V ₅	174.5	0.0075	0.14	0.24
HeV ₆	225	0.0029	0.05	0.12	He ₃ V ₆	186	0.004	0.07	0.14
HeV ₇	231	0.005	0.09	0.21	He ₃ V ₇	197.5	0.0021	0.04	0.08
HeV ₈	237	0.0049	0.09	0.21	He ₄ V ₃	144.5	0.0225	0.41	0.59
HeV ₉	243	0.0034	0.06	0.15	He ₄ V ₄	159	0.005	0.09	0.14
He ₂ V ₂	154	0.0266	0.48	0.74	He ₄ V ₅	173.5	0.0023	0.04	0.07
He ₂ V ₃	163	0.0578	1.05	1.71	He ₅ V ₃	140	0.1409	2.56	3.58
He ₂ V ₄	172	0.0179	0.33	0.56	He ₅ V ₄	153	0.0033	0.06	0.09
He ₂ V ₅	181	0.0089	0.16	0.29	He ₆ V ₄	137	0.0025	0.05	0.06
He ₂ V ₆	190	0.0076	0.14	0.26	He ₇ V ₄	126	0.0206	0.37	0.47

Table 4-5. Positron lifetimes and concentrations of the major clusters at point III.

Clusters	Theoretical positron lifetime (ps)	Concentration (#/nm ²)	Percentage (%)	Lifetime contribution	Clusters	Theoretical positron lifetime (ps)	Concentration (#/nm ²)	Percentage (%)	Lifetime contribution
HeV	150	0.0048	2.93	4.40	He ₁₅ V ₁₂	200	0.0069	4.22	8.44
He ₂ V ₂	154	0.0404	24.69	38.03	He ₁₆ V ₁₂	200	0.0024	1.47	2.93
He ₃ V ₂	140	0.001	0.61	0.86	He ₁₅ V ₁₃	204.2	0.0028	1.71	3.49
He ₃ V ₄	153	0.001	0.61	0.94	He ₁₆ V ₁₃	204.2	0.0066	4.03	8.24
He ₆ V ₅	157.5	0.0022	1.34	2.12	He ₁₇ V ₁₃	204.2	0.0038	2.32	4.74
He ₇ V ₆	130	0.0031	1.89	2.46	He ₁₆ V ₁₄	208.4	0.0016	0.98	2.04
He ₈ V ₇	144	0.0031	1.89	2.73	He ₁₇ V ₁₄	208.4	0.0052	3.18	6.62
He ₉ V ₇	140	0.0023	1.41	1.97	He ₁₈ V ₁₄	208.4	0.0047	2.87	5.99
He ₉ V ₈	153	0.0027	1.65	2.53	He ₁₉ V ₁₄	208.4	0.0011	0.67	1.40
He ₁₀ V ₈	149	0.0041	2.51	3.73	He ₁₈ V ₁₅	212.6	0.0034	2.08	4.42
He ₁₀ V ₉	162	0.0021	1.28	2.08	He ₁₉ V ₁₅	212.6	0.0046	2.81	5.98
He ₁₁ V ₉	156	0.0056	3.42	5.34	He ₂₀ V ₁₅	212.6	0.0018	1.10	2.34
He ₁₂ V ₉	156	0.0017	1.04	1.62	He ₁₉ V ₁₆	216.8	0.002	1.22	2.65
He ₁₁ V ₁₀	169	0.0015	0.92	1.55	He ₂₀ V ₁₆	216.8	0.0036	2.20	4.77
He ₁₂ V ₁₀	169	0.0062	3.79	6.40	He ₂₁ V ₁₆	216.8	0.0022	1.34	2.92
He ₁₃ V ₁₀	169	0.0037	2.26	3.82	He ₂₀ V ₁₇	221	0.001	0.61	1.35
He ₁₃ V ₁₁	182	0.0056	3.42	6.23	He ₂₁ V ₁₇	221	0.0025	1.53	3.38
He ₁₄ V ₁₁	182	0.0058	3.55	6.45	He ₂₂ V ₁₇	221	0.0021	1.28	2.84
He ₁₅ V ₁₁	182	0.0011	0.67	1.22	He ₂₃ V ₁₈	225.2	0.0014	0.86	1.93
He ₁₄ V ₁₂	200	0.0042	2.57	5.13	He ₂₄ V ₁₈	225.2	0.0017	1.04	2.34

Although the method is simple, it can give a much more straightforward view of how the long lifetime of positron changes at different annealing stages. Fig. 4-6 indicates the measured and modeling results. As shown in the figure, the long lifetime decreases from 197 ps to 149 ps for the two stages of after irradiation and annealing at 573 K; then it goes up from 140 ps to 178 ps for the two annealing stages. The basic tendency of the curve is consistent with the experimental results. However, the model underestimates the values of the positron lifetime and the increasing value from I to II is larger than that from II to III, because the linear assumption is too simple to accurately describe the complete physical process of positron annihilation since it does not include the effect of positron binding to specific defects and the samples used in the experiments are not ideally pure while some other defects exist, such as dislocations, small voids, etc. Overall, the model provides qualitative agreement with the experimental observations.

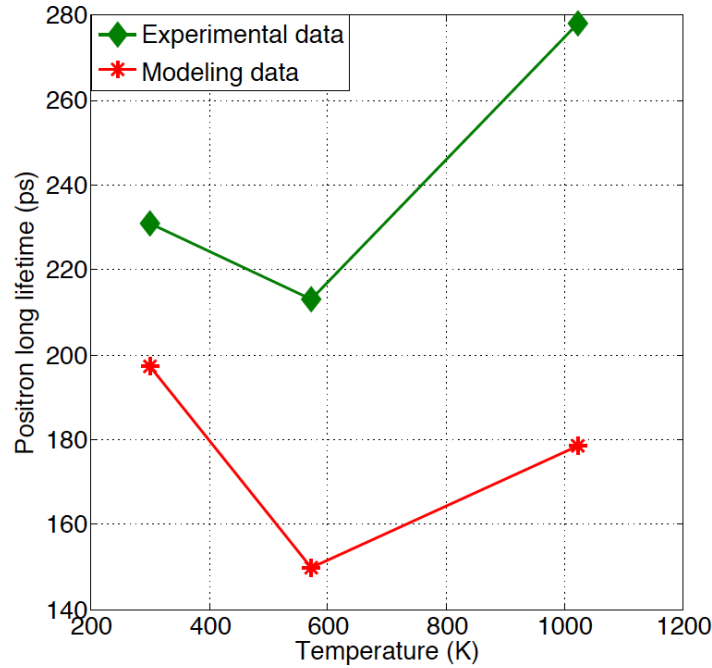


Figure 4-6. Measured and calculated positron long lifetimes for the three selected points.

4.4 Comparison of the cluster evolutions predicted by the model using two different batches of energetic parameters

In Section 3.5.4, the He-vacancy cluster evolutions for the modeling conditions of two different fluences are briefly discussed, which show completely distinct dynamic features. Note that the simulations of the higher purity single crystal iron samples require a new parameter optimization of some thermodynamics and kinetic properties of important small clusters, as discussed previously in this chapter. In this section, the He-vacancy cluster evolution as modeled using the newly-acquired energetic and kinetic parameters are compared to the previous results to demonstrate the sensitivity of the He-

vacancy cluster populations to the binding energies of these important small clusters. In Figs. 4-7 and 4-8, the temperature-evolving distributions of He-vacancy clusters in the phase space at a selected depth of 37 nm (approximate the midpoint between the peak Frenkel pair production depth and the most probable stopping position of He ions during implantation) are presented for the lower (10^{18} He/m²) and higher (10^{19} He/m²) fluence specimens implanted with 10 keV He ions, respectively.

The model predictions using the two sets of parameters (i.e., denoted by A and B, respectively) for cluster evolutions at lower implanted helium fluence are shown in Fig. 4-7. At 100 °C, for both cases, the He-vacancy clusters are rather small, with most clusters containing less than 10 He and less 10 V, and the composition distribution is rather diffuse in both He and V directions. Note that the He direction is confined by a boundary corresponding to a He/V ratio of 2.5 in both cases. As the temperature is increased to 350 °C, the two cases show similar behavior that the concentrations of He₂V and other small clusters with low He/V ratio (e.g., HeV₂, HeV₃, He₂V₅) are significantly reduced because of the low binding energies of He or V, respectively. In both A and B, the model predicts that the clusters above the He/V diagonal ratio of 2.5 evolve towards higher vacancy numbers, 26 and 42, respectively. For the case B, the binding energies of the important small clusters are relatively smaller, which means more small clusters are dissolved faster to provide the free He and vacancies as the source for the growth of larger clusters. At temperatures of 750 °C and 900 °C, very different features show up for these two modeling cases. For the case A, as shown in Fig. 4-7(a), after the extensive shrinkage of the clusters releasing He and vacancies, the remaining clusters exist along the diagonal and continue to dissolve with further increasing temperature. Eventually, only HeV and V are retained in the BCC temperature region. Interestingly, as shown in Fig. 4-7(b) for Case B, the growth paths for these two temperatures are very different. Up to 750 °C, a large number of clusters still exist along the diagonal and from 750 °C to 900 °C, the path becomes narrower accompanying continuous dissolution of clusters. This discrepancy derives from the pre-formed stable He-vacancy clusters at lower temperature regime.

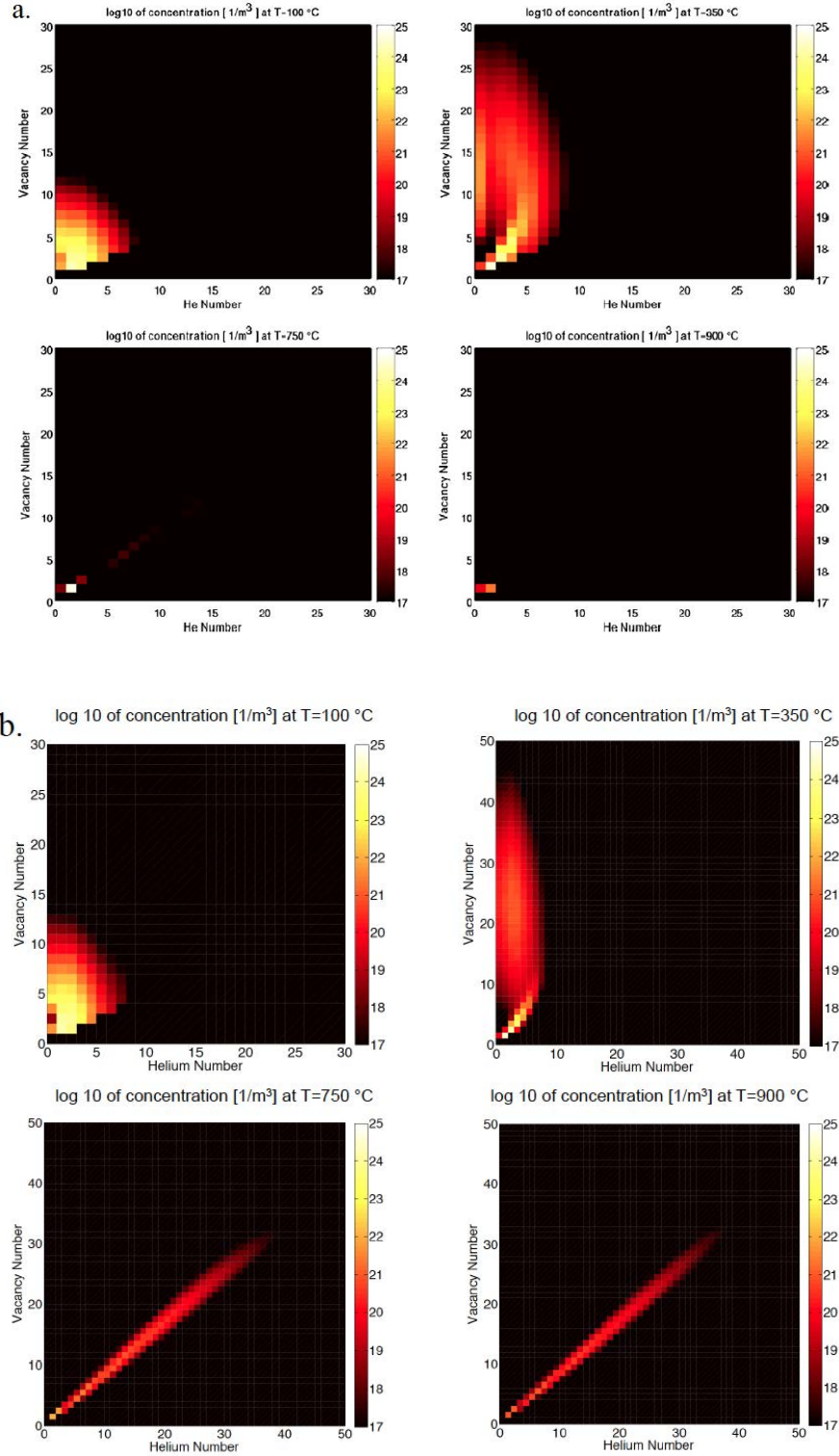


Figure 4-7. He-vacancy cluster phase space snapshots showing the cluster distribution evolution during the thermal annealing (at $1\text{ }^{\circ}\text{C/s}$ heating rate) at a depth of 37 nm for the specimen implanted with 10 keV He to a fluence of 10^{18} He/m^2 for two different cases: (a) using the energetic parameters for the modeling of the old samples; (b) using the energetic parameters for the modeling of the new samples.

The model predictions using the two sets of parameters (i.e., denoted by A and B, respectively) for cluster evolutions at higher implanted helium fluence are shown in Fig. 4-8, and each set follows quite a different path. At 100 °C and 350 °C, the two modeling cases share the same features. Compared to the low fluence specimens, the cluster distribution is preferentially elongated along the He direction at 100 °C. Then the diffuse cluster distribution rapidly evolves into a line in the phase space with a He/V ratio of ~ 1.6 by 350 °C. As shown in Fig. 4-8(a), as the temperature continues to rise, the growing path shrinks due the emission of He and vacancies for Case A, while slowly changing the slope towards smaller He/V ratios. Eventually, the ratio saturates toward 1. The increase of He and vacancies in the matrix leads to the formation of larger clusters since the He- and V-binding energies increase as the cluster size increases at a fixed ratio of ~ 1 . This process thus can be called a He-vacancy coordinated Ostwald ripening [72]. The cluster can grow up to $\text{He}_{400}\text{V}_{400}$ at the end of BCC temperature regime. As shown in Fig. 4-8(b), the smaller binding energies of the important clusters in Case B induce the early violent release of He and vacancy, cutting off the supply for the formation of the bigger clusters with hundreds of He and vacancies. However, the cluster evolution path still grows from 750 °C to 900 °C a little bit with the final maximum clusters containing up to 60 He and 50 vacancies. Fewer He atoms are retained at the end of BCC temperature regime, which can explain the observation, shown in Fig. 4-1, that the helium desorption of the new batch samples is less significant than that of the old samples when the temperature is greater than 720 °C. Due to the continuous loss of He, the growth of the ripened larger clusters may slow or completely stop at some temperature within FCC regime, which of course depends on the remaining concentrations of the ripened clusters and the energetics and kinetics of He in FCC iron.

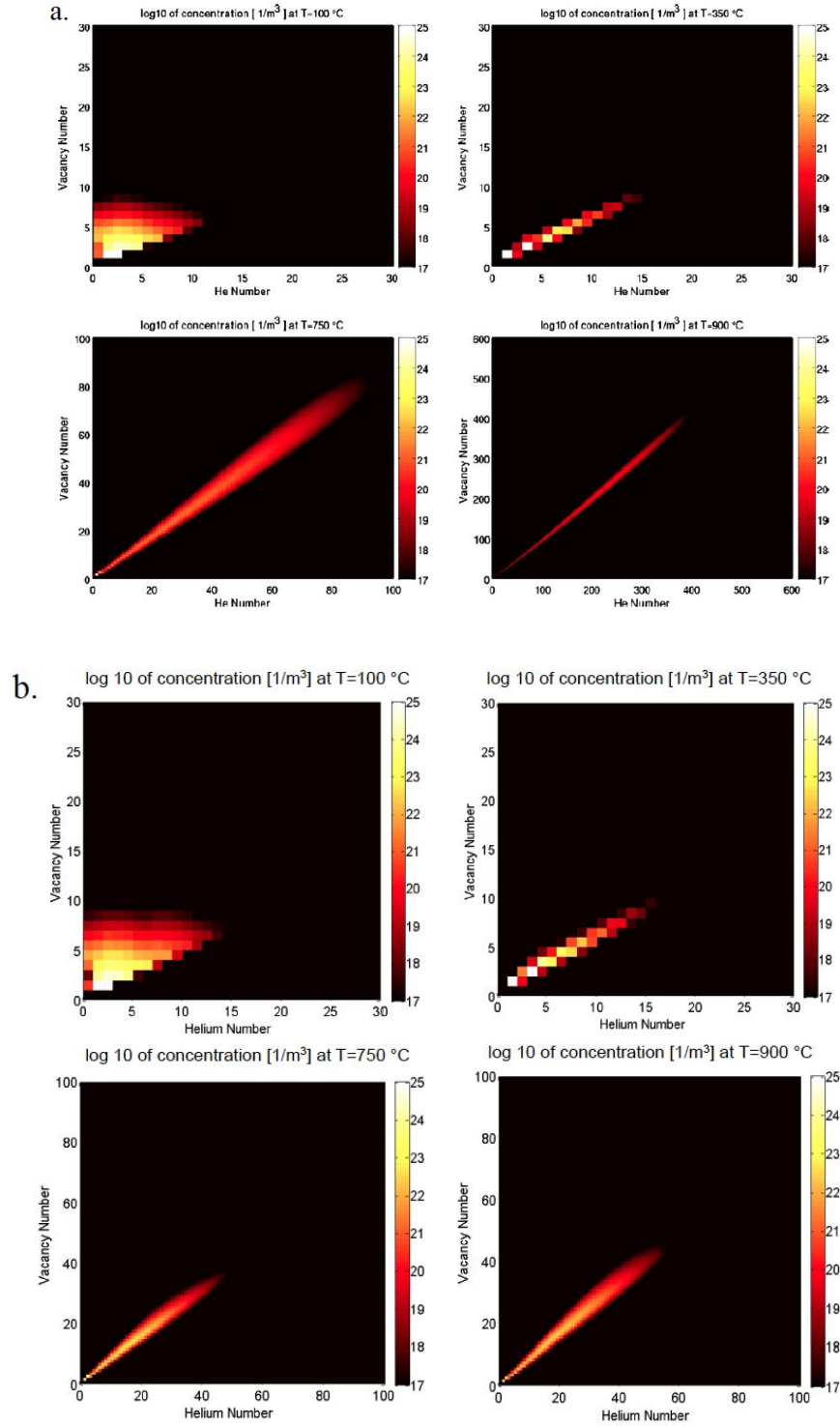


Figure 4-8. He-vacancy cluster phase space snapshots showing the cluster distribution evolution during the thermal annealing (at 1 °C/s heating rate) at a depth of 37 nm for the specimen implanted with 10 keV He to a fluence of 10^{19} He/m² for two different cases: (a) using the energetic parameters for the modeling of the old samples; (b) using the energetic parameters for the modeling of the new samples.

4.5 Conclusion

In this chapter, the influence of carbon on the energetics and kinetics of He – point defects interactions has been evaluated by analyzing the experimental observations and modeling optimizations for two different batches of He-implanted single crystal iron samples. Moreover, the measured positron lifetime distribution has been modeled and compared through applying the model predictions of helium-defect cluster distributions at conditions of irradiation and annealing. This provides more opportunities for the validation of the self-consistence of the developed cluster dynamic model. The analysis of the sensitivity of cluster dynamic evolution to the applied energetic and kinetic parameters highlights the importance of the accurate atomistic calculations of the He – point defect interactions.

Chapter 5

Influence of the Interactions of Helium and Self-interstitials on Helium Behavior in Iron

The spatially dependent cluster dynamics model introduced previously only considers four types of clusters, i.e., vacancy-, self-interstitial-, helium-clusters, and He-vacancy clusters. The He-SIA clusters have been excluded based on the consideration that the interactions between helium and SIAs are generally weaker than He-vacancy interactions. However, the influence of the He-SIA interactions on the helium desorption and helium clusters evolution is not understood. In this chapter, a more comprehensive model including He-SIAs interactions is applied to simulating the helium desorption spectrum of the sample implanted with 10 keV helium ions to a fluence of $1 \times 10^{14} \text{ He/cm}^2$. As well, MD simulations are used to investigate observed phenomena. Furthermore, the MD simulation results provide an opportunity for direct comparison and validation of the developed cluster dynamic model.

5.1 Influence of He-SIA interactions on THDS simulation

5.1.1 Inclusion of He-SIA interactions in the model

As discussed in Chapter 3, the 2-D phase space consisting of He (positive axis x), V (positive axis y), and SIA (negative axis y), as shown in Fig. 5-1, is the basis to describe the physical interaction of all clusters. In the model discussed previously, only the clusters contained in the jade-green region ($x \geq 0, y > 0$ and $x = 0, y < 0$) are included, while clusters in the yellow region ($x > 0, y < 0$) were excluded. For the binary reactions describing the cluster transitions due to the trapping of mobile species (i.e., He, I, I_2 , V) or dissociations of single point defects (i.e., He, I, V), the dissociations of single vacancy from He clusters are forbidden to avoid the generation of He-SIA clusters, shown by a dash circle in Fig. 5-1.

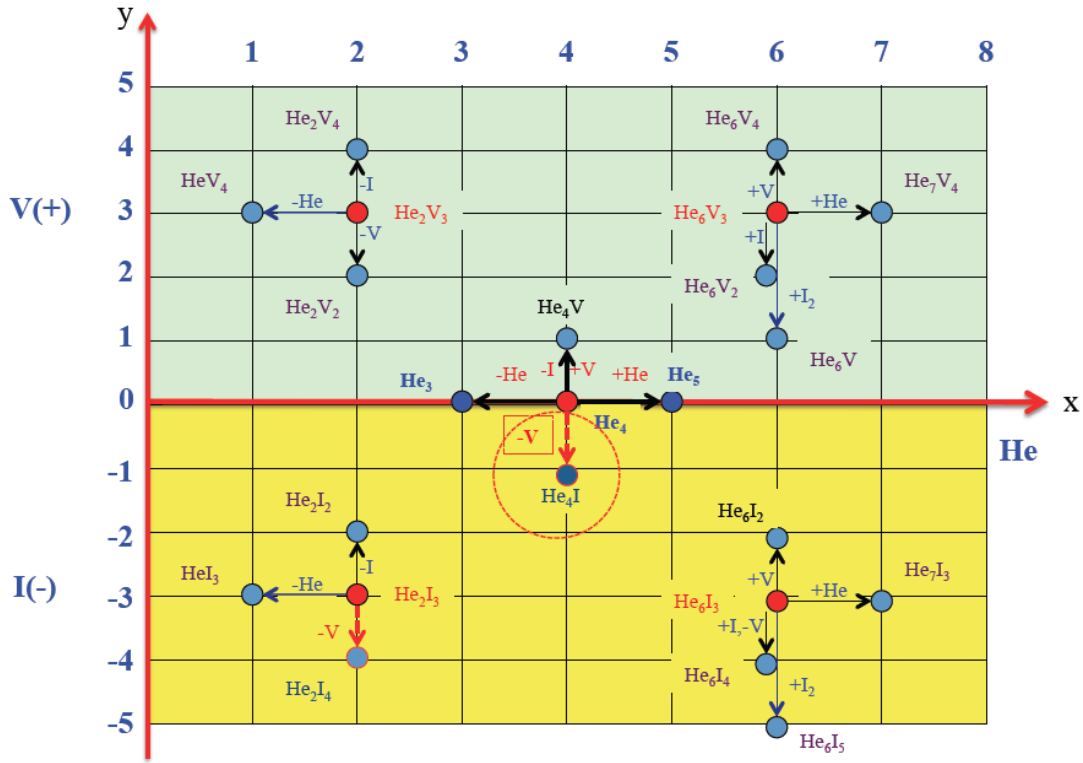


Figure 5-1. Schematic illustration of the cluster transitions in a 2-D phase space.

In order to complete the model, the He-SIA (yellow region shown in Fig. 5-1) clusters must be added, so the 2-D phase space expands to the entire regime of $x \geq 0$. All of the clusters considered in the old model can be annihilate or be generated by absorbing mobile specie or emitting a single point defect. Likewise, the newly added He-SIA cluster phase space needs to be able to experience similar dynamic evolution. This requires the following modifications. First, the vacancy-emission induced annihilations of He clusters, resulting in the generation of He_nI, are added. For He-SIA clusters, single He, V, SIA, and di-SIA are considered to be mobile and only single He, V, I can be emitted during a cluster dissociation event. Fig. 5-1 indicates the transition processes of He-SIA clusters, denoted in the yellow region. For example, a He₂I₃ (immobile) can be generated by trapping events, such as a HeI₃ (immobile) trapping a nearby interstitial He (mobile), a He₂I₂ (immobile) trapping a nearby self-interstitial (mobile), a He₂I (immobile) trapping a nearby di-SIA (mobile), or a He₂I₄ (immobile) trapping a nearby vacancy (mobile). Furthermore, a He₂I₃ cluster can also be generated by a He₃I₃ (immobile) that emits a He, by a He₂I₄ (immobile) emitting a SIA, or by a He₂I₂ (immobile) emitting a vacancy. On the other hand, the He₂I₃ cluster can transform to another cluster and thus annihilate by trapping a mobile specie around it, i.e., trapping a He to result in a He₃I₃; trapping a V to result in a He₂I₂; trapping a SIA to result in a He₂I₄; or trapping a I₂ to result in a He₂I₅. Additionally, a He₂I₃ cluster can be annihilated by emitting He, I, or V to produce a HeI₃, He₂I₂, or He₂I₄, respectively. Note that all of the newly considered He-SIA clusters are assumed to be immobile. The mathematical

expressions describing the rates at which He-SIA cluster transitions occur are the same as those used for He-V clusters based on the classical rate theory.

As shown in Chapter 3, the binding energies of He, SIA, vacancy to the clusters are crucial to the description of the He-SIA transitions and the construction of the coupled partial differential equations. So in the following section, the binding energies used are discussed in detail.

5.1.2 Energetics of He-SIA clusters

It is well known that self-interstitial atoms in metals interact with substitutional He, resulting in SIA vacancy recombination and kick-out of the He to an interstitial position in the metallic lattice [30, 58]. However, the interactions between SIA clusters and interstitial He atoms have not been investigated extensively using atomistic simulations. Caspers et al. [140] investigate the energetics of the interactions of one He with small SIA clusters, which approaches saturation as the number of SIA contained in the clusters increases. Ventelon et al. [62] characterized many interactions between He and SIA clusters by conducting MD simulations; their molecular statistics calculations were used to demonstrate a relatively small interaction trapping radii of about 1 nm between interstitial He and SIA cluster complexes, but strong binding energies from 1.3 to 4.4eV, as shown in Fig. 5-2.

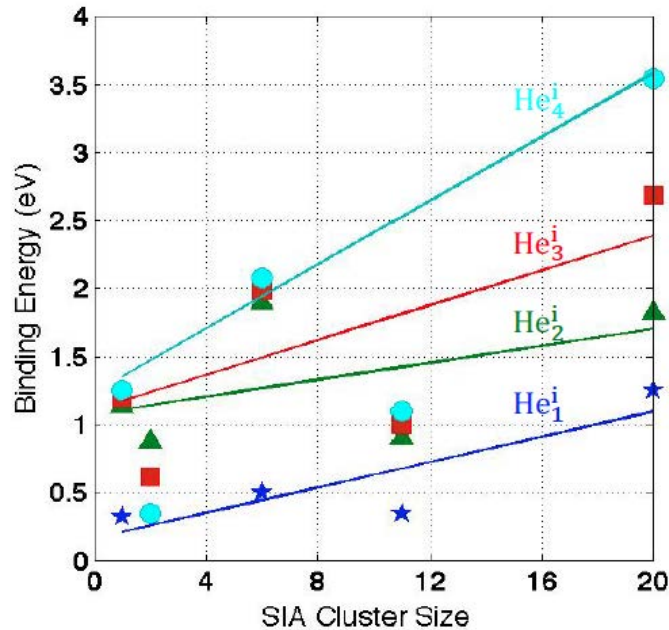


Figure 5-2. The He-binding energies of complexes containing 1, 2, and 4 interstitial heliums with 1, 2, 6, 11, and 20 SIA clusters obtained from conjugate gradient molecular statics calculations, as reproduced from Ref.[62]. The data of the complex containing 3 interstitial helium is obtained by interpolation of the existing data.

Since the simulation requires thermodynamic data on the cluster formation or binding energies for the entire phase space, which includes the maximum He-SIA cluster size, a continuous description of the binding energies for all the clusters in the phase space are necessary. Since there are scarce atomistic calculations of the binding energies of He-SIA clusters, extensive interpolations and extrapolations based on the known values are required to spread the binding energies to the entire phase space. Note that the resulting binding energies are quite uncertain because of the limitation of the accurate known values.

For the helium binding energies to the He-SIA clusters, it is known that the binding energies approach saturation with increasing SIA number contained in the complex while the number of He is fixed [140]. The saturation energies can be derived from the following questions, namely,

$$E_{b,He}(He_m I_n) = E_f(He) + E_f(He_{m-1} I_n) - E_f(He_m I_n). \quad (5-1)$$

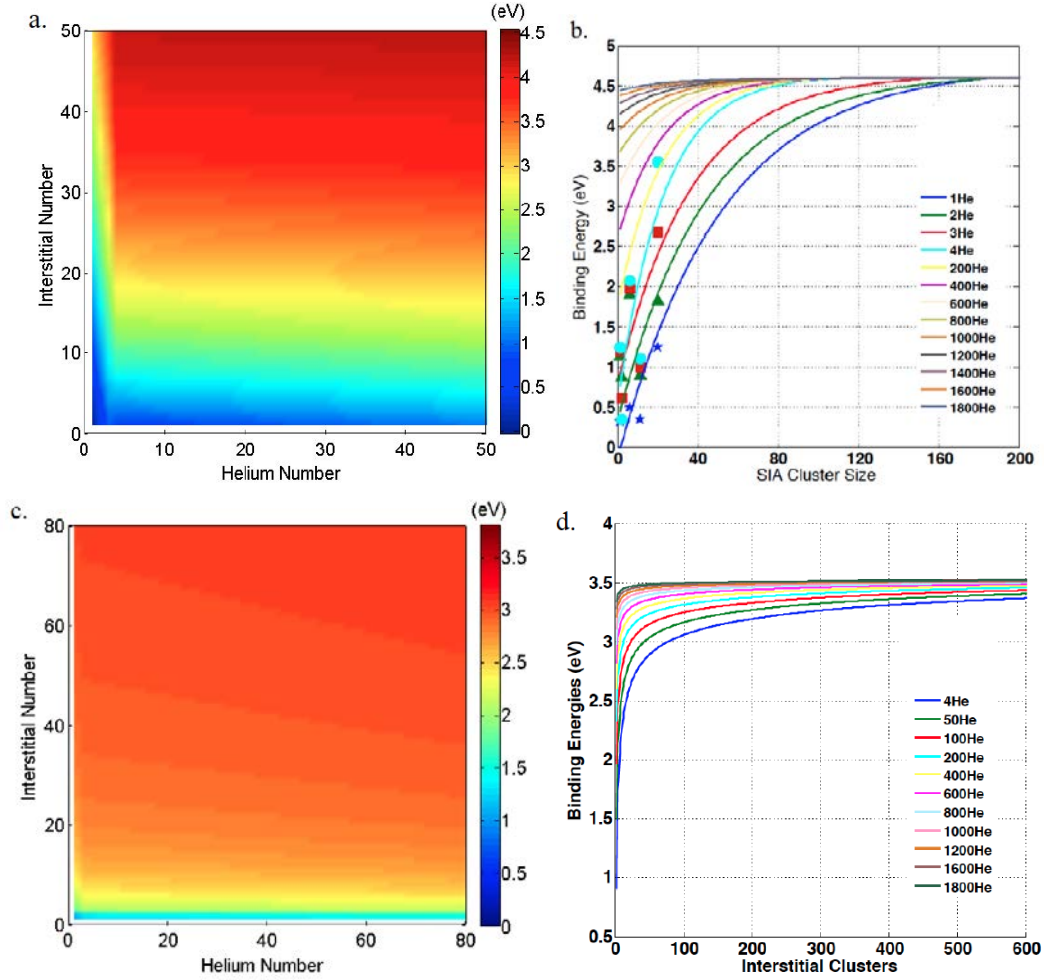


Figure 5-3. Binding energies of (a, b) He and (c, d) self-interstitial to He-SIA clusters.

When the clusters are sufficiently large, $E_f(He_{m-1}I_n) \cong E_f(He_mI_n)$, so the He binding energy will be approximately equal to the formation energy of an interstitial He in the bulk of the metal, 4.6 eV. Likewise, the ultimate binding energies of SIA and vacancy to He_mI_n are 3.77 eV and 2.07 eV, respectively, assuming the ab initio calculated formation energies are correct.

Fig. 5-3 shows the resulting binding energies of He and self-interstitial to He-SIA clusters obtained by extrapolation and interpolation from the known atomistic modeling values. The He binding energies achieve saturation along both the He and SIA directions, as shown in Fig. 5-3(a) and (b). The binding energies of SIA shown in Fig. 5-3(c) and (d) indicate that the saturation process along the SIA direction is faster than that along the He direction, although the binding energies eventually do reach saturation for large He-SIA clusters. It is worth emphasizing again that the binding energies derived here have uncertainties due to the lack of an extensive atomistic database. Nevertheless, the basic

trends of these binding energies are reasonable and it is acceptable for the purpose of demonstration of the inclusions of He-SIA clusters.

5.1.3 Modeling results

This model including He-SIA interactions has been used to simulate the THDS measurement of single crystal iron implanted by 10 keV He ion to a fluence of 10^{14} He/cm², in order to directly compare with the model that did not include He-SIA clusters. The same binding energies for He-vacancy clusters are applied for both cases. Note that the focus here is to investigate the influence of including He-SIA clusters on the modeling results, so all other diffusion parameters and binding energies for He-vacancy clusters are consistent between these two modeling cases.

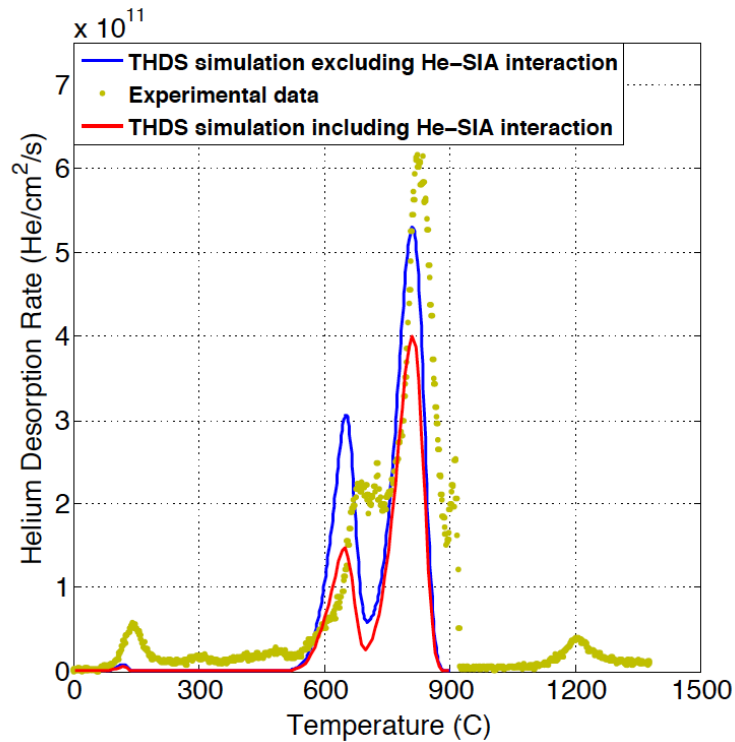


Figure 5-4. Comparison of the simulations that include and exclude He-SIA interactions for the THDS measurement of the single crystal iron implanted by 10 keV He ion to a fluence of 10^{14} He /cm².

Fig. 5-4 indicates the predicted helium desorption spectra using two different sets of parameters that exclude and include He-SIA interactions. Both successfully reproduce the major groups of He desorption. The positions of the observed peaks are in reasonably good agreement with the experimental data. Another common feature is that both modeling methods underestimate the total helium desorption compared to the experimental result. Comparing these two sets of parameters, the inclusion of He-SIA

cluster binding reduces the total He desorption predicted to occur within the BCC range, compared to the parameter set that excludes this binding, even though the release peaks occur at the same temperatures. The comparison indicates that the inclusion of He-SIA interaction only affects the predicted amount of He released without changing other features.

The lower integrated release of He implies that He atoms are captured by He-SIA clusters that are stable at higher temperatures. Fig. 5-5 shows the amount of helium in different form (*i.e.*, He-V, He-SIA, free He) during the annealing process. Overall, interstitial He is at a very low level, even for the as-irradiated condition, which provides further evidence that the helium bonds with vacancies to form He-V clusters. Note that the existence of interstitial clusters also contributes to He trapping at the beginning of the annealing process. The first release peak around 140 °C indicates slightly decreased He capture by He-V clusters, but a small increase in the He captured by He-SIA clusters. It indicates that some unstable He-V clusters at this temperature emit He. A part of the generated He atoms are captured by He-SIA clusters while many remain in the form of interstitial He and diffuse to the surface to desorb. In the regime from 150 °C to about 600 °C, the quantity of He in the three different forms remains constant and the ratio of He in He-V to that in He-SIA clusters is around 4.8. Meanwhile, the predicted desorption spectrum shown in Fig. 5-4 is quite flat without obvious He desorption in this temperature regime. With increasing temperatures, a major He desorption regime occurs from 600 °C to about 900°C, in which dramatic changes occur. The He contained in He-V clusters decreases significantly. The existence of the small shoulder around 750 °C results from the transition stage between the 2nd and 3rd major He desorption peaks shown in Fig. 5-4. Interestingly, a large fraction of He released from He-V clusters are captured by He-SIA clusters, inducing an increase in the amount of He in He-SIA clusters. The helium behavior for the two sets of parameters are quite similar, but in some major differences. Eventually, the He contained in He-V cluster drops to a very low level while the He in He-SIA clusters becomes sizeable.

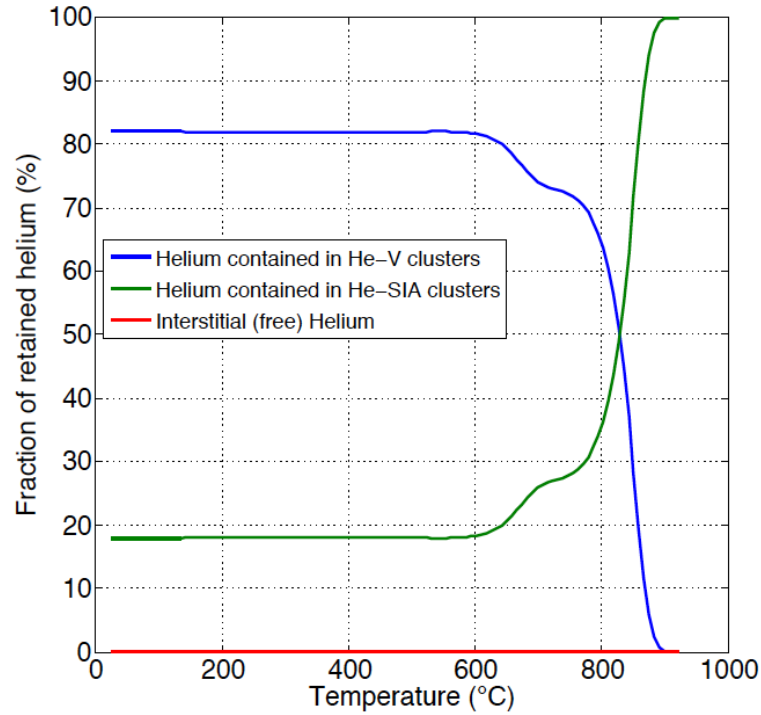


Figure 5-5. The fraction of retained He in different complexes during the annealing process.

The inclusion of He-SIA binding expands the phase space that must be included in the model and it is necessary to investigate its impact on the cluster evolution. Fig. 5-6 shows the cluster distribution evolution in the full 2-D phase space for the single crystal iron sample implanted by 10 keV He to a fluence of 10^{14} /cm² during the thermal annealing process. The He-V cluster evolution indicates a very similar path as that in the parameter set that excludes He-SIA clusters, as shown in Fig. 5-4~5-7(a). The only difference is that the concentration is slightly lower in the current modeling. However, the He-SIA clusters exhibit a totally different evolution path. At 100 °C, large He-SIA clusters with up to 100 He and 140 SIAs have been formed. As well, the clusters in the elliptic region containing 40 ~ 80 He and 40 ~ 120 SIAs have a relatively high concentration. Meanwhile, the He-V clusters are confined to a small regime, containing less than 20 He and vacancies. The rapid formation of larger He-SIA clusters relative to He-vacancy clusters is driven by the much smaller SIA migration energy (0.34 eV) in BCC iron compared to vacancy migration energy (0.8 eV). The concentrated elliptic region derives from the large He and SIA binding energies in this regime. At 350 °C, the upper part of this phase space dissolves along the line with a He/SIA ratio of around 2. With increasing temperature, more and more unstable He-SIA clusters begin to dissolve and this produces the shrinkage of the phase space region. Note that the concentration of He-SIA clusters is only 15% of that of He-V clusters, although the He-SIA clusters occupy a much larger phase space region. At 750 °C, a ‘crescent’ shape is achieved and bound by two lines with He/SIA ratios of 1 and 1.5, respectively. In the dramatic evolution from 350 °C to 750 °C, the clusters shrink in the interstitial direction while the front of the growth path elongates to larger values along the number of He. From 750 °C to 900 °C, the clusters

continue to grow by expanding to larger He number. Consequently, the narrow region of He-SIA clusters is retained at the end of BCC temperature regime at 912 °C.

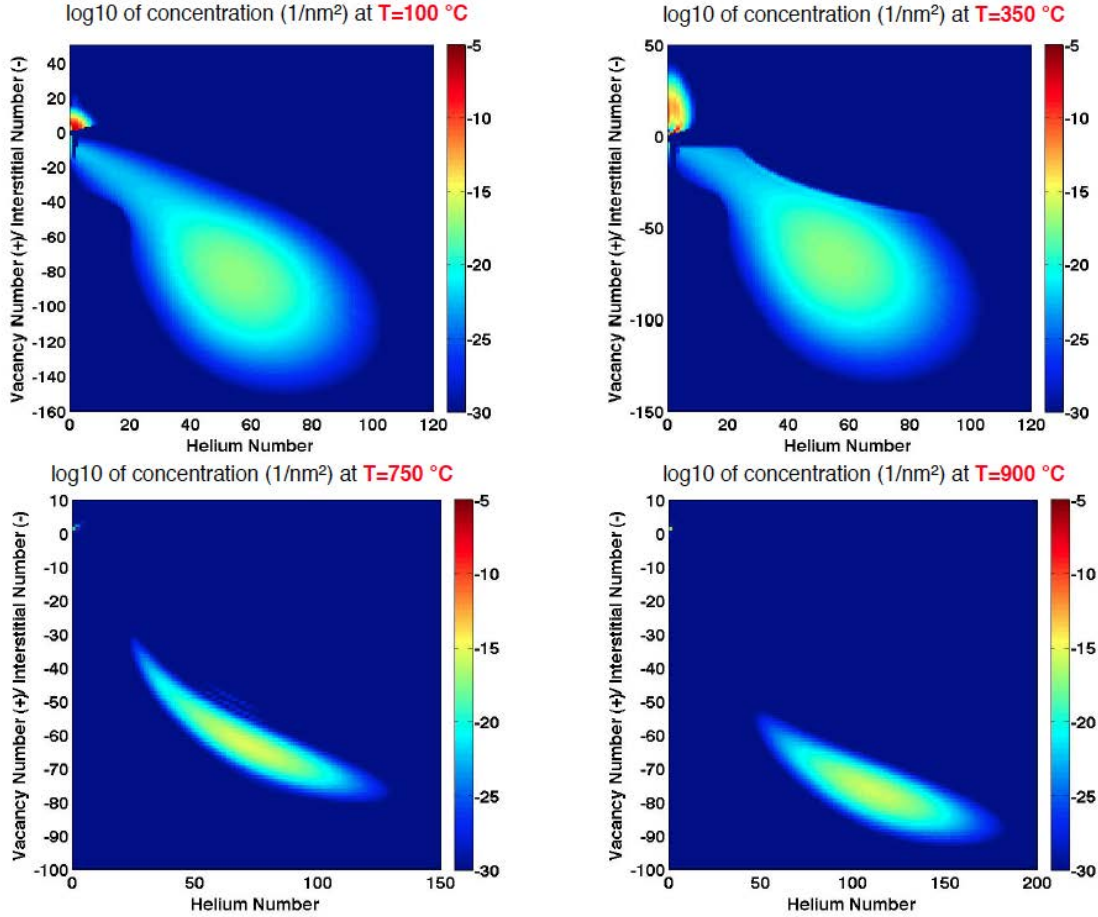


Figure 5-6. He-vacancy/SIA cluster phase space snapshots showing the cluster distribution evolution during the thermal annealing (at 1 °C/s heating rate) at a depth of 37 nm for the specimen implanted with 10 keV He to a fluence of 10^{14} He/cm².

It is important to emphasize here that the predicted evolution of He-SIA clusters depends very sensitively on the precise values of the He-, SIA- and V-binding energies, which reveal the thermal stability of these clusters. This discussion shows a basic idea about how the inclusion of He-SIA clusters will impact cluster distributions. The inclusion of He-SIA interactions helps to move the model closer to reality, although the model further needs to incorporate mobilities of multiple sizes of SIA clusters and small He-SIA clusters. Moreover, this discussion also highlights the importance of validating the binding energies of He to various types of defect clusters that are required to accurately predict He influence on defect evolution of iron-based steels exposed to fusion neutron environments.

5.2 MD simulations of the influence of self-interstitial loop on He clustering in BCC iron

The modeling results show the likelihood of large He-SIA clusters at very high temperature, namely, 900 °C. In order to validate this prediction, MD simulations have been used to investigate the interactions between He and a large SIA cluster loop in BCC iron at high temperature. The atomistic simulations were performed using the LAMMPS [141] MD code. The Fe-Fe interaction was described by the Ackland version of the Finnis-Sinclair potential [142]. The Fe-He and He-He interactions were described by pair-wise potentials. The Fe-He interaction was recently fit by Juslin [143]. The Janzen potential [144] was used to describe the He-He interactions.

For the purpose of comparison, two simulation conditions were performed, *i.e.*, helium implantation in a perfect iron computational cell and helium implantation in a computational cell including a dislocation loop. The semi-empirical MD simulations were performed using a computational cell of $40a_0 \times 40a_0 \times 40a_0$ (containing 64 000 atoms), where a_0 is the Fe lattice parameter and periodic boundary conditions have been applied in all directions. The pre-existing dislocation loop consists of 91 self-interstitial atoms. For both conditions, one He atom is randomly added to the computational cell every 8 ps until the number of the He reaches 300, corresponding to an implanted He concentration of 4687 appm. The simulations were performed at 900 °C.

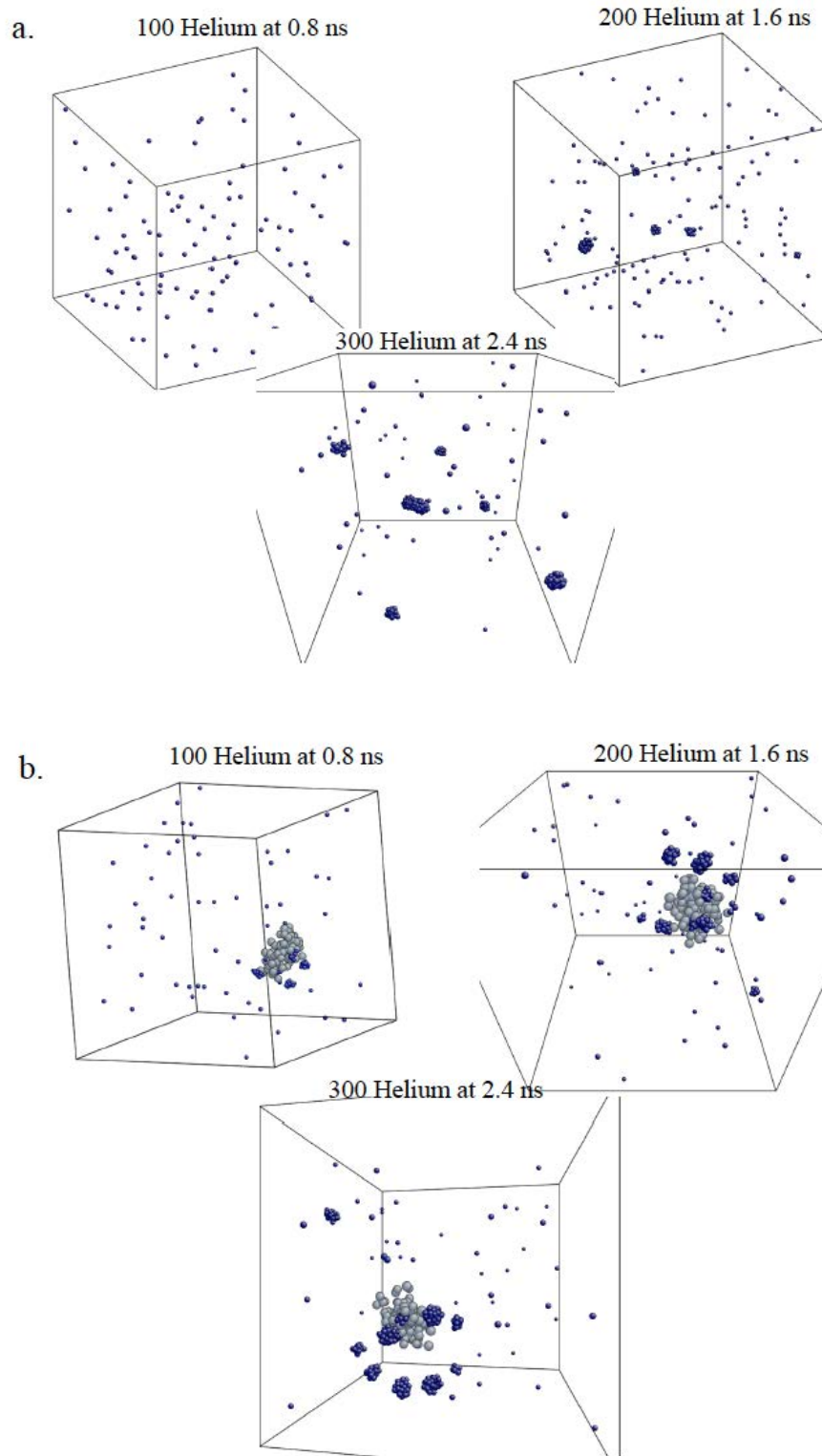


Figure 5-7. Snapshots of the different stages for the helium implantation in BCC iron: (a) without dislocation loop; (b) with dislocation loop. SIA atoms are denoted by grey color; He atoms are denoted by blue color.

Fig. 5-7 shows snapshots of three different stages of the helium implantation process for these two different MD simulation conditions. For the MD without a dislocation loop (Fig. 5-7(a)), the implanted helium atoms are distributed randomly without obvious formation of clusters before 160 He atoms are implanted. Starting after 160 He atoms are implanted, significant clustering occurs. The clusters grow further after implantation is complete. Note that the distribution of the clusters is stochastic. The MD simulation with a pre-existing dislocation loop (Fig. 5-7(b)) indicates a quite different path. A quite dramatic clustering process occurs when the implanted helium is about 625 appm (not shown in Fig. 5-7(b)). With increasing number of the implanted He, more and more clusters are formed and begin to grow. The clusters are preferentially located in the periphery of the dislocation loop, while some of them are even attached or co-located on the loop. This observation can be rationalized by the presence of the strong strain field induced by the dislocation loop, which attracts the implanted He to accumulate locally around the loop.

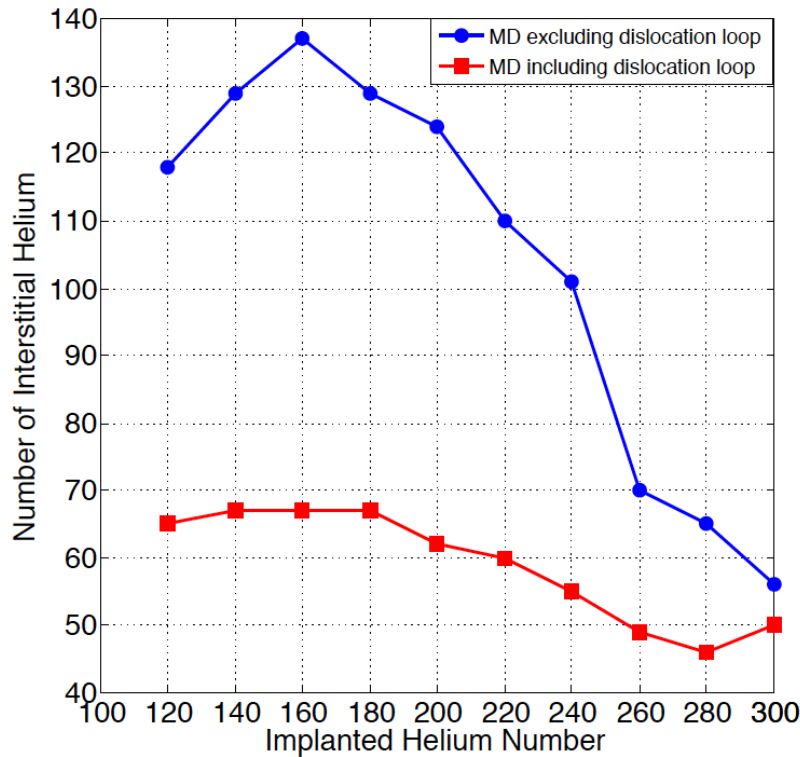


Figure 5-8. Number of interstitial helium not in clusters during the implantation process for the two simulation conditions that included a dislocation loop versus being performed in an otherwise perfect crystal.

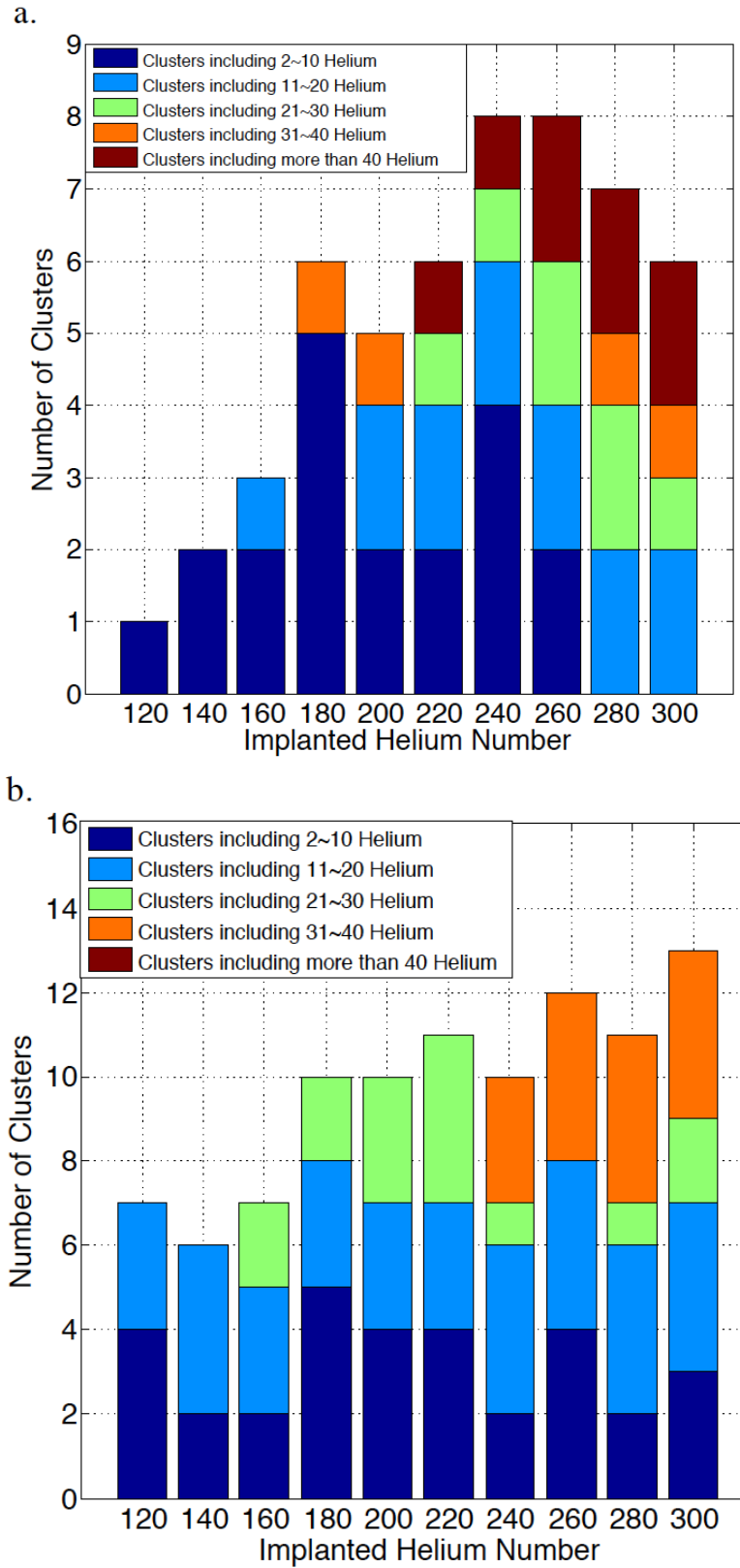


Figure 5-9. Cluster distribution analysis in the He implantation process for two simulation conditions: (a) without dislocation; (b) with dislocation.

Fig. 5-7 provides qualitative indication of the He implantation in BCC iron with and without pre-existing dislocation loops. Further quantitative analysis is provided in Fig. 5-8 and 5-9. The free (interstitial) He existing in the computational cell is shown in Fig. 5-8 as a function of implanted He for the two different conditions. For the simulation in perfect iron, the implanted He are located randomly in interstitial sites before 160 He atoms are inserted. After this, a clear indication of He cluster is observed, especially as implanted He reaches 3750 ~ 4062 appm resulting in reduced number of free He in the cell. The consumption of free He atoms due to clustering is more significant than generation by implantation. For MD simulation containing the dislocation loop, the free helium remains at a low level during the implantation process. When the implanted He number is less than 2812 appm, the quantity of free He is almost constant, indicating that all implanted He atoms participate in the clustering process. Fewer free He atoms exist at the same level of implanted He. Fig 5-9 demonstrates the helium cluster distribution throughout the He implantation process for the two simulation conditions. In order to clarify the statistics, all clusters are sorted into five different groups based on the number of He contained in the cluster: i. clusters including 2 ~ 10 He; ii. clusters including 11 ~ 20 He; iii. clusters including 21 ~ 30 He; iv. clusters including 31 ~ 40 He; v. clusters including more than 40 He. Overall, the number of clusters for the simulation including the dislocation is larger than that for the case excluding the dislocation. At the early stage, various clusters occur in the computational cell with a dislocation. In this condition, the cluster distribution is dominated by small clusters consistent with a nucleation phenomena. The MD simulation results in perfect iron indicate that large clusters (type v) start to form after 220 He atoms (3437 appm) are implanted. The number of large clusters increases with increasing He concentration. The MD simulation results indicate that the He clustering is enhanced by the existence of the SIA loop and extensive interactions occur between SIA clusters and He clusters that promote cluster nucleation.

5.3 Comparison of MD simulation and cluster dynamic modeling on the helium implantation in BCC iron

In Chapters 3 and 4, various experimental conditions were used to compare with the developed cluster dynamics model. In addition, mutual comparisons of different modeling methods/parameter sets are also necessary. The helium implantation in pure BCC iron is taken as a representative condition to compare MD simulation described in Section 5.2 with the cluster dynamics model.

The MD simulation allows atoms to interact with each other for a period of time, providing a view of the atom motion. In the most common version, the trajectories of motion are determined by numerically solving Newton's equations of motion for a system of interacting particles, where the forces between the particles and potential energy are defined by interatomic force fields. Due to the limitation of computing capability, the simulation time and length scale are from ps to ns and from atomic to nm, respectively, which inhibits direct comparison with experimental observations. Phenomena at the mesoscale have typically been simulated using models based on reaction rate theory, such as rate theory based cluster dynamics models. The CD model is

appropriate for application to problems that involve intermediate-length scales, and time scales from that characteristic of diffusion to long-term microstructural evolution ($\sim \mu\text{s}$ to years). The evolution of defect clusters can be described in terms of a defect size distribution function (SDF) in the framework of the mean field approximation [145]. Evolution of this SDF can be accounted for in the context of a CD model through the use of a master equation that describes both growth and dissolution of the clusters due to reactions with mobile defects, thermal emission of these same species, and cluster coalescence if the clusters are mobile. One advantage of this model is that it can compare with a broad range of experimental observations. The simulations of a specific case using these two totally different models are investigated in the following.

In the MD simulation, 300 He atoms are implanted into the computational cell with 64000 iron atoms in 2400 ps, which is equivalent to a He implantation rate of $8.1 \times 10^7 / \text{s} / \text{nm}^3$. Eventually, the He concentration reaches 4687 appm. All of the implanted helium atoms are assumed to be located in the interstitial sites based on the calculations conducted by Erhart et al. [112].

The simulation of He implantation in iron has been included in the cluster dynamics model as the first step to study the helium desorption spectrum. Considering that the MD simulation concerns the atomistic scale, the modified cluster dynamics model excludes the spatial dependence of the defects. Meanwhile, the phase space remains the same, i.e., a 2-D space consisting of He and V/I. Different from the previous model, all implanted He atoms are constrained inside the computational cell without the possibility of desorption. The formation, thermal desorption and any interaction of the clusters occur homogeneously. To simplify the model, the He-SIA interaction is not considered here.

The binding energies of the He, V and SIA to He-V clusters are derived based on MD calculations. Similar to the previous parameter sets, four mobile species are considered and the migration energies of He, SIA, I_2 , and V are 0.078 eV, 0.058 eV, 0.33 eV, 0.74 eV, respectively [72]. The preliminary calculation of the modified model predicts a He-V distribution at the end of the He implantation process, as shown in Fig. 5-10(a). The free He and He_2 are the dominant species while the complexes containing one vacancy also have a significant concentration. In addition, the concentrations of the other species are at a low level. In order to make a direct comparison with the MD simulation, the concentrations of all of the clusters containing the same He number are integrated. A comparison of these two modeling methods is shown in Fig. 5-11, for which a very obvious discrepancy exists. The MD simulation predicts a saturating trend for clusters. On the other hand, the cluster dynamics model predicts a decreasing curve. Note that the concentrations of the clusters including one He have a reasonable agreement.

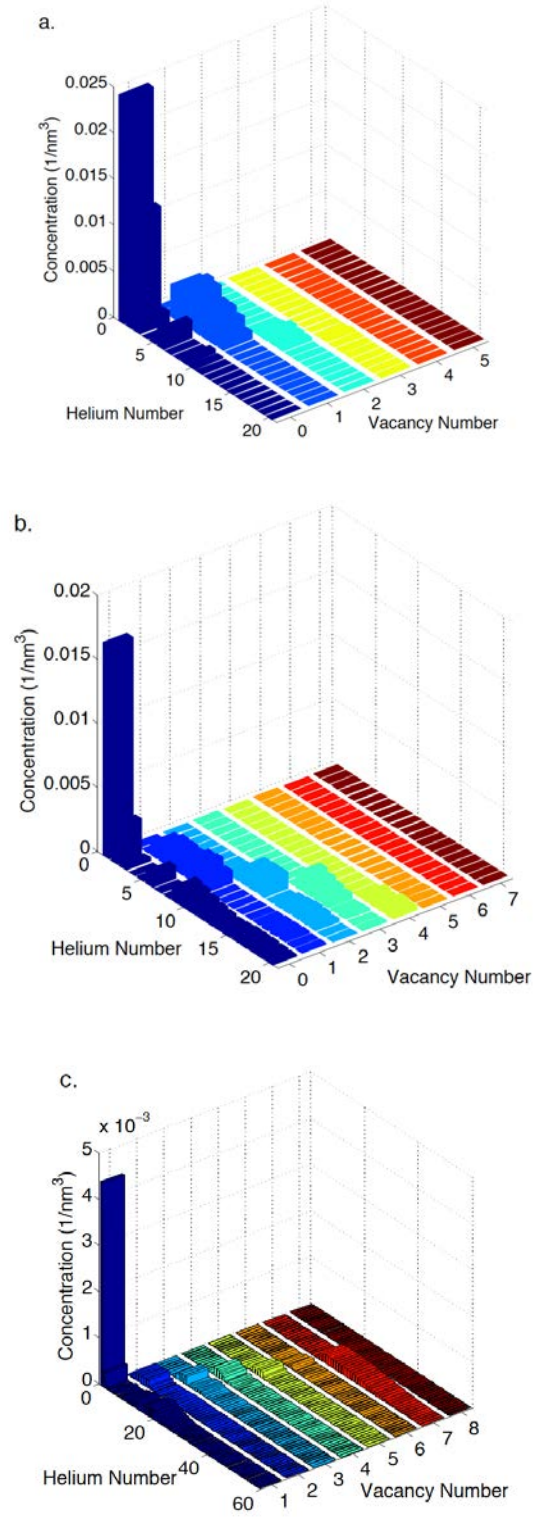


Figure 5-10. He-V cluster distribution at the end of the He implantation process: (a) simulation with one mobile He cluster; (b) simulation with six mobile He clusters; (c) simulation with six mobile He clusters and modified D_0 .

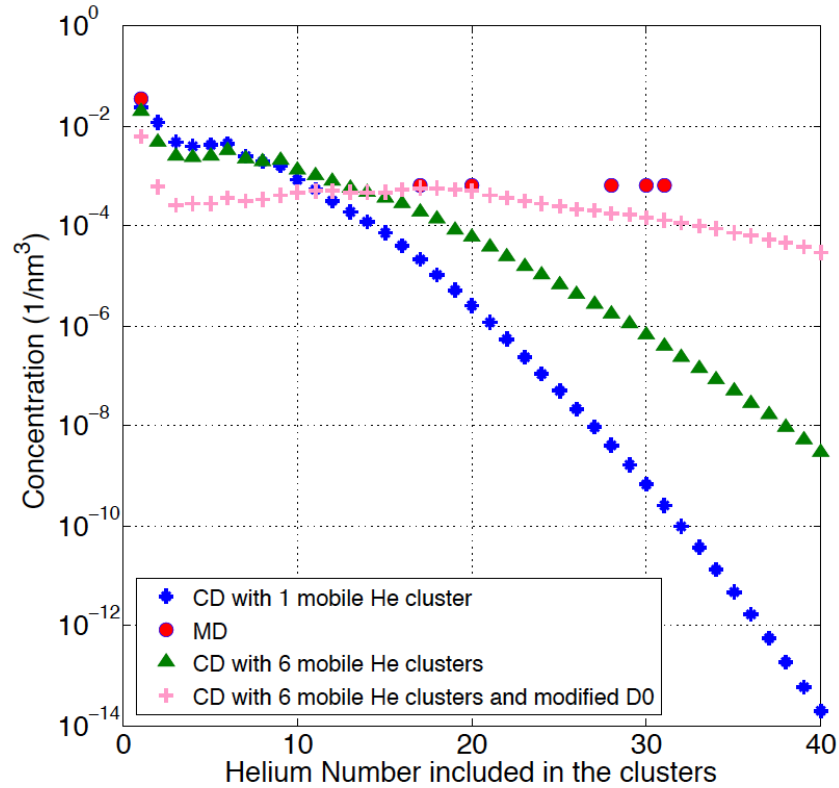


Figure 5-11. Comparison of the results from MD and three different clusters dynamic simulations.

The disagreement can be rationalized by the simplification of the cluster dynamics model, which does not reflect all of the real physical processes. For example, MD simulation reveals that interstitial He cluster with He number up to 6 are mobile, however, only single He is considered to be mobile in the continuum model, which leads us to investigate the effect of more mobile species in the model. To improve the cluster dynamic modeling results, He₂, He₃, He₄, He₅, and He₆ are treated as mobile in addition to the previously considered mobile clusters. The migration energies and the diffusivity coefficients of these clusters are listed in Table 5-1 [66]. Surprisingly, the He₅ cluster has an even lower activation barrier of only 0.03 eV, based on MD simulations performed below 400 K. At 400 K and higher, this cluster ejects an SIA to become He₅V which is essentially immobile.

Table 5-1. Migration energies and diffusivity coefficients of the mobile He clusters.

Helium Clusters	Migration Energies (eV)	$D_0 (1.37 \times 10^{11} \text{ nm}^2/\text{s})$
He ₁	0.078	1
He ₂	0.05	1/2
He ₃	0.15	1/2
He ₄	0.313	1/2
He ₅	0.03	1/2
He ₆	0.277	1/2

The He-V cluster distribution predicted by the cluster dynamics modeling result including 6 mobile He clusters is shown in Fig. 5-10(b). Compared to the initial calculation, clusters having higher He number (up to 20) are formed due to the involvement of more mobile clusters. Note that there are still not many clusters containing more than 5 vacancies, which is ascribed to the much larger migration energy of vacancy, imposing restrictions to the formation of large vacancy clusters. However, it does not improve the agreement with the MD simulations except increasing the tail of the size distribution, as shown in Fig. 5-11. Based on these two calculations, the cluster dynamics model underestimates the concentrations of He-V clusters. Increasing the mobility of the mobile species may help to improve the agreement. Stewart et al. [66] indicate that the pre-factors vary significantly, which provides an opportunity to optimize this parameter. Note that the pre-factors for the He clusters are set to be 1/2 of that for interstitial He. Fig. 5-10(c) shows the cluster distribution when D_0 is modified to be seven times the original value. The clusters with significant concentrations are extended to a larger regime, up to 60 He and 8 V. Furthermore, the new cluster dynamics modeling result has a much better agreement with the MD simulation, shown in Fig. 5-11. It is emphasized that the modification of the pre-factors are equivalent to the optimization of the migration energies of the mobile species. After a reasonable parameter optimization, the MD simulation results can be re-produced by the CD model, which reflects the self-consistence of the developed CD model at least for this condition.

5.4 Conclusion

The previously introduced cluster dynamics model has been extended by the inclusion of interactions of He and self-interstitials. The simulation results indicate that the influence of He-SIA binding interactions on the helium desorption from He-implanted single crystal irons is to reduce the total desorption flux as compared to that only including He-vacancy interactions. However, the inclusion of He-SIA binding does not impose significant effects on the evolution of He-vacancy clusters. MD simulations indicate that

the presence of SIA clusters enhances the He clustering process and there are extensive interactions between He and SIA clusters. The mutual validation between MD and CD results from conducting a parameter optimization. As to the future work, the mechanisms of the He-SIA interactions should be investigated to provide a pathway for the accurate calculation of the binding energies.

Chapter 6

Influence of Pre-existing Point Defects and Defect Clusters on Helium Behavior in Iron

As introduced in Chapter 1, the structural materials used in fission and fusion reactors are exposed to intense neutron radiation fields, inducing changes in mechanical properties as a consequence of changes at the microstructural level. Due to the complex and extreme environments, the generation of helium in the structural materials is not insular, but occurs simultaneously with the generation of lattice defects in the bulk metal. In this chapter, the influence of pre-existing point defects and defect clusters on helium behavior in iron is investigated through simulations of helium desorption from single crystal iron exposed to neutron irradiation followed by subsequent He ion implantation, which leads to the introduction of a large amount of point defects and defect clusters prior to introducing He. Note that experimental comparison and validation will be performed in the future, since single crystal iron specimens are neutron irradiated at Oak Ridge National Laboratory (ORNL) high flux isotope reactor (HFIR) at 300 °C, 500 °C and 650 °C to dose of 1.2 and 9.6 dpa.

6.1 Plans of the experimental study

Consistent with previous discussions, this study of the influence of pre-existing defects on helium behavior in iron will be realized by coordinated experiments and modeling. The experiments include several stages: introduction of defects by neutron irradiation, TEM analysis of the post-irradiated samples, helium implantation, and THDS.

The exposure to the neutron irradiation of the materials is considered as the source for the introduction of the defects in the structural materials. Single crystal iron with high purity (99.98%) has been purchased from Goodfellow and placed in HFIR at ORNL for various irradiation conditions, as indicated in Table 6-1.

Table 6-1. Irradiation conditions for single crystal irons placed in HFIR.

Parameters	Sample 1	Sample 2	Sample 3	Sample 4
Temperature (°C)	300	500	650	650
Dose (dpa)	1.2	1.2	1.2	9.6

After these capsules have been irradiated and radiologically cooled for an appropriate amount of time, TEM will be employed to observe and record the cluster distribution

after irradiation, providing an opportunity to validate the neutron irradiation modeling. A new thermal helium desorption spectrometry system coupled with an in-situ He ion gun is currently under construction at ORNL. The single crystal iron following neutron irradiation will be transferred to the new THDS system and exposed to helium implantation followed by desorption. The helium desorption spectra will be recorded and compared with the modeling results, similar to the previous studies discussed in Chapters 2, 3, and 4.

Note that the plans for the experimental study are only briefly introduced here, and the focus of this chapter is on the modeling prediction of these processes. In the near future, the combination of experiment and modeling will be performed and the results of the comparison will be presented elsewhere.

6.2 Neutron irradiation

6.2.1 Model construction

Free vacancies and self-interstitial atoms (SIAs) as well as spherical vacancy clusters and SIA clusters in the form of planar, prismatic dislocation loop are continuously formed and will evolve in pure iron under neutron irradiation. The cluster dynamics model is used here to predict the evolution of the clusters. Different from the model introduced in Chapter 3, only intrinsic defects and their clusters are considered in this study. Further, since the probability that SIA and vacancy co-exist in a single cluster is very low due to their strong binding tendency for recombination, no mixed I-V clusters were considered, and it is thus sufficient to define any cluster using just one number, with its absolute value being the number of point defects (I or V) contained and its sign (‘-’ for SIA clusters, or ‘+’ for V-clusters, consistent with previous models) indicating the character of the cluster. Two numbers, NI and NV are chosen as the number of interstitials in the largest I-cluster, and the number of vacancies in the largest V-cluster, respectively. Physically, these numbers prescribe the ‘phase space’ within which the clusters can interact with each other, and ensure the conservation of point defects. Note that the generation of Frenkel pairs in iron did occur by helium ion implantation in the previous model. However, the irradiation effects in the metal induced by ions and neutrons are completely different. Since the energy transfer cross section for ions is an atomic cross section ($\sim 10^{-17} \text{ cm}^2$) while that for neutrons is a nuclear cross section ($\sim 10^{-24} \text{ cm}^2$), neutrons have a much larger range when travelling in metals than ions. The damage production varies weakly along the depth direction for neutron irradiation and therefore, it is reasonable to treat the distribution of the clusters as homogeneous. Thus an explicit spatial dimension is no longer necessary in this model. Likewise, the NI and NV should be chosen large enough so that the computational results are not affected by the prescribed phase space, meaning computer memory limitations.

Since there is no spatial dependence, the concentration of each cluster is only a function of time and ordinary differential equations can be employed to describe the defect cluster evolution. The binary reactions discussed in Chapter 3 are still appropriate and become

simpler here because there are only two defects (V- and SIA-clusters) considered during the neutron irradiation. The generic form to describe the evolution of a cluster is:

$$\frac{dC_i}{dt} = \phi \times P_i + G_{-T} + G_{-E} - A_{-T} - A_{-E}, \quad (6-1)$$

where C_i refers to the volumetric concentration (in $1/\text{nm}^3$) of the i -th cluster, ϕ is neutron flux (in $\text{neutron}/\text{nm}^2/\text{sec}$), P_i is the production ‘probability’ of the i -th cluster by neutron irradiation, G_{-T} , G_{-E} , A_{-T} , and A_{-E} indicates the cluster transitions and have the same explanations as those shown in Chapter 3. The detailed construction of the coupled system of ODE is thus ($\Lambda = [-NI, NV]$ is the prescribed phase space):

$$\frac{dC_i}{dt} = \phi \times P_i + \sum_{\substack{m+p=i \\ m,p \neq 0 \\ m.p \in \Lambda}} k_{m,p}^+ C_m C_p - \sum_{\substack{m \neq i \\ m \neq 0 \\ m.m+i \in \Lambda}} k_{m,i}^+ C_m C_i - k_i^- C_i \quad (6-2)$$

for $i=NV$ or $-NI$, and

$$\frac{dC_i}{dt} = \phi \times P_i + \sum_{\substack{m+p=i \\ m,p \neq 0 \\ m.p \in \Lambda}} k_{m,p}^+ C_m C_p + k_{i+1}^- C_{i+1} - \sum_{\substack{m \neq i \\ m \neq 0 \\ m.m+i \in \Lambda}} k_{m,i}^+ C_m C_i - k_i^- C_i \quad (6-3)$$

for $\frac{NV}{2} < i < NV$, and

$$\frac{dC_i}{dt} = \phi \times P_i + \sum_{\substack{m+p=i \\ m,p \neq 0 \\ m.p \in \Lambda}} k_{m,p}^+ C_m C_p + k_{i+1}^- C_{i+1} - \sum_{\substack{m \neq i \\ m \neq 0 \\ m.m+i \in \Lambda}} k_{m,i}^+ C_m C_i - 2k_{i,i}^+ (C_i)^2 - k_i^- C_i \quad (6-4)$$

for $2 \leq i \leq \frac{NV}{2}$, and

$$\frac{dC_i}{dt} = \phi \times P_i + \sum_{\substack{m+p=i \\ m,p \neq 0 \\ m.p \in \Lambda}} k_{m,p}^+ C_m C_p + 2k_2^- C_2 + \sum_{\substack{m > 2 \\ m \in \Lambda}} k_m^- C_m - \sum_{\substack{m \neq i \\ m \neq 0 \\ m.m+i \in \Lambda}} k_{m,i}^+ C_m C_i - 2k_{i,i}^+ (C_i)^2 \quad (6-5)$$

for $i=1$, and

$$\frac{dC_i}{dt} = \phi \times P_i + \sum_{\substack{m+p=i \\ m,p \neq 0 \\ m,p \in \Lambda}} k_{m,p}^+ C_m C_p + 2k_{-2}^- C_{-2} + \sum_{\substack{m < -2 \\ m \in \Lambda}} k_m^- C_m - \sum_{\substack{m \neq i \\ m \neq 0 \\ m,m+i \in \Lambda}} k_{m,i}^+ C_m C_i - 2k_{i,i}^+ (C_i)^2 \quad (6-6)$$

for $i = -1$, and

$$\frac{dC_i}{dt} = \phi \times P_i + \sum_{\substack{m+p=i \\ m,p \neq 0 \\ m,p \in \Lambda}} k_{m,p}^+ C_m C_p + k_{i-1}^- C_{i-1} - \sum_{\substack{m \neq i \\ m \neq 0 \\ m,m+i \in \Lambda}} k_{m,i}^+ C_m C_i - 2k_{i,i}^+ (C_i)^2 - k_i^- C_i \quad (6-7)$$

for $-\frac{NI}{2} \leq i \leq -2$, and

$$\frac{dC_i}{dt} = \phi \times P_i + \sum_{\substack{m+p=i \\ m,p \neq 0 \\ m,p \in \Lambda}} k_{m,p}^+ C_m C_p + k_{i-1}^- C_{i-1} - \sum_{\substack{m \neq i \\ m \neq 0 \\ m,m+i \in \Lambda}} k_{m,i}^+ C_m C_i - k_i^- C_i \quad (6-8)$$

for $-NI < i < -\frac{NI}{2}$, where k^+ is the forward reaction rate constant and k^- is the

backward reaction rate constant. The detailed expressions for k^+ and k^- are provided in Chapter 3. Note that for emission ($C \rightarrow A + B$), only those events in which at least one of the two products is a monomer (i.e., I or V) are considered since it is in general more energetically favorable for a cluster to emit a monomer than emit a dimer, trimer or multimer, which is consistent with the previous model.

6.2.2 Parameterization

In the rate theory based reaction-diffusion cluster dynamics models, the mobile species determine the complication of the binary reactions and the burden of the computation. In previous modeling, only V, SIA and di-SIA have been considered as mobile in order to simplify the model. However, it has been shown in the literature [120, 121, 123] that interstitial loops containing a few to several hundreds SIAs in BCC iron are highly mobile with nearly size-independent migration energies close to or even lower than the single SIA migration energy. Therefore, in this modeling of neutron irradiation, all of the interstitial loops are considered mobile. MD simulations performed by Marian et al. [123] indicated that the migration energy of I_n initially decreases but quickly stabilizes with increasing n , following an expression of $E_m(n) = 0.06 + 0.07n^{-1.3}$ (eV), and the diffusivity pre-factors could be expressed as $D_0(n) = 8.98 \times 10^{11} n^{-0.61}$ (nm^2/s). MD studies by Osetsky et al. [146] in BCC iron also revealed lower and even less size-dependent migration energies ranging from 0.02 to 0.03 eV for all I_n clusters and pre-factors with similar power-law dependence on cluster size. Quite differently, however, ab initio calculations in BCC iron performed by Fu et al. [147] revealed increasing migration energies from single interstitial to di-interstitial cluster, and the ab initio values of 0.34

and 0.42 eV, are very close to the E_m^I determined in earlier experimental resistivity recovery studies in iron [148]. Unfortunately, the migration energies of other interstitial clusters containing three or more interstitials were not examined by ab initio calculations. More recently, a TEM experimental study by Arakawa et al. [149] observed and analyzed the motion of interstitial loop in bcc iron containing thousands of single interstitials, and reported a size-independent migration energy of 1.3 eV for all the observed loops, and pre-factors that followed the form of $D_0(n) = (2.3 \pm 0.3) \times 10^{15} n^{-(0.80 \pm 0.02)} (\text{nm}^2 / \text{s})$. Arakawa et al. explained this large migration energy value as the result of combined kink formation and impurity dragging mechanisms, and argued that typical values of impurity migration energy of ‘naked’ loops could be deduced to be ~ 0.4 eV, which is close to the values determined for I and I₂ in ab initio calculations and for I in resistivity recovery experiments. Table 6-2 lists the set of mobility data chosen on an empirical basis by considering the various studies mentioned above. The selected parameter set is quite similar to that chosen by Xu in a recent study [115].

Table 6-2. Mobility set for interstitial clusters/loops and single vacancy.

	V	I ₁₋₇	I ₈	I ₉	I ₁₀	I ₁₁	I ₁₂	I ₁₃	I ₁₄	I ₁₅	I _{n>15}
E_m (eV)	0.75	0.34	0.375	0.385	0.395	0.45	0.50	0.60	0.70	0.80	1.11
D_0 (nm ² /s)	1.37×10^{11}					$1.37 \times 10^{11} / n$					$1.37 \times 10^{11} n^{-0.7}$

Another very important parameter, P_i , needs to be determined and provides in-cascade clustering production of the defects/defect clusters due to neutron irradiation. In our specific modeling of the neutron irradiation in HFIR, the PKA energy spectrum of neutron irradiation in iron was calculated by SPECTER, the results of which are shown in Fig. 6-1. The total displacements, created by the PKA were calculated by a Lindhard model [150], within which the kinetic energy (T) of a PKA is partitioned between electronic and nuclear stopping. The expression for the number of displacements is

$$v = \xi(T, Z) \left(\frac{T}{2E_d} \right), \quad (6-9)$$

where $\xi(T, Z)$ is a function of T and Z (atomic number), and is used to describe the part of the PKA kinetic energy that is available to generate atomic displacements by elastic collisions. E_d is the displacement energy, taken as the reference value of 40 eV for iron. This partitioning coefficient is computed by

$$\xi(T, Z) = \frac{1}{1 + 0.134 Z^{2/3} A^{-1/2} (3.4 \epsilon^{1/6} + 0.4 \epsilon^{3/4} + \epsilon)}, \quad (6-10)$$

$$\epsilon = \frac{T}{2 Z^2 e^2 / a}, \quad (6-11)$$

$$a = \frac{0.626 a_{bohr}}{Z^{1/3}}, \quad (6-12)$$

where A is the atomic mass of the matrix element, a_{bohr} is Bohr radius, 0.529 Å, and $e^2 = 14.4 \text{ eV} \cdot \text{Å}$. Based on Eqs. (6-9) ~ (6-12), the total displacements (Frenkel pairs) can be calculated from the given PKA kinetic energy.

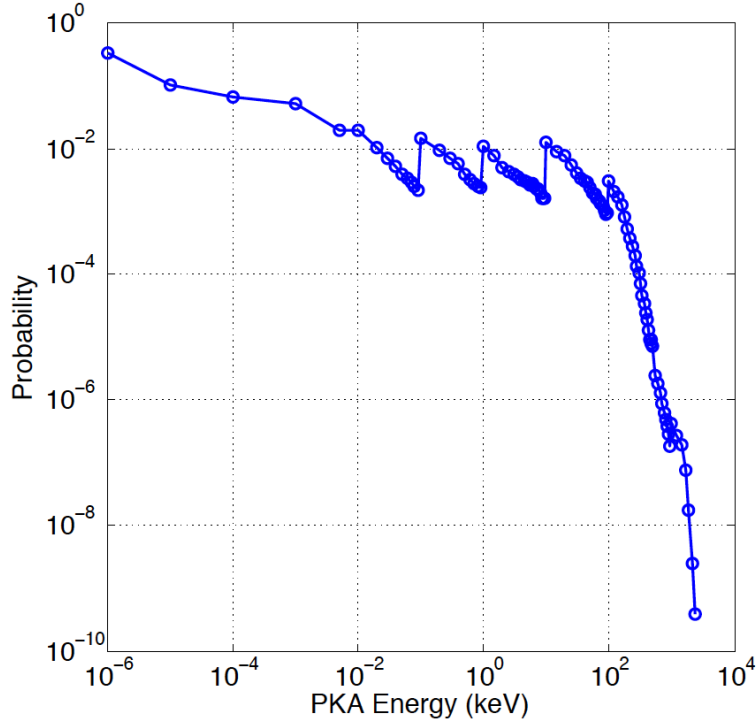


Figure 6-1. PKA spectrum in neutron irradiated iron in HFIR.

Different from the previous model, employing the Frenkel pair production mode, here, intra-cascade cluster production mode is used. Previous MD simulations on cascades in BCC iron showed that PKAs with a few keV or more kinetic energy could directly produce small interstitial and vacancy clusters rather than only isolated Frenkel pairs. Table 6-3 shows the fractions of total surviving point defects that are contained in small clusters $I_1 \sim I_{20}$ and $V_1 \sim V_9$ and the surviving efficiency of point defects for four cascade

energy intervals starting from 1 keV, based on analysis of an MD cascade simulation database in BCC iron that was provided by Stoller et al. [120]. The survival efficiency, f , refers to the number of interstitials and vacancies that survive in the rapid recovery stage in a cascade of MD simulations, as well as following the initial cascade aging when the remaining mobile interstitial and vacancy clusters diffuse through and away from the vacancy rich core of the cascade. In the MD stage of cascade healing/in-cascade recombination, Stoller [120] reported that this survival efficiency varies from one at low PKA energy to about 1/3 for PKA energies greater than 10 keV. Monasterio and co-workers [151] used kinetic Monte Carlo simulations to evaluate the additional recombination during the initial interstitial diffusion stage following cascades and observed sufficient recombination occurring to reduce this value to about 0.4 for low energy PKAs and further to about 0.12 for PKA energies of 20 keV and above.

Table 6-3. Fractions of surviving point defects contained in small clusters and survival efficiency of point defects, for four different cascade energy intervals.

Cluster		Fraction of surviving point defects contained in a cluster			
Type	Size	$1 < \xi T \text{ (keV)} \leq 2$	$2 < \xi T \text{ (keV)} \leq 10$	$10 < \xi T \text{ (keV)} \leq 20$	$\xi T \text{ (keV)} > 20$
Interstitial Cluster	-20	0	0	0	0.017
	-16	0	0	0	0.027
	-12	0	0	0.011	0.025
	-9	0	0	0.041	0.038
	-8	0	0	0	0.051
	-7	0	0.035	0.097	0.074
	-6	0	0.089	0.11	0.076
	-5	0	0.149	0.115	0.085
	-4	0.069	0.139	0.11	0.102
	-3	0.104	0.134	0.11	0.127
	-2	0.374	0.178	0.138	0.157
	-1	0.453	0.276	0.268	0.221
Vacancy cluster	1	0.905	0.667	0.463	0.305
	2	0.095	0.333	0.242	0.211
	3	0	0	0.161	0.158
	4	0	0	0.134	0.126
	5	0	0	0	0.105
	9	0	0	0	0.095
survival efficiency (f)		0.4	0.25	0.134	0.12

Consequently, the survival point defects in the cascade, $(\xi T / 2E_d) \times f$, will be partitioned into small clusters according to the clustering fractions listed in Table 6-3. For

those PKAs with $\xi T < 1 \text{ keV}$, only individual Frenkel pairs, i.e., I and V, were added in the amount $\xi T / 2E_d$. The numbers of clusters produced by all of the kinetic energies in the PKA spectrum are then multiplied by the corresponding probabilities. The resulting cluster production ‘probability’ in $1 / \text{PKA}$ is listed in Table 6-4.

Table 6-4. Intra-cascade cluster production probabilities P_i in $1/\text{PKA}$.

Type	Cluster Size	Probability (1/PKA)
Interstitial Clusters	-20	0.0024
	-16	0.0048
	-12	0.0064
	-9	0.0144
	-8	0.0183
	-7	0.0413
	-6	0.0572
	-5	0.0838
	-4	0.1165
	-3	0.1794
	-2	0.3539
	-1	1.1215
Vacancy Clusters	1	1.8264
	2	0.5005
	3	0.1782
	4	0.1073
	5	0.0602
	9	0.0302

Note that the cluster production probabilities listed in Table 6-4 have the unit of $1/\text{PKA}$, however what is really needed is the cluster production rate with respect to a specific neutron flux. This requires the PKA production rate to be specified. From SPECTER (neutron damage calculations for materials irradiations) calculations, the displacement cross section of the neutron irradiation is also given, which provides us an opportunity to compute the total displacement rate (R_d) in iron, as defined in Eq. (6-13),

$$R_d \left[\frac{1}{cm^3 \cdot s} \right] = \phi \left[\frac{1}{cm^2 \cdot s} \right] \sigma_d [cm^2] N \left[\frac{1}{cm^3} \right], \quad (6-13)$$

where $\phi = 7.8 \times 10^{14} \left[\frac{neutron}{cm^2 \cdot s} \right]$, $\sigma_d = 192 \text{ barn} = 1.92 \times 10^{-22} cm^2$, and $N = 8 \times 10^{22} / cm^3$.

The displacement cross section for iron under neutron irradiation in HFIR has a low value due to the incorporation of thermal neutrons in the neutron flux energy spectrum, which in general do not cause direct displacements through elastic scattering. The damage rate of the iron samples exposed to the HFIR reactor is $\phi \sigma_d, 1.5 \times 10^{-7} dpa / s$.

Fortunately, there is an other way to calculate the displacement rate, as defied in Eq. 6-14,

$$R_d \left[\frac{1}{cm^3 \cdot s} \right] = \lambda \left[\frac{PKA}{cm^3 \cdot s} \right] P_d \left[\frac{displacements}{PKA} \right], \quad (6-14)$$

where the displacements per PKA can be computed by the Lindhard model and the PKA spectrum,

$$P_d = 31.2 \left[\frac{displacements}{PKA} \right]. \quad (6-15)$$

Combining Eqs. (6-13) and (6-14) yields the PKA production rate,

$$\lambda \left[\frac{PKA}{cm^3 \cdot s} \right] = \frac{\phi \left[\frac{1}{cm^2 \cdot s} \right] \sigma_d [cm^2] N \left[\frac{1}{cm^3} \right]}{P_d \left[\frac{1}{PKA} \right]} = 3.84 \times 10^{14} \left[\frac{PKA}{cm^3 \cdot s} \right]. \quad (6-16)$$

Thus, the intra-cascade cluster production probabilities can be obtained by multiplying the values in Table 6-4 with PKA production rate, and noted in Table 6-5.

Table 6-5. Intra-cascade cluster production rates in $1/(cm^3 \cdot s)$.

Type	Cluster	Production Rate ($1/cm^3/s$)
	Size	
Interstitial Clusters	-20	9.35×10^{11}
	-16	1.86×10^{12}
	-12	2.47×10^{12}
	-9	5.53×10^{12}
	-8	7.01×10^{12}
	-7	1.58×10^{13}
	-6	2.19×10^{13}
	-5	3.32×10^{13}
	-4	4.47×10^{13}
	-3	6.89×10^{13}
	-2	1.36×10^{14}
	-1	4.30×10^{14}
Vacancy Clusters	1	7.01×10^{14}
	2	1.92×10^{14}
	3	6.84×10^{13}
	4	4.11×10^{13}
	5	2.31×10^{13}
	9	1.16×10^{13}

In addition to the generation terms induced by the neutron irradiation, the expressions for the transitions of the clusters are also needed. The energetics and expressions of V_n and I_n transitions are the same as discussed in Chapter 3.

6.2.3 Results

To allow for the future comparison between the experimental characterization and modeling, the modeling predictions of experimental observables are extracted. Here, the interstitial clusters are used to demonstrate defect evolution in two neutron irradiation conditions, having the same damage level, 1.2 dpa, at two different temperatures, 300 °C, and 500 °C, respectively. The damage level, 1.2 dpa, corresponds to a neutron exposure time of $8 \times 10^6 s$ (i.e., 3 months).

Both computational and experimental studies [115, 121] have suggested interstitial clusters exist in the form of two-dimensional loop in irradiated BCC metals. Hence their sizes are determined as:

$$d = 2r = 2 \times \left(\frac{nV_a}{\pi b} \right)^{1/2}, \quad (6-17)$$

where d is the diameter, r is the radius, V_a is the atomic volume of iron ($1.18 \times 10^{-2} \text{ nm}^3$), and b is the magnitude of the Burgers vector ($\vec{b} = \frac{a}{2} \langle 111 \rangle$, $|b| = 0.2482 \text{ nm}$, where a is the lattice constant of iron). The resolution limit in TEM experiments varies slightly with material conditions as well as TEM operating conditions (e.g., plane-view vs. 3D tomography), but is generally assumed to be in the range of 1.3 ~ 1.5 nm. Note that in iron a 1.3 nm diameter corresponds to I_{28} . In this chapter, we define the diameter of visible interstitial clusters to be greater than 1.3 nm.

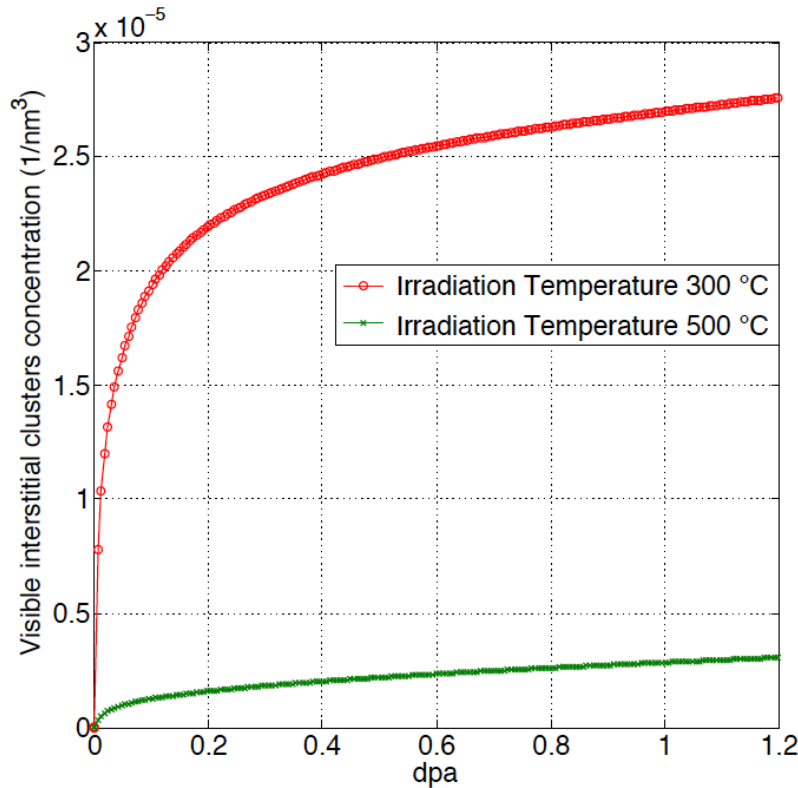


Figure 6-2. Visible interstitial clusters (with diameters greater than 1.3 nm) concentrations during the neutron irradiation process.

Fig. 6-2 shows the evolution of the volumetric density of visible interstitial clusters during the neutron irradiation at irradiation temperatures of 300 °C versus 500 °C. The cluster concentration levels are higher for the lower irradiation temperature, as expected. It is clear that the visible interstitial cluster density exhibits a trend toward saturation, where the generation and annihilation of clusters starts to build a dynamic equilibrium, which takes shorter time for the neutron irradiation at a higher temperature.

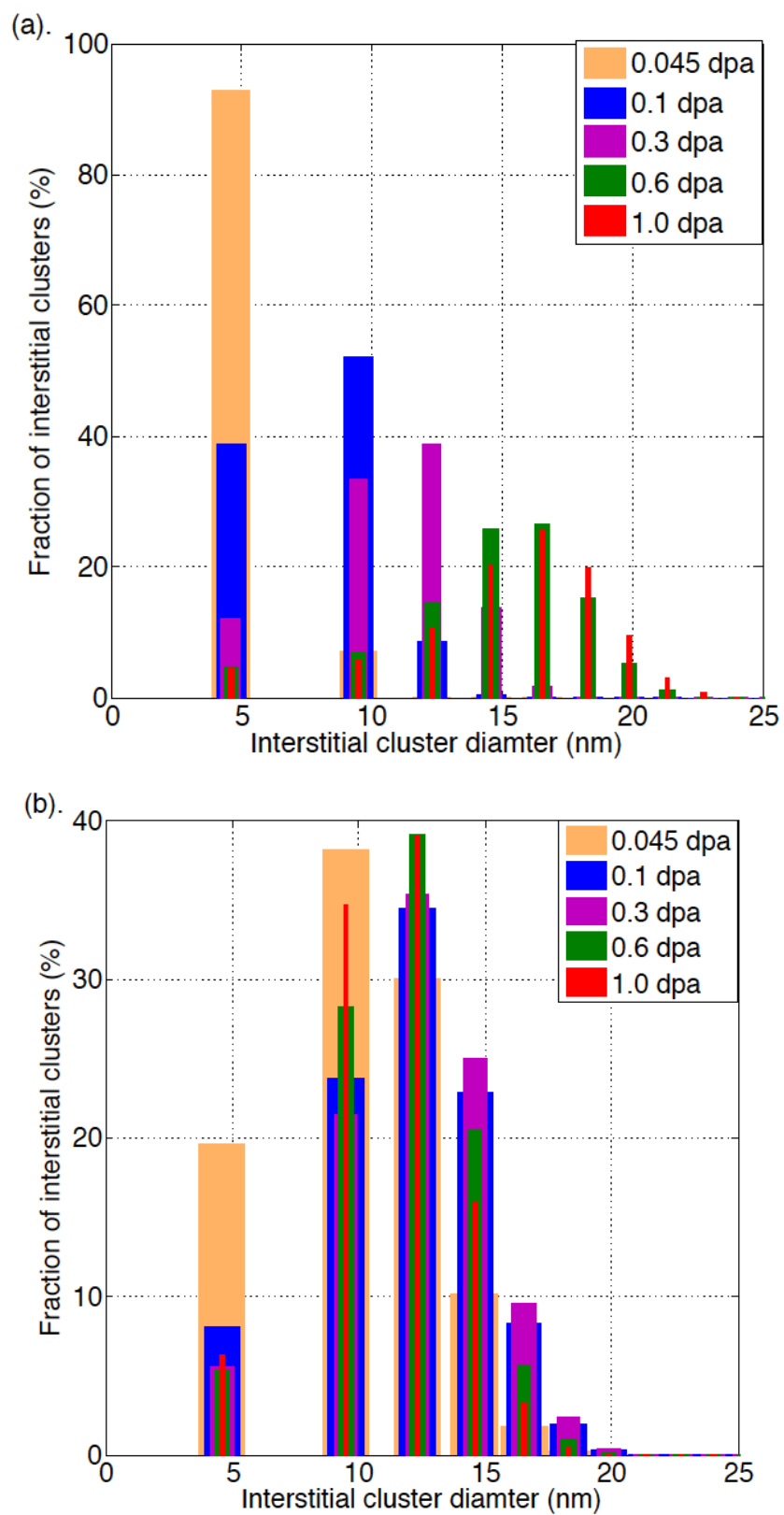


Figure 6-3. Model predictions of the evolution of interstitial cluster size distribution in iron exposed to neutron irradiation in HFIR at (a) 300 °C and (b) 500 °C.

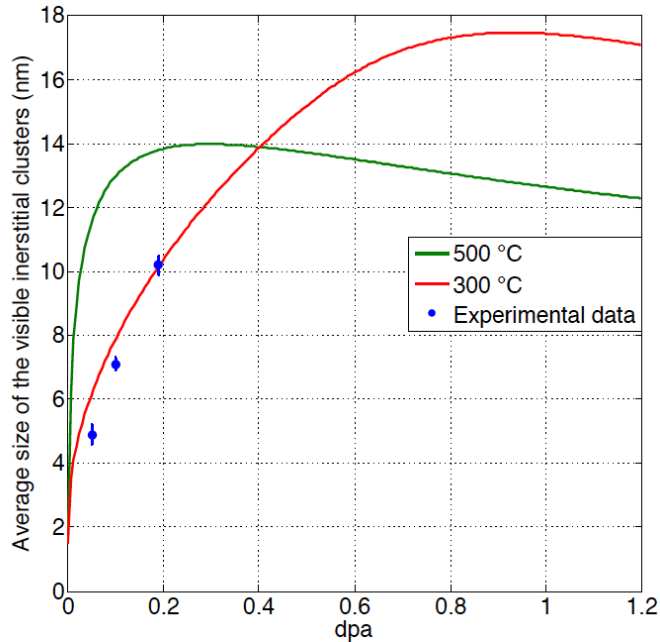


Figure 6-4. The average size of the visible interstitial clusters as a function of irradiation damage. The experimental data are from Ref. [152].

Fig. 6-3 shows the model predictions of the visible interstitial cluster evolution in iron exposed to neutron irradiation in HFIR at two different temperatures. In order to analyze the cluster distribution, all of the clusters are classified into ten groups based on their sizes, listed in Table 6-6.

Table 6-6. Groups of the visible interstitial clusters.

Group	1	2	3	4	5	6	7	8	9	10
Diameter (nm)	1.3~8.0	8.0~11.0	11.0~13.5	13.5~15.6	15.6~17.5	17.5~19.1	19.1~20.6	20.6~22.0	22.0~23.4	>23.4

For the irradiation at 300 °C, it is obvious that the clusters shift to larger sizes with increasing irradiation dose. When the irradiation damage is less than 0.1 dpa, most visible clusters have sizes less than 11.0 nm. The majority of the visible clusters are in the range of 13.5 nm to 20.6 nm when the irradiation dose is 1.0 dpa. For the irradiation at 500 °C, the clusters have a larger diameter when the damage level is less than 0.3 dpa. However, the average size of the visible clusters actually is predicted to decrease with the damage level for doses above 0.3 dpa, as shown in Fig. 6-4, which plots the average size of the visible interstitial clusters at 300 °C versus 500 °C. The maximum average size is reached at lower damage level when the irradiation temperature is higher because of the increased mobility of the clusters, and more vacancy absorption at loops driven by the higher vacancy mobility at 500 °C.

Neutron irradiated iron has been extensively studied in the literature [152, 153], however, the previous experimental studies of neutron irradiated high purity iron [152] are limited to a lower radiation damage level of less than 0.19 dpa. Here, we conduct a partial comparison with the modeling results by using the available data from Ref. [152], as shown in Fig. 6-4. The three known data points agree well with the model predictions. However, the overall modeling predictions cannot be validated due to the lack of experimental data, and thus we conclude that more experimental analysis are necessary for the neutron irradiated iron samples at higher damage levels. Note that the concentrations of visible clusters are predicted to increase, although the average sizes decreasing after reaching the maximum size at 500 °C, due to the continued nucleation of loop embryo in displacement cascades.

6.3 Thermal helium desorption

Neutron irradiation is the source for pre-existing defect clusters in iron. By comparing the THDS results for samples that are helium implanted with and without neutron irradiation, the influence of pre-existing defect clusters on helium behavior can be evaluated. In addition, a detailed analysis of the He-vacancy cluster evolutions in the model will demonstrate how these populations vary. In this part of the dissertation, samples pre-neutron irradiated at 300 °C are taken as an example to model He implantation and THDS.

In order to simulate the helium desorption spectrum, the model introduced in Chapter 3 is employed, including two stages, helium implantation and helium desorption. The final state of the neutron irradiation at 300 °C obtained in Section 6.2 is used as the initial condition for this simulation. The THDS results for the samples implanted with 10 keV He ions to fluences $1 \times 10^{18} / m^2$ and $1 \times 10^{19} / m^2$ are used here to be predicted by the hybrid model and compared with the previous modeling results that do not include pre-existing (neutron-induced) defect clusters.

6.3.1 THDS of He implanted samples at lower fluence ($1 \times 10^{18} / m^2$)

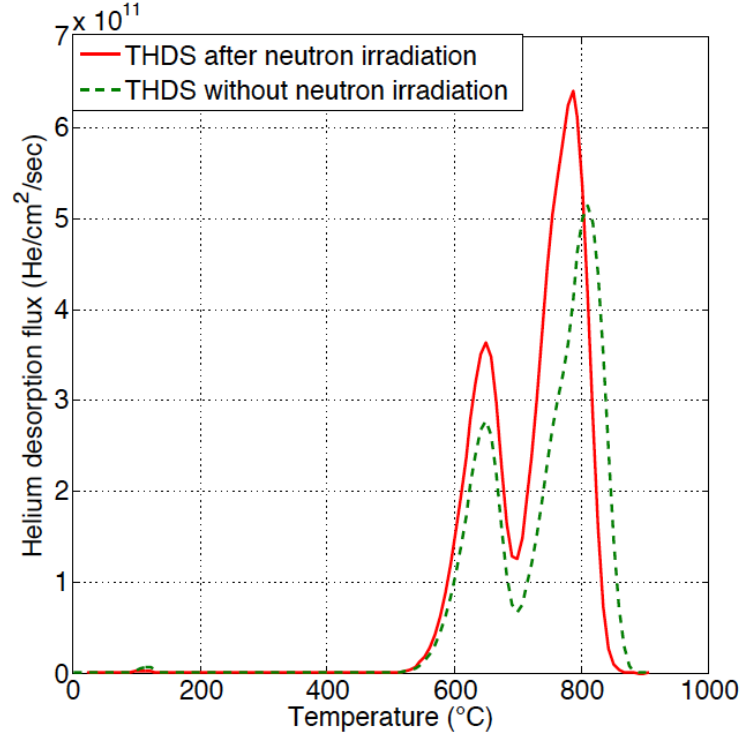


Figure 6-5. Modeling predictions comparing the influence of pre-existing defect microstructures induced by neutron irradiation at 300 °C and 1.2 dpa on the THDS for the samples implanted with 10 keV He to a fluence of 10^{18} He/m².

Fig. 6-5 compares two modeling predictions of THDS spectra, one for He implantation after neutron irradiation and the previous results without considering pre-existing defect microstructures, during a linear temperature ramp of 1 °C /s. Both modeling predictions indicate multiple He desorption groups. The positions of the first two He releasing peaks are similar while the third one differs for these two conditions. The maximum He release peak for the simulation including pre-existing defect clusters shifts to lower temperature. The other obvious feature from this simulation is that the total quantity of desorbed helium in BCC iron is greater with pre-existing damage than the old simulation excluding neutron irradiation.

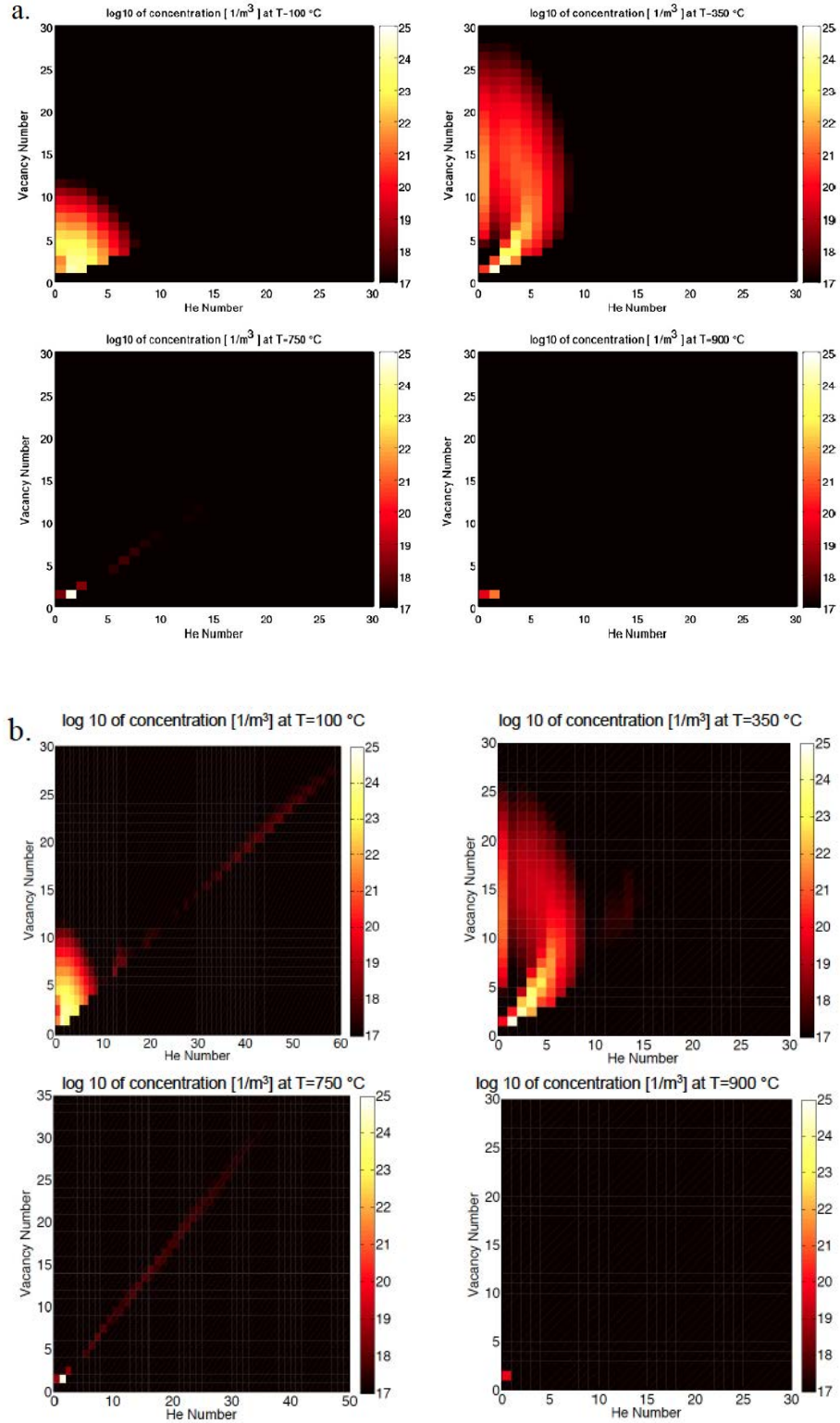


Figure 6-6. He-vacancy cluster phase space snapshots showing the cluster distribution evolution during the thermal annealing (at 1 °C/s heating rate) at a depth of 37 nm for the specimen implanted with 10 keV He to a fluence of 10^{18} He/m² for two different cases: (a) previous results without neutron irradiation; (b) new modeling including neutron irradiation.

Analysis of the He-vacancy cluster evolution reveals more details of the interactions between helium and point defects. As shown in Fig. 6-6 for the lower fluence implantation: at 100 °C, for both cases, most of the He-vacancy clusters are rather small, containing less than 10 He and less 10 V, and the composition distribution is rather diffuse in both He and V phase space. A very significant discrepancy between Fig. 6-6 (a) and (b) at 100 °C is that larger He-vacancy clusters (up to 60 He and 30 vacancies) are formed at this stage following a path with a He/vacancy ratio of 2.0 for the simulation including neutron irradiation. Due to the pre-existing vacancy clusters, more implanted helium atoms combine with vacancy and vacancy clusters compared to the simulation without neutron irradiation. The clusters with He/V ratio greater than 2.0 are essentially not formed because their binding energies with He are either very small positive or even negative within the thermodynamic model of binding energies [71, 72]. At 350 °C, the two figures show very similar behavior while the simulation with pre-existing defects predicts an isolated region with 10~15 He and 10~16 V which survives the dissociation of the larger clusters driven thermodynamically. When the temperature is 750 °C, the new simulation with pre-existing damage produces an extended grow path with a He/V ratio of 1.0 up to 35 He and 35 V, which is not observed without neutron irradiation. This is consistent with Fig. 6-5, which indicates more helium is released at higher temperatures. However, extensive shrinkage of the clusters is predicted to occur when the temperature increases from 750 °C to 900 °C. Eventually, only HeV and V are retained in the BCC temperature region in Fig. 6-6 (a), however, Fig. 6-6 (b) suggests that HeV cluster has dissociated to contribute the increase of desorbed helium in Fig. 6-5. From this comparison, it is clear that the pre-existence of the defect clusters does change the He-vacancy cluster evolution at lower implanted He fluence.

6.3.2 THDS of He implanted samples at higher fluence ($1 \times 10^{19} / m^2$)

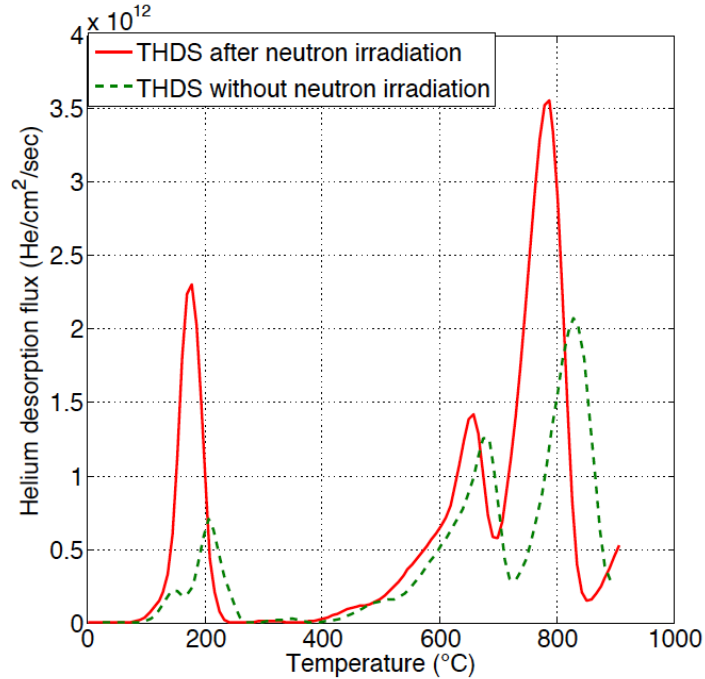


Figure 6-7. Modeling predictions including and excluding neutron irradiation of the THDS for the samples implanted with 10 keV He to a fluence of 10^{19} He/m^2 .

At higher fluence of implanted He, the modeling predictions for these two conditions predict significantly different observations. Overall, the new simulation coupled with neutron irradiation predicts more helium desorption and each of the three helium release peaks shift to relatively lower temperatures, which is consistent with the lower implanted He fluence. Interestingly, a big helium desorption peak shows up at 190 °C. Both of the two new simulations shown in Fig. 6-5 and 6-7 indicate that less helium will be retained in FCC temperature regime following pre-neutron irradiation and this will be investigated by the future experiments.

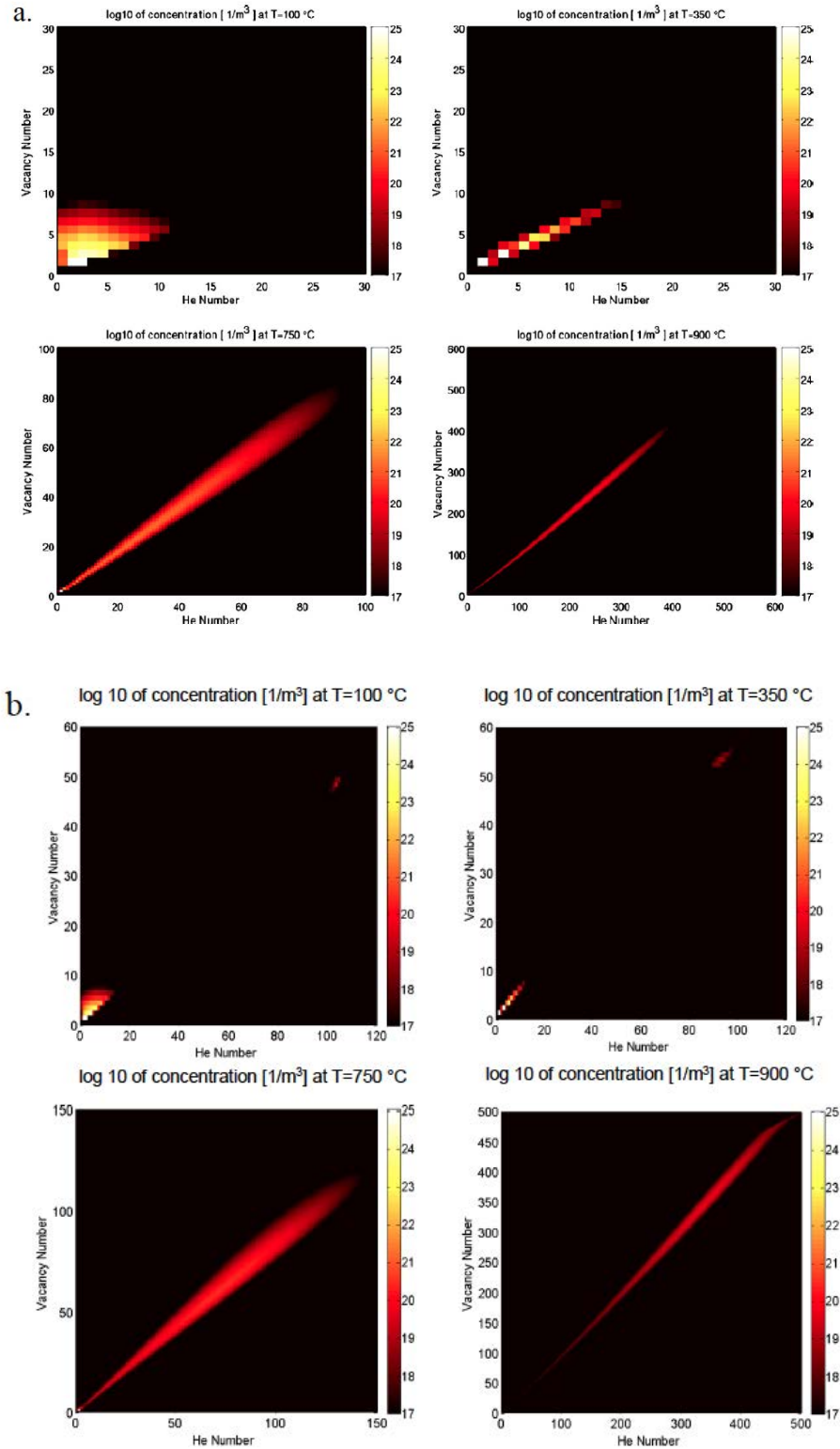


Figure 6-8. He-vacancy cluster phase space snapshots showing the cluster distribution evolution during the thermal annealing (at $1\text{ }^{\circ}\text{C/s}$ heating rate) at a depth of 37 nm for the specimen implanted with 10 keV He to a fluence of 10^{19} He/m^2 for two different cases: (a) previous results without neutron irradiation; (b) new modeling including neutron irradiation.

The evolution of He-vacancy clusters are shown in Fig. 6-8 for the simulations with and without neutron irradiation at the higher level of implanted He fluence. If the defect clusters induced by neutron irradiation are introduced, the evolution develops in a slightly different way. During the 10 keV He implantation, the pre-existing vacancy clusters experience thermal dissociation and reaction with helium atoms. After the implantation and room temperature relaxation at 100 °C, the implanted helium atoms exist not only in the small cluster region (less than 15 He and 10 V), but also in a small zone with clusters of larger sizes. This indicates that more helium atoms are captured because of the existence of large vacancy clusters, compared to the case without considering neutron irradiation. From 100 °C to 350 °C, the He-vacancy cluster evolution shows a similar behavior in the small size region for both cases, as shown in Fig. 6-8 (a) and (b), while the isolated island at larger size region grows slightly, following a growth path of He/V ratio of 1.6. Starting from 500 °C (not shown in Fig. 6-8), the clusters enter a fast growth stage based on two source points, the small cluster region and the isolated region (100~110 He and 55~60 V). At 750 °C, the two growth paths overlap and continue to grow together. Comparing Fig. 6-8 (a) and (b), the He-vacancy clusters are in a larger region (up to 150 He and 120 V) at 750 °C for the simulation with neutron irradiation. Eventually, the clusters grow to very large sizes of $\text{He}_{500}\text{V}_{500}$ at the end of BCC temperature regime along a growth path of He/V ratio of 1.0, where a significant quantity of He atoms are still retained in the He-V clusters that will be desorbed in the FCC temperature region.

6.4 Conclusion

The preliminary simulations of neutron irradiation and the subsequent THDS are discussed in this chapter. A simple picture of how the pre-existing defect clusters affect the helium behavior in iron is shown by comparing to simulations without considering neutron irradiation. Since the results are a bit counter-intuitive in suggesting more He release during THDS measurements of 300 °C neutron pre-irradiated specimens, it must be emphasized that it is necessary to validate these modeling results by comparison with experiments that will be performed in the future.

Chapter 7

Kinetics of Hydrogen Desorption from Zirconium Hydride and Zr Metal in Vacuum

Zirconium hydride is a major concern in the nuclear material community, and in particular, hydrogen behavior during vacuum annealing of used nuclear fuel and other dehydrating processes is an area of significant renaissance interest. In this chapter, the hydrogen desorption behavior from zirconium hydride and Zr metal in vacuum is studied by coordinated experimental and modeling techniques. The production and verification of the desired δ -zirconium hydride is introduced, while Thermal Desorption Spectroscopy (TDS) is used to directly obtain the hydrogen desorption spectra. In addition, a one-dimensional, two-phase moving boundary model coupled with a kinetic description of hydrogen desorption from a two-phase region of δ -ZrH_{1.6±n} and α -Zr is developed to reproduce the TDS experimental results.

7.1 Synthesis of Zirconium Hydride

7.1.1 Hydriding system

The desired material stoichiometry for kinetics analysis is δ -zirconium hydride, which can be used for hydride fuel due to its good neutron economics and mechanical properties, and was synthesized in this study. Manufacturing procedures of massive, crack-free hydrides in industry are well established [154-158]. The basic idea for manufacturing zirconium hydride is the following: place pure zirconium in an oxygen-free environment, increase the temperature to the desired value and control the amount of hydrogen introduced to the system.

A closed system used to produce δ phase zirconium hydride has been built at Oak Ridge National Laboratory, as shown in Fig. 7-1. The system consists of a tube furnace, a high purity hydrogen generator, a vacuum system, an Ar cylinder, control system, and a processing tube. The tube of the furnace is 4.5" in diameter, 72" in length, with a 53" long three-zone working region, which enables the system to produce zirconium hydride in large dimensions (i.e. long zircaloy cladding). A 316 Stainless Steel tube is placed in the furnace as the sample chamber. Hydrogen with a purity of 99.9995% was supplied by the VWR hydrogen generator with a maximum gas flow rate and pressure range of 300 cc/min and 965 torr to 5908 torr, respectively.

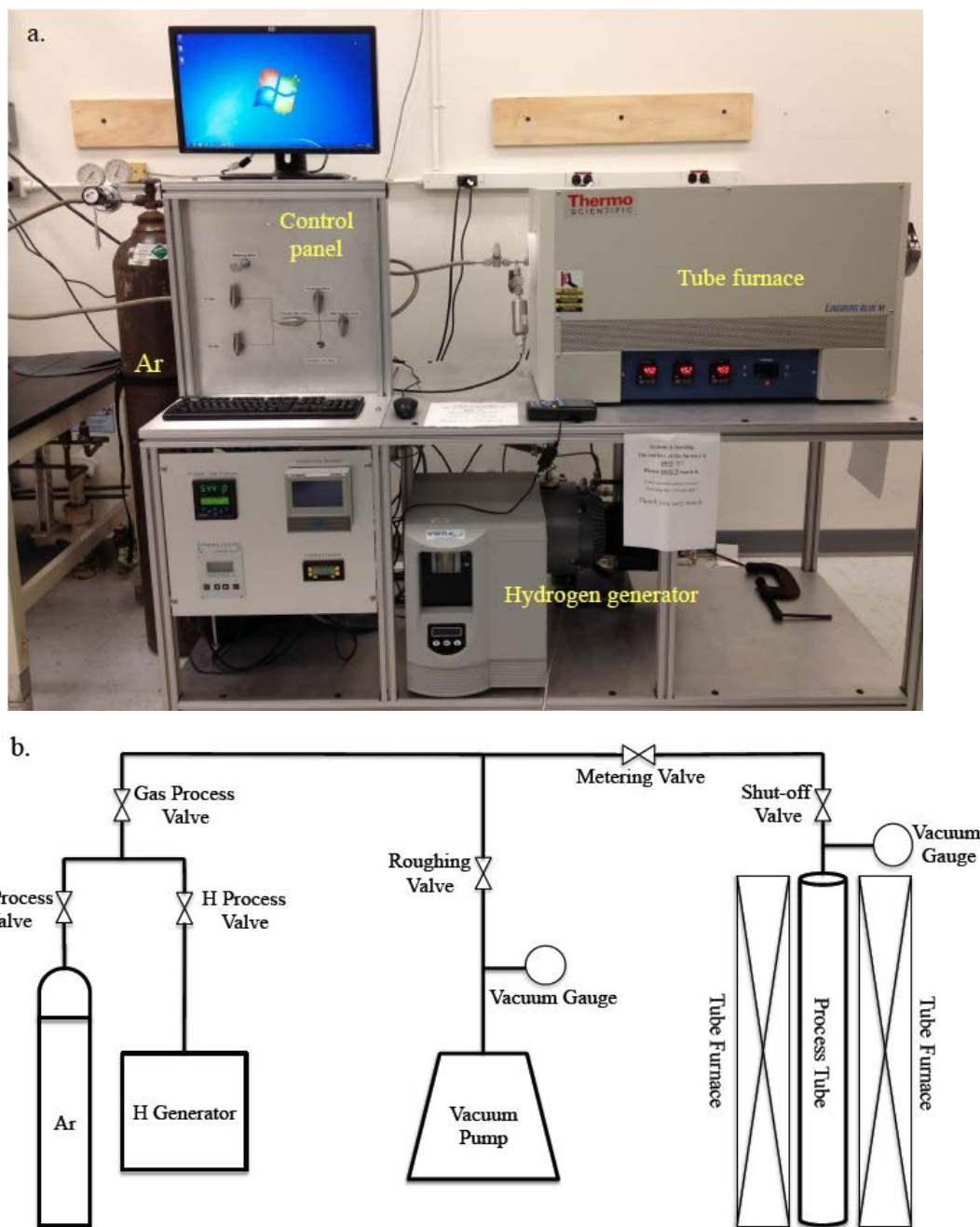


Figure 7-1. (a) Picture of the hydriding system; (b) Schematic illustration of the hydriding system.

7.1.2 Experimental procedure

The main challenges associated with the zirconium hydride production are stoichiometry control, cracking avoidance and synthesis speed. Temperature, time and initial amount of hydrogen are the most important factors in determining the quality of the resulting zirconium hydride. The binary Zr-H phase diagram is the major reference for this experiment, and is shown in Fig. 7-2. High temperatures prevent cracking through stress

relaxation (large thermal creep rate) and allow longer time periods in single-phase (β phase) hydriding. Meanwhile, high temperature also enhances hydrogen diffusion to accelerate the synthesis process. But if the temperature is too high and hydrogen uptake is too fast, this can lead to cracking. The fine control of temperature ramp rate can also help avoid cracking. The length of time and the amount of hydrogen required to reach the desired H/Zr ratio should be predicted before the synthesis starts. This value can be estimated based on the time for hydrogen to diffuse throughout the whole sample. Note that the length of the hydrogen diffusion path is the half-thickness of the specimen ($l/2$). Given the hydrogen diffusion coefficient reported by Majer et al. [159], the characteristic diffusion time, shown in Fig. 7-3, can be estimated by calculating l^2/D . The desired H/Zr ratio, the specimen weight and the volume of the system allow calculation of the required hydrogen quantity, represented in the form of the system pressure. The hydrogen input to the system is usually higher than the calculated value, considering the permeability of hydrogen in stainless steel (SS). The leakage rate of hydrogen from the vessel can be written in terms of parameters shown in Eq. (7-1), where ϕ_0 and H_ϕ are the pre-exponential and activation energy of the permeation process, respectively. δ is the thickness of the vessel wall. Permeation of hydrogen through stainless steel has been extensively studied [160] and the activation energy is reported as 60 kJ mol⁻¹. The pre-exponential term and activation energy were determined as 1.1×10^{-4} mol H₂ m⁻¹s⁻¹MPa^{-1/2} and 53 kJ mol⁻¹, respectively [90].

$$R_{leak} = \phi_0 \frac{1}{\delta} \sqrt{p} \exp\left(-\frac{H_\phi}{RT}\right). \quad (7-1)$$

The hydrogen permeation rate is expressed by the pressure drop rate through a simple calculation for the hydriding system, shown in Fig. 7-4.

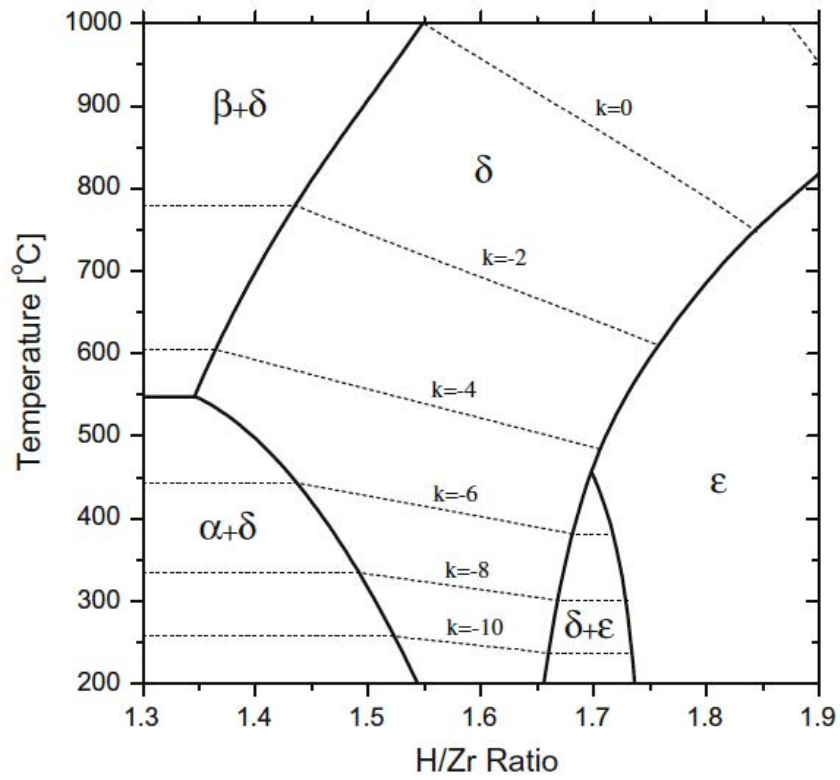


Figure 7-2. Phase diagram for Zr-H system [161] with equilibrium H_2 isobars labeled as $P_{H_2} = 10^k (MPa)$.

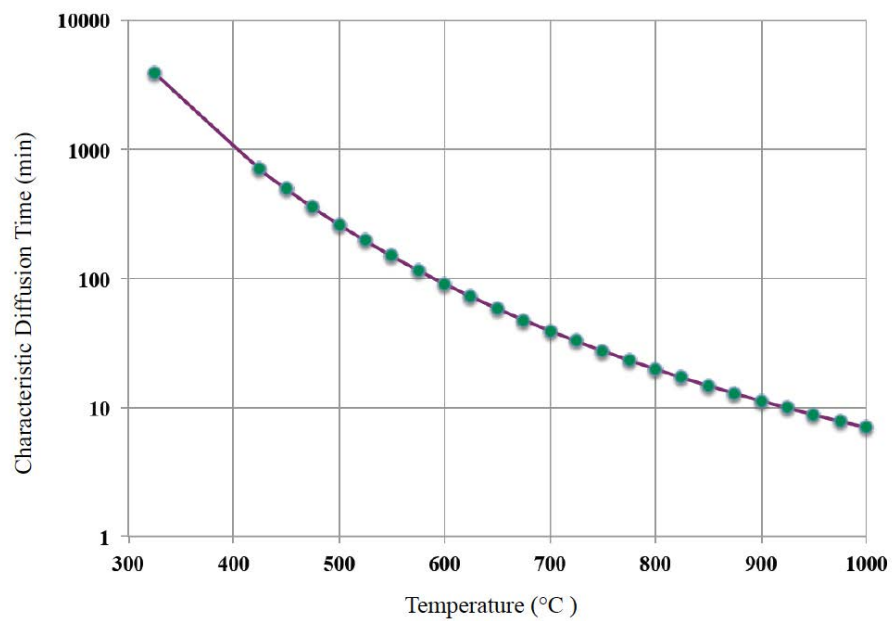


Figure 7-3. Characteristic diffusion times as a function of temperature for a specimen with a thickness of 1 mm.

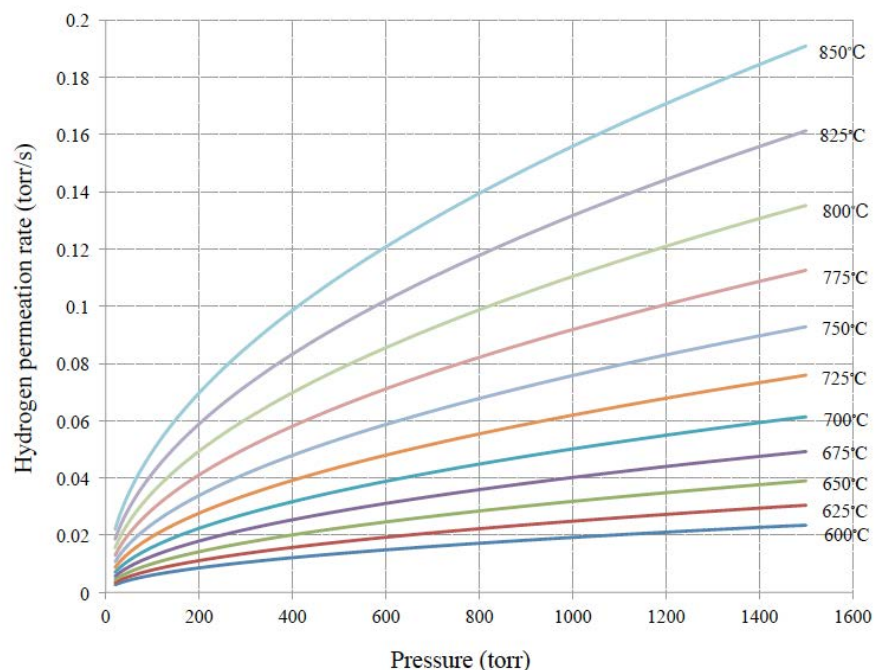


Figure 7-4. Hydrogen permeation rate as a function of system pressure under different temperature conditions.

Small zircaloy-4 discs (0.8~1.2 mm in thickness, 12.7 mm in diameter) were cut from a zircaloy-4 rod using a low speed diamond saw. The samples were initially cleaned by mechanical polishing and alcohol rinse using an ultrasonic cleaner. After measuring the dimensions and weight, the samples were placed in a quartz boat and inserted into the processing tube. In order to acquire an oxygen-free environment, multiple high-purity Ar purges are applied to the system. Before introducing hydrogen to the system, the hydrogen generator requires purging for at least 15 minutes to get rid of the remaining gas in the connection hoses. Following this step, the hydrogen, whose flow rate is controlled by a metering valve, is introduced to the processing tube until the pressure of the system reaches the pre-calculated value. The tube furnace is turned on to heat the system to the predetermined temperature profile. By using this system, the hydriding process is static that helps to reduce the influence of hydrogen temperature gradient. This is a very different procedure from previous studies that apply dynamic processing (e.g., with temperature gradient) [90, 93, 94], where hydrogen was supplied continuously whenever the pressure was lower than the equilibrium value at a given temperature. However, the amount of hydrogen introduced is hard to determine and a microbalance is usually mounted in the system to provide weight change information, which makes the system more complicated.

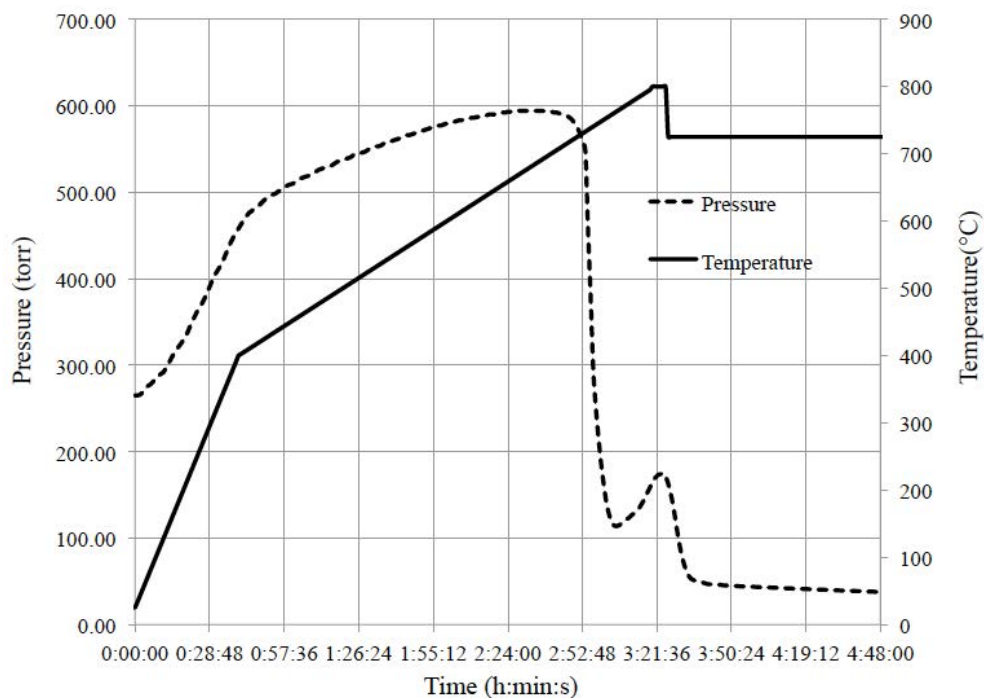
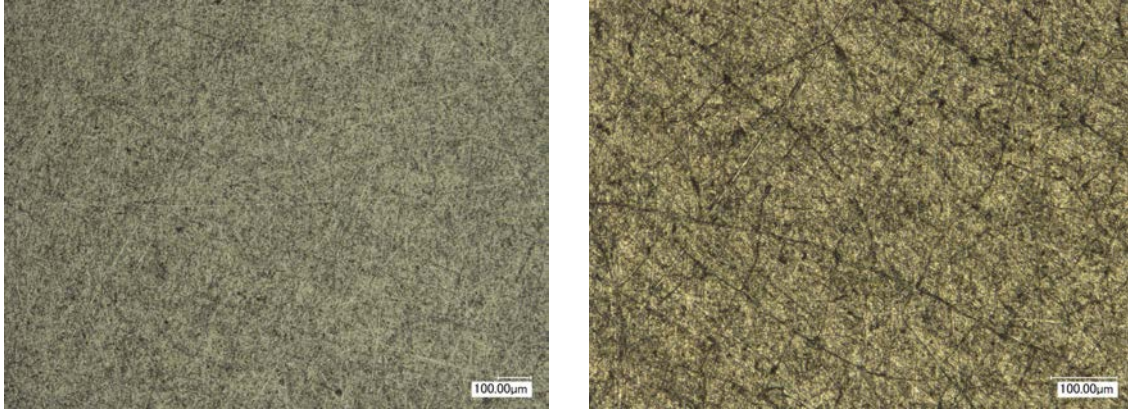


Figure 7-5. Temperature profile and hydrogen pressure during a typical hydriding process.

The other factor to be emphasized here is the predetermined temperature profile. A typical temperature profile along with the hydrogen pressure change during processing is shown in Fig. 7-5. The samples are heated up to 400 °C at a relatively fast ramp rate of 10°C/min, in the hydrogen atmosphere, while the pressure also increases linearly. Since the adsorption rate and diffusivity of hydrogen in this low temperature region are small, the ramp rate can be large to decrease the experiment duration. Beyond this region (400 °C~800 °C), the ramp rate should be slower, about 2.6 °C/min, to reduce the probability of cracking. When the temperature exceeds 600 °C, the intercalation of hydrogen into zirconium becomes more and more intensive. The pressure change results from a competition process of hydrogen absorption, hydrogen leakage and temperature increasing. Finally, the pressure reaches equilibrium at 700 °C. Then hydrogen uptake of the metal becomes dominant and a significant pressure drop occurs. The hydrogen level in the system is lower and insufficient to support further hydriding at higher temperature. The small peak starting at 760 °C indicates that the pressure in the system is lower than the equilibrium value and hydrogen desorption from the samples dominates. Given the fact that the equilibrium phase diagram of hydrogen and zirconium is well established [161], the temperature should be decreased to ensure sufficient hydrogen supply. Then a constant temperature region will allow the absorbed hydrogen to diffuse sufficiently throughout the whole disc, which flattens the hydrogen concentration profile toward a uniform distribution. The experiment time is determined by a rough diffusion calculation, shown in Fig. 7-3. A very conservative value is usually applied to guarantee that the hydrogen concentration is uniform under a hydrogen atmosphere, which is higher than the equilibrium pressure.



a. Before Hydriding

b. Post Hydriding

Figure 7-6. Surface view of ZrHTGA-2 (a) before and (b) after hydriding.

7.1.3 Characterization of the produced zirconium hydride

The surface of the sample ZrHTGA-2 after removal from the processing tube shows a dark yellow color and tiny cracks. A comparison of the pre- and post-hydriding surfaces is shown in Fig. 7-6. Zirconium is very sensitive to oxygen and nitrogen, thus when the samples are heated up to a higher temperature, oxidation and nitridation occur. A very thin impurity layer is formed on the surface, as shown in Fig.7-6b. Cracks are induced by the expansion of samples due to the absorption of hydrogen. Note that the cracking only exists in the thin impurity layer, which can be easily removed by abrasive polishing.

The H/Zr ratio is commonly used as the index to assess the quality of the synthesized zirconium hydride, and also helps to identify the phase region of the products. In order to obtain an accurate hydrogen concentration, three different analysis methods have been used. First, the H/Zr ratio can be roughly calculated by the weight change while hydrogen absorption is assumed to be the only cause of mass change. Second, X-ray diffractometry (XRD) is used to identify the phases of the products and to derive the H/Zr based on Eq. (7-2), reported by Yamanaka et al. [162].

$$a = 0.4706 + 0.004382 \times C_H \quad (7-2)$$

The third method is gas extraction, which is straightforward and can provide a direct measure of hydrogen content.

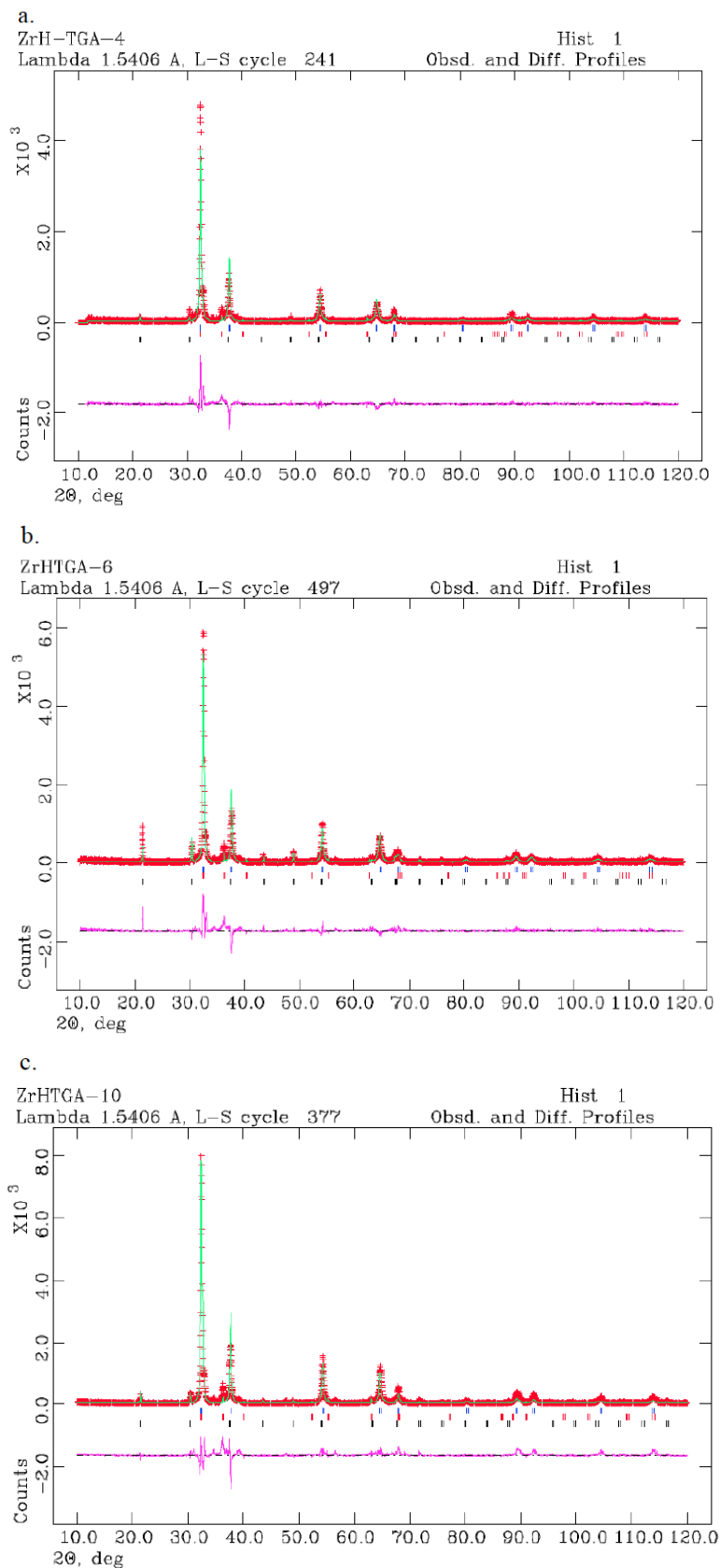


Figure 7-7. Powder X-ray diffraction patterns for (a) ZrHTGA-4, (b) ZrHTGA-6, and ZrHTGA-10.

XRD samples were prepared by depositing zirconium hydride powder on a low background silicon single-crystal sample holder using a slurry of powder and ethanol. Samples were also mixed with lanthanum hexaboride (LaB₆) powder, used as an internal standard during pattern refinement. High-resolution diffraction patterns were obtained using a Phillips PNAlytical X'Pert Pro instrument with a Cu K α source. Rietveld refinement was performed on the experimental patterns for the three samples shown in Fig 7-7. Detailed results are presented in Table 7-1. The lattice parameters of δ -ZrH_{1.6 \pm x} (Fm-3m) for the three samples are accurately determined as 4.7780 Å, 4.7761 Å, and 4.7772 Å, respectively, while the reference value is 4.7770 Å [163]. Thus, the synthesis of δ -zirconium hydride is confirmed.

Table 7-1. Lattice parameters of phases present in the samples determined through Rietveld refinement.

Parameters	ZrHTGA-4	ZrHTGA-6	ZrHTGA-10
LaB ₆ wt%	2.3	8.2	2.8
ZrH _x - Tetragonal			
wt%	1.6	5.1	1.5
a (Å)	3.4979	3.5021	3.4894
error	1	1	1
c (Å)	4.8124	4.4716	4.4959
error	2	2	2
ZrH _x -Cubic			
wt%	96.1	86.7	95.7
a (Å)	4.7780	4.7761	4.7772
error	1	2	2
χ^2	2.96	3.17	4.08

Table 7-2. H/Zr ratio calculated by different methods for the three samples.

Methods	Parameters	ZrHTGA-4	ZrHTGA-6	ZrHTGA-10
Weight change	Pre-weight (g)	0.95239	0.72968	0.63132
	Post-weight (g)	0.96906	0.74239	0.64253
	H/Zr ratio	1.60	1.59	1.62
XRD	Lattice parameter (Å)	4.7780(1)	4.7761(2)	4.7772(2)
	H/Zr ratio	1.64	1.60	1.62
Gas extraction	H (wt ppm)	15878	15746	15464
	H/Zr ratio	1.460	1.448	1.421

The analysis results of the three different methods of measuring hydrogen content are shown in Table 7-2. H/Zr ratios predicted by XRD and weight change are similar, while the gas extraction provides much lower values. However, while this is a direct measurement, the results of gas extraction are not as reliable when the gas content exceeds 10000 ppm due to the saturation of the detecting capability. Considering the existence of impurities and the measurement errors of the weight change method, the H/Zr ratio extracted from XRD will be used throughout the following analysis.

7.2 Thermal desorption spectrometry (TDS)

In the previous studies [93, 94], thermogravimetric experiments have been usually applied to obtain the weight information of δ -zirconium hydride under a given temperature profile. Then the first derivative of the curve is used to calculate the weight change rate, which can be converted to a hydrogen flux. Moreover, the hydrogen gas pressure-buildup experiment [90] can also be used to study the dehydriding process.

TDS is employed in order to determine the kinetics of hydrogen desorption from zirconium hydride and Zr metal in vacuum. Partial hydrogen current is measured using the Berkeley ultrahigh vacuum thermal desorption system described in Chapter 2 as a function of time during a predetermined annealing history. The hydrogen current is then converted to an instantaneous desorption rate by multiplying by a proportionality coefficient determined by a simple calculation.

Due to the limitation of the crucible size, ZrHTGA-10 with a H/Zr ratio of 1.62 is cut to a square shape. Then the sample is cleaned by abrasive polishing to remove the impurity layer. The final sample has a surface area of 18 mm² and a thickness of 0.47 mm. As shown in Fig. 7-8, the temperature is increased to 525 °C with a 1 °C/s ramp rate and held for two hours. The choice of 525 °C is based on the consideration that the zirconium hydride should stay in the δ phase (550°C is the phase transformation point) and that the temperature should be high enough to provide a reasonable experiment time as a result of the enhancement in hydrogen diffusivity. The duration of the experiment can be evaluated by the characteristic diffusion time discussed above. Hydrogen will desorb from the sample continuously when the temperature is kept at 525°C. The loss of hydrogen will induce the phase change where α -Zr will form as hydrogen diffuses to the surface, which gradually dissolves the δ -zirconium hydride.

In the TDS experiment, the mass spectrometer provides the electric current of hydrogen ions directly. A calibration is required to convert this current to a hydrogen desorption rate. In this case, the integration of the hydrogen desorption spectrum over time is 0.0033 Coulombs. It is reasonable to assume that all desorbed gas from the zirconium hydride is hydrogen whose quantity can be calculated by the weight change (0.0007gram) of the sample pre- and post-dehydriding. Therefore, a conversion coefficient of 0.212 mol·H/(A·s) has been used to determine hydrogen flux. This involves dividing the desorption rate by the sample area to determine the hydrogen flux from the surface of the sample. Since the test runs under ultrahigh vacuum on the order

of 10^{-8} torr and the sample is thin (1/10 of the length), the measured hydrogen flux can be assumed to be the hydrogen desorption rate on the surface.

As shown in Fig. 7-8, the temperature control is good except an overshoot during the transition region from the ramp increase to the constant temperature region. No obvious hydrogen release is observed until the temperature is 372°C . In the temperature ramp stage, the hydrogen desorption rate increases with the temperature. When the temperature reaches the maximum value, the flux increases for additional 170 s. Then it drops to a slower rate. When the time is increased beyond 2820 s, the flux reduces dramatically which indicates that there is not enough excess hydrogen left in the sample. The diffusion of hydrogen to the surface will induce the phase transformation. However, insufficient information can be obtained from the experimental data. In the next section, a combination of one-dimensional two-phase moving interface model and experimental data will be used to provide a more explicit view of the phase transformation process.

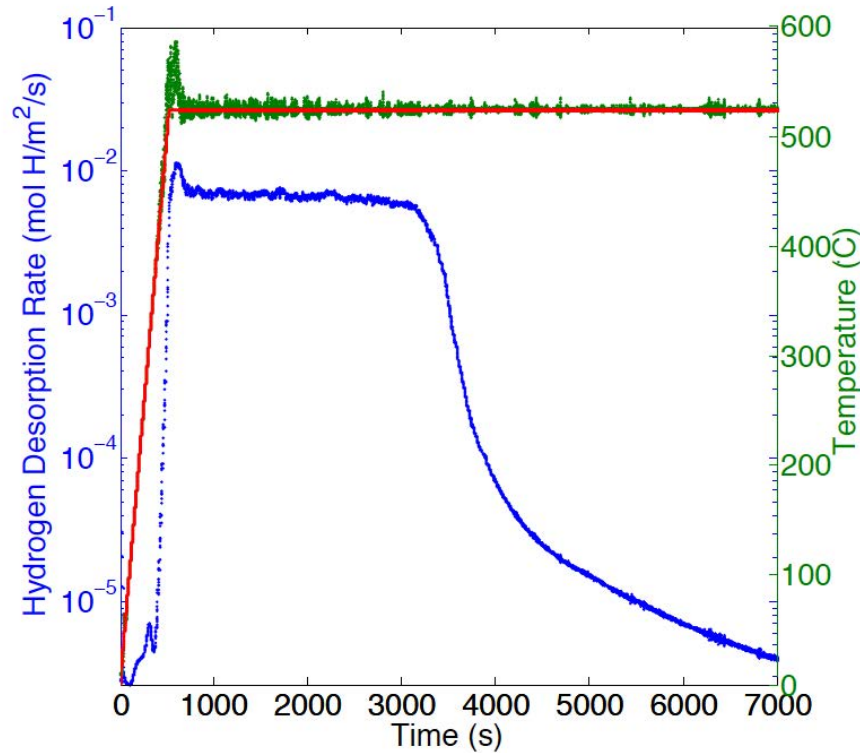


Figure 7-8. Hydrogen desorption spectrum and temperature profiles in TDS experiment of ZrHTGA-10.

7.3 A continuous hydrogen desorption model from zirconium hydride and subsequent metal in vacuum

For systems consisting of distinct compositional domains, a change of phase caused by diffusion often occurs [164]. Examples include growth and subsequent dissolution of a

second phase in a solid during a solutionizing heat treatment [165], growth of an intermediate layer in thermal barrier coatings [166], growth or/and shrinkage of the liquid phase in transient liquid-phase bonding [167, 168], and liquid phase sintering [169]. Problems of this sort are often called Stefan problems [164] and arise in numerous modeling situations throughout the science. What makes these problems difficult to solve is the presence of the moving boundary, at which the phase change occurs. A variety of numerical methods have been proposed to solve Stefan problems, and Crank [170] provides a good introduction to Stefan problems and presents an elaborate collection of numerical methods used for these problems.

One critical concern for a Stefan problem is that the boundary conditions of the system as well as the initial conditions must be stated to complete the expression. For example, zero-flux boundary conditions are most appropriate in the case of homogenization and the solution must satisfy mass conservation of the solute. However, most materials science scenarios are not conservative in the studied region, since the solute will diffuse to the boundaries, experience a surface reaction, and then desorb, especially when the solute is a gas species [95, 96]. Consequently, a surface gas flux of the solute will be observed. This is the case discussed in the present work. It is important to emphasize that the most suitable boundary and initial conditions of Stefan problems really depend on the nature of the situation to be modeled.

The other major consideration is how to verify the accuracy and applicability of the various numerical methods. In previous studies [164, 171, 172, 173, 174], both computational simulations and engineering experiments are employed to assess the precision of the developed numerical methods in a variety of systems. Similarly, in the current work, the model prediction is also validated by comparison to experimentally obtained data.

Here, an accurate, fully implicit, finite-difference model [172] is employed for the simulation of hydrogen desorption kinetics from δ zirconium hydride (δ -ZrH_{1.6±n}), which is a two-phase, moving boundary problem. The validity of the computed results is compared directly with hydrogen desorption experiments.

7.3.1 Problem description

The one-dimensional, two-phase, moving boundary problem can be described with reference to the schematic illustration shown in Figure 7-9(a), where the concentration of solute (C , in which the solute is hydrogen) varies with position (x). The location of the moving boundary $S(t)$ and the thickness of the sample (d) are also labeled.

It is routine to use Fick's laws to model the solute concentration evolution due to diffusion [175]. Expressions of this type have been the subject of much research and are well understood. However, the analysis is complicated by the fact that the diffusive processes occur simultaneously in two distinct phases. The two concentrations located on the interface are generally fixed by thermodynamic constraints and can be obtained from

the well-developed Zr-H phase diagram [88, 91] for different temperatures. The diffusion rate of hydrogen towards the two-phase interface from $\delta\text{-ZrH}_{1.6\pm n}$ is not necessarily equal to that of hydrogen from the interface to $\alpha\text{-Zr}$. Therefore, the interface must move to conserve hydrogen. The following differential equations are thus used to model the complete system:

$$\frac{\partial C(x,t)}{\partial t} = \frac{\partial}{\partial x} \left[(D_\delta(x,t) \frac{\partial C(x,t)}{\partial x}) \right] \quad 0 \leq x \leq S(t) \quad , \quad (7-3)$$

$$\frac{\partial C(x,t)}{\partial t} = \frac{\partial}{\partial x} \left[D_\alpha \frac{\partial C(x,t)}{\partial x} \right] \quad S(t) \leq x \leq d/2 \quad , \quad (7-4)$$

$$\frac{dS(t)}{dt} = \frac{1}{C_\delta - C_\alpha} \left(-D_\delta(x,t) \frac{\partial C(x,t)}{\partial x} \Big|_{x=S^-} + D_\alpha \frac{\partial C(x,t)}{\partial x} \Big|_{x=S^+} \right) \quad , \quad (7-5)$$

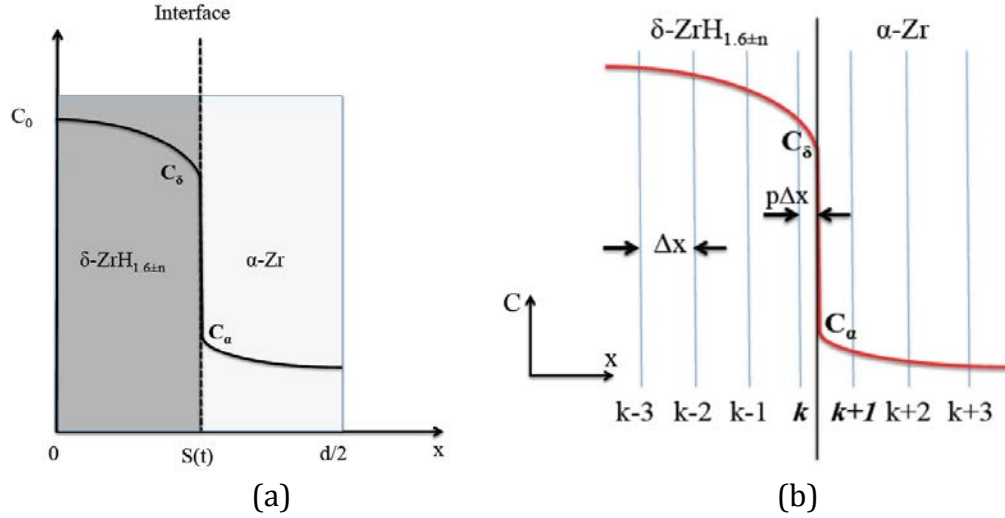


Figure 7-9. (a) Schematic illustration of the concentration profile at time t in the vicinity of the two-phase interface in planar geometry; (b) Numerical method employed to analyze movement of the interface.

where $C(x,t)$ is the H/Zr ratio at position x and time t . If one wishes to calculate the number density of hydrogen, the conversion can be gained simply by multiplying by the Zr number density in $\delta\text{-ZrH}_{1.6\pm n}$ or $\alpha\text{-Zr}$. As stated in [164], many of the situations in which Stefan problems are encountered typically involve isothermal conditions. It is therefore reasonable to assume that the diffusion coefficients are functions of composition only. D_α is the hydrogen diffusivity in the $\alpha\text{-Zr}$ phase, which is independent of hydrogen concentration. D_δ is the hydrogen diffusivity in $\delta\text{-ZrH}_{1.6\pm n}$, which is a function of H/Zr ratio and can be expressed as

$$D_{\delta}=7.29 \times 10^{-3} \left(1 - \frac{C}{2}\right) \exp\left(-\frac{58.8[\text{kJ mol}^{-1}]}{RT[\text{K}]}\right) \text{ cm}^2/\text{s} , \quad (7-6)$$

where R is the gas constant and T is temperature [177].

Equation (7-3) describes hydrogen diffusion in $\delta\text{-ZrH}_{1.6\pm n}$ left of the interface; Equation (7-4) refers to hydrogen diffusion in $\alpha\text{-Zr}$; Equation (7-5) indicates the moving boundary condition at the interface, and is derived by the local hydrogen conservation. Together, these equations form a coupled system of nonlinear differential equations.

7.3.2 Determination of initial and boundary conditions by applying the kinetics of hydrogen desorption from $\delta\text{-ZrH}_{1.6\pm n}$ and $\alpha\text{-Zr}$

As mentioned, the initial and boundary conditions are necessary to complete the problem. Before elaborating on these conditions, it is important to note that the $\delta\text{-ZrH}_{1.6\pm n}$ dehydriding process consists of two stages: hydrogen desorption from the pure $\delta\text{-ZrH}_{1.6\pm n}$ until the surface hydrogen concentration decreases to the lower equilibrium limit of the $\delta\text{-ZrH}_{1.6\pm n}$ phase region at which point $\alpha\text{-Zr}$ begins to form through precipitation, which then introduces a two-phase region, which is of course a moving boundary problem.

The first stage can be expressed using the same form of Equation (7-3), with the only difference that the spatial range spans the whole half thickness of the sample. Since a δ zirconium hydride disk with H/Zr ratio of 1.62 is the starting condition for the TDS experiment, the initial condition required to solve Equation (7-3) is

$$C(x,0)=1.62 \quad 0 \leq x \leq d/2 . \quad (7-7)$$

To solve Equation (7-3), two boundary conditions are also required. The hydrogen concentration profile throughout the sample thickness is symmetric, which means the hydrogen flux (J) at $x=0$ is zero, providing the first boundary condition (Neumann boundary condition), as

$$J(0,t) = -D_{\delta}(0,t) \left. \frac{dC(0,t)}{dx} \right|_{x=0} = 0 . \quad (7-8)$$

Note that hydrogen will desorb from the sample surface continuously during the annealing process in the experiment. Thus hydrogen flux at the surface can be used as the second boundary condition. The kinetics of hydrogen desorption from $\delta\text{-ZrH}_{1.6\pm n}$ have been studied recently. Terrani et al. [90] reported that there is no discernible hydrogen concentration dependence for the hydrogen desorption process and zeroth-order desorption kinetic was determined. The hydrogen desorption flux can be expressed as

$$J(d/2,t) = \exp\left(27.0 \pm 0.9 + \frac{-205 \pm 8 [\text{kJ mol}^{-1}]}{RT[\text{K}]}\right) \text{ mol H m}^{-2} \text{ s}^{-1} . \quad (7-9)$$

Equations (7-3), (7-7), (7-8), and (7-9) can now be combined to form a complete system and solved numerically. The results are shown in the following section after a brief description of the numerical method.

When the first stage is finished, α -Zr precipitates on the disk surface. Therefore, the process enters the two-phase moving boundary stage, as described at the beginning of this section. The final hydrogen distribution profile at the first stage will be used as the initial condition for the Stefan problem.

Equations (7-3) and (7-4) each require two boundary conditions. When the moving interface is located at a known position, as shown in Figure 7-9(a), it is straightforward to define the restrictions of Equation (7-3). At the position of the sample half thickness, a Neumann boundary condition is still appropriate. Since the two-phase interface implies that the boundary hydrogen concentration in δ phase reaches the equilibrium lower limit, this gives us the second boundary restriction, namely that

$$C(S(t)^-, t) = C_{\delta} \quad , \quad (7-10)$$

where C_{δ} is the temperature-dependent hydrogen equilibrium concentration lower limit in δ -ZrH_{1.6±n} phase. Similarly, the first boundary condition can be obtained for Equation (7-4),

$$C(S(t)^+, t) = C_{\alpha} \quad , \quad (7-11)$$

where C_{α} is the temperature-dependent hydrogen solubility limit in α -Zr phase. C_{δ} and C_{α} can be obtained from the well-studied phase diagram of the H-Zr binary system [88, 91].

The other boundary condition of Equation (7-4) can be obtained in the form of a hydrogen flux at the surface. However, zeroth-order kinetics is no longer suitable, since the hydrogen is desorbing from α -Zr rather than δ -ZrH_{1.6±n}. Hence, the kinetics of hydrogen desorption from α -Zr must be known.

Naito [96] and Ichimura et al. [95] investigated the kinetics of hydrogen desorption from α -Zr and concluded that the hydrogen desorption rate obeyed second-order kinetics with respect to the hydrogen concentration. Note that the rate-limiting step of this process is not the diffusion process but the second-order surface association reaction of hydrogen molecules diffusion from the bulk to the surface. The hydrogen desorption rate can thus be expressed as

$$R_{\text{des}} = 44.9 \exp\left(\frac{-2\epsilon}{RT}\right) (C(d/2, t))^2 \quad \text{mol H m}^{-2} \text{ s}^{-1} \quad , \quad (7-12)$$

where ϵ is the activation energy of desorption determined to be $56.8 \pm 1.8 \text{ kJ mol}^{-1}$ by fitting the experimental data. Now all of the required restriction conditions are ready and the Stefan problem can be solved.

7.3.3 Numerical analysis

The simplest method [178, 179] to solve the problem consists of discretizing space with a fixed mesh and imposing the requirement that the modeled position of the interface coincides with a mesh point. This constrains the motion of the interface to move in a step-wise manner and also reduces the accuracy. By including the interface position as a continuous variable in the model and solving a finite-difference form of Equation (7-5) to predict its motion, it is possible to overcome this problem [172, 180].

The space domain is divided into $N-1$ equally spaced intervals of length Δx , namely, $x_j = (j-1)\Delta x$, $j=1,2,3,\dots,N$, where j represents a given mesh point. The interface lies between the nodes $j = k$ and $k+1$, and $p = [S(t) - (k-1)\Delta x] / \Delta x$, where $0 \leq p \leq 1$ and $k=1,2,3,\dots$ as described in Figure 7-9(b).

The first step is to discretize the equations utilizing the Crank-Nicolson scheme [181], in which time is discretized with the trapezoid rule and space with central difference. Here, Equation (7-3) is taken as an example to show the discretization form,

$$\begin{aligned} & \frac{1}{\Delta t} (C_i^{j+1} - C_i^j) \\ &= \frac{1}{2\Delta x} \left[D_{i+\frac{1}{2}}^{j+1} \left(\frac{\partial C}{\partial x} \right)_{i+\frac{1}{2}}^{j+1} - D_{i-\frac{1}{2}}^{j+1} \left(\frac{\partial C}{\partial x} \right)_{i-\frac{1}{2}}^{j+1} + D_{i+\frac{1}{2}}^j \left(\frac{\partial C}{\partial x} \right)_{i+\frac{1}{2}}^j - D_{i-\frac{1}{2}}^j \left(\frac{\partial C}{\partial x} \right)_{i-\frac{1}{2}}^j \right], \quad (7-13) \end{aligned}$$

where i and j indicate the spatial node and time step, respectively.

The discretized form for the nodes k and $k+1$, between which the moving interface is located, is complicated by the existence of the interface. Crank [170] gives linear expressions for the approximation of the 2nd differential terms near the moving interface by interpolation:

$$(\partial^2 C)_k = 2 \left(\frac{C_{k-1}}{1+p} - \frac{C_k}{p} + \frac{C_{k+1}}{p(1+p)} \right), \quad (7-14)$$

$$(\partial^2 C)_{k+1} = 2 \left(\frac{C_k}{(1-p)(2-p)} - \frac{C_{k+1}}{1-p} + \frac{C_{k+2}}{2-p} \right). \quad (7-15)$$

However, Equations (7-14) and (7-15) have singularities at $p=0$ in Equation (7-14) and $p=1$ in Equation (7-15). Introducing a quadratic expression for the concentration profile near the interface, in an attempt to better estimate the fluxes and thus improve the accuracy of the method, can overcome this problem [172].

At every computing step, the newly generated concentration profile is used to determine the new location of the moving interface by solving Equation (7-5). Here, the modified

Euler method (implicit scheme) is applied [172]. Let Equation (7-5) be equal to $f[S(t), t]$, and the computing scheme is:

$$S^0(t+\Delta t) = S(t) + \Delta t f[S(t), t] \quad , \quad (7-16)$$

$$S^{m+1}(t+\Delta t) = S(t) + (\Delta t/2) \{f[S(t), t] + f[S^m(t+\Delta t), t+\Delta t]\} \quad , \quad (7-17)$$

where $m=0, 1, 2, \dots$, and the iteration at each time step is performed until

$$\left| \frac{S^{m+1}(t+\Delta t) - S^m(t+\Delta t)}{S^m(t+\Delta t)} \right| < 10^{-6} \quad . \quad (7-18)$$

This method for Equation (7-5) improves the calculation accuracy; the error is $O(\Delta t^3)$, and much larger integration time steps are therefore possible.

7.3.4 Results and discussions

Given the methodology introduced in Sections 7.3.2 and 7.3.3, the two-phase, moving boundary model is now compared to the experimental hydrogen desorption rate. As discussed in Section 7.3.2, the differential equations describing hydrogen diffusion in $\delta\text{-ZrH}_{1.6\pm n}$ must be solved first to provide the initial conditions for the Stefan problem. Combining the boundary and initial conditions indicated in Section 7.3.2, the hydrogen concentration distribution is obtained as a function of time. Fig. 7-10 shows the evolution of the hydrogen concentration across the $\delta\text{-ZrH}_{1.6\pm n}$ sample at different times.

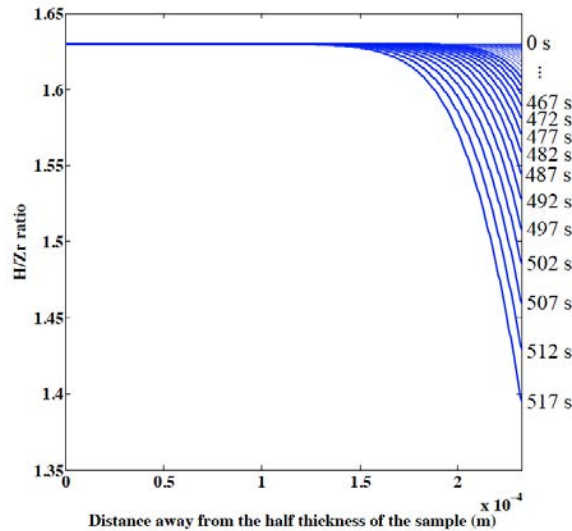


Figure 7-10. Evolution of H/Zr ratio distribution throughout the $\delta\text{-ZrH}_{1.6\pm n}$ disc.

Once the surface hydrogen concentration reaches the equilibrium limit, the dehydriding process enters the Stefan problem stage. The final state of the hydrogen distribution together with other boundary conditions completes the restrictions of Equations (7-3), (7-4), and (7-5).

The simulation of the Stefan problem stage consists of three steps: 1. Since the hydrogen desorption from $\delta\text{-ZrH}_{1.6\pm n}$ ends at 517 seconds, the Stefan problem starts in the temperature ramp stage; 2. As shown in Fig. 7-8, the simulation enters the long-term constant temperature region; 3. After sufficient time, the $\delta\text{-ZrH}_{1.6\pm n}$ is completely transferred to $\alpha\text{-Zr}$, and the problem becomes that of hydrogen diffusion in the $\alpha\text{-Zr}$ phase.

The hydrogen desorption rate during the annealing process shown in Fig. 7-8 is expected to be reproduced by the model, and as such, the predicted hydrogen flux should be used to compare with the experimental results. In addition, the model can provide very detailed information about the hydrogen concentration distribution across the sample at any computing step. The comparison between predicted and measured hydrogen flux is shown in Fig. 7-11.

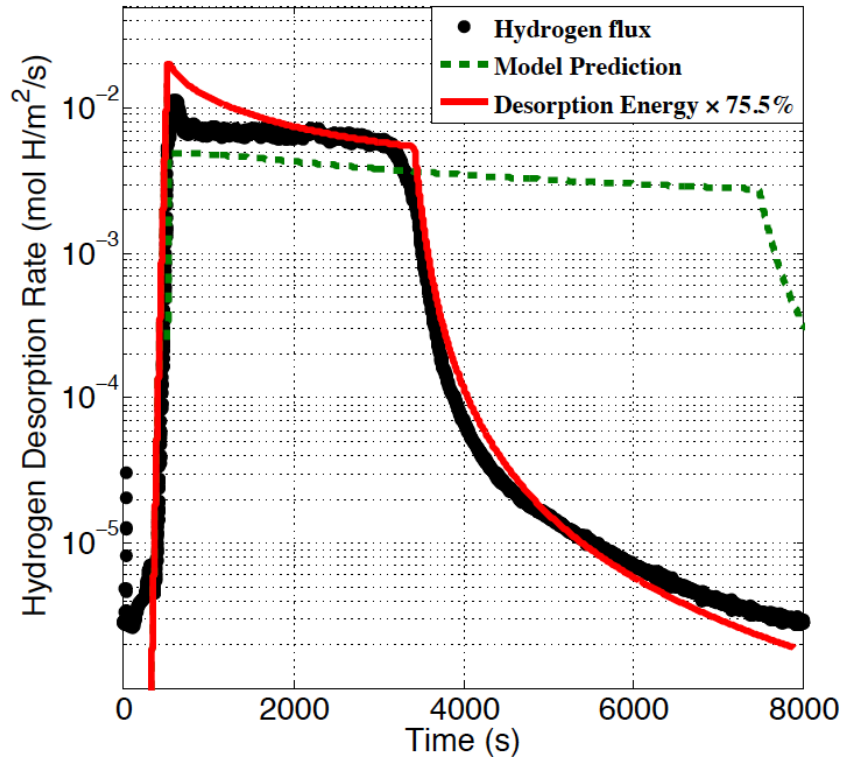


Figure 7-11. Comparison between the experimental and modeling results for hydrogen flux on the surface of the sample. The green dashed line indicates the modeling prediction with the original desorption activation energy; the red solid line refers to the modeling result with a desorption activation energy of 75.5% of the original value.

The model reproduces the zeroth-order desorption region, when the sample is single-phase $\delta\text{-ZrH}_{1.6\pm n}$, which occurs between 300 and about 517 seconds; however, it does not agree as well in the two-phase moving boundary region of the experiment if the original desorption activation energy (shown in Equation (7-12)) associated with second-order kinetics is used. It has been pointed out that the desorption activation energy could vary with experimental conditions [95, 96]. Therefore we varied this value and obtained much better agreement with the experimental data as the desorption activation energy decreases. The best comparison occurred with a value of $\epsilon = 42.9$ kJ/mol in the two-phase regime and is also plotted in Fig. 7-11 as the red curve denoting 75.5% of the original value of ϵ .

In the transient region, when the system transitions from single $\delta\text{-ZrH}_{1.6\pm n}$ phase to a two-phase regime, a sharp peak appears in the modeling results. Compared to the smooth transition of the experimental data, this is an obvious disagreement. In reality, the precipitation of $\alpha\text{-Zr}$ involves a nucleation stage that is ignored in this model. The instantaneous transition from the δ -hydride to the α -metal in the model produces a different hydrogen release profile than what is observed experimentally which involves a gradual conversion of the surface from the hydride to the metal via nucleation and growth processes of the $\alpha\text{-Zr}$. On the other hand, the model does reproduce the major features of the experimentally obtained hydrogen desorption flux on the sample surface following the experimental annealing process.

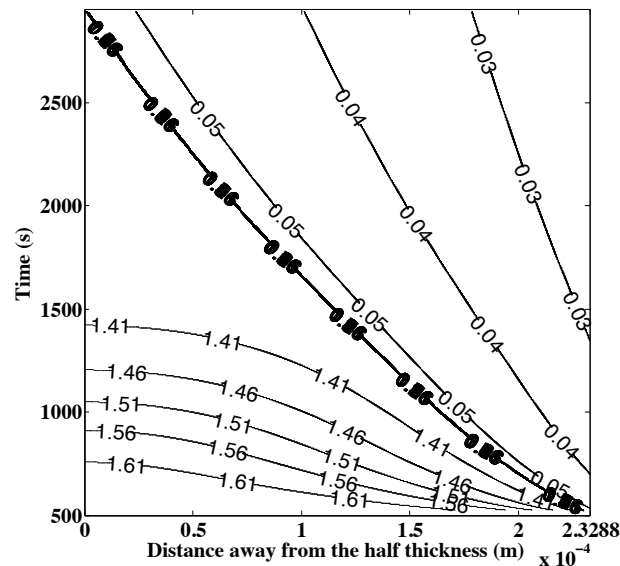


Figure 7-12. Evolution of hydrogen concentration across the disc as a function of time.

Since the Stefan problem has been applied to model the phase change in the $\delta\text{-ZrH}_{1.6\pm n}$ dehydriding process, it is interesting to show how the two-phase interface moves. Fig. 7-12 shows a contour plot that demonstrates the evolution of hydrogen concentration and

the motion of the interface (the overlapped lines, which mean two concentrations, C_δ and C_α , appear at the same position) in this process.

As to the modeling of the one-dimensional, two-phase, moving boundary problem, the accuracy and efficiency of the solution really depends on the exact nature of the problem itself [182]. In this study, for example, the specimen dimensional changes induced by the different densities of these two phases are not considered in the model and also contribute to the loss of accuracy during prediction of the hydrogen flux profile. In order to validate the model, more experimental conditions are needed. In addition to the application in the zirconium hydride, this model can easily be modified to simulate any other physical conditions involving Stefan problem.

7.4 Conclusion

δ phase zirconium hydride has been successfully produced and verified by XRD analysis. Hydrogen desorption results from the TDS experiment of these specimens provides evidence that the zeroth order kinetic model of hydrogen desorption are appropriate even in the lower temperature region, 430°C~525°C, however it is not appropriate in a broader time range at higher fixed temperature, i.e., 525°C. The TDS coordinated with a 1D two-phase moving interface model is applied to investigate the process of α -Zr precipitation from zirconium hydride at 525°C during hydrogen desorption. The evolution of the two-phase interface is calculated. The coordinated experimental and modeling study of hydrogen desorption from δ -zirconium hydride provides insight and a modeling paradigm that could be used to predict the performance of the hydride fuel and the cladding failure under vacuum annealing of used nuclear fuel, as well as severe reactor accidents.

Chapter 8

Conclusion and Future Work

This dissertation has investigated two cases of gas behavior in metals, namely, the helium-point defect interactions in iron and the kinetics of hydrogen desorption from zirconium hydride. This research has involved an extensive combination of experimental and modeling studies, with the objective of improving the knowledge of helium effects on structural materials in fusion and fission environments. Furthermore, this work has demonstrated the kinetics of hydrogen diffusion in zirconium hydride and Zr metal that are crucial for understanding the behavior of used nuclear fuel during vacuum annealing and long-term storage as well as cladding failure during accidents and the hydride fuel. In this final chapter, the key results are summarized and some ideas for future work are suggested.

8.1 Conclusion

8.1.1 Fundamental study of helium-point defect interactions in iron

The interactions of helium and point defect were explored by coordinated experimental and modeling methods. THDS was employed to obtain the helium desorption spectra of the He-implanted single crystal irons and PAS was applied to provide the information of He-vacancy clusters evolution, both of which provided an opportunity to verify the self-consistence of the developed rate theory based reaction-diffusion cluster dynamics model. The combination of experiments and modeling led to a better understanding of the helium-point defects in iron.

The major results are summarized as:

- THDS experiments of a different batch (i.e., higher purities) of single crystal irons with various He-implanting conditions were conducted as an addition to the previous experimental results, which enriched the database for the validation of the developed model.
- The He-vacancy cluster evolution was analyzed qualitatively by the employment of PAS at three selected points for the single crystal iron implanted by 40 keV He ions to a fluence of $1 \times 10^{15}/\text{cm}^2$.
- A rate theory based cluster dynamics model was introduced and used to model the experimental data. In addition to modeling the THDS performed under a linear annealing process, a new THDS result for a single crystal iron implanted

by 5 keV He ions to a fluence of 10^{15} He/cm² with a step-like temperature profile was successfully re-produced by the model.

- A phase-cut method was proposed to improve the computing efficiency of the model.
- The influence of carbon on the helium-point defect interactions was first discussed by demonstrating the THDS results for the He ion implanted single crystal iron samples of different purities. Then, the combination of the cluster dynamic model and the THDS results quantitatively indicated the influence of impurities on the energetics and kinetics of the He-point defect interactions.
- Mechanistic interpretation of helium desorption peaks and helium-vacancy cluster evolutions was achieved through detailed analysis of the modeling results. The helium-vacancy cluster evolutions predicted by the model were generally consistent with the PAS measurements. Moreover, a simple model was proposed to predict positron lifetimes, which could be compared with the experimental data directly.
- The rate theory based cluster dynamics model was extended by including the He-self-interstitial interactions.
- MD simulation was conducted to investigate the effects of the self-interstitial cluster on the helium clustering. The mutual validation of MD and cluster dynamic model was discussed.
- The influence of pre-existing defects on the helium behavior in iron was studied by modeling. A cluster dynamics model coupled with intra-cascade defects production mode was proposed to predict the final defect state of the single crystal iron samples exposed to neutron irradiation to different damage levels, which was used as the initial condition for the helium implantation and desorption modeling.

8.1.2 Kinetics of hydrogen desorption from zirconium hydride

The hydrogen desorption process from zirconium hydride and the subsequent metal in vacuum was also studied by coordinated experimental and modeling methods. The production and characterization of the desired δ -zirconium hydride was introduced while TDS was employed to obtain the hydrogen desorption spectra directly. In addition, a one-dimensional, two-phase moving boundary model coupled with a kinetic description of hydrogen desorption from a two-phase region of δ -ZrH_{1.6±n} and α -Zr was developed to reproduce the TDS experimental results.

8.2 Future work

8.2.1 Future work for the helium-point defect interactions in iron

The future work will be focused on extending the application and increasing the accuracy of the cluster dynamics model, and increasing the experimental database. The rate theory based cluster dynamics model could be improved by including more mobile species,

providing more accurate energetics parameters of the clusters, enhancing its computing efficiency, conducting more validation by comparing to additional experimental data, etc. The analysis introduced in Chapter 5 highlights the importance of helium-self-interstitial interactions. MD/MS, KMC, and ab initio methods can be applied to investigating the energetics and kinetics of the interactions. The influence of the pre-existing defects on helium behavior will be studied further based on the current modeling results. In order to verify the modeling predictions, additional experimental results are necessary. TEM will be employed to observe the cluster distribution of the single crystal iron samples after being exposed to neutron irradiation in HFIR for different damage levels. Such results will be compared directly to the predictions of the developed neutron irradiation model.

Furthermore, a new THDS system coupled with an in situ 20 keV He ion gun is under construction at Oak Ridge National Laboratory (ORNL), TN. Different from the THDS in Berkeley, the new system will have better background (i.e. desired vacuum level of 10^{-10} torr), finer temperature control, more accurate calibration system, more efficient mass spectrometer, etc. Meanwhile, the combination of the helium implantation and THDS helps to reduce the unexpected factors (e.g., risk of the sample damage, oxidation) during the sample transportation. The samples after neutron irradiation will be placed in this new system for He ion implantation and thermal desorption, which will provide new data of the helium desorption spectrum for comparison with the modeling results discussed in Chapter 6. In addition, a new positron annihilation spectroscopy is under development at ORNL to study the irradiation effects on the materials.

All of these studies will provide a better understanding of the irradiation effects on the materials and pave a road for predicting the long-term performance of the structural materials in fusion reactors.

8.2.2 Future work for the kinetics of hydrogen desorption from zirconium hydride and Zr

δ phase zirconium hydride will be produced under a better stoichiometry control so that the products with known H/Zr ratio will be strictly located in the δ phase. The TDS experiments for different samples with different H/Zr ratio under various annealing processes should be performed. The continuous model for the hydrogen desorption from zirconium hydride and the subsequent metal in vacuum will be improved by considering more factors, such as the dimension changes and the α -precipitation process. More efficient numerical methods should also be studied. Furthermore, the effects of the zirconium hydride on the mechanical properties of claddings in light water reactors and the irradiation effects on the microstructures of zirconium hydride used in hydride fuels will be studied further.

References

- [1] World Nuclear Association (December 2010), *World Energy Needs and Nuclear Power*, Accessed 19th December 2010, <http://www.world-nuclear.org/info/Current-and-Future-Generation/World-Energy-Needs-and-Nuclear-Power/#.UWmjFL80qgw>
- [2] Energy Information Administration, Washington, DC, Report DOE/EIA-0219, 2003.
- [3] J. Stringer and L.L. Horton, *Basic Research Needs to Assure a Secure Energy Future: A Report to the Basic Energy Sciences Advisory Committee*, OSTI document 811872 (Office of Science and Technical Information, Oak Ridge, TN, 2003).
- [4] J. P. Holdren, *Energy in Transition*, Scientific Am. 263 (1990) 157.
- [5] E.E. Bloom, S.J. Zinkle, F.W. Wiffen, *Materials to deliver the promise of fusion power – progress and challenges*, J. Nucl. Mater. 329-333 (2004) 12-19.
- [6] V. Barabsh et al., *Materials challenges for ITER- Current status and future activities*, J. Nucl. Mater. 367-370 (2007) 21-32.
- [7] A Technology Roadmap for Generation IV Nuclear Energy Systems, US Department of Energy, Office of Nuclear Energy, Science and Technology, GIF-002-00, 2002.
- [8] Global Nuclear Energy Partnership technology development plan. GNEP-TECH-TR-PP-2007-00020, rev. 0, Idaho Natl. Lab., Idaho Falls, ID.
- [9] Basic research needs for advanced nuclear energy systems, Rep. Basic Energy Sci. Workshop Basic Res. Needs Adv. Nucl. Energy Sys. July 31–Aug. 3, 2006, Rockville, MD.
- [10] R. Goldston, M. Abdou, C. Baker, M. Campbell, V. Chan, et al. 2002. *A plan for the development of fusion energy*. J. Fus. Energy 21:61–111
- [11] IAEA, *International Status and Prospects for Nuclear Power 2012*, Board of Governors General Conference, GOV/INF/2012/12-GC(56)/INF/6.
- [12] Ansolabehere SD, Deutsch J, Driscoll M, Gray PE, Holdren JP, Joskow, PL, et al. *The future of nuclear power*. Cambridge: MIT Press, (2003).

- [13] International Energy Agency IEA, *Costs of electricity*. (2010) Paris, France.
- [14] Committee on America's Energy Future, *America's Energy Future: Technology and Transformation*. National Academies Press, Washington (2009).
- [15] J. Koomey, N.E. Hultman, *A reactor-level analysis of busbar costs of US nuclear plants*. Energy Policy 35:5630-42, (2007).
- [16] A. Grubler, *The costs of the French nuclear scale-up: A case of negative learning by doing*. Energy Policy 38:5274-88, (2010).
- [17] K. Ehrlich. *The development of structural materials for fusion reactors*. Philos. Trans. R. Soc. London Ser. A 357 (1999) 595–623.
- [18] S.J. Zinkle, N.M. Ghoniem. *Operating temperature windows for fusion reactor structural materials*. Fus. Eng. Des. 51–52 (2000) 55–71.
- [19] H. Bolt, V. Barabash, W. Krauss, J. Linke, R. Neu, et al. *Materials for the plasma-facing components of fusion reactors*. J. Nucl. Mater. 329–333 (2004) 66–73.
- [20] S.J. Zinkle. *Advanced materials for fusion technology*. Fus. Eng. Des. 74 (2005) 31–40.
- [21] S.J. Zinkle. *Fusion materials science: overview of challenges and recent progress*. Phys. Plasmas 12 (2005) 058101.
- [22] W.R. Corwin. *U.S. Generation IV reactor integrated materials technology program*. Nucl. Eng. Technol. 38 (2006) 1–28.
- [23] E.E. Bloom, J.T. Busby, C.E. Duty, P.J. Maziasz, T.E. McGreevy, et al. *Critical questions in materials science and engineering for successful development of fusion power*. J. Nucl. Mater. 367–370 (2007) 1–10.
- [24] T.R. Allen, J.T. Busby, R.L. Klueh, S.A. Maloy, M.B. Toloczko. *Cladding and duct materials for advanced nuclear recycle reactors*. JOM 60 (2008) 15–23.
- [25] G.S. Was. *Materials degradation in fission reactors: lessons learned of relevance to fusion reactor systems*. J. Nucl. Mater. 367–370 (2007) 11–20.
- [26] www.engineeringchallenges.org/cms/8996/9221.aspx
- [27] E. E. Bloom, *The challenge of developing structural materials for fusion power systems*. J. Nucl. Mater. 258–263 (1998) 7–17.
- [28] B.D. Wirth, K. Nordlund, D.G. Whyte, D. Xu. *Fusion materials modeling*:

Challenges and opportunities. MRS Bull 36 (2011) 216.

- [29] L.K. Mansur, A.F. Rowcliffe, R.K. Nanstad, S.J. Zinkle, W.R. Corwin, R.E. Stoller, *Materials needs for fusion, Generation IV fission reactors and spallation neutron sources – similarities and differences.* J. Nucl. Mater. 329–333 (2004) 166–172.
- [30] L.K. Mansur, E.H. Lee, P.J. Maziasz, A.P. Rowcliffe, *Control of helium effects in irradiated materials based on theory and experiment.* J. Nucl. Mater. 141–143 (1986) 633–646.
- [31] E.V. Kornelsen, *The interaction of injected helium with lattice defects in a tungsten crystal.* Radiat. Eff. 13 (1972) 227–236.
- [32] L.K. Mansur and W.A. Coghlan, *Mechanisms of helium interaction with radiation effects in metals and alloys: A review.* J. Nucl. Mater. 119 (1983) 1–25.
- [33] H. Trinkaus, *Energetics and formation kinetics of helium bubbles in metals,* Radiat. Eff. 78 (1983) 189 – 211.
- [34] H. Trinkaus and B. N. Singh, *Helium accumulation in metals during irradiation – where do we stand?* J. Nucl. Mater. 323 (2003) 229 – 242.
- [35] P.J. Maziasz and C.J. McHargue. *Microstructural evolution in annealed austenitic steels during neutron irradiation.* Intern. Mater. Rev. 32 (1987) 190 – 219.
- [36] G. R. Odette, T. Yamamoto, H. J. Rathbun, M. Y. He, M. L. Hribernik, and J. W. Rensman. *Cleavage fracture and irradiation embrittlement of fusion reactor alloys: mechanisms, multiscale models, toughness measurements and implications to structural integrity assessment.* J. Nucl. Mater. 323 (2003) 313 – 340.
- [37] R. Schaublin, J. Henry, Y. Dai. *Helium and point defect accumulation: (i) microstructure and mechanical behavior.* C. R. Physique 9 (2008) 389 – 400.
- [38] F.W. Wiffen and E. E. Bloom. *Effect of high helium content on stainless steel swelling.* Nuclear Technology 25 (1975) 113.
- [39] H. Schroeder, W. Kesternich and H. Ullmaier. *Helium effects on the creep and fatigue resistance of austenitic stainless steels at high temperatures.* Nuclear Engineering and Design/Fusion, 2 (1985) 65 – 95.
- [40] N. Baluc, R. Schaublin, P. Spatig, M. Victoria. *On the potentiality of using ferritic/martensitic steels as structural materials for fusion reactors.* Nuclear Fusion 44 (2004) 56 – 61.
- [41] H. Schroeder and H. Ullmaier. *Helium and hydrogen effects on the embrittlement*

- of iron- and nickel-based alloys*. J. Nucl. Mater. 179 – 181 (1991) 118 – 124.
- [42] A. Kohyama, A. Hishinuma, D.S. Gelles, R.L. Klueh, W. Dietz, K. Ehrlich. *Low-activation ferritic and martensitic steels for fusion application*. J. Nucl. Mater. 233 – 237 (1996) 138 –147.
 - [43] D.S. Gelles. *On quantification of helium embrittlement in ferritic/martensitic steels*. J. Nucl. Mater. 283 – 287 (2000) 838–840.
 - [44] M.J. Caturla, C.J. Ortiz, C.C. Fu. *Helium and point defect accumulation: (ii) Kinetic modeling*. C. R. Physique 9 (2008) 401 – 408.
 - [45] G. R. Odette, B. D. Wirth, D. J. Bacon and N. M. Ghoneim, *Multiscale-Multiphysics Modeling of Radiation-Damaged Materials: Embrittlement of Pressure Vessel Steels*, MRS Bulletin 26 (2001) 176.
 - [46] B.D. Wirth, G.R. Odette, J. Marian, L. Ventelon, J.A. Young and L.A.Zepeda-Ruiz. *Multiscale modeling of radiation damage in Fe-based alloys in the fusion environment*. Journal of Nuclear Materials 329-333 (2004) 103-111.
 - [47] K. Arakawa, R. Imamura, K. Ohota, and K. Ono. *Evolution of point defect clusters in pure iron under low-energy He⁺ irradiation*. J. Applied Physics. 89 (2001) 4752-4757.
 - [48] K. Ono et al., *Release of helium from irradiation damage in Fe–9Cr ferritic alloy*. J. Nucl. Mater. 329–333 (2004) 933-937.
 - [49] M.B. Lewis and K. Farrell. *Migration behavior of helium under displacive irradiation in stainless steel, nickel, iron and zirconium*. Nucl. Instrum. Methods Phys. Res. B 16 (1986) 163-170.
 - [50] T. Ishizaki, Q. Xu, T. Yoshiie, S. Nagata, T. Troev. *The effect of hydrogen and helium on microvoid formation in iron and nickel*. J. Nucl. Mater. 307-311 (2002) 961-965.
 - [51] R. Sugano, K. Morishita, A. Kimura. *Helium accumulation behavior in iron based model alloys*. Fusion Sci. Technol. 44 (2003) 446-449.
 - [52] R. Vassen, H. Trinkaus, P. Jung. *Helium desorption from Fe and V by atomic diffusion and bubble migration*. Phys. Rev. B 44 (1991) 4206-4213.
 - [53] D. Xu, T. Bus, S.C. Glade, B.D. Wirth. *Thermal helium desorption spectrometry of helium-implanted iron*. J. Nucl. Mater. 367–370 (2007) 483-488.
 - [54] D. Xu and B.D. Wirth. *Post-implantation thermal desorption of helium from poly- and single-crystal iron*. J. Nucl. Mater. 386–388 (2009) 395-399.

- [55] J. Rothaut, H. Schroeder and H. Ullmaier. *The growth of helium bubbles in stainless steel at high temperatures*. Philosophical Magazine A. 47(5) 1983 781-795.
- [56] Q. Xu, X. Cao, K. Sato, T. Yoshiie, and T. Iwai. *He bubble formation and emission of He in irradiated Fe*. Phy. Status Solidi C, 6 (2009) 2336-2338.
- [57] K.C. Russell. *The theory of void nucleation in metals*. Acta. Metallurgica. 26 (1978) 1615-1630.
- [58] N.M. Ghoniem, S. Sharafat, J.M. Williams and L.K. Mansur. *Theory of helium transport and clustering in materials under irradiation*. J. Nucl. Mater. 117 (1983) 96-105.
- [59] R.E. Stoller and G.R. Odette. *Anlytical solutions for helium bubble and critical radius parameters using a hard sphere equation of state*. J. Nucl. Mater. 131 (1985) 118-125.
- [60] K. Morishita, R. Sugano and B.D. Wirth. *Thermal stability of helium-vacancy clusters and bubble formation – multiscale modeling approach for fusion materials development*. Fusion Science and Technology. 44 (2003) 441-445.
- [61] C.C. Fu and F. Willaime. *Ab initio study of helium in α -Fe: Dissolution, migration, and clustering with vacancies*. Physical Review B 72 (2005) 064117.
- [62] L. Ventelon, B.D. Wirth, and C. Domain. *Helium-self-interstitial atom interaction in α -Fe*. J. Nucl. Mater. 351 (2006) 119-132.
- [63] T. Seletskaiia, Y.N. Osetsky, R.E. Stoller, G.M. Stocks. *Calculation of helium defect clusering properties in iron using a multi-scale approach*. J. Nucl. Mater. 351 (2006) 109-118.
- [64] H.L. Heinisch, F. Gao, R.J. Kurtz, E.A. Le. *Interaction of helium atoms with edge dislocations in α -Fe*. J. Nucl. Mater. 351 (2006) 141-148.
- [65] R.J. Kurtz, H.L. Heinisch. *The effects of grain boundary structure on binding of He in Fe*. J. Nucl. Mater. 329-333 (2004) 1199-1203.
- [66] D. Stewart, Y. Osetskiy and R.E. Stoller. *Atomistic studies of formation and diffusion of helium clusters and bubbles in BCC iron*. J. Nucl. Mater. 417 (2006) 1110-1114.
- [67] C.J. Ortiz and M.J. Caturla. *Simulation of defect evolution in irradiated materials: Role of intracascade clustering and correlated recombination*. Physical Review B. 75 (2007) 184101.

- [68] M.J. Caturla and C.J. Ortiz. *Effects of self-interstitial cluster migration on helium diffusion in iron*. J. Nucl. Mater. 362 (2007) 141-145.
- [69] S.I. Golubov, A.M. Ovcharenko, et al. *Grouping method for the approximate solution of a kinetic equation describing the evolution of point-defect clusters*. Philosophical Magazine A. 81(3) (2001) 643-658.
- [70] S.I. Golubov, R.E. Stoller, S.J. Zinkle, A.M. Ovcharenko. *Kinetics of coarsening of helium bubbles during implantation and post-implantation annealing*. J. Nucl. Mater. 361 (2007) 149-159.
- [71] D. Xu and B.D. Wirth. *Spatially dependent rate theory modeling of thermal desorption spectrometry of helium-implanted iron*. Fusion Science and Technology 56 (2009) 1064-1068.
- [72] D. Xu and B.D. Wirth. *Modeling spatially dependent kinetics of helium desorption in BCC iron following He ion implantation*. J. Nucl. Mater. 403 (2010) 184-190.
- [73] J.R. Lamarsh and A.J. Baratta, *Introduction to Nuclear Engineering*. Third Edition ed. 2001, Upper Saddle River, NJ: Prentice Hall.
- [74] Lemaignan, C. and A.T. Motta, *Zirconium Alloys in Nuclear Applications, in Materials Science and Technology, A Comprehensive Treatment*, R.W. Cahn, P. Haasen, and E.J. Kramer, Editors. 1994, VCH: New York. p. 1-51.
- [75] M. Steinbruck. *Hydrogen absorption by zirconium alloys at high temperatures*. J. Nucl. Mater. 334 (2004) 58-64.
- [76] A.T. Motta and L.Q. Chen. *Hydride formation in zirconium alloys*. JOM. 64 (2012) 1403-1408.
- [77] R. Yang, O. Ozer, and H. Rosenbaum, *Light Water Reactor Fuel Performance Meeting*, ed. P. Macdonald (Park City, UT:ANS, 2000).
- [78] G.P. Sabol, R. Comstock, G. Schoenberger, H. Kunishi, and D.L. Nuhfer, *Proceedings of International Topical Meeting on Light Water Reactor Fuel Performance*, Portland, OR (1997), p. 397.
- [79] J. Desquines, D.A. Koss, A.T. Motta, B. Cazalis, and M. Petit. *The issue of stress state during mechanical tests to assess cladding performance during a reactivity-initiated accident (RIA)*. J. Nucl. Mater. 412 (2011) 250-267.
- [80] J.C. Clayton. *Cladding corrosion and hydriding in irradiated defected Zircaloy-4 fuel rods*. Corrosion, 45(12) (1989) 996-1002.

- [81] J.J. Kearns. *Dissolution kinetics of hydride platelets in Zircaloy-4*. J. Nucl. Mater. 27 (1968) 64-72.
- [82] J.J. Kearns. *Terminal solubility and partitioning of hydrogen in the alpha phase of zirconium, Zircaloy-2 and Zircaloy-4*. J. Nucl. Mater. 22(1967) 292-303.
- [83] McMinn, E.C. Darby, J.S. Schofield. *The Terminal Solid Solubility of Hydrogen in Zirconium Alloys*. Zirconium in the Nuclear Industry: The Twelfth International Symposium. ASTM STP 1354 (2000) 173-195.
- [84] D.L. Douglass, *The Metallurgy of Zirconium*. (Vienna: International Atomic Energy Agency Supplement, 1971).
- [85] C.E. Ells. *Hydride precipitates in zirconium alloys*. J. Nucl. Mater. 28 (1968) 129-151.
- [86] R.S. Daum, Y.S. Chu, and A.T. Motta. *Identification and quantification of hydride phases in Zircaloy-4 cladding using synchrotron X-ray diffraction*. J. Nucl. Mater. 392 (2009) 453-463.
- [87] N.F. Davies, R.E. Forrester, *Effects of Irradiation on Hydrided Zirconium–Uranium Alloy NAA 120-4 Experiment*, AI-AEC-12963, SNAP Program.
- [88] M.T. Simnad. *The U-ZrH_x alloy: its properties and use in TRIGA fuel*. Nucl. Eng. Design. 64 (1981) 403–422.
- [89] Full issue, *Hydride fueled LWRs*. Nucl. Eng. Design. 239 (2009) 1373-1570.
- [90] K. A. Terrani, M. Balooch et al. *The kinetics of hydrogen desorption from and adsorption on zirconium hydride*. J. Nucl. Mater. 397 (2010) 61–68.
- [91] N. Dupin, I. Ansara et al. *A thermodynamic database for zirconium alloys*. J. Nucl. Mater. 275 (1999) 287–295.
- [92] W.E. Wang and D.R. Olander. *Thermodynamics of the Zr-H system*. J. Am. Ceram. Soc. 78 (1995) 3323-3328.
- [93] D. Wongsawaeng and S. Jaiyen. *High-temperature absolute hydrogen desorption kinetics of zirconium hydride under clean and oxidized surface conditions*. J. Nucl. Mater. 403(2010) 19-24
- [94] D. Gutkowski, *Kinetics of hydrogen uptake and release from zirconium hydride*, M.S. Thesis, Dept. of Nuclear Engineering, University of California at Berkeley, 2005.

- [95] K. Ichimura et al. *Absorption and desorption of hydrogen, deuterium, and tritium for Zr-V-Fe getter*. J. Vac. Sci. Technol. A 2 (1984) 1341-1347.
- [96] S. Naito. *Kinetics of hydrogen absorption by α -zirconium*. J.Chem. Phys. 79 (1983) 3113-3120.
- [97] G. Carter. *Thermal resolution of desorption energy spectra*. Vacuum. 12 (1962) 245-254.
- [98] P.A. Redhead. *Thermal desorption of gases*. Vacuum. 12 (1962) 203-211.
- [99] E. Kautto, O-P. Kahkonen, J. Kuhalainen, M. Manninen. *Facility for thermal helium desorption (THDS) measurements*. Nucl. Instr. and Meth. in Phys. Res. B 103 (1995) 376-382.
- [100] van Veen, A. Warnaar, L.M. Caspers. *Clustering of krypton in tungsten observed by helium desorption spectrometry*. Vacuum 30 (1980) 109-115.
- [101] W.A. Johnson, R.F. Mehl. *Reaction Kinetics in Processes of Nucleation and Growth*. Trans. Am. Inst. Min. Metall. Eng. 135 (1939) 416-442.
- [102] M. Avrami, *Kinetics of Phase Change. I General Theory*. J. Chem. Phys. 7 (1939) 1103-1112.
- [103] J.F. Ziegler, J.P. Biersack, U. Littmark, *The Stopping and Range of Ions in Matter*, Pergamon, New York, 1984.
- [104] R.W. Siegel. *Positron annihilation spectroscopy*. Ann. Rev. Mater. Sci. 10 (1980) 393-425.
- [105] E. Kuramoto, H. Abe, M. Takenaka, F. Hori, Y. Kamimura, M. Kimura, K. Ueno. *Positron annihilation lifetime study of irradiated and deformed Fe and Ni*. J. Nucl. Mater. 239 (1996) 54-60.
- [106] A. Seeger. *The study of defects in crystals by positron annihilation*. Appl. Phys. 4 (1974) 183-199.
- [107] I. Prochazka. *Positron annihilation spectroscopy*. Materials Structure. 8 (2001) 55-60.
- [108] T.E.M. Staab, R. Krause-Rehberg, B. Kieback. *Review: Positron annihilation in fine-grained materials and fine powders-an application to the sintering of metal powders*. J. Mater. Sci. 34 (1999) 3833-3851.

- [109] H. Saito, Y. Nagashima, T. Kurihara, T. Hyodo. *A new positron lifetime spectrometer using a fast digital oscilloscope and BaF2 scintillators*. Nucl. Instr. Meth. A 487 (2002) 612-617.
- [110] J. Kansy. *Microcomputer program for analysis of positron annihilation lifetime spectra*. Nucl. Instr. Meth. A 374 (1996) 235-244.
- [111] T. Troev, E. Popov, P. Staikov, N. Nankov. *Positron lifetime studies of defects in α -Fe containing helium*. Phys. Status Solidi C. 6 (2009) 2373-2375.
- [112] P. Erhart, J. Marian. *Calculation of the substitutional fraction of ion-implanted He in an α -Fe target*. J. Nucl. Mater. 414 (2011) 426-430.
- [113] T.R. Waite. *Theoretical treatment of the kinetics of diffusion-limited reactions*. Physical review. 107 (1957) 463-470.
- [114] C.J. Ortiz, et al. *A physically based model for the spatial and temporal evolution of self-interstitial agglomerates in ion-implanted silicon*. J. Appl. Phys. 96 (2004) 4866-4877.
- [115] D. Xu, B.D. Wirth, M. Li and M.A. Kirk. *Combining in situ transmission electron microscopy irradiation experiments with cluster dynamics modeling to study nanoscale defect agglomeration in structural metals*. Acta Materialia. 60 (2012) 4286-4302.
- [116] H.L. Heinisch, F. Gao, R.J. Kurtz, E.A. Le. *Interaction of helium atoms with edge dislocations in α -Fe*. J. Nucl. Mater. 351 (2006) 141-148.
- [117] J.N. Bronsted. Z. Phys. Chem. 102 (1922) 169-207
- [118] M. von Smoluchowski. Z. Phys. Chem., Stoechiom. Verwandtschaftsl. 92 (1917) 129.
- [119] C.J. Ortiz, M.J. Caturla, C.C. Fu and F. Willaime. *He diffusion in irradiated α -Fe: An ab-initio-based rate theory model*. Physical Review B. 75 (2007) 100102.
- [120] R.E. Stoller, G.R. Odette, B.D. Wirth. *Primary damage formation in bcc iron*. J. Nucl. Mater. 251 (1997) 49-60.
- [121] B.D. Wirth, G.R. Odette, D. Maroudas, G.E. Lucas. *Energetics of formation and migration of self-interstitials and self-interstitial clusters in α -iron*. J. Nucl. Mater. 244 (1997) 185-194.
- [122] N. Soneda, T. Diaz de la Rubia. *Defect production, annealing kinetics and damage evolution in α -Fe: An atomic-scale computer simulation*. Phil. Mag. A 78 (1998) 995-1019.

- [123] J. Marian, B.D. Wirth, B. Sadigh, G.R. Odette, J.M. Perlado and T. Diaz de la Rubia. *Dynamics of self-interstitial cluster migration in pure α -Fe and Fe-Cu alloys*. Phys. Rev. B 65 (2002) 144102.
- [124] A.F. Calder and D.J. Bacon. *A molecular dynamics study of displacement cascades in α -iron*. J. Nucl. Mater. 207 (1993) 25-45.
- [125] H.L. Heinisch, B.N. Singh, S.I. Golubov. *The effects of one-dimensional glide on the reaction kinetics of interstitial clusters*. J. Nucl. Mater. 283-287 (2000) 737-740.
- [126] C.C. Fu, J.D. Torre, F. Willaime, J.L. Bocquet and A. Barbu. *Multiscale modeling of defect kinetics in irradiated iron*. Nature Materials. 4 (2005) 68-74.
- [127] D. Xu, B.D. Wirth, M. Li, M.A. Kirk. *Defect microstructural evolution in ion irradiated metallic nanofoils: Kinetic Monte Carlo simulation versus cluster dynamics modeling and in situ transmission electron microscopy experiments*. Appl. Phys. L. 101 (2012) 101905.
- [128] D. Xu, X. Hu, B.D. Wirth. *A phase-cut method for multi-species kinetics: Sample application to nanoscale defect cluster evolution in alpha iron following helium ion implantation*. Appl. Phys. L. 102 (2013) 011904.
- [129] O. Schenk, K. Gartner. *Solving unsymmetric sparse systems of linear equations with PARDISO*. Future Gener. Comp. Sys. 20 (2004) 475-487.
- [130] O. Schenk, K. Gartner. *On fast factorization pivoting methods for sparse symmetric indefinite systems*. Elec. Trans. Numer. Anal. 23 (2006) 158-179.
- [131] Rafiei, M. Bollhofer. *Robust incomplete factorization for nonsymmetric matrices*. Numer. Math. 118 (2011) 247-269.
- [132] A. Fick. *Ueber diffusion*. Annalen der Physik. 170 (1855) 59-86.
- [133] C.J. Ortiz, M.J. Caturla, C.C. Fu, F. Willaime. *Impurity effects on He diffusion in α -Fe*. J. Nucl. Mater. 386-388 (2009) 33-35.
- [134] K. Morishita, R. Sugano, B.D. Wirth, T. Diaz de la Rubia. *Thermal stability of Helium-vacancy clusters in iron*. Nucl. Instrum. Methods. Phys. Res. B 202 (2003) 76-81.
- [135] C. Domain, C.S. Becquart, J. Foct. *Ab initio study of foreign interstitial atom (C, N) interactions with intrinsic point defects in α -Fe*. Phys. Rev. B 69 (2004) 144112.

- [136] C.J. Först, J. Slycke, K.J. Van Vliet, S. Yip. *Point defect concentration in metastable Fe-C alloys*. Phys. Rev. Lett. 96 (2006) 175501.
- [137] A. Hardouin-Duparc, A. Barbu. *Clustering of point defects under electron irradiation in dilute iron alloys and an iron manganese nickel alloy*. Mater. Res. Soc. Symp. Proc. 439 (1997) 509.
- [138] M. Kiritani. *History, present status and future of the contribution of high-voltage electron microscopy to the study of radiation damage and defects in solids*. Ultramicroscopy 39 (1991) 135.
- [139] S. Takaki, J. Fuss, H.K.U. Dedek, H. Schultz. *The resistivity recovery of high purity and carbon doped iron following low temperature electron irradiation*. Radiat. Eff. 79 (1983) 87.
- [140] L.M. Caspers, A. Van Veen, M.R. Ypma, R. Fastenau. *Interaction of helium with small self-interstitial platelets in α -Fe*. Phys. Stat. Sol. (a) 52 (1979) 61-64.
- [141] LAMMPS Molecular Dynamics Simulator. Sandia National Laboratory.
<http://lammps.sandia.gov>
- [142] G.J. Ackland, D.J. Bacon, A.F. Calder, T. Harry. *Computer simulation of point defect properties in dilute Fe - Cu alloy using a many-body interatomic potential*. Philos. Mag. A 75 (1997) 713.
- [143] N. Juslin, K. Nordlund. *Pair potential for Fe-He*. J. Nucl. Mater. 382 (2008) 143-146.
- [144] A.R. Janzen, R.A. Aziz. *An accurate potential energy curve for helium based on ab initio calculations*. J. Chem. Phys. 107 (1997) 914-919.
- [145] R.E. Stoller, S.I. Golubov, C. Domain, C.S. Becquart. *Mean field rate theory and object kinetic Monte Carlo: A comparison of kinetic models*. J. Nucl. Mater. 382 (2008) 77-90.
- [146] Y.N. Osetskiy, D.J. Bacon, A. Serra, B.N. Singh, S.I. Golubov. *One-dimensional atomic transport by clusters of self-interstitial atoms in iron and copper*. Philos. Mag. A 83 (2003) 61-91.
- [147] C.C. Fu, F. Willaime, P. Ordejon. *Stability and mobility of mono- and di-interstitials in α -Fe*. Phys. Rev. Lett. 92 (2004) 175503.
- [148] P. Asoka-Kumar, B.D Wirth, P.A. Sterne, R.H. Howell, G.R. Odette. *Composition and magnetic character of nanometer Cu-precipitates in reactor pressure vessel steels: Implications for nuclear power plant lifetime extension*. Philos. Mag. Lett. 82 (2002) 609.

- [149] K. Arakawa, K. Ono, M. Isshiki, K. Mimura, M. Uchikoshi, H. Mori. *Observation of the One-Dimensional Diffusion of Nanometer-Sized Dislocation Loops*. Science 318 (2007) 956-959.
- [150] M.T. Robinson. BNES nuclear fusion reactors. London: British Nuclear Energy Society; 1970
- [151] P.R. Monasterio, B.D. Wirth, G.R. Odette. *Kinetic Monte Carlo modeling of cascade aging and damage accumulation in Fe–Cu alloys*. J. Nucl. Mater. 361 (2007) 127-140.
- [152] F. Bergner, A. Almazouzi, M. Hernandez-Mayoral, M. Lambrecht, A. Ulbricht. *In Combined TEM, PAS and SANS Investigations of Neutron Irradiated Pure Iron*, Workshop Proceedings Karlsruhe, Germany, June 4–6, 2007; Nuclear Energy Agency, No. 260, OECD, 2008, 283–290.
- [153] A. Gokhman, F. Bergner. *Cluster dynamics simulation of point defects in neutron irradiated pure iron*. Radiation Effects & Defects in Solids: Incorporating Plasma Science & Plasma Technology. 165 (2010) 216-226.
- [154] U. Merten et. al. *The Preparation and Properties of Zirconium-Uranium-Hydrogen Alloys*. Proceedings of the Second Conference on Peaceful Uses of Atomic Energy. (1958) 789.
- [155] M. Simnad. *Method of Fabricating a Fuel Element*. US Patent number 3,154,845 (1964).
- [156] R. Van Houten. *Massive Metal Hydride Structures and Methods for Their Preparation*. US Patent Number 3,720,752 (1973).
- [157] M. Simnad et. al. *Method of Hydriding*. US Patent number 3,135,697 (1964).
- [158] U. Merten. *Production of Zirconium Hydride*. US Patent Number 3,070,526 (1962).
- [159] G. Majer, W. Renz, R. Barnes. *The mechanism of hydrogen diffusion in zirconium dihydrides*. J. Phys.: Condens. Matter 6 (1994) 2935
- [160] C. San Marchi, B. Somerday, S. Robinson, *Permeability, solubility and diffusivity of hydrogen isotopes in stainless steels at high gas pressures*. Int. J. Hydrogen Energy 32 (2007) 100-116.
- [161] K. Moore, W. Young. *Phase study of the Zr-H system at high hydrogen concentrations*. J. Nucl. Mater. 27 (1968) 316-324.

- [162] S. Yamanaka, K. Yamada, et al. *Characteristics of zirconium hydride and deuteride. J. Alloy and Compounds*. 330-332 (2002) 99-104.
- [163] R. Beck. *Zirconium-hydrogen phase system*. Trans. Am. Soc. Met. 55 (1962) 542-555.
- [164] T.C. Illingworth and I.O. Golosnoy. *Numerical solutions of diffusion-controlled moving boundary problems which conserve solute*. Journal of Computational Physics, 209 (2005) 207–225.
- [165] R. A. Tanzilli and R. W. Heckel. *An analysis of interdiffusion in finite-geometry, two-phase diffusion couples in the Ni–W and Ag–Cu systems*. Metallurgical and Materials Transactions A, 2 (1971) 1779–1784.
- [166] K. Bhanumurthy, G. B. Kale, S. K. Khera, and M. K. Asundi. *Solid-State diffusion reaction and formation of intermetallic compounds in the nickel-zirconium system*. Metallurgical and Materials Transactions A, 21 (1990) 2897–2903.
- [167] D. S. Duvall, W. A. Owczarski and D. F. Paulonis. *TLP Bonding: A New Method for Joining Heat Resistant Alloys*. Welding Journal, 53 (1974) 203–214.
- [168] I. Tuah-Poku, M. Dollars, and T. B. Massalsi. *A study of the transient liquid phase bonding process applied to a Ag/Cu/Ag sandwich joint*. Metallurgical and Materials Transactions A, 19 (1988) 675–686.
- [169] W. A. Kaysser, W. J. Huppmann, and G. Petzow. *Analysis of Dimensional Changes During Sintering of Fe–Cu*. Powder Metallurgy, 23 (1980) 86–91.
- [170] J. Crank, *Free and Moving Boundary Problems*, Clarendon Press, Oxford, 1984.
- [171] T.C. Illingworth, I.O. Golosnoy, V. Gergely, and T. W. Clyne. *Numerical modeling of transient liquid phase bonding and other diffusion controlled phase changes*. Journal of Materials Science, 40 (2005) 2505–2511.
- [172] Y. Zhou and T. H. North. *Kinetic modeling of diffusion-controlled, two-phase moving interface problems*. Modeling and Simulation in Materials Science and Engineering, 1 (1993) 505–516.
- [173] P. Reverberi. E. Scalas, and F. Veglio. *Numerical solution of moving boundary problems in diffusion processes with attractive and repulsive interactions*. Journal of Physics A: Mathematical and Theoretical, 35 (2002) 1575–1588.

- [174] E. Javierre, C. Vuik, F. J. Vermolen, and S. van der Zwaag. *A comparison of numerical models for one-dimensional Stefan problems*. Journal of Computational and Applied Mathematics, 192 (2006) 445–459.
- [175] J. Crank, *The Mathematics of Diffusion*, second ed., Clarendon Press, Oxford, 1976.
- [176] N. Dupin, I. Ansara, C. Servant et al. *A thermodynamic database for zirconium alloys*. Journal of Nuclear Materials, 275 (1999) 287–295.
- [177] K. A. Terrani et al. *Transient hydride fuel behavior in LWRs*. Journal of Nuclear Materials, 392 (2009) 192–199.
- [178] H. Nakagawa, C.H. Lee, and T.H. North. *Modeling of base metal dissolution behavior during transient liquid-phase brazing*. Metallurgical and Materials Transactions A, 22 (2) (1991) 543–555.
- [179] S.R. Cain, J.R. Wilcox, and R. Venkatraman. *A diffusional model for transient liquid phase bonding*. Acta Materialia, 45 (2) (1997) 701–707.
- [180] T. Shinmura, K. Ohsasa, and T. Narita. *Isothermal Solidification Behavior during the Transient Liquid Phase Bonding Process of Nickel Using Binary Filler Metals*. Materials Transactions, 42 (2) (2001) 292–297.
- [181] J. Crank and P. Nicolson. *A practical method for numerical evaluation of solutions of partial differential equations of the heat-conduction type*. Mathematical Proceedings of the Cambridge Philosophical Society, 43 (1947) 50–67.
- [182] R.M. Furzeland. *A comparative study of numerical methods for moving boundary problems*. Journal of the Institute of Mathematics and its Applications, 26 (1980) 411–429.
- [183] D. Xu, X. Hu, Reports in Wirth’s research group.